INFORMATION TO USERS

This manuscript has been reproduced from the microfilm master. UMI films the text directly from the original or copy submitted. Thus, some thesis and dissertation copies are in typewriter face, while others may be from any type of computer printer.

The quality of this reproduction is dependent upon the quality of the copy submitted. Broken or indistinct print, colored or poor quality illustrations and photographs, print bleedthrough, substandard margins, and improper alignment can adversely affect reproduction.

In the unlikely event that the author did not send UMI a complete manuscript and there are missing pages, these will be noted. Also, if unauthorized copyright material had to be removed, a note will indicate the deletion.

Oversize materials (e.g., maps, drawings, charts) are reproduced by sectioning the original, beginning at the upper left-hand corner and continuing from left to right in equal sections with small overlaps.

Photographs included in the original manuscript have been reproduced xerographically in this copy. Higher quality 6" x 9" black and white photographic prints are available for any photographs or illustrations appearing in this copy for an additional charge. Contact UMI directly to order.

Bell & Howell Information and Learning
300 North Zeeb Road, Ann Arbor, MI 48106-1346 USA

UMI®
800-521-0600

FINITE ELEMENT SIMULATION OF FLOW IN TWIN SCREW EXTRUDER MIXING ELEMENTS

By

VICTOR BRAVO

A Thesis

Submitted to the School of Graduate Studies

in Partial Fulfillment of the Requirements

for the Degree

Doctor of Philosophy

McMaster University

FINITE ELEMENT SIMULATION OF FLOW IN TWIN SCREW EXTRUDER MIXING ELEMENTS

To the memory of my father, Rafael Bravo Medina

DOCTOR OF PHILOSOPHY (1998)
(Chemical Engineering)

McMASTER UNIVERSITY
Hamilton, Ontario

TITLE: Finite Element Simulation of Flow in Twin Screw Extruder Mixing Elements

AUTHOR: Victor Bravo
Mech. Eng. (Universidad del Zulia, Venezuela)
M. Eng. (McMaster University)

SUPERVISOR: Drs. A. N. Hrymak and J. D. Wright
(Chemical Engineering)

NUMBER OF PAGES: xxi, 197.

ABSTRACT

In the plastics industry, twin screw extruders are widely used for melting, dispersing and homogenizing polymers. There are a diversity of designs employed throughout the polymer industry, each one having different operating principles and applications. Among the different arrangements of twin screw systems, the intermeshing co-rotating configuration has been found to be one of the most efficient mixers and it is one of the most commonly used pieces of equipment among the continuous mixers due to its self wiping properties.

The problem of mixing of polymers involves aspects of fluid dynamics and rheology. Mixing is usually obtained through a combination of mechanical motion of the mixing device and the resulting deformation induced in the flowing material. The quantitative description of the flow patterns is now feasible even in the most complicated geometries through the development of computational fluid dynamics (CFD) tools and the continuous increase in computer resources at lower costs. Intermeshing co-rotating twin screw extruders (ICRTSE) are usually built in a modular fashion to meet the diversity of tasks performed by this type of machine. There are two main types of elements: full flight conveying elements and kneading block mixing elements. The kneading blocks have been the focus of attention for the theoretical analysis of flow due to their significant contribution to the mixing performance of the extruder and the fact that kneading blocks normally work under a fully filled channel condition, which is one of the fundamental assumptions in CFD simulations.

The objective of this thesis is to understand the flow mechanisms in the kneading disc section of co-rotating twin screw extruders. This is done by means of the 3D numerical simulation of the flow process within the complex geometry involving intricate passages and continuously moving surfaces. A quasi-steady state finite element model was developed assuming isothermal, non-Newtonian flow. The intricate geometry of the kneading disc section required the development of a tailored finite element mesh generator.

An analysis based on particle trajectories, calculated from the obtained velocity field, was carried out to study the effect of geometry on the mixing performance. The

approach used for the initial location of the particle tracers was to cover the entire cross section of the kneading blocks. The problem of particles leaving the flow field due to time discretization was addressed by determining the locations where particles crossed the solid surfaces of the discs and reincorporating them into the flow field. The calculation of particle trajectories and deformation history give valuable information about the rapid fluctuations in shear stress experienced by different particles within the flow field.

A rigorous examination of the model results was carried out. Comparisons of the 3D model against experimental pressure data in the radial and axial directions are presented. The simulation results were also compared against experimental results of velocity obtained via particle image velocimetry. Results confirmed the ability of the model to predict the flow behavior. It was determined that inlet and outlet boundary conditions play a significant role in the development of flow patterns in the kneading disc section. The assumption of isothermal flow introduces limitations in the predictions made by the model. Future work should include the addition of the energy equation to the model.

Acknowledgements

For the development and writing of this thesis I feel a deep sense of gratitude:

-To Dr. Andrew Hrymak for the years of support, insightful advice and continuous encouragement.

-To Dr. J. Wright for his precise and enlightening suggestions to improve my work.

-To my wife, Edith, for providing me the peace of mind necessary to focus on my work.

-To Shaffiq Jaffer for his excellent work on the experimental visualization of flow.

-To Barbara Owen and Sara Gallo-O'Toole for their professionalism and competence.

-To Dr. J. Vlachopoulos and Dr. E.Agur for all the good advice.

-To everyone in CAPPA-D for accepting me as part of the clan.

-To the National Science and Engineering Research Council and Indesca (Investigación y Desarrollo, C.A.) for the financial support.

TABLE OF CONTENTS

LIST OF FIGURES

Figure **Page**

LIST OF TABLES

Table **Page**

LIST OF SYMBOLS

B	Clearance disc-barrel.
C_L	Centre-to-centre distance of screws.
D	Characteristic diameter of the extruder.
I_j	j^{th} invariant of a tensor.
G	Clearance between discs.
J	Jacobian of the isoparametric transformation for the volume integral.
L/D	Length to Diameter Ratio.
N	Shape function.
N_p	Shape function for pressure.
n	Normal vector to an element's face.
P	Pressure.
Q	Volumetric flowrate.
R	Residual Vector.
Re	Reynolds number.
R_x	Residual Vector of the x-momentum equation.
R_y	Residual Vector of the y-momentum equation.
R_z	Residual Vector of the z-momentum equation.
R_c	Residual Vector of the continuity equation.
t	Flight depth.
U	Characteristic Velocity.
u	Velocity vector.
u	x-component of the velocity vector.
v	y-component of the velocity vector.
w	z-component of the velocity vector.
X	Vector of unknowns.
x	Coordinate vector (x,y,z).

Greek characters.

α	Tip angle of the disc; angle between the left rotor tip and the x-axis.
δ	Kronecker delta.
ε	Tolerance level.
ζ	Element parent coordinate.
η	Viscosity function; element parent coordinate.
η_0	Zero-shear viscosity.
$\dot{\gamma}$	Shear-rate tensor.
μ	Viscosity coefficient.
ξ	Element parent coordinate.
ρ	Density.
ρ_c	Ratio of centre line distance between screws to barrel diameter.
σ	Total stress tensor
τ	Extra-stress tensor.
ϕ	Stagger angle between discs.
ψ	Angle of the flank of the kneading disc.
Ω	Spatial domain.

Mathematical Symbols.

$\partial/\partial t$	Partial derivative.
D/Dt	Substantial derivative.
e	Exponential.
•	Dot product.
×	Cross-product.

Superscripts.

(e)	Element approximation.
i	Nodal value for the shape functions.

n	Power-law index.
T	Transpose.
'	Dimensional value.

Subscripts.

b	Barrel bore.
i	Nodal value; root of disc.
ij	Tensor component.
o	Reference value; tip of disc.
w	Wall value.
x	$\partial/\partial x$.
y	$\partial/\partial y$.
z	$\partial/\partial z$.

Abbreviations

ICRTSE: Intermeshing Co-Rotating Twin Screw Extruder

FAN: Flow Analysis Network

FDM: Finite Difference Method

FEM: Finite Element Method

SEM: Spectral Element Method

TSE: Twin Screw Extruder

Chapter One

INTRODUCTION

1.1 Overview of twin screw extruders

Twin screw extruders (TSE) include many machine configurations with widely different characteristics. In general, a twin screw extruder can be described as two parallel screws placed in a figure-of-eight shaped barrel section. The relative position of the screws and their direction of rotation define different types of TSE (Cheremisinoff, 1987), as shown in Figure 1.1. According to the relative position of the screws, twin screw extruders can be classified as intermeshing and non-intermeshing. The intermeshing design can be further classified into fully intermeshing and partially intermeshing. Non-intermeshing machines are divided into separated and tangential depending on whether the tips of the screws define trajectories that are tangent to one another or not.

A screw system open in the longitudinal direction facilitates the interchange of material along the channel. In closed arrangements, there is less interchange of material and the extruder behaves more like a positive displacement pump. Whether the screws are open lengthwise or crosswise, or have a closed chamber geometry, has a direct effect on the conveying properties, mixing action and pressure buildup capacity of the system. The relationship between the intensity, uniformity, and location of maximum and minimum shear stresses define the basic differences between co-rotating and counter-rotating intermeshing twin screw extruders with identical screw geometries.

Many papers have been published providing comparisons between single screw extruders and twin screw extruders. The works of Campbell (1972), Street (1969) and Adams (1972) are good examples. One major difference between single and twin screw

extruders is the type of material transport that takes place in each. Material transport in a single screw extruder is drag-induced, with frictional drag in the solids conveying zone and viscous drag in the melt conveying zone. There are many materials, with unfavorable

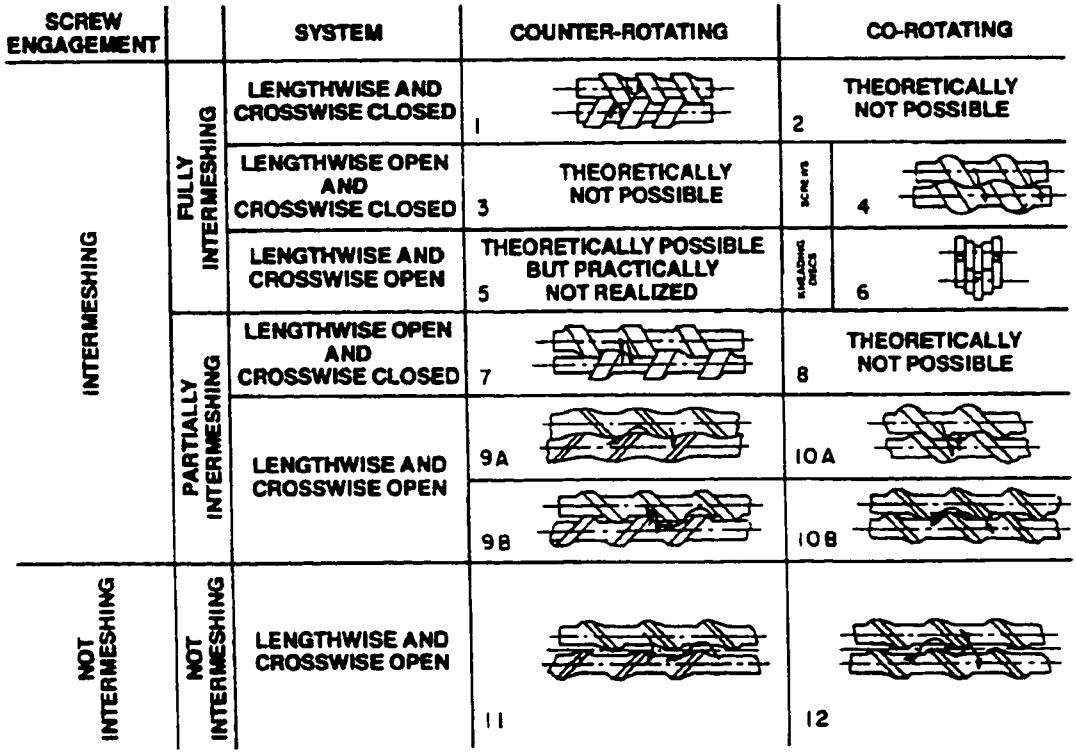

Figure 1.1. Classification of twin screw extruders (Cheremisinoff, 1987)

frictional properties, that have severe feeding problems in a single screw extruder (Rauwendaal,1986). On the other hand, the mechanism of transport in a twin screw extruder is a positive displacement type of transport. As discussed before, the degree of positive displacement depends on how well the flight of one screw closes the opposing channel of the other screw. Another important difference between single and twin screw extruders is the velocity pattern observed in each configuration. For a fully filled channel, the velocity profile in the melt zone of a single screw extruder is well defined. On the other hand, the velocity profile in a twin screw extruder is quite complex and more difficult to describe. However, these complex flow patterns produce several processing advantages, such as good mixing properties, good heat transfer, large melting

capacity and good devolatilization capacity. One disadvantage of the complex flow pattern is the difficulty of uniquely describing such flow behavior based on the geometry, polymer properties and operating conditions. To overcome these difficulties, the modular design of the screw arises as the best alternative to obtain the optimal configuration in terms of the shear and mixing action required. These machines have removable screw and barrel elements, and they can be altered by changing the sequence of the screw elements along the shaft.

Among all the different types of twin screw extruders, the intermeshing co-rotating configuration is of special importance due to its high efficiency in mixing, elimination of stagnant zones, and self wiping action of the elements.

1.2 Intermeshing co-rotating twin screw extruder (ICRTSE)

Twin screw extruders have gained importance over the years as one of the major polymer processing pieces of equipment. TSE are widely used in industry for melting, dispersing and homogenizing polymers. TSE are more complicated machines than single screw extruders (SSE) from the points of view of design and manufacture. However, there are important reasons to select TSE over SSE for specific applications. There are characteristic features of TSE that set this type of machine apart from the single screw machines. The first designs of TSE were motivated by problems in the transport of solids associated with SSE (Janssen, 1978). The mechanism of transport in TSE is more of a positive displacement type of transport than a drag type of transport, as in SSE. On the other hand, one of the main motivations to add more than one screw to the machine is to produce the kneading action generated by the interaction between the screws, necessary for the mixing of highly viscous materials. Multiple screw machines are also capable of generating secondary and back flows that improve the mixing ability of the machine without sacrificing pumping capacity or throughput. Over the years, engineers have invented many designs involving two or more screws in a diversity of geometrical configurations. White (1990) presented an overview of the various designs of multiple-screw extruders. Multiple-screw extruders can be co-rotating, counter-rotating or a combination of both. There are a diversity of designs employed throughout the polymer

industry, each one having different operating principles and applications. Among the different arrangements of twin screw systems, the intermeshing co-rotating configuration has been found to be one of the most efficient mixers. Canedo and Valsamis (1994) have presented a thorough analysis of the selection of continuous compounding equipment based on key design and processing characteristics that make intermeshing co-rotating twin screw extruders (ICRTSE) one of the most widely used pieces of equipment in plastics compounding. ICRTSE produce relatively uniform shear rate distribution in the conveying screw sections of the extruder (Rauwendaal, 1995) while providing a self wiping action.

ICRTSE are usually built in a modular fashion to meet the diversity of tasks performed by this type of machine. There are two main types of elements: full flight conveying elements and kneading block mixing elements. The screw conveying element is characterized by its pitch and length, and it is used for the transport of material at any point along the screws from the feed section at the base of the hopper to the die. The second class of elements, the kneading blocks, are the focus of attention for the theoretical analysis of flow due to their significant contribution to the mixing performance of the extruder and the fact that kneading blocks very frequently work under a fully filled channel condition.

Mixing is an essential function of TSE. The problem of mixing in TSE, and specifically in ICRTSE, has been the focus of attention and intense study by researchers in recent years. The mixing of polymers involves aspects of fluid dynamics and rheology. The process of mixing usually involves a combination of mechanical motion of the mixing device and the resulting deformation induced in the flowing material. The quantitative description of the flow patterns is now feasible even in the most complicated geometries through the development of computational fluid dynamics and the continuous increase in available computer resources. The flow in TSE has been traditionally analyzed by calculating approximate velocity profiles within the extruder channels. The rate of deformation is obtained from these velocity profiles at different locations in the flow field. Researchers have assumed that the rheology is a generalized Newtonian fluid with uniform properties to simplify the models, although in many cases the material can

have non-uniform properties and viscoelastic behavior. The flow through the flight clearances is neglected, and usually a two-dimensional flow pattern is considered. However, experimental work (Kalyon et al., 1989; Bigio and Erwin, 1984) has shown that the flow in this geometry is essentially three dimensional. For many years, three-dimensional numerical simulations were extremely expensive and time consuming, precluding the use of these techniques. With the development of computers and simulation software packages, researchers moved from 2-D models into more rigorous 3-D models. Computer simulations together with experimental work can provide insight for a better understanding of the flow and mixing phenomena within the complex geometry of ICRTSE.

1.3. Mathematical models

Kaplan and Tadmor (1974) provided a simple theoretical model for non-intermeshing twin screw extruders based on the "three parallel plate" model, which is the counterpart of the "parallel plate" model in single screw extrusion. Janssen (1978) and Martelli (1983) reviewed the analytical models for the different classes of twin screw extruders. Rauwendaal (1986) devoted a section of his work on polymer extrusion to the study of twin screw extruders. White (1990) presented a detailed classification of the different types of twin screw extruders and described some of the models developed for each one of these types of machines. Simplified models are limited to the prediction of pressure drop based on given flow rates and the use of geometrical correction factors is necessary to incorporate the effect of one screw on the drag and pressure terms of the other screw. A more rigorous mathematical description of the complex flow passages encountered in the extruders is necessary. Tadmor et al. (1974) used a control volume method for solving two dimensional flow problems in geometries with narrow gaps of variable thickness and different shapes. The technique, called the Flow Analysis Network (FAN), is based on the division of the flow field into control volumes. The FAN technique was later used by Szydlowski et al. (1987) on the unwrapped flow channel of a TSE neglecting variations in the radial direction with the use of the "lubrication approximation". The method used by Szydlowski et al. allowed them to analyze the flow

distribution in a 2-D rectangular area with the assumptions of an isothermal Newtonian fluid, and the application of the Reynolds lubrication theory. The unwound domain of the twin screw kneading disc region was divided into a grid of rectangular elements designated as (i,j). The i elements are along the transverse periphery of the screws. The j elements are along the screw axis. The flow balance on an element is of the form:

$$S_{i,j}\, q_{i-1,j} + E_{i,j}\, q_{i,j-1} - W_{i,j}\, q_{i,j+1} - N_{i,j}\, q_{i+1,j} = 0 \qquad (1.1)$$

where $S_{i,j}$, $E_{i,j}$, $W_{i,j}$ and $N_{i,j}$ are arrays of contact of element (i,j) with the surrounding elements. By applying the Reynolds lubrication theory, the flow was considered as flow between two parallel plates where one of the plates is in motion and there is a pressure gradient. Szydlowski et al. defined six types of flow within the kneading disc region, as displayed in Figure 1.2: main inflow to the next disc (Q_E), main outflow to the next disc (Q_W), inflow above the tip (Q_S), outflow above the tip (Q_N), gap inflow caused by staggering (Q_{W2}) and gap outflow caused by staggering (Q_{E2}). The mixing effects are assumed to be produced by the Q_{W2} and Q_S flows.

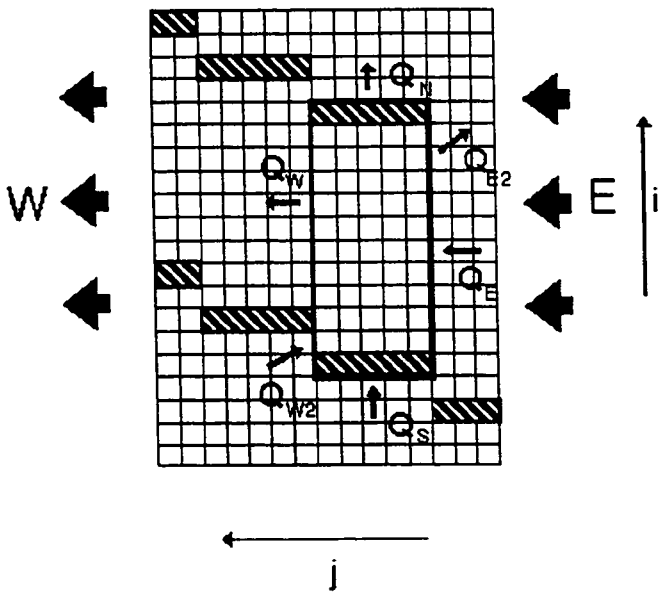

Figure 1.2. Discretization of the domain for the FAN method. Flow balance in the kneading disc region.

Sebastian and Rakos (1990) used a variation of the FAN technique for the simulation of flow in the kneading disc sections of an ICRTSE. The purpose was to demonstrate the advantages of the improved FAN method over existing FAN and FEM methods and to show that the method is capable of predicting pressures with engineering accuracy. The simulations were done using only 704 quadratic elements, which precluded an accurate definition of the geometry.

Chen and White (1991) derived a set of algebraic equations from the conservation of mass and momentum equations and made dimensionless calculations for throughput and pressure gradients using non-Newtonian fluids in screw and kneading elements. The flow was assumed to be isothermal. Results include pressure profiles and fill factor along the screw composed of conveying and kneading elements. The model proposed by Chen and White has its application as an aid for screw design but has limited application in the analysis of mixing in TSE.

The accurate mathematical description of the screw geometry for intermeshing co-rotating twin screw extruders can be attributed to Booy (1978). Booy described the cross section geometry of fully wiped co-rotating twin screws. The work presents calculations of the free volume between screws and barrel surface areas. The cross section of a TSE has a unique shape for a given diameter, centerline distance, and number of parallel channels because of the requirement that one screw must wipe its mate in any position. Booy (1980) worked on a mathematical flow model, with the assumption of stationary screw and rotating barrel, using the hypothetical case of a flexible barrel that moves around the screws with a velocity $\pi D_S N$ following the contour of the eight-shaped barrel.

Kiani et al. (1992) note that the 2-D control volume technique provides some useful insights in twin screw extruders, but it cannot be applied in the case of kneading blocks where the geometry shows abrupt changes in the passages between successive discs. Another 2-D approach has been adopted by Kalyon et al. (1988) and more recently by Kiani et al. (1992) and Lawal et al. (1993) with the implementation of the finite element method (FEM) for a plane in the cross section of the flow channels. This approach allows the analysis of some local behavior in the intermeshing and nip regions,

but completely neglects the flow in the axial direction.

Gotsis et al. (1990) proposed a model for the isothermal flow of a Newtonian fluid reducing the number of assumptions in the definition of geometry and used a finite element discretization. The objective is to simulate realistic flow patterns in the radial and axial directions. Mathematical complications arise as a consequence of considering the actual geometry. The flow pattern is time dependent because the flow boundaries change as the kneading discs rotate. To solve the problem of the time dependence of the flow, they constructed a 3-D mesh covering the entire space within the barrel that may be occupied either by the fluid or by the kneading discs. At each time step, the elements of the mesh are checked to find out whether they correspond to free space occupied by the fluid or space occupied by the kneading blocks. The part of the space that is found to correspond to the fluid is assumed to obey the conservation equations whereas the part that is occupied by the kneading blocks during that time step is forced to rotate as a rigid body (Gotsis et al. 1990). Lawal and Kalyon (1993) followed the approach used by Gotsis et al. (1990) for the full three-dimensional calculation over the entire flow volume. Lawal and Kalyon (1993) utilized various tools of dynamics, namely the Lyapunov exponent, the horseshoe mapping, the Poincare section and Melnikov's method, to analyze the mixing occurring in ICRTSE and to capture the relative differences in the mixing mechanism of continuous processors. Lawal and Kalyon (1995) presented a study of intensity of segregation based on the three-dimensional simulation of the flow in two-tipped mixing elements of an ICRTSE. The intensity of segregation, I, is defined as:

$$I = \frac{S^2}{\sigma_0^2} \tag{1.2}$$

Equation (1.2) is the ratio of the measured variance divided by the variance of a completely segregated system. It takes the value of 0 when the concentration is uniform and 1 when segregation is complete (Tadmor and Gogos, 1979). The intensity of segregation distributions were determined by introducing a tracer blob numerically and tracking the concentration of tracer particles as a function of location and time. Studies were conducted for two-tipped kneading discs using stagger angles of 30, 45,60 and 90 degrees. The Lyapunov exponent was calculated for each stagger angle as an indication

of the chaotic nature of the flow in twin screw systems. Lawal and Kalyon were able to establish clear differences between single screw systems and twin screw systems in their abilities to create the reorientation of material interfaces and hence to produce good distributive mixing. However, they were not able to establish a clear difference in the mixing performance of the various stagger angles. Their model also lacks sufficient accuracy in the definition of the narrow clearances between discs at the critical intermeshing zone, thus affecting the calculation of velocity and pressure fields necessary for the analysis using the tools of dynamics. The complexity of the models used for the characterization of flow and mixing has increased dramatically with the understanding of the flow mechanisms and the availability of increasingly faster computers. Kalyon et al. (1997) presented results for a study of the extrusion of filled polymers in ICRTSE, which includes the effects of material viscoplasticity, heat transfer and wall slip. The results were compared with experimental pressure data to show that the model accounts for the viscoplastic and wall slip encountered in concentrated suspensions.

An alternative approach to the transient nature of the problem was used by Manas-Zloczower et al. (1989,1992) in which steady state flow calculations are made for each time step. The finite element mesh is generated for every time step to describe the geometry of the volume occupied by the fluid. The boundary conditions are imposed according to the no-slip condition at the walls and the calculated velocities at the surfaces of the kneading blocks based on the radius and the shaft rotation speed. The assumption of creeping flow is taken based on the fact that polymer melts have very large viscosities and very low Reynolds numbers (of order 10^{-3} or less). The term $D\vec{u}/Dt$ is neglected from the momentum equations and the transient flow can be reasonably approximated as a sequence of steady state flows. Under these assumptions, the velocity and pressure fields adjust instantaneously relative to the rate at which the boundary configuration changes and consequently always appear to be in steady state with respect to the current configuration. However, the geometrical configuration still depends on the change of the boundary position with respect to time. Yang (1993) used the same quasi-steady state approximation. The boundary conditions imposed were the no-slip condition for the chamber wall and rotor surfaces, and a nominal value for the normal stress difference at

the entrance and exit planes. The normal stress ($\sigma_{xx} = -p + \tau_{xx}$) at the entrance surface was set $\sigma_{xx} = \Delta\sigma_{xx}$ whereas at the exit plane was set to zero. Cheng and Manas-Zloczower (1997) used a fluid dynamics analysis package, FIDAP™ (Fluent Inc.), to simulate the three-dimensional isothermal flow patterns in two different configurations of kneading discs. Comparisons are made to determine the relative mixing performance of the two configurations based on the determination of shear stress and elongational flow components. The work developed by Cheng and Manas-Zloczower and Yang use a common approach for the analysis of mixing based on the calculation of the average value of the parameter λ. The parameter λ relates the magnitudes of the rate-of-strain tensor and the vorticity tensor as

$$\lambda = \frac{|\dot{\gamma}|}{|\dot{\gamma}| + |\omega|} \tag{1.3}$$

. The results showed that λ remains almost unchanged throughout the cycle of rotation, thus allowing the analysis of a single position of the rotor to characterize mixing. Particle tracer results obtained during the course of the present thesis show that particles starting at different points undergo different levels of strain rate. It is possible that two processes having the same average values of λ can have very different mixing performances. This suggests that the use of the volume average λ to characterize mixing could be misleading in some cases.

Kiani and Samann (1993) have simulated various mixing elements by employing the spectral element method (SEM) (Patera, 1984), with similar results to those obtained by the finite element method, but with reduced computational time.

Liu and Funatsu (1996) studied flow and mixing in conveying elements of an ICRTSE using the finite element method for the solution of the conservation equations. In their simulations, Liu and Funatsu used a moving coordinate system having a speed equivalent to that of the axial motion of the flights, allowing the geometry to remain constant. In the same line of work, Kajiwara et al. (1996) developed an analysis technique for the evaluation of mixing performance in conveying elements of intermeshing co-rotating and counter-rotating TSE. Comparisons are based on the study of velocity, stress fields, and the spatial distribution of particle tracers. Higashi et al.

(1996) presented the study of mixing performance in the kneading blocks of ICRTSE, using the finite element method for the determination of the three-dimensional velocity and pressure fields and an analysis based on the determination of particle trajectories.

1.4. Experimental work

Rauwendaal (1981) made an experimental evaluation of twin screw extruders. Experiments with two laboratory scale intermeshing twin screw extruders were carried out. One of the extruders was co-rotating and the other was counter-rotating. Comparisons of the two extruders were made based on power consumption, residence time distribution and mixing characteristics. Rauwendaal (1981) came to the conclusion that the overall extruder performance appeared to be dominated by the effect of the intermeshing region. Analyses of twin screw extruders should be centered on the flow behavior and mixing characteristics of the intermeshing region. This conclusion is now widely accepted and has been the main motivation for moving from 2-D models into more rigorous 3-D models.

One of the major challenges in the study of twin screw extruders is the experimental validation of the results obtained by numerical models. In the area of flow visualization, Kalyon et al. (1991) studied the degree of fill and melt densification in fully intermeshing co-rotating twin screw extruders, with an analysis of the effects of the various reverse and forward stagger angles for a configuration of kneading discs. An APV 50.8 mm clam shell design twin screw extruder was employed under isothermal conditions. A plasticized, transparent thermoplastic elastomer was used to determine the degree of fill and density distributions. In consecutive experiments, the kneading disc sections were systematically staggered at various reverse and forward angles. The degree of fill in the kneading section was found to be less than one with forward stagger angles, thus generating a partially full channel. The distribution depended on the degree of the forward staggering. The degree of fill was one with the reverse and neutral kneading discs, i.e. a completely full channel at the kneading disc block. More recently, Kalyon et al. (1997) combined simulation and experiments in the mixing section of ICRTSE for the processing of filled polymers. Measurements of pressure and temperature were taken, but

more significant is the analysis of the degree of mixing of the filled polymer and the use of the wide angle X-ray diffractometry. Qualitative analysis of distributive mixing by x-ray diffraction is accomplished by identification of the particular diffraction pattern of a substance from the standard diffraction bases. A quantitative analysis of mixing involves a measure of homogeneity of the mixture by calculating the extent to which the concentration values at various regions of the mixture differ from the mean concentration. Kalyon et al. report good agreement of their model with experimental axial pressure profiles and claim to have compared for the first time extrusion data for a concentrated suspension that exhibits viscoplasticity and wall slip with the results of numerical simulations.

Sastrohartono et al. (1990) studied the flow patterns within a partially intermeshing co-rotating twin-screw extruder. They stated that this is an extremely complex three-dimensional problem. In order to simplify it, a slice perpendicular to the axis of the twin-screw extruder was considered for flow analysis as a two-dimensional or a quasi three-dimensional problem. The flow in this slice was considered to consist of a nip region (located between the two screws) and a translation region in which the movement of the material is very similar to the one found in single-screw extruders. The flow in these two regions was studied separately. Newtonian as well as non-Newtonian behavior was investigated. The influence of such factors as the geometry, the material properties (the power-law index for shear rate dependent viscosity) and processing conditions were studied.

1.4.1. Residence time distribution

Oberlehner et al. (1994) determined the local residence time distribution (RTD) in a co-rotating twin screw extruder using a UV tracer method. This method was used to test the RTD response to a pulse input into the different elementary screw elements, such as right-and left-handed screw elements and mixing elements. Experimental RTD data were used in order to compare the local dynamic response of the basic screw elements. These results were qualitatively discussed on the basis of flow patterns developed in the pumping section of the extruder. On the other hand, fitting of the RTD functions was

attempted using classical chemical engineering models such as axial dispersion and ideal stirred tanks in series. Although these models fit quite well the shape of the RTD functions, the long tail of the distribution was not correctly described.

One of the most recent investigations in the area of flow visualization was presented by Kim and White (1994), with the utilization of screw and kneading disc elements from a Werner and Pfleiderer ZSK-30 and barrel sections with windows. In their experiments, Kim and White used five different screw configurations with various combinations of forward and reverse conveying elements and forward and reverse kneading blocks. The visualization experiments included qualitative observations of aluminum flakes and platelets through the glass windows. Measurements of residence time were also carried out by taking samples of the aluminum tracers from the die exit and from intermediate positions. Kim and White observed that the fluid moves in three directions according to the model proposed by Szydlowski et al. (1987). No quantitative data is given for these flows based on experimental results. They found that kneading discs and reverse conveying elements increase residence time and broaden the residence time distribution. The conclusions obtained by Kim and White are mostly qualitative and are an attempt to explain the flow mechanisms rather than to compare the mixing performance of the different configurations.

Burbank et al. (1991) explored several element types, screw configurations, and process conditions in the application of criteria for mixing incompatible fluids into polymers using a co-rotating intermeshing twin screw extruder. Results indicated that turbine mixing elements are more efficient than kneading blocks for incorporating incompatible additives.

1.4.2. Pressure measurements

Todd (1989) and McCullough and Hilton (1993) have measured experimental pressure profiles on ICRTSE. Todd presents a study of complex flow phenomena by measuring the pressure flow term for different configurations of kneading discs in a vertically mounted barrel, by pumping a viscous Newtonian fluid upwards to ensure 100% fill. The data provided by McCullough and Hilton is not limited to measurements

of pressure and temperature at the die, but include measurements along the barrel at different axial and radial positions. Chapter 4 of this thesis is devoted to the comparison of pressure profiles obtained by computer simulation at various axial positions and the experimental results obtained by McCullough and Hilton. Previously, Bravo (1995) compared the simulation results obtained using a Newtonian fluid for one axial position on the kneading blocks. The comparison with the experimental data has allowed a rigorous validation of the numerical model and the combination of simulation and experimental data provides a better understanding of the flow phenomena.

Christiano and Lindenfelzer (1997) have extended the experimental determination to dynamic pressure profiles. In their work, Christiano and Lindenfelzer made time dependent pressure measurements by recording eight radial data values at every axial position along each mixing element. The eight radial pressures from the transducers are read simultaneously at each axial location. Software was developed to remap the pressure data files into one file so the entire pressure distribution over the full length of the mixing element for a given screw position could be analyzed. These results have the potential of being readily usable for the purpose of validation of mathematical models when the data is released. The analysis of the dynamic pressure gradients aids in understanding the flow patterns and may give an indication of the type of mixing occurring in the system.

1.5 Objectives

There are three main objectives pursued in this thesis:

1) Undertake a comprehensive analysis of the flow mechanisms in the kneading disc section of co-rotating twin screw extruders. This is done by means of 3-D finite element numerical simulation of the flow process within the complex geometry involving intricate passages and continuously moving surfaces. In modelling the flow within a twin screw extruder, the quasi-steady state approach has been used for obtaining the solution of the flow fields. In the quasi-steady state solution, a number of sequential geometries at defined angles of rotor position are selected to represent a complete cycle in the time dependent moving boundary problem. This approximation is taken under the assumption

that polymer melt flows tend to have very low Reynolds numbers (10^{-3}), such that the transient flow can be reasonably approximated as a sequence of steady state flows at intermediate times.

2) Perform the experimental validation of the proposed numerical model. The validation is done against experimental results for pressure (McCullough and Hilton, 1993) and velocity profiles (Jaffer, 1998) as a way to establish the use of the model as a tool for the analysis and design of mixing elements in intermeshing co-rotating twin screw extruders. Experimental verification identifies aspects of the numerical model that can be modified in order to improve the model predictions.

3) Characterize mixing through the determination of particle trajectories. Particle trajectories are obtained from the calculated velocity fields and the strain rate history was calculated along the particle trajectories. Residence time distributions were measured for various configurations of kneading blocks. Particles were initially located to cover a cross section at the inlet of the kneading block.

1.6 Outline

Chapter 2 is devoted to the description of the mathematical background. This includes the governing equations, the finite element method for the solution of the system of non-linear differential equations, the definition of boundary conditions as a fundamental part of the mathematical model and numerical considerations involved in the solution of the complex problem. Chapter 3 presents the validation of the pressure profiles calculated from the numerical simulations by comparing them with experimental pressure profiles measured by McCullough and Hilton (1993). Chapter 4 describes the work done on the relative mixing performance of three different length-to-diameter ratios (L/D) of kneading blocks. The analysis is based on the calculation of particle trajectories from the determined velocity fields. Chapter 5 describes the validation of the developed numerical model against experimental velocity data. This includes the description of the comparisons between velocity profiles calculated from the numerical model and experimental velocity profiles measured by Jaffer (1998) by particle image velocimetry (PIV). Finally, Chapter 6 gives an overview of the work done and summarizes the main

conclusions and thesis contributions obtained during the course of the research work. Chapter 6 also includes a section with recommendations for the future work.

Chapter Two

FLOW IN THE KNEADING DISC SECTION OF AN ICRTSE

2.1 Introduction

A complete description of the mathematical model is presented in this chapter. The mathematical model includes the description of the three-dimensional geometry, an overview of the equations of conservation of mass and momentum, the description of the Carreau constitutive equation, and the method of solution using the finite element method.

2.2 Geometry

The generation of the complex geometry involved in the kneading discs section of a twin screw extruder is based on the work done by Booy (1978). The calculation of the flow field within a twin screw extruder requires a complete knowledge of the geometry. The cross section of a twin screw has a unique shape given by diameter, centerline distance, and number of parallel channels because of the requirement that one screw must, in any position, wipe its mate (Booy, 1978).

The relative proportions of all the geometries used are based on the dimensions of the Werner & Pleiderer ZSK-30 type co-rotating extruder, shown in Table 2.1. A stagger

Barrel bore diameter (D_b)	30.85 mm
Screw outside diameter (D_o)	30.7 mm
Screw root diameter (D_i)	21.3 mm
Flight depth (t)	4.7 mm
Center distance of screws (C_L)	26.2 mm
Clearance between discs (G)	0.2 mm
Clearance disc-barrel (B)	0.075 mm

Table 2.1. Technical data ZSK 30 extruder.

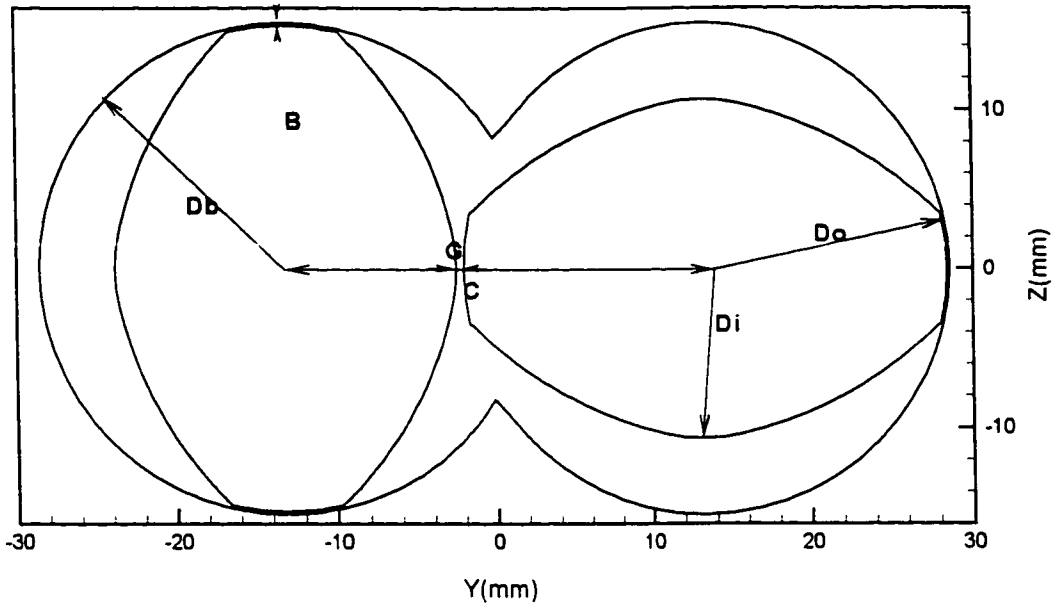

2.1. Cross section geometry of two-tipped kneading discs.

angle (ϕ) of 45° in a forward configuration was used for the simulations. Figure 2.1 describes the geometry of the cross section of kneading discs. The shape of the surface of one disc was generated using the equations developed by Booy (1978). The coordinates describing the surface of the disc were subsequently rotated by the stagger angle and translated to produce the rest of the discs. The resulting 3-D geometry represents the free volume between the kneading discs and the twin barrel. The geometry of the kneading discs is shown in Figure 2.2. The 3-D geometry of the free volume occupied by the fluid is shown in Figure 2.3. The transient nature of the flow problem in the kneading discs of an ICRTSE requires the re-generation of the geometry and the finite element mesh for every position of the rotors. Gotsis et al. (1990) proposed a method where a single three-dimensional mesh covered the entire volume inside the barrel that may be occupied either by the fluid or by the kneading discs. This approach allowed Gotsis et al. to eliminate the need for re-generating the finite element mesh for every position of the discs thus reducing one of the main complications in the solution of the time-dependent

problem. The approach, although very appealing, has its limitations in the inaccuracies of the description of the rotor surfaces and especially the narrow gaps encountered in these systems.

Bertrand et al. (1994) used a method called the fictitious domain method for solving problems that involve enclosures containing moving internal parts. This method also uses one 3D finite element mesh representing the enclosure without considering the internal moving parts. The moving parts are treated as kinematic constraints in the variational formulation of the conservation equations using the augmented Lagrangian method. This method is not exempt of problems, particularly in the narrow clearances between the moving internal parts and the enclosure walls. The re-generation of the finite element mesh can be a tedious and time-consuming process.

In this work, an automatic mesh generator was developed in order to overcome the problems associated with the multiple re-generation. Seven sequential geometries were specified to represent one quarter of the complete cycle of rotation for a geometry of five kneading discs in a forward configuration with a 45° stagger angle, according to Figure 2.4. Due to symmetry, only one quarter of the complete cycle is necessary to represent the complete sequence of geometries. Variable α represents the angle between the left rotor tip and the y-axis for the first disc. Increments of 12.86° for each time step were taken, corresponding to a time interval of 2.1429×10^{-2} seconds for a rotation speed of 100 rpm.

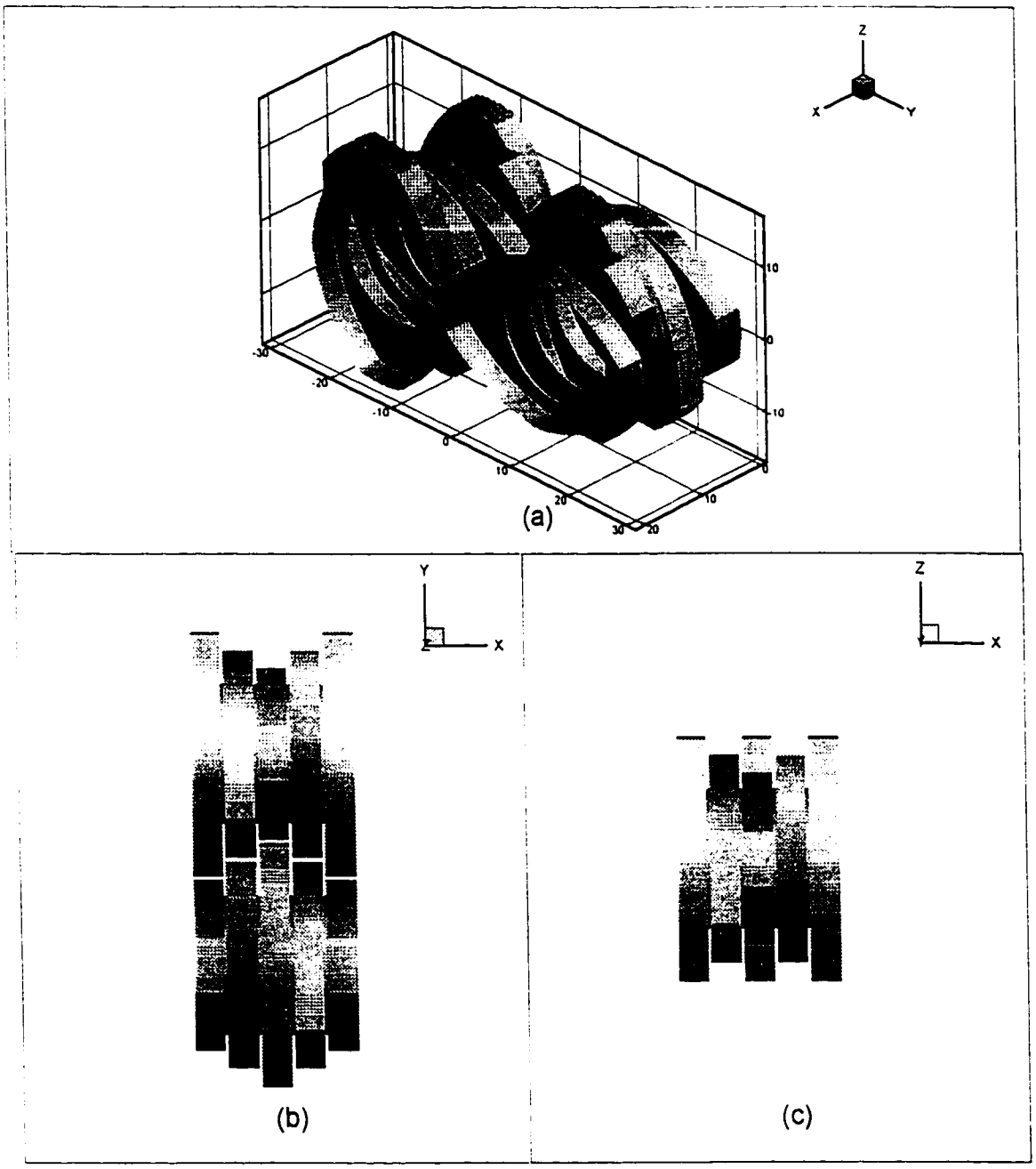

Figure 2.2. a) Isometric view of the kneading disc geometry; b) Top view (x-y plane) with axial and transverse gaps; c) Side view (plane x-z).

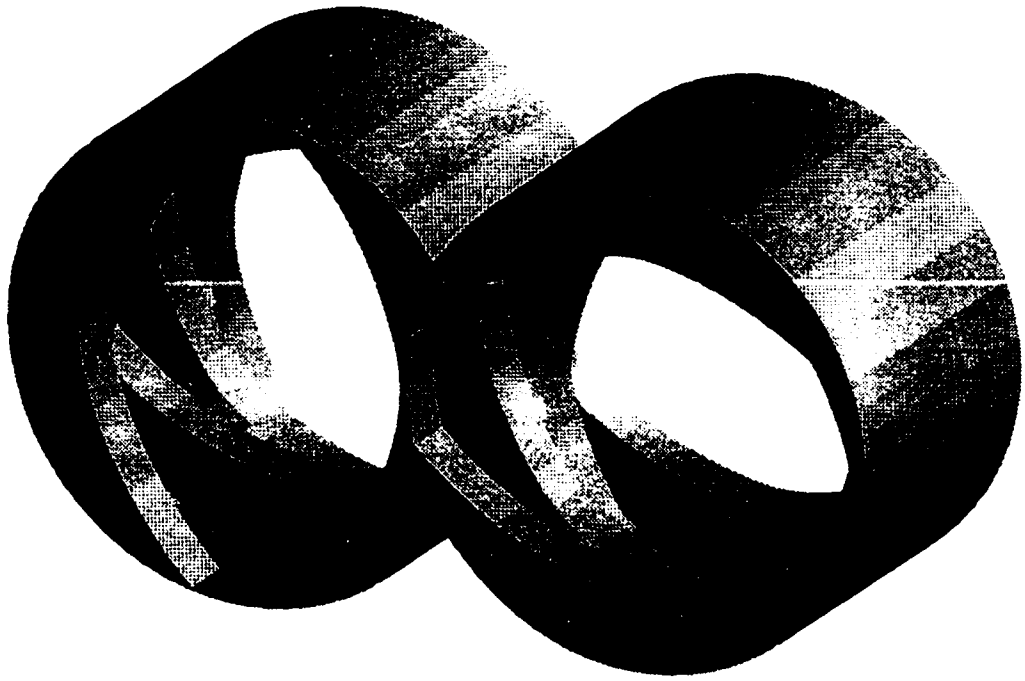

Figure 2.3. Free volume occupied by the fluid in the kneading disc region

2.3 Governing equations

The flow of molten polymers within the kneading disc region in a co-rotating twin screw extruder is modeled assuming that the flow is in steady state, isothermal, creeping, incompressible and with no body forces.

The governing equations are the momentum equations without inertia terms and the continuity equation, which can be written in dimensionless tensorial form as:

$$\Delta \cdot \tau - \Delta P = 0 \tag{2.1}$$

$$\Delta \cdot \boldsymbol{u} = 0 \tag{2.2}$$

where τ is the extra stress tensor, P the pressure and $\boldsymbol{u}$ the velocity vector. A Generalized

Newtonian constitutive equation (Bird et. al, 1984) is used to model the stress-strain relation for polymers:

$$\tau_{ij} = \eta\left(\frac{\partial u_i}{\partial x_j} + \frac{\partial u_j}{\partial x_i}\right) \tag{2.3}$$

The viscosity dependence on shearing is fitted with a Carreau model as:

with

$$\eta(\dot{\gamma}) = (\mu_0 - \mu_\infty)\left[1 + (\lambda\dot{\gamma})^2\right]^{\frac{(n-1)}{2}} e^{-\beta T} \tag{2.4}$$

$$\dot{\gamma} = \sqrt{\frac{1}{2} II_{\dot{\gamma}}} \tag{2.5}$$

$$II_{\dot{\gamma}} = \dot{\gamma}_{ij} : \dot{\gamma}_{ji} \tag{2.6}$$

$$\dot{\gamma}_{ij} = \frac{\partial u_j}{\partial x_i} + \frac{\partial u_i}{\partial x_j} \tag{2.7}$$

where μ_0, μ_∞, λ and n are rheological property parameters. The dimensionless groups and variables used in equations (2.1) to (2.7) are:

$$\begin{aligned} \boldsymbol{x} &= \frac{\boldsymbol{x}'}{D} \quad \boldsymbol{u} = \boldsymbol{u}'/U \\ P &= \frac{P'D}{\mu_0 U} \quad \tau = \frac{\tau' D}{\mu_0 U} \\ \mu &= \frac{\mu'}{\mu_0} \end{aligned} \tag{2.8}$$

where D is the characteristic diameter (in this case, the outer diameter of the screw), U is the total average velocity (total flow rate over total area), μ_0 is the zero-shear viscosity of the fluid and the prime (') denotes a dimensional variable.

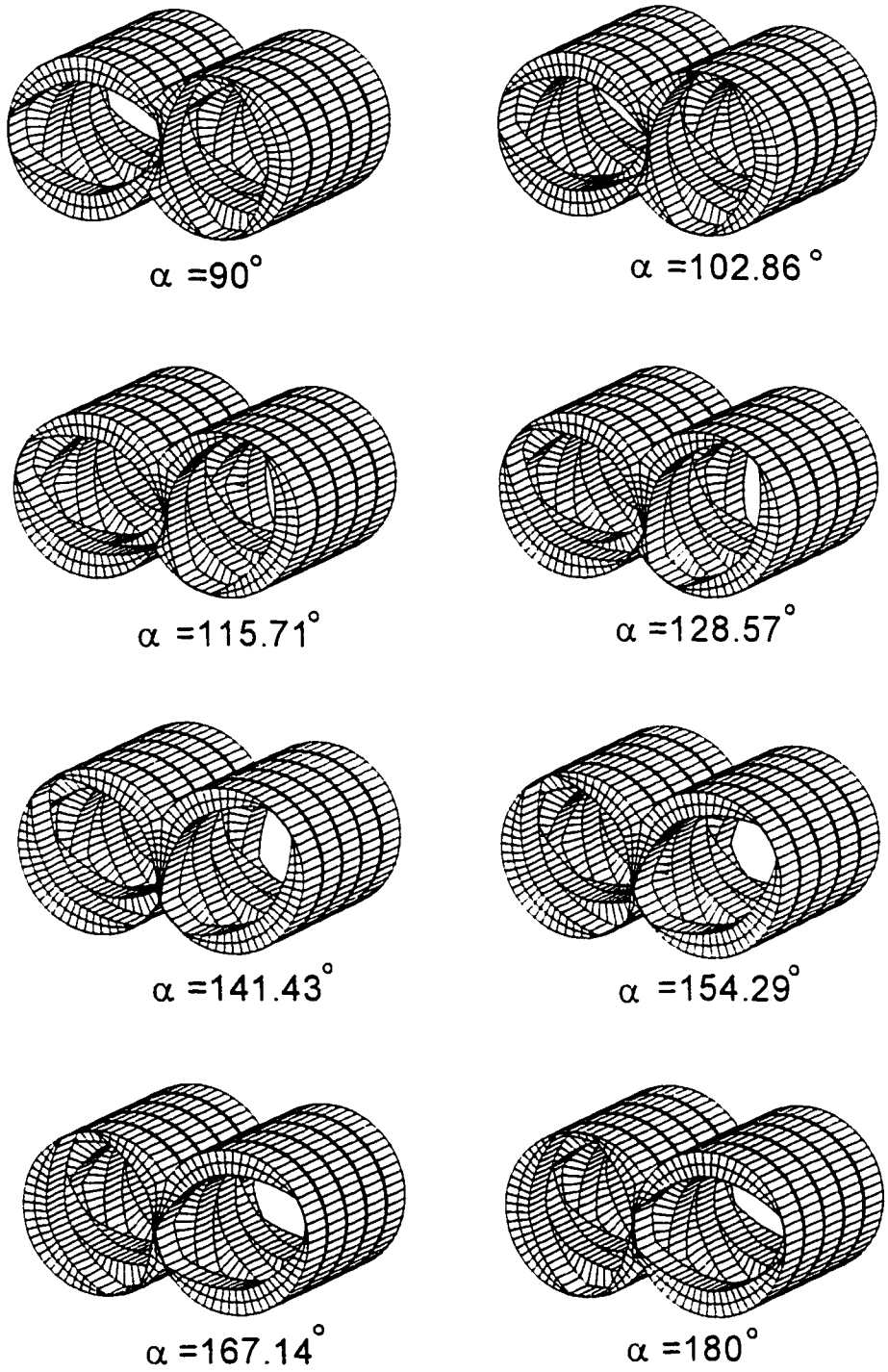

Figure 2.4. Sequential geometries representing one quarter of the rotation cycle.

2.4. Finite Element Formulation

A three-dimensional finite element method is used to discretize the governing equations **(2.1)** and **(2.2)** in the kneading disc region. Several texts provide the necessary mathematical background of the method applied to fluid mechanics problems (Taylor and Hughes, 1981; Dhatt and Touzot, 1984).

The field variables (velocities and pressures) are approximated by 27-node triquadratic brick elements for velocities and 8 node trilinear brick elements for pressure (Reddy, 1984). Within an element, nodal coordinates, velocity and pressure are interpolated by:

$$\begin{aligned} u^{(e)} &= \sum_i N^i(\xi,\eta,\zeta)\, u_i \\ x^{(e)} &= \sum_i N^i(\xi,\eta,\zeta)\, x_i \\ P^{(e)} &= \sum_i N_P^i(\xi,\eta,\zeta) P_i \end{aligned} \qquad \textbf{(2.19)}$$

where $\boldsymbol{u}$ is the vector of velocities (u v, w), $\boldsymbol{x}$ is the coordinate vector, P is the pressure, N_P^i is the linear interpolating function and N^i is the quadratic interpolating function.

The Galerkin method is used to construct the weak form of the governing equations (Reddy, 1984; Burnett, 1987). Standard application of this procedure leads to:

$$\int_\Omega \{\nabla \cdot \sigma\}\, N^i d\Omega = 0 \qquad \textbf{(2.20)}$$

where σ is the total stress tensor $\sigma = P\delta - \tau$ and Ω is the 3D flow domain. The same procedure for the continuity equation yields:

$$\int_\Omega \{\nabla \cdot u\}\, N_p^i d\Omega = 0 \qquad \textbf{(2.21)}$$

Application of the divergence theorem gives:

$$R_x^i = \int_{-1}^{1}\int_{-1}^{1}\int_{-1}^{1}\left[(-P + 2\mu u_x)N_x^i + \mu(u_y + v_x)N_y^i + \mu(u_z + w_x)N_z^i\right]|J|\,d\xi d\eta d\zeta \qquad (2.22)$$

$$R_y^i = \int_{-1}^{1}\int_{-1}^{1}\int_{-1}^{1}\left[\mu(u_y + v_x)N_x^i + \mu(-P + 2\mu v_y)N_y^i + \mu(v_z + w_y)N_z^i\right]|J|\,d\xi d\eta d\zeta \qquad (2.23)$$

$$R_z^i = \int_{-1}^{1}\int_{-1}^{1}\int_{-1}^{1}\left[\mu(u_z + w_x)N_x^i + \mu(v_z + w_y)N_y^i + \mu(-P + 2\mu w_z)N_z^i\right]|J|\,d\xi d\eta d\zeta \qquad (2.24)$$

$$R_c^i = \int_{-1}^{1}\int_{-1}^{1}\int_{-1}^{1}\left[u_x + v_y + w_z\right]N_p^i|J|\,d\xi d\eta d\zeta \qquad (2.25)$$

In the above equations, $|J|$ is the Jacobian for the isoparametric transformation for the volume integrals defined as:

$$|J| = x_\xi y_\eta z_\zeta + x_\zeta y_\xi z_\eta + x_\eta y_\zeta z_\xi - x_\xi y_\zeta z_\eta - x_\eta y_\xi z_\zeta - x_\zeta y_\eta z_\xi \qquad (2.26)$$

The above procedure reduces the set of differential equations **(2.1)** and **(2.2)** in the flow domain to a set of algebraic equations to calculate the state variables defined at each node. The coupled set of equations for all the elements leads to a system of the form:

$$R(X) = 0 \qquad (2.27)$$

where R is the vector of residuals and X is the vector of unknowns, defined respectively as:

$$R^T = \left[R_x^T, R_y^T, R_z^T, R_c^T\right] \qquad (2.28)$$

$$X = \left[u^T, v^T, w^T, P^T\right] \qquad (2.29)$$

A Newton-Raphson procedure is used to solve the system of equations. **(2.27)**. A detailed explanation of the Newton-Raphson procedure applied to finite element

calculations can be found in Dhatt and Touzot (1984). The Jacobian terms ($\partial R/\partial X$) are calculated analytically and checked by a central difference scheme (Mavridis, 1988).

For the discretization of the twin screw domain, various densities of 27-node triquadratic brick element meshes were tested as shown in Figure 2.5. The meshes in Figure 2.5 were generated with an automatic mesh generator developed by the author. The automatic mesh generator allows the creation of a finite element mesh from the definition of the geometry parameters specified on Table 2.1, i.e. stagger angle, number of elements in the radial, circumferential and axial directions and angle of rotation of the screws. Once all the geometry parameters are defined, it is only necessary to change the angle of rotation of the screws to obtain the sequence of finite element meshes. The automatic mesh generator also imposes the inlet and outlet boundary conditions and the solid boundary conditions for which a rotation speed needs to be provided. Finally, the automatic mesh generator performs a reordering algorithm developed by Sloan & Randolph (1983) in order to obtain an optimum elimination order. The algorithm first renumbers the nodes, and then uses this result to re-sequence the elements. The renumbering of the nodes is based on a modification of King's algorithm (1970). After the elements have been renumbered, the new node numbering scheme can be discarded. The renumbering of nodes is necessary because of the nature of the frontal solution procedure, which assembles variables on an element by element basis but eliminates them node by node. For a mesh of 2,016 elements and 20,881 nodes, the automatic element reordering algorithm, the maximum frontwidth was reduced from 2500 to 1192.

The calculation of flow rate in an arbitrary plane involves the computation of the velocities in such plane. This computation can be done from the isoparametric transformation (Kistler and Scriven, 1983). Integration of u over the plane η–ζ gives:

$$\int u.n\,dA = \int_{\zeta}\int_{\eta} u.n|J|^{*}\,d\eta\,d\zeta \qquad \textbf{(2.30)}$$

where

$$\boldsymbol{u} = [u, v, w] \qquad \textbf{(2.31)}$$

The normal to plane η–ζ (Figure 2.6) is:

$$n = \frac{[a_x, a_y, a_z]}{\sqrt{a_x^2 + a_y^2 + a_z^2}} \tag{2.32}$$

and the Jacobian

$$|J|^{\cdot} = \sqrt{a_x^2 + a_y^2 + a_z^2} \tag{2.33}$$

where

$$a_x = \frac{\partial y}{\partial \eta}\frac{\partial z}{\partial \zeta} - \frac{\partial y}{\partial \zeta}\frac{\partial z}{\partial \eta} \tag{2.34}$$

$$a_y = \frac{\partial x}{\partial \zeta}\frac{\partial z}{\partial \eta} - \frac{\partial x}{\partial \eta}\frac{\partial z}{\partial \zeta} \tag{2.35}$$

$$a_z = \frac{\partial x}{\partial \eta}\frac{\partial y}{\partial \zeta} - \frac{\partial x}{\partial \zeta}\frac{\partial y}{\partial \eta} \tag{2.36}$$

The projected area in the plane y-z for each element can be obtained from:

$$Area = \int_{\zeta}\int_{\eta} |J|^{\cdot} \, d\eta d\zeta = \int_{\zeta}\int_{\eta} \sqrt{a_x^2 + a_y^2 + a_z^2}\, d\eta d\zeta \tag{2.37}$$

and the flow rate on the projected area is:

$$Q = \int_{\zeta}\int_{\eta} u \cdot n |J|^{\cdot} \, d\eta d\zeta = \int_{\zeta}\int_{\eta} (u\, a_x + v\, a_y + w\, a_z) d\eta d\zeta \tag{2.38}$$

When the angle between planes η–ζ and y-z is zero, then equation (2.38) becomes:

$$Q = \int_{\zeta}\int_{\eta} u \cdot n |J|^{\cdot} \, d\eta d\zeta = \int_{\zeta}\int_{\eta} (u\, a_x) d\eta d\zeta \tag{2.39}$$

The frontal solver routine of Taylor and Hood (1973) is used to solve equation set **(2.27)**. The solver allows a core solution (no disk access needed) or a disk-storage routine, for problems where the required memory exceeds the computer RAM capacity.

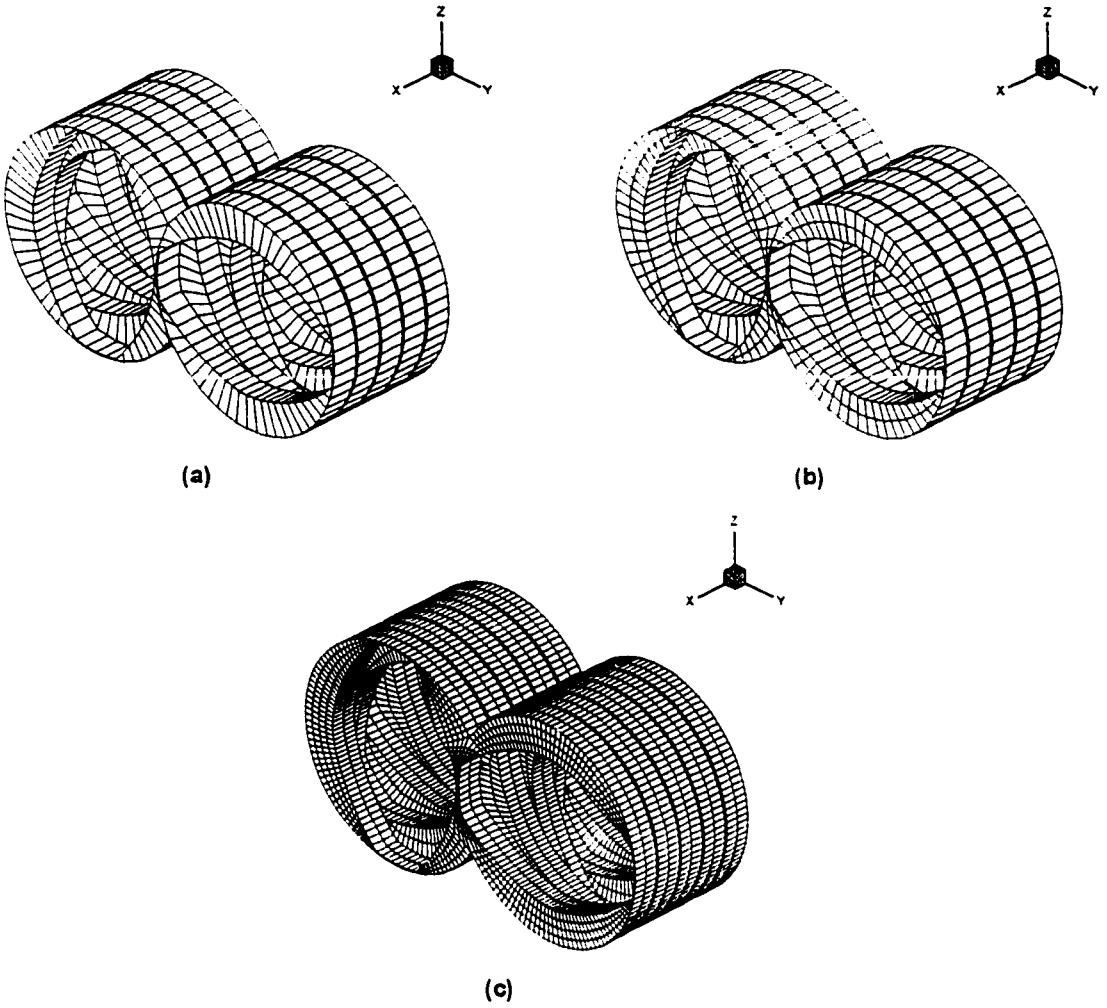

Figure 2.5. Finite element mesh with various element densities: a) 1,008 elements and 12,369 nodes; b) 2,016 elements and 20,881 nodes; c) 4,032 elements and 37,905 nodes

2.4.1. Boundary conditions.

In a flow problem, the equations of conservation of mass and momentum must be solved with the appropriate boundary conditions in order to obtain meaningful results. At the barrel wall and the rotor surfaces, the standard no-slip boundary condition is used. The fluid at the barrel surface remains stationary whereas the fluid at the rotor surfaces moves according to the local rotation speed. The surface linear velocity can be calculated as the product of the angular velocity multiplied by the radius between the nodal point and the rotation axis as:

$$u(x,y,z,t) = \omega \times r(x,y,z,t) \tag{2.40}$$

where ω is the angular velocity of the rotors and r is the position vector with respect to the center of each rotor.

The boundary conditions at the disc section inlet and outlet are more complicated to address because the section is being isolated from the upstream and downstream sections. As Yang (1993) points out, it is very difficult to calculate *a priori* the true velocity profiles at the entrance and exit planes. The kneading disc sections are usually fed by screw conveying sections. The boundary condition at the inlet of the kneading disc section should be the exit values of the preceding element section, and it is expected that both the elements before and after the studied sections affect the velocity profiles at the meeting planes. The complete specification of the inlet velocity profile would require the calculation of the flow field in the screw conveying section in conjunction with the kneading disc section. Kiani and Samman (1993) treated the boundary velocity condition between the two axial surfaces as periodic. Gotsis et al. (1990) imposed pressure boundary conditions at the entry and exit of the kneading disc section. There is no explicit description of the way this pressure boundary condition was implemented. Yang (1993) used a nominal value for the normal stress difference, combining pressure and viscous stresses, in the axial direction between the two planes. Yang explains that this condition is used as a pressure boundary condition when viscosity is low and therefore the viscous term in the total normal stress term ($\sigma_{xx} = -p + \tau_{xx}$) becomes negligible. This condition is not attained when polymer melts are the subject of study. Additionally, the rotation of the discs at the inlet and outlet boundaries create a pressure

profile in the y-z plane that forces a variation of the extra stress term at the same plane if the total stress term remains constant.

The normal stress boundary condition, combining pressure and viscous stress, is used in the results presented in this work. The main features of this approach are the ability to impose positive and negative pressure gradients between inlet and outlet, allowing the calculation of flow rate as a function of pressure and drag flows, and the elimination of the need for calculating inlet and outlet velocities *a priori*.

Application of the Galerkin method to the momentum equation produces:

$$R_m^i = \int_\Omega \{\nabla \cdot \sigma\} N^i d\Omega = \int_\Omega \{\nabla \cdot N^i\} \sigma d\Omega - \int_\Gamma n \cdot \sigma N^i d\Gamma \qquad \textbf{(2.41)}$$

where the first term on the right hand side applies to the entire domain, while the second term applies to the boundaries. Let us consider the boundary term,

$$F_i = \int_\Gamma n \cdot \sigma N^i \, d\Gamma \qquad \textbf{(2.42)}$$

This term can be expanded to obtain:

$$F_x = \int_\Gamma n_x \sigma_{xx} N^i d\Gamma + \int_\Gamma n_y \sigma_{xy} N^i d\Gamma + \int_\Gamma n_z \sigma_{xz} N^i d\Gamma \qquad \textbf{(2.43)}$$

$$F_y = \int_\Gamma n_x \sigma_{yx} N^i d\Gamma + \int_\Gamma n_y \sigma_{yy} N^i d\Gamma + \int_\Gamma n_z \sigma_{yz} N^i d\Gamma \qquad \textbf{(2.44)}$$

$$F_z = \int_\Gamma n_x \sigma_{zx} N^i d\Gamma + \int_\Gamma n_y \sigma_{zy} N^i d\Gamma + \int_\Gamma n_z \sigma_{zz} N^i d\Gamma \qquad \textbf{(2.45)}$$

In equations (2.43), (2.44) and (2.45), F_i represents the resultant forces and N^i represents the shape functions. Also n_x ,n_y and n_z are the components of the normal unit vector at the boundary, defined in equation (2.32).

A normal stress difference between the entrance and exit surfaces was assumed and then adjusted until the desired flow rate was obtained. It is arguable that the value of the normal stress involving the pressure and viscous terms ($\sigma_{xx} = -p + \tau_{xx}$) can be constant over an entire cross section of the extruder channel. At the same time, it is impossible to know *a priori* the actual normal stress profile at the inlet and outlet boundaries. To overcome this problem the normal stress boundary condition is applied at a specific distance from the area of interest, as shown in Figure 2.7. With this approach, the effect of the constant normal stress on the flow field is reduced due to the creeping nature of the flow and their short developing lengths. The problem of the formulation of appropriate boundary conditions at inflow and outflow planes has been a controversial one. Sometimes it is possible to obtain seemingly acceptable solutions for the finite flow field that are, in reality, poor approximations of the real problem (Vrentas et al, 1985). Validation via experimental flow visualization and velocity measurements is the best way to assess model boundary conditions.

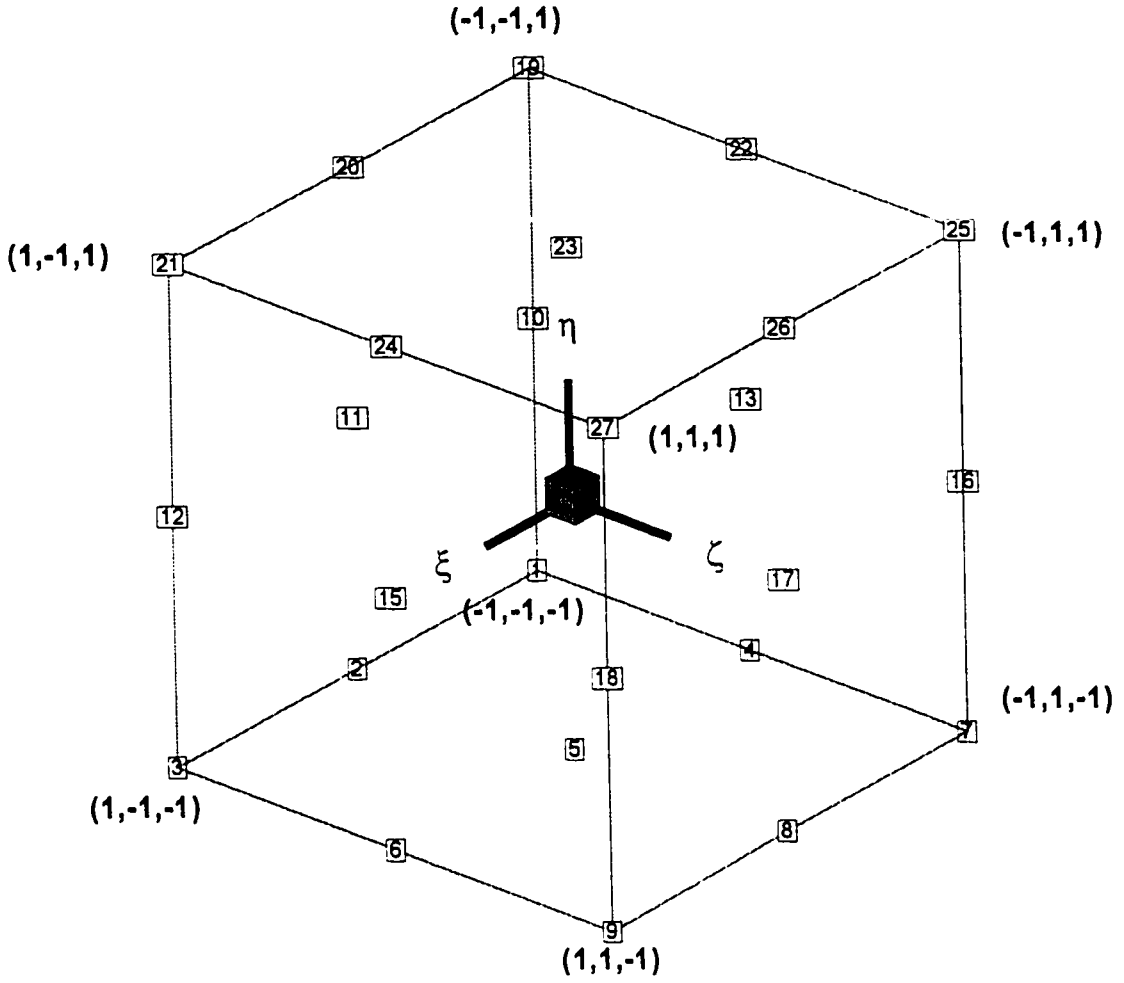

Figure 2.6. Local numbering for the 27-node triquadratic element. ξ–ζ–η coordinate system of the parent element.

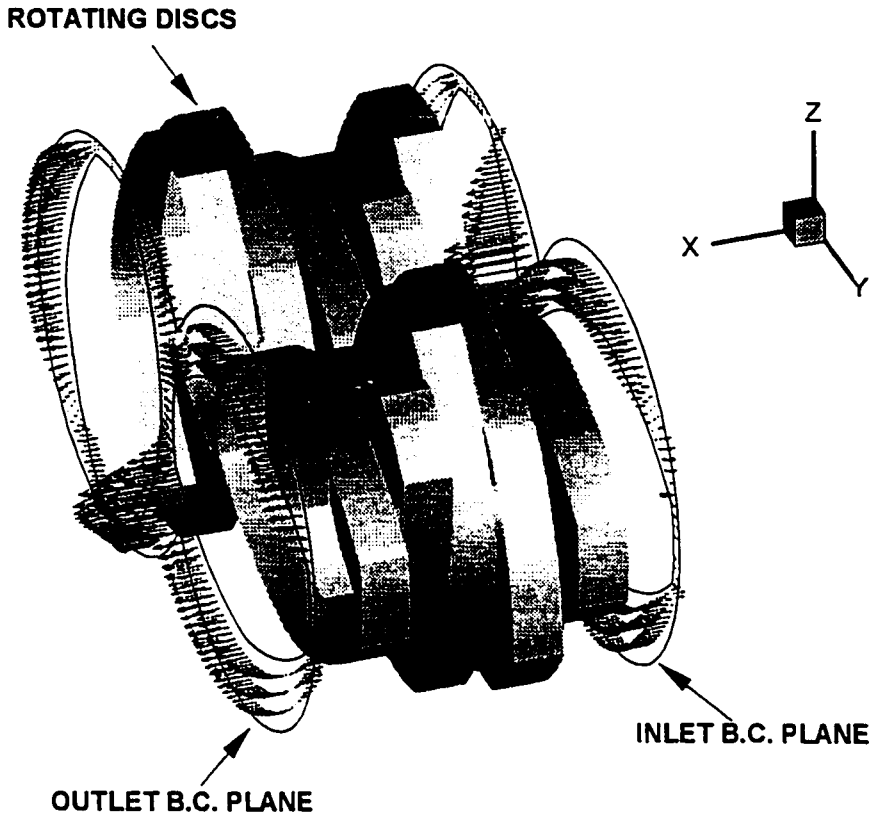

Figure 2.7. Inlet and outlet boundary conditions.

Chapter Three

EXPERIMENTAL VALIDATION: PRESSURE PROFILES

3.1 Introduction

The objective of this chapter is to validate, via comparison with experimental data available, the results obtained from the numerical simulation of polymer melt flow in the kneading disc section of an intermeshing co-rotating twin screw extruder. A quasi-steady state, 3-D solution of the conservation equations via the finite element method was obtained and comparisons were made with experimental pressure profiles measured by McCullough and Hilton (1993) on various kneading block elements. Todd (1989), White et al. (1990a) and Kalyon et al. (1997) have done comparisons with experimental pressure profiles, all using axial pressure measurements. Todd conducted studies for the analysis of flow in ICRTSE by measuring axial pressure profiles on a vertically mounted barrel. A Newtonian fluid was pumped upward to ensure 100% fill while the screws remained stationary. These results were used by Bravo(1995) for the validation of axial pressure profiles. Todd kept the screws stationary, thus eliminating the presence of steep pressure gradients in the circumferential direction that occur when the screws rotate. White et al. (1990a) made qualitative comparisons between predicted pressure profiles and the presence of starvation zones for screws with conveying and kneading elements. Kalyon et al. (1997) compared experimentally obtained axial pressure profiles with simulation results for a section of conveying elements. The large variation of the dynamic pressures as a function of time demands a high speed data acquisition system in order to be able to capture the pressure peaks. The work by Kalyon et al. does not specify the frequency of the data acquisition or the type of averaging used to obtain the axial pressure values.

The results obtained in the present work confirm the importance of a fully 3-D model for this type of geometry, where the model predicts the development of flow patterns in the radial and circumferential directions and within the intermeshing region. The influences of inlet and outlet boundary conditions were studied and it was determined that they play an important role in the physical significance of the model solution. Comparisons of the simulation results with experimental data by McCullough and Hilton (1993) for two different configurations of kneading discs showed good agreement, with some differences in the peaks of pressure produced at the narrow clearances encountered in intermeshing co-rotating twin screw extruders. Differences between simulation and experiments are attributed to a number of factors. It is difficult to measure the very steep pressure gradients generated over small lengths. The assumptions of isothermal flow and quasi-steady state may over-predict the pressure peaks. Simulation results describe the general trends and produce good quantitative agreement in most of the kneading disc region.

3.2 Geometry

The generation of the complex geometry involved in the kneading discs section of a twin screw extruder is based on the work done by Booy (1978). The calculation of the flow field within a twin screw extruder requires a complete knowledge of the geometry. The cross section of a twin screw has a unique shape given by diameter, centerline distance, and number of parallel channels because of the requirement that one screw must, in any position, wipe its mate (Booy, 1978). The dimensions of the Werner & Pleiderer ZSK-30 type co-rotating extruder are shown in Table 2.1.

For the discretization of the twin screw domain, different densities of 27-node triquadratic brick element meshes were tested. The results shown in this work correspond to a mesh of 2,016 elements and 20,881 nodes, as depicted Figure 3.1. The calculation of flow rate in a arbitrary plane involves the computation of the velocities in such plane. This computation can be done from the isoparametric transformation (Kistler and Scriven, 1983).

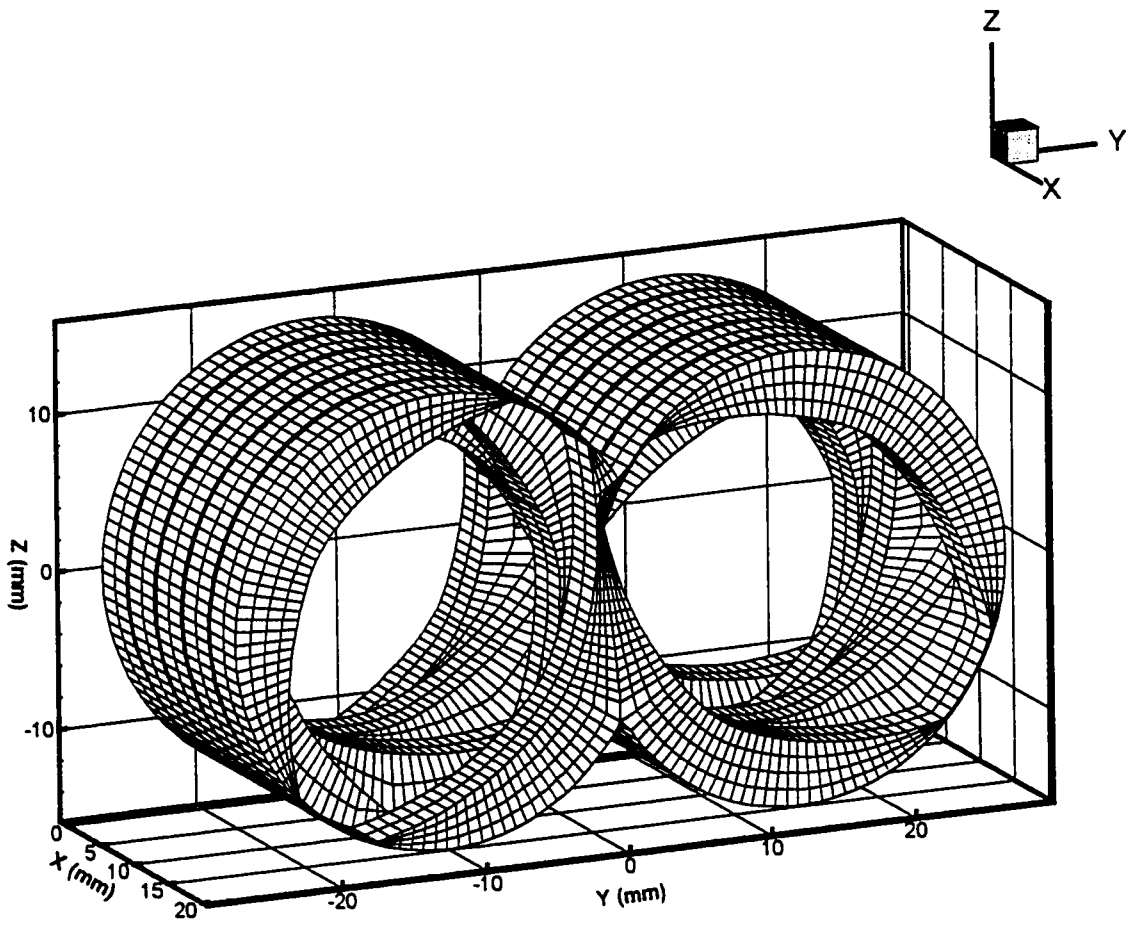

Figure 3.1. Finite element mesh with 2,016 elements and 20,881 nodes

A commercial package, TECPLOT v.7 (1996) was used for the visualization of the post-processed data files. This facilitated the visualization of results by allowing analysis in different cross sections as well as the study of the individual variables over the 3-D surfaces of the kneading discs.

The finite element code was used to obtain the velocity profiles and the pressure distributions of the flow field according to experimental stagger angles and operating conditions by McCullough and Hilton (1993).

3.3 Boundary conditions

A normal stress difference between the entrance and exit surfaces was set as $\Delta\sigma_{xx}$, such that the desired flow rate was obtained. Equations (2.43), (2.44) and (2.45) are applied over the inlet and outlet boundaries. The average pressure rise measured in the apex ports over the length of 42 mm in the 45/5/42 configuration was approximately 650 kPa , and the average pressure rise measured in the side ports was 500 kPa. The reference value of σ_{xx} was set zero at the entrance plane and $\Delta\sigma_{xx}$ was set to 1035 kPa to match the experimental flow rate of 4.35 Kg/h.

3.4. Comparison with experimental pressure profiles

Traditional twin screw extrusion process data are limited to pressures and temperatures measured at the die. Measurements are not normally made along the barrel since the best measurement locations are a function of screw configuration. Steep pressure gradients are likely to appear in both the axial and rotation directions. McCullough and Hilton (1993) developed an experimental apparatus consisting of a 30 mm diameter TSE using a 2L/D feed adapter, an instrumented 6L/D test barrel section and standard die assembly. The configuration of the apparatus is shown in Figure 3.2. The reverse kneading elements at the end of the kneading disc section restricted the flow and raised the pressure within the system. Figure 3.2a shows an end view of the barrel section from the feed end with the location of the pressure transducer at the top

of the apex and the side of the main screw on the right. To obtain the required pressure data, McCullough and Hilton equipped the barrel with five ports evenly spaced every 30 mm along the top and bottom of the center apex region, and three ports along the sides spaced every 60 mm. The TSE assembly was mounted on a movable lathe bed. This allowed the barrel section to be moved back and forth along the screw elements for the various measurements. High-speed data measurements confirmed that the pressure transducers were capable of responding as fast as 800 MPa/s. Response time is critical because at 100 rpm (or 600 degrees/s) pressure can fluctuate as much as 8 MPa in 0.05 seconds, or 160 MPa/s. The data collection frequency was set to record pressure data at each degree of screw rotation: 360 records/second at 60 rpm and 800 records per second at 140 rpm.

Results are presented for runs at 60 and 140 rpm using a low density polyethylene. Pressures were measured at the side of the main screw and at the top of the apex, for different arrays of kneading discs, according to Figure 3.2b. Of special interest for the comparisons with simulation data are two of the configurations depicted in Figure 3.2b. The configuration of forward kneading discs are 45/5/20 (where 45 is the stagger angle, 5 is the number of discs and 20 stands for a total disc section length of 20 mm) and 45/5/42. The pressure measurements are plotted as a function of the amount of rotation.

The axial pressure drop plots show average, maximum and minimum values over one cycle of rotation for apex and side measurements. For the simulations, the average side pressure drop was used as an initial guess for the normal stress difference imposed as boundary condition and then adjusted to obtain the correct flow rate. The average side pressure was used since it is the most representative of the average behavior in the system. The pressure fluctuations in the apex region are more intense than at the side due to the interaction of the two screws at the intermeshing region. The flow rate was kept at 4.35 Kg/hr to match experimental conditions. The complete set of operating conditions and material properties (McCullough and Hilton, 1993) are presented in Tables 3.1 and 3.2 and Figure 3.3.

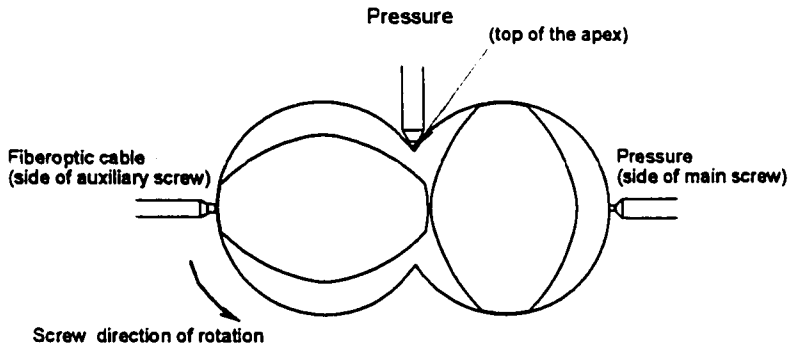

(a)

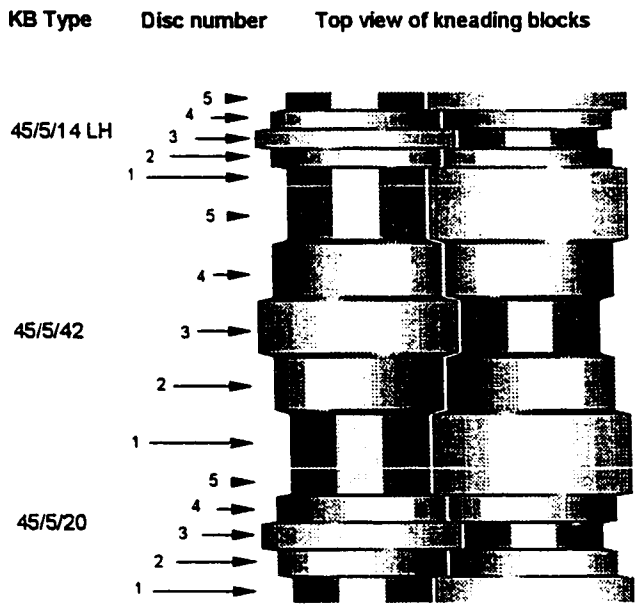

(b)

Figure 3.2. Apparatus used by McCullough and Hilton (1993); a) transducer locations, b) kneading block orientation.

Flow rate	4.35 Kg/hr
$\Delta\sigma_{ex}$	1035 kPa
RPM	60/140
Kneading blocks	45/5/20, 45/5/42
Location of ports	Apex and side

Table 3.1. Operating conditions

Material Properties	
Material	LDPE 641I (Dow Chemical)
Melt Density	740 Kg/m^3
Average melt temperature	223 °C
Rheological parameters for Carreau model	
μ_0	1290 Pa.s
λ	0.112483 s
N	0.5590

Table 3.2. Material properties and rheological parameters

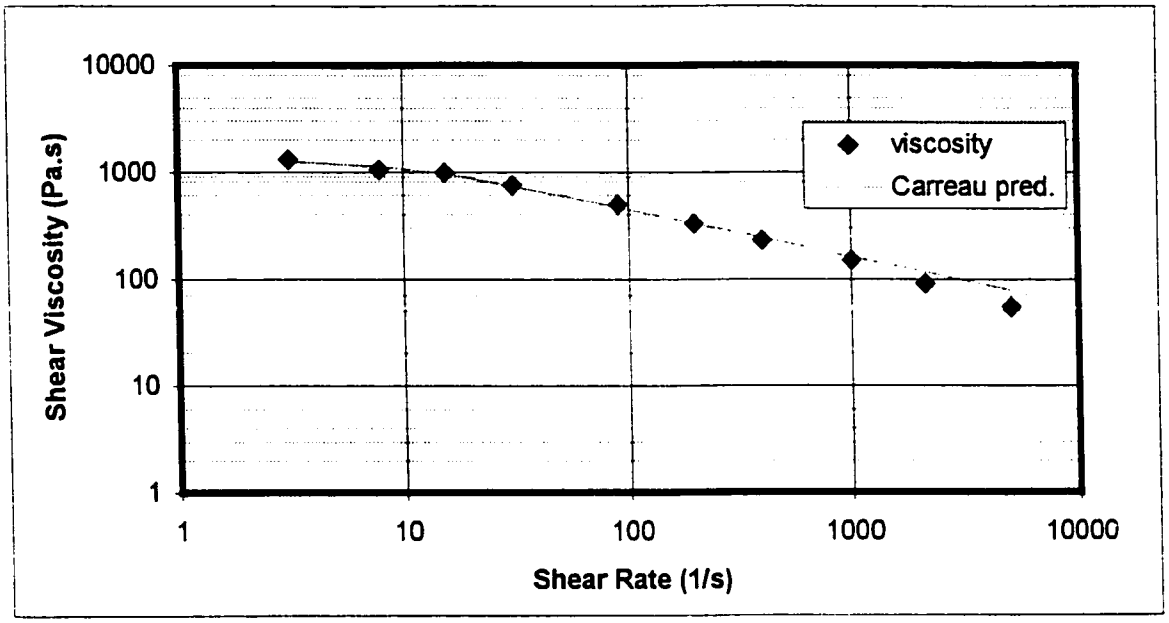

Figure 3.3. Viscosity vs shear rate at 230 °C (McCullough and Hilton, 1993)

A total of 7 steady state solutions with increments of 12.86° are used to complete one quarter of a revolution. Due to the symmetry of the system, calculation of only one quarter of a revolution is necessary to describe the complete cycle. Figure 3.4 gives a schematic view of the symmetry of the problem. The complete set of solutions is obtained by means of spatial transformation to rotate the first quarter geometry 180° around the x-axis to obtain the second quarter. Once the solution for a half revolution is obtained, symmetry applies again making the second half revolution identical to the first half. An isometric view of the combination of kneading blocks used for the experimental work is shown in Figure 3.5.

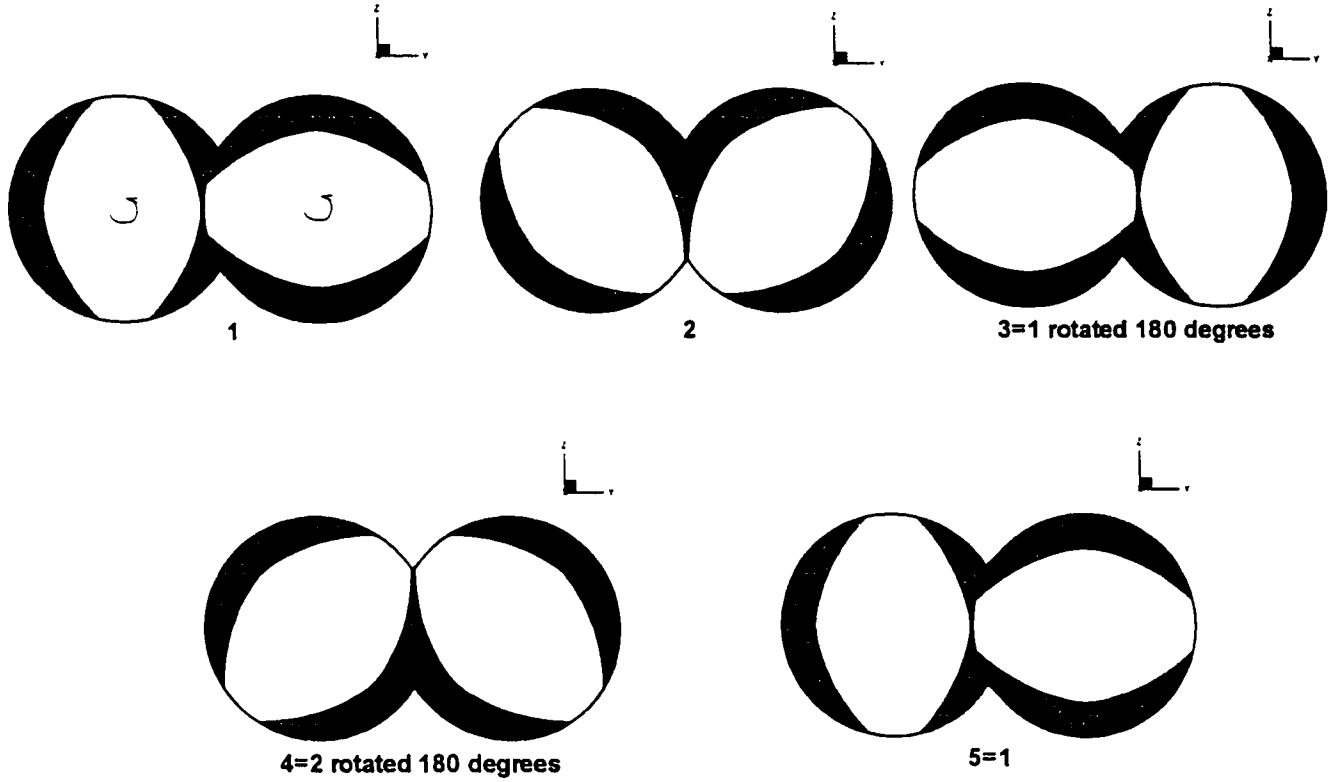

Figure 3.4. Symmetry conditions for one cycle of rotation.

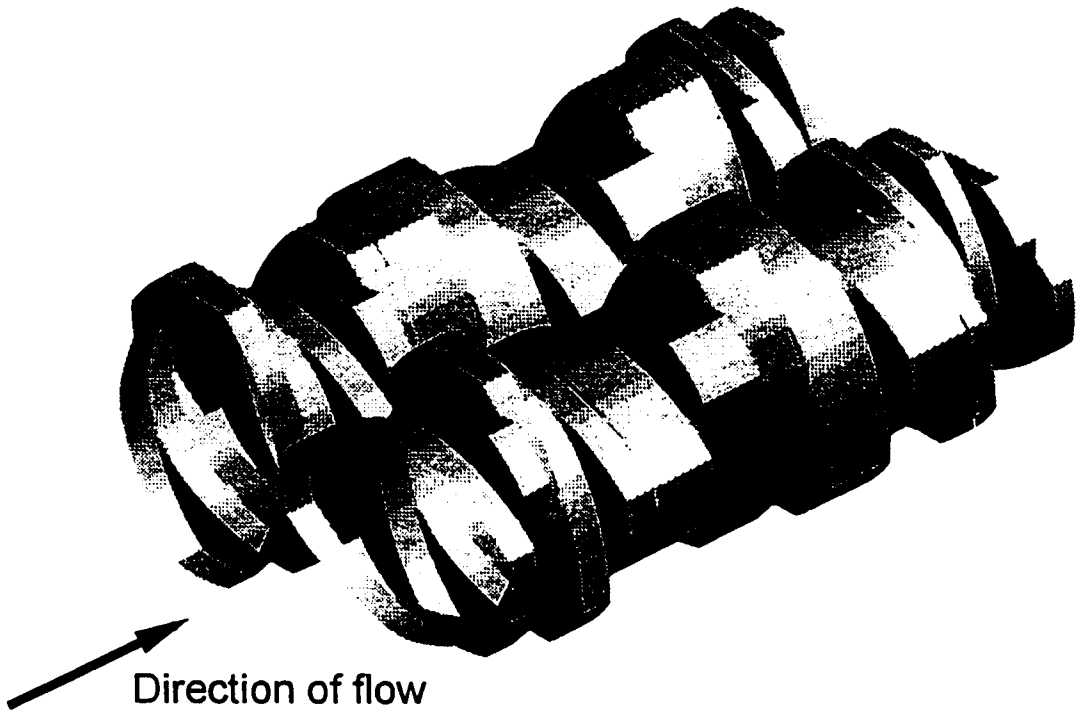

Figure 3.5. Isometric view of the combination of kneading blocks used in the experimental work by McCullough and Hilton (1993).

The numerical determination of pressures at the side and apex is done by interpolating the values at the locations equivalent to the location of the pressure transducers in the experimental setup. Since the reported experimental pressure value is at a point, nine calculated pressure values are interpolated in a cross-like figure as shown in Figure 3.6 to cover a 1mm diameter circle which corresponds to the area exposed to the pressure transducer in the experimental setup. An average of the nine points is then taken to account for the pressure on the 1mm diameter circle. The pressure values are interpolated from the nodal values previously obtained through the FEM calculations. Once the coordinate of the point where the pressure needs to be calculated is determined, an algorithm searches for the element of the mesh that contains that coordinate. The pressure is then interpolated from the nodal values using the element's interpolation functions. For a full revolution, the numerical procedure of determining the pressure at the apex and side ports is repeated 28 times for every disc.

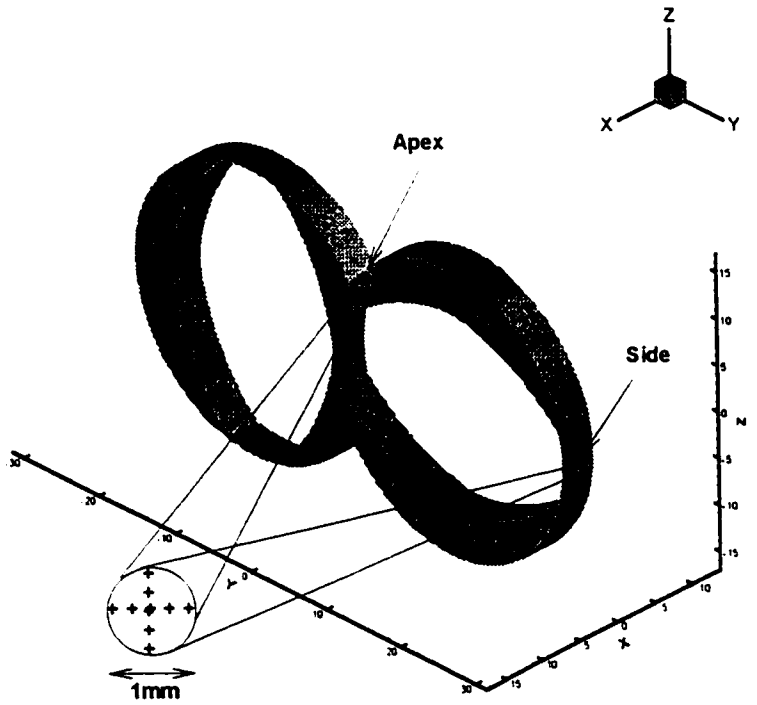

Figure 3.6. Numerical determination of pressure at side and apex ports.

For the simulation of the 45/5/42 configuration the geometry depicted in Figure 3.1 representing 5 pairs of discs was used. For the 45/5/20 configuration a system with two pairs of discs was used, one to emulate the preceding pair to a second one which is the focus of our attention.

The curves in Figure 3.7 and 3.8 are the apex and side pressures measured by McCullough and Hilton for disc 1 to 5 of the 45/5/42 array. The peaks are 180° of rotation apart as expected for 2-lobed elements and successive peaks in the axial direction are offset by approximately 45° of rotation. The simulation performed in the present work captures this behavior, as shown in Figures 3.9 and 3.10. Figure 3.7 shows how the amplitude of the pressure changes from disc1 to disc 5. In disc 1 the pressure fluctuates from a low of 2350 kPa to a high of 3310 kPa, or a maximum variation of 960 kPa. At the end of the kneading block at disc 5, adjacent to the reverse configuration of kneading blocks, the pressure varies from a low of 3390 kPa to a high of 3680 kPa for a total variation of 290 kPa. The average pressure increases from the first to the last disc. This pressure rise is commonly seen in kneading blocks that precede reverse elements that produce the filled channel necessary for an optimal mixing performance. Figure 3.8 shows pressure measurements for the side port with the same trends as for the apex port measurements, but with smaller variations from minimum to maximum pressures. For the side port, the maximum variation for disc1 is 250 kPa whereas for disc 5 the maximum pressure variation is 110 kPa.

Figures 3.11 and 3.12 show the comparison between simulation and experimental variation in pressure for a complete cycle of disc 5 in the 45/5/20 configuration; at this location the pressure fluctuations are the largest in the system. The experimental peaks for the apex port reach 4250 kPa whereas the minimum pressure is 1750 kPa. Figure 3.11 shows the pressure profiles at the side port, where the amplitude of the fluctuations is less than for the apex port.

Figure 3.13 displays a comparison between experimental and simulation pressure profiles in the axial direction, measured and calculated at the apex port of the 45/5/42 configuration. The values presented are average, minimum and maximum axial pressure. The comparison of

experimental and simulation values for axial pressure at the side port is presented in Figure 3.14.

Figures 3.15 to 3.19 present experimental and simulation results for the individual discs of the 45/5/42 configuration at the apex port. Figures 3.20 to 3.24 show the experimental and simulation results at the side port of the 45/5/42 configuration.

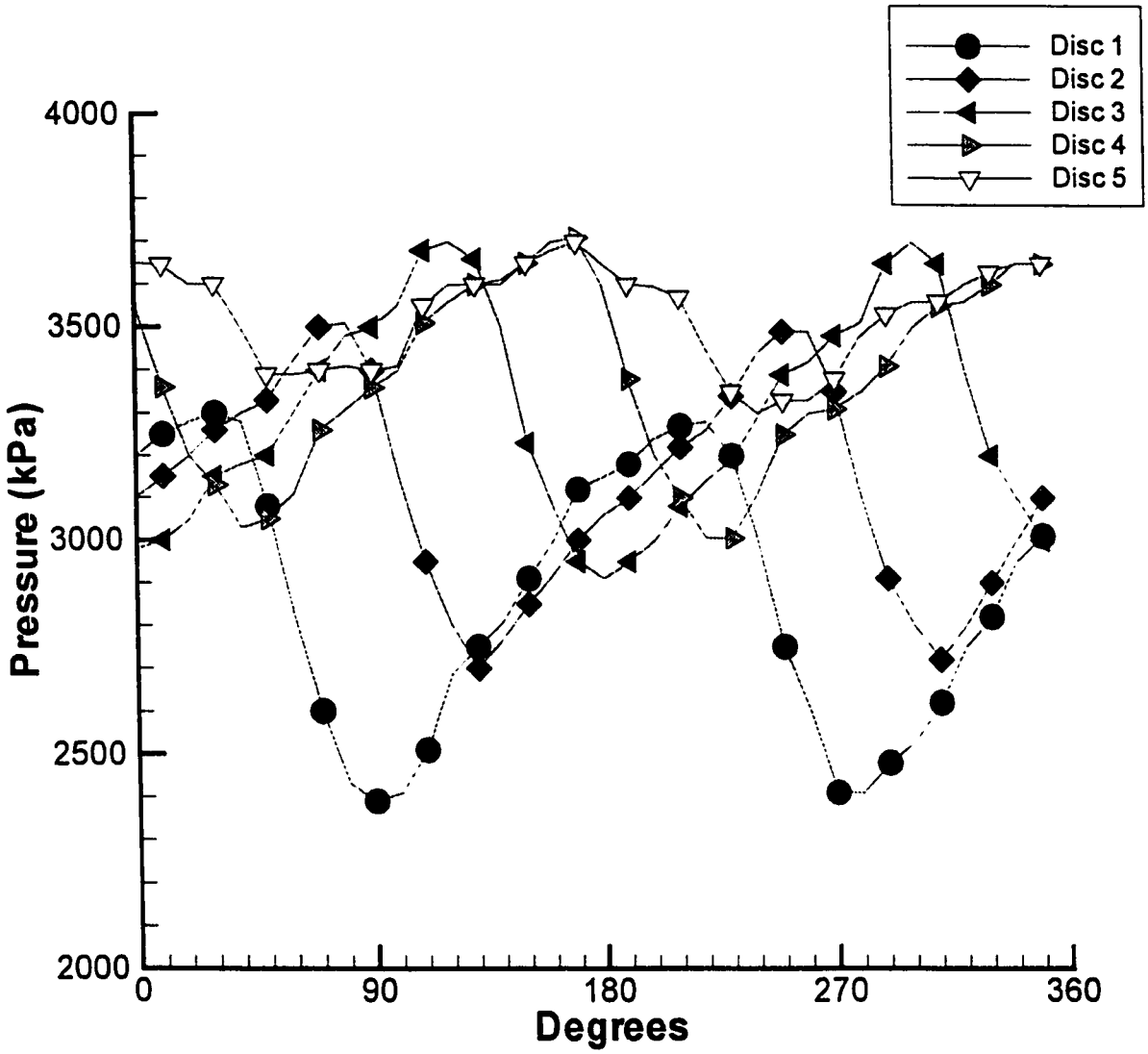

Figure 3.7. Experimental pressure profiles as a function of rotation angle. Apex port of the 45/5/42 configuration of kneading blocks (McCullough and Hilton, 1993).

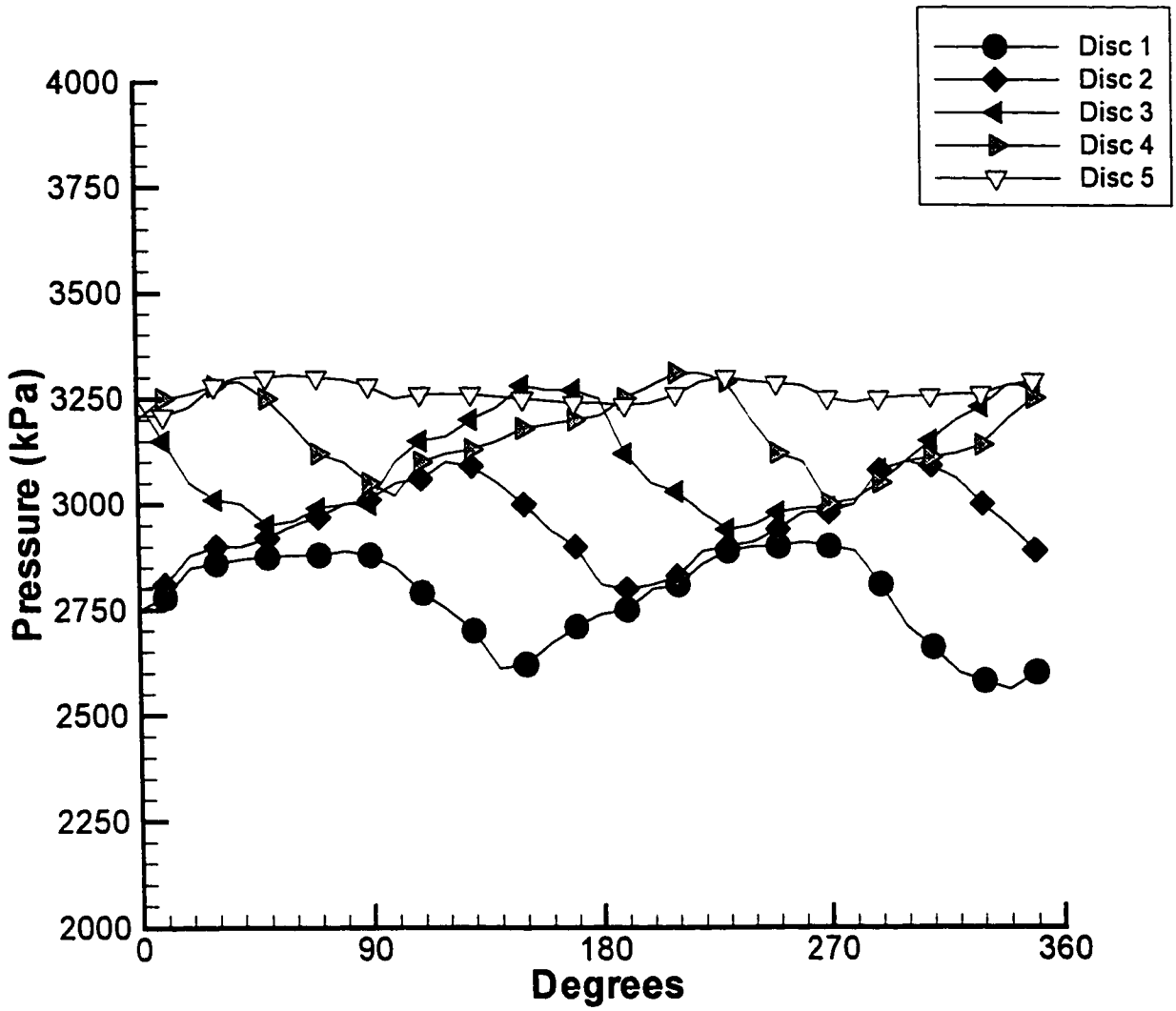

Figure 3.8. Experimental pressure profiles as a function of rotation angle. Side port of the 45/5/42 configuration of kneading blocks (McCullough and Hilton, 1993).

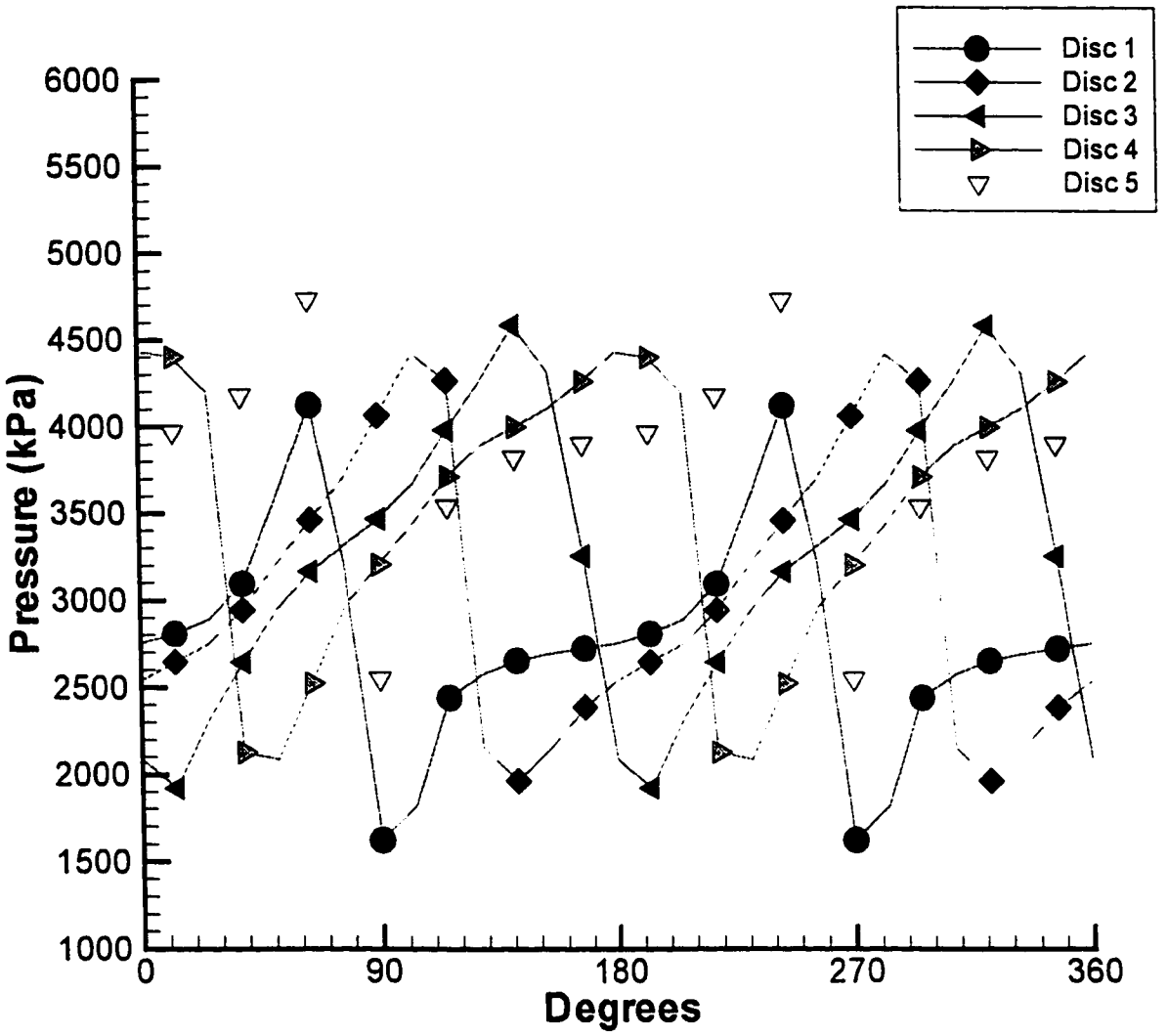

Figure 3.9. Simulation pressure profiles as function of rotation angle. Apex port of the 45/5/42 configuration of kneading blocks.

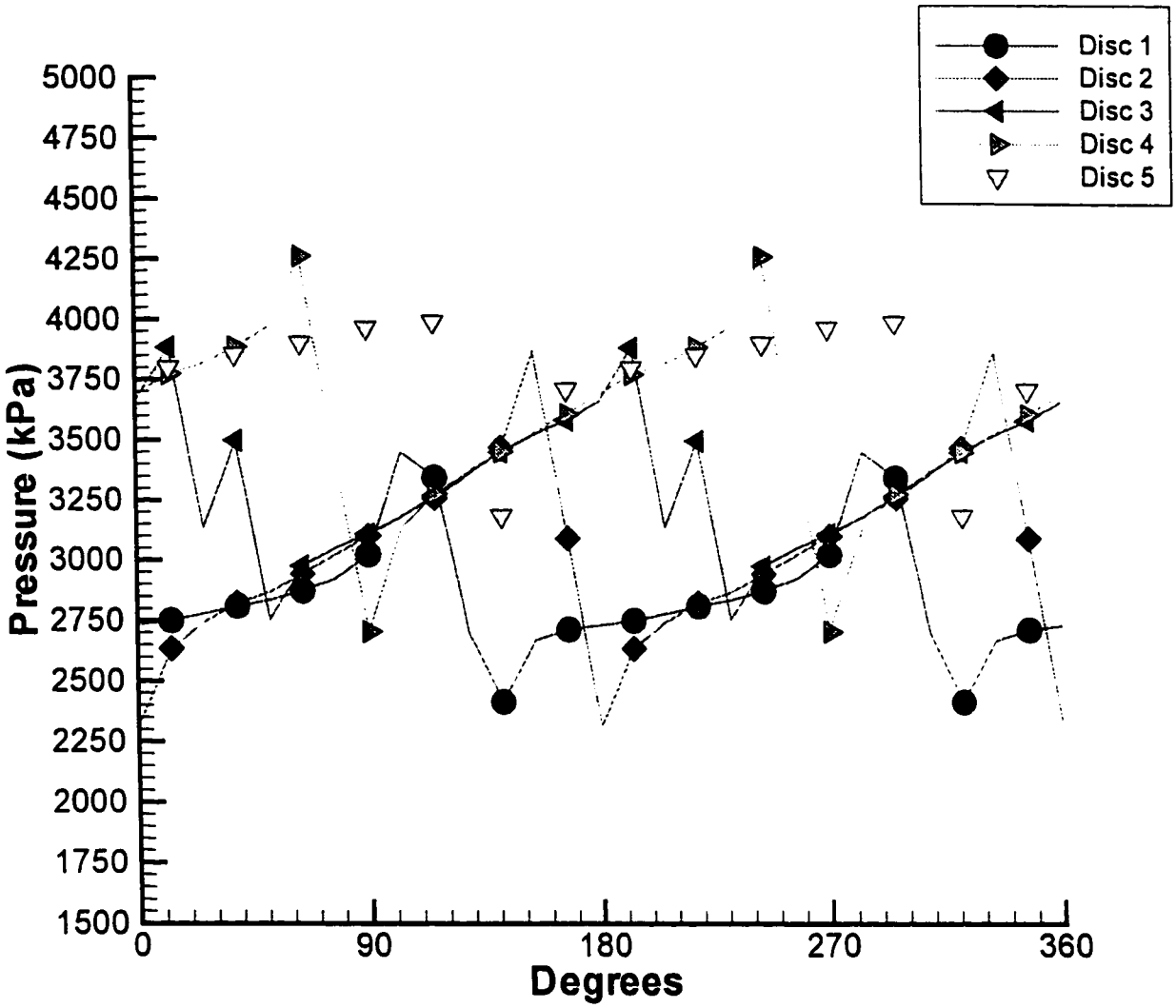

Figure 3.10. Simulation pressure profiles as function of rotation angle. Side port of the 45/5/42 configuration of kneading blocks.

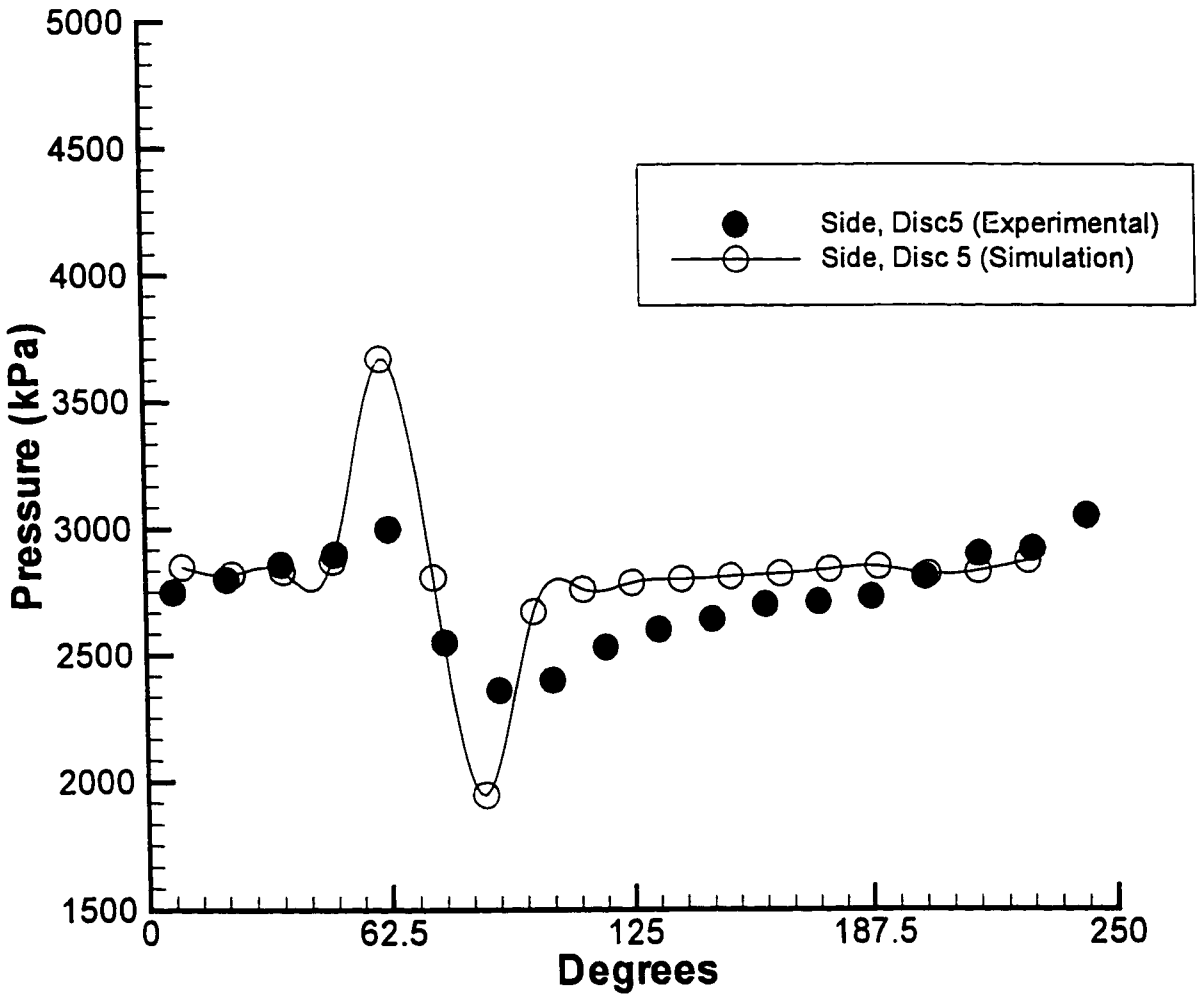

Figure 3.11. Experimental and simulation pressure profiles. Side port on disc 5 of the 45/5/20 configuration of kneading blocks.

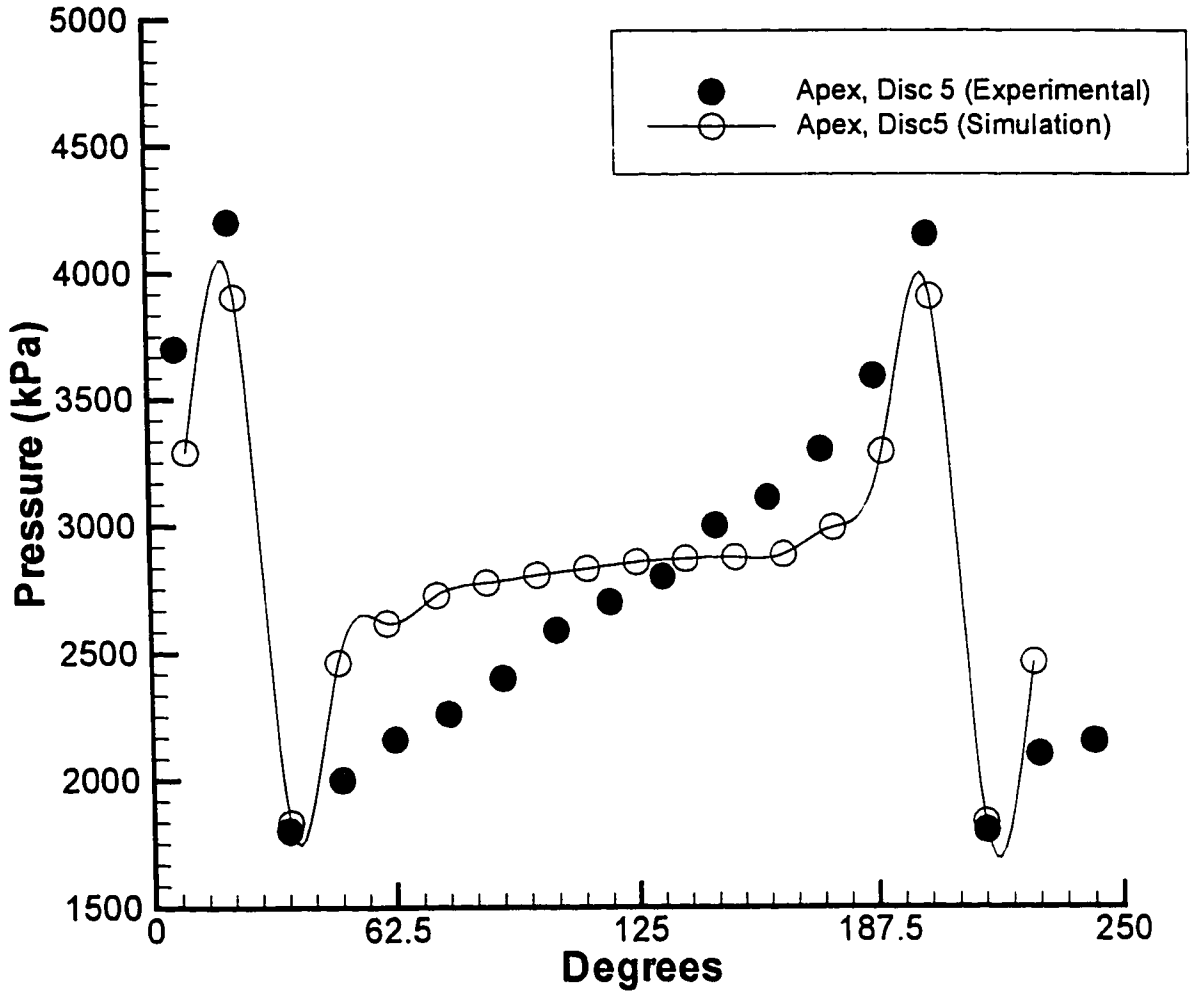

Figure 3.12. Experimental and simulation pressure profiles. Apex port on disc 5 of the 45/5/20 configuration of kneading blocks.

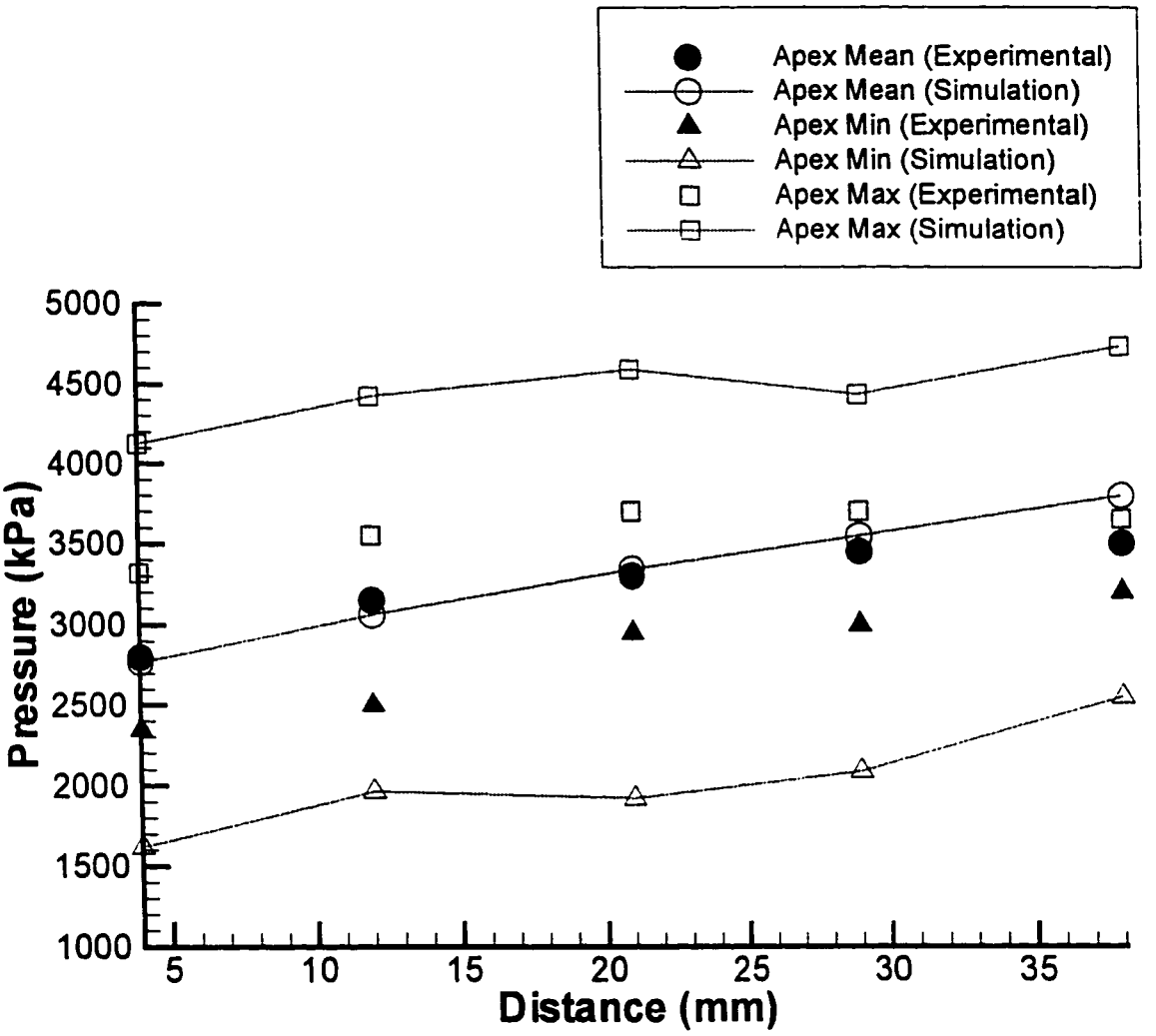

Figure 3.13. Experimental and simulation axial pressure profiles. Apex port of a 45/5/42 configuration of kneading blocks.

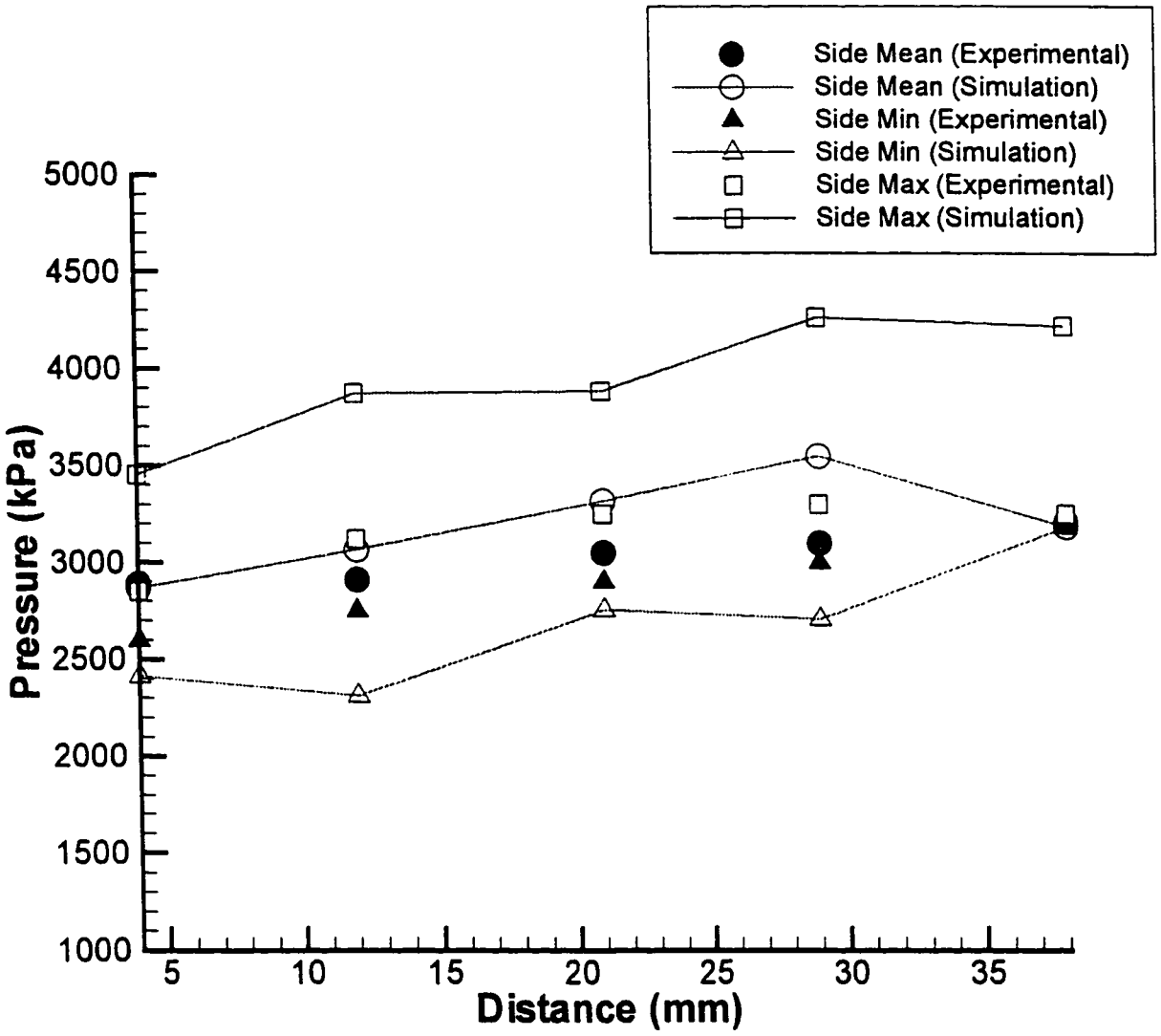

Figure 3.14. Experimental and simulation axial pressure profiles. Side port of a 45/5/42 configuration of kneading blocks.

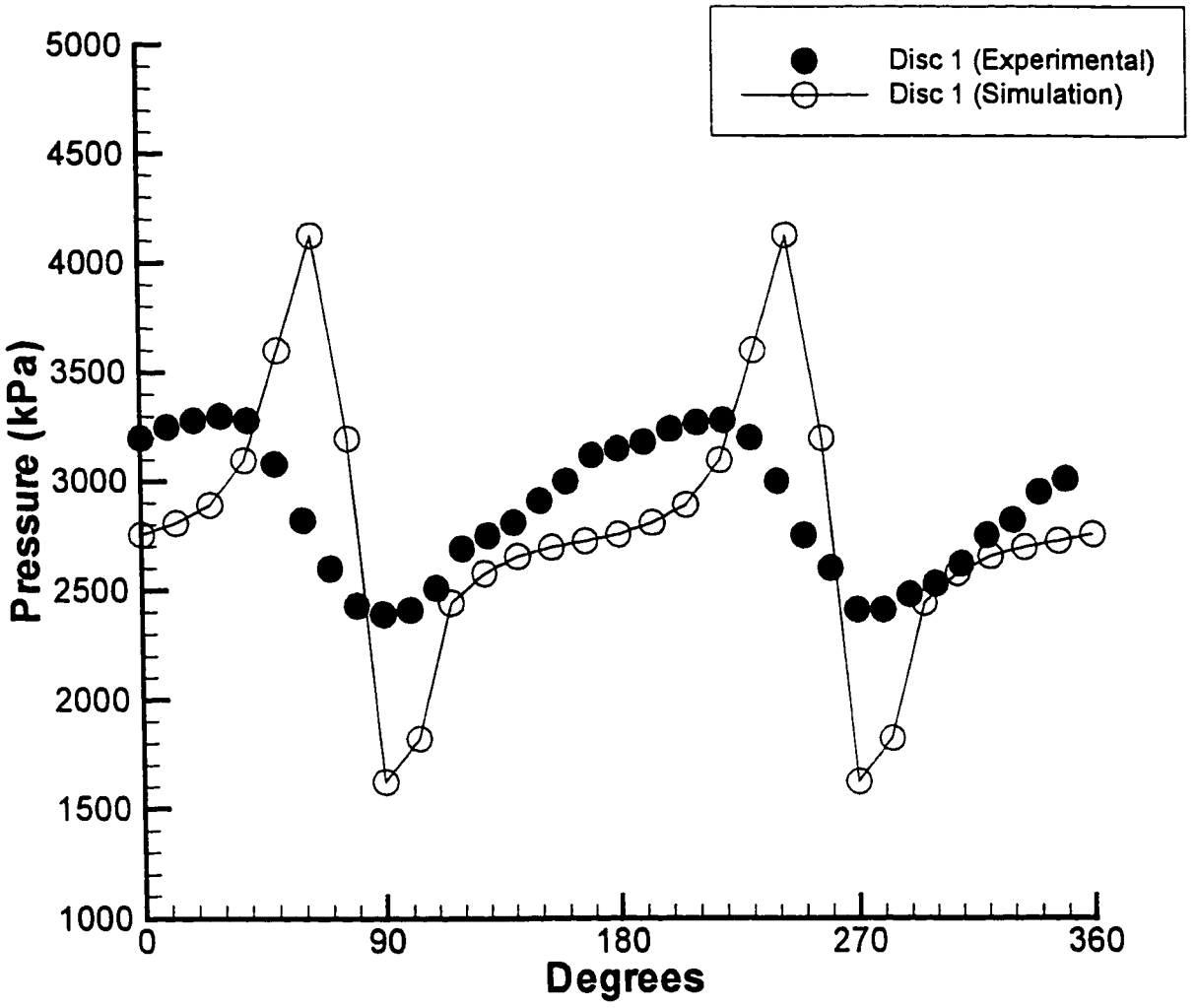

Figure 3.15. Experimental and simulation pressure profiles as function of rotation angle for disc 1. Apex port of the 45/5/42 configuration of kneading blocks.

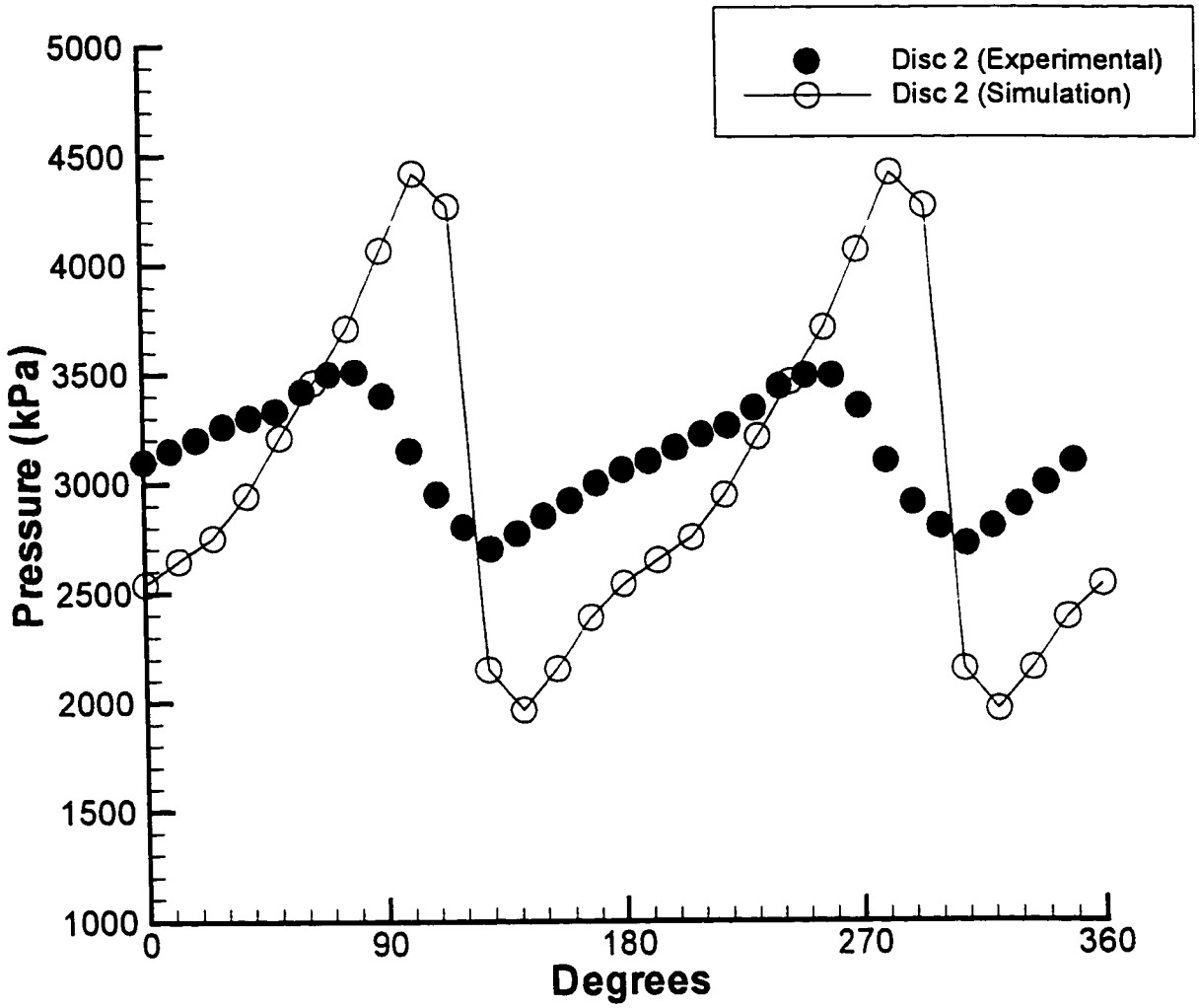

Figure 3.16. Experimental and simulation pressure profiles as function of rotation angle for disc 2. Apex port of the 45/5/42 configuration of kneading blocks.

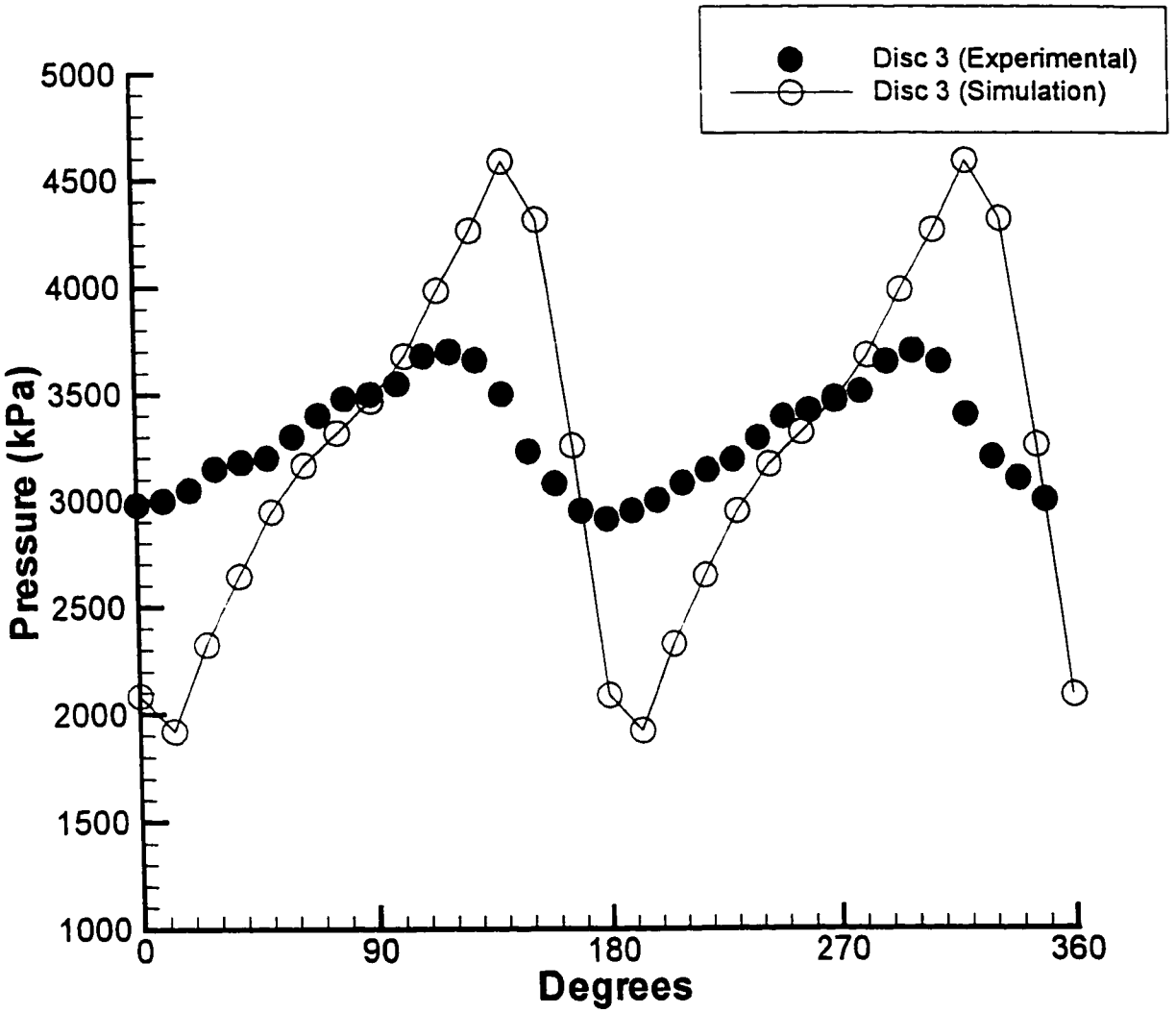

Figure 3.17. Experimental and simulation pressure profiles as function of rotation angle for disc 3. Apex port of the 45/5/42 configuration of kneading blocks.

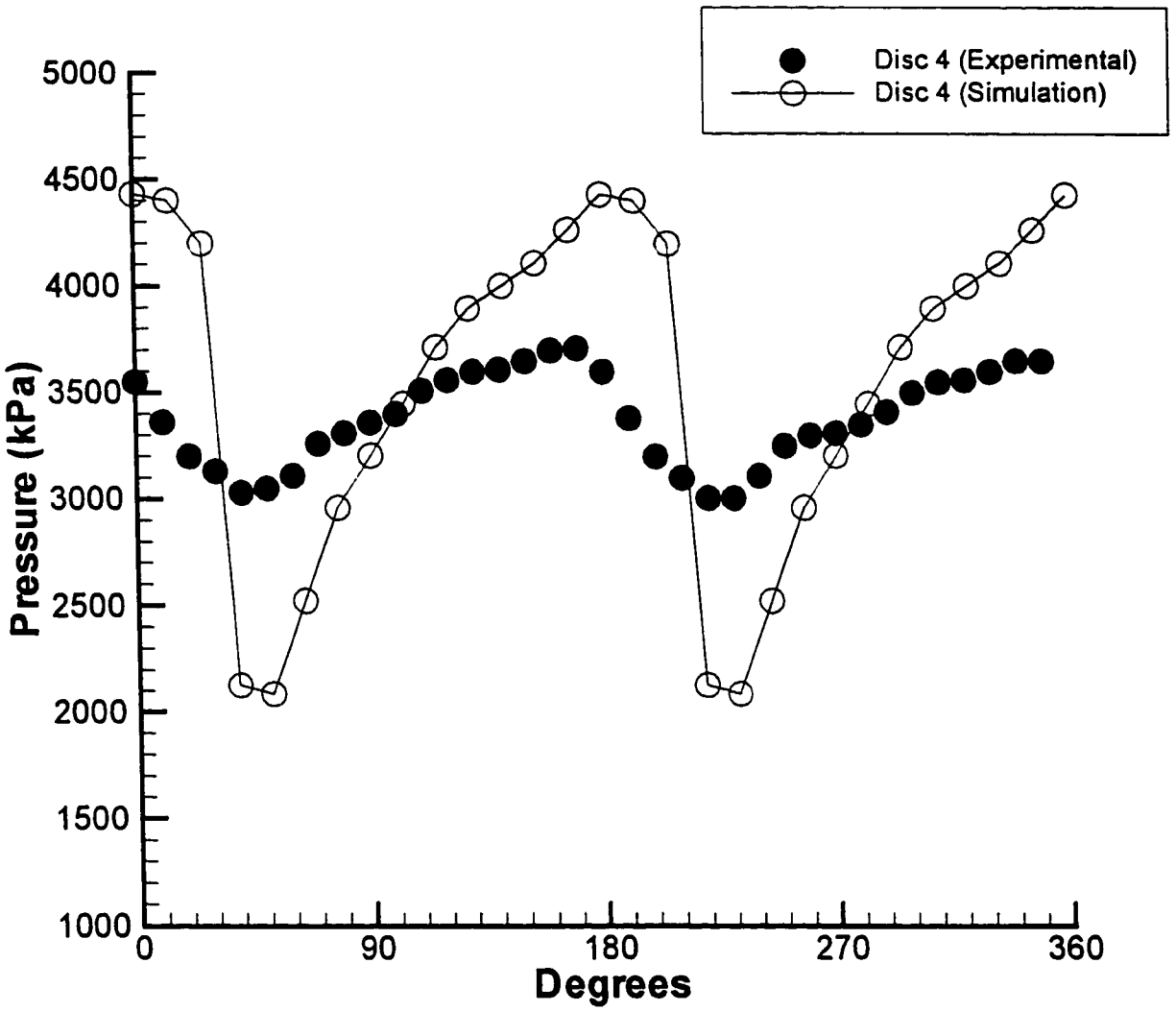

Figure 3.18. Experimental and simulation pressure profiles as function of rotation angle for disc 4. Apex port of the 45/5/42 configuration of kneading blocks.

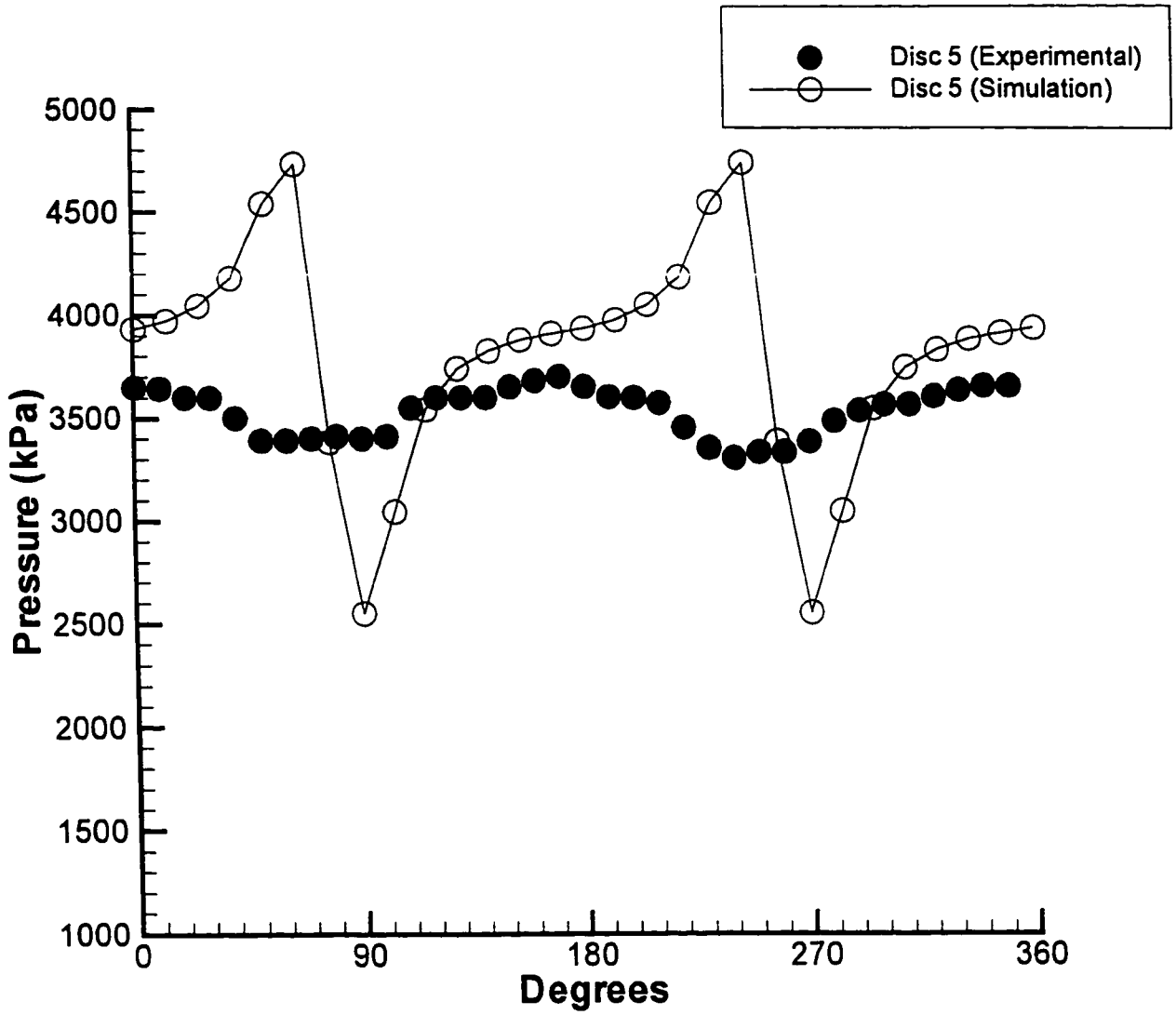

Figure 3.19. Experimental and simulation pressure profiles as function of rotation angle for disc 5. Apex port of the 45/5/42 configuration of kneading blocks.

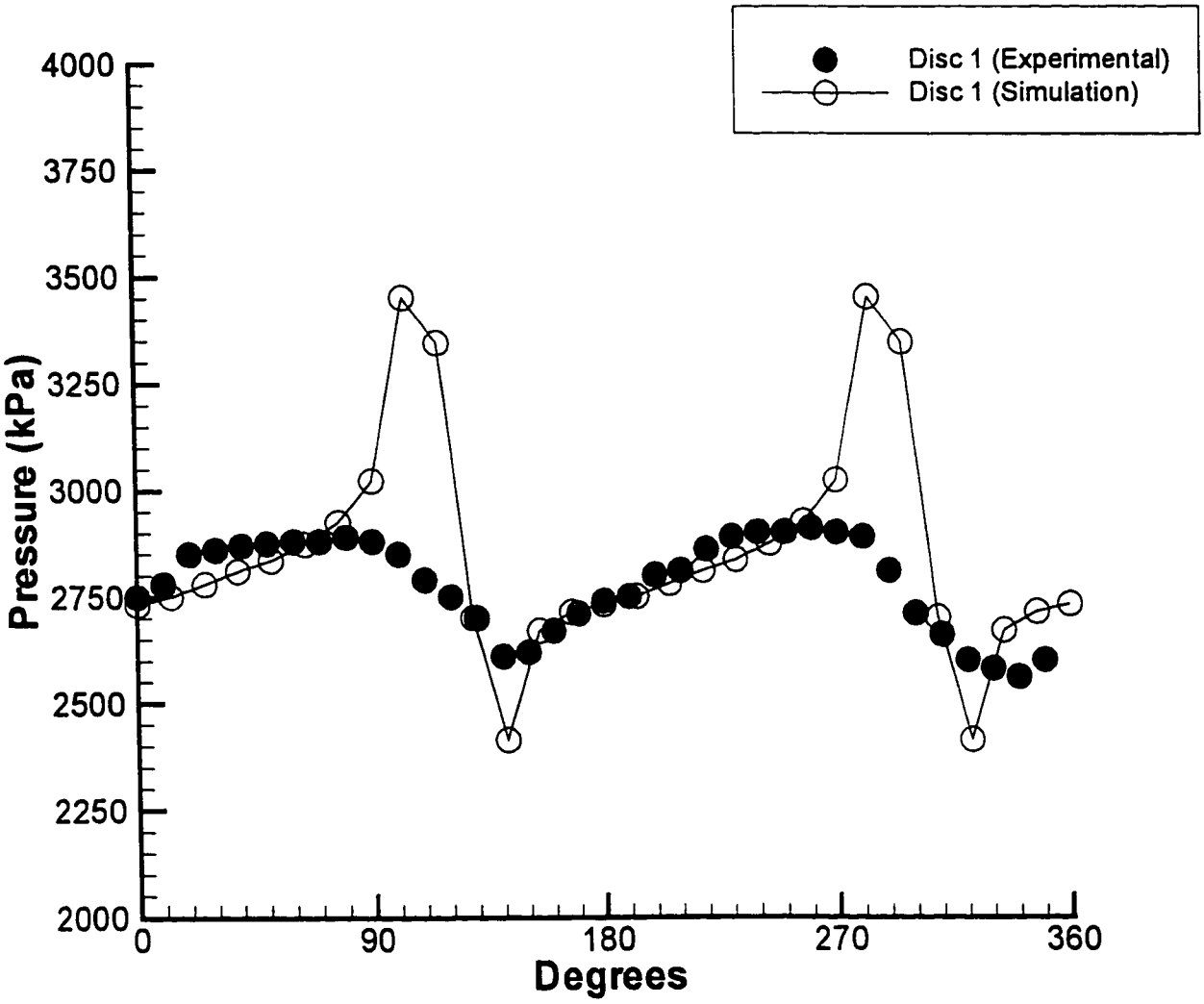

Figure 3.20. Experimental and simulation pressure profiles as function of rotation angle for disc 1. Side port of the 45/5/42 configuration of kneading blocks.

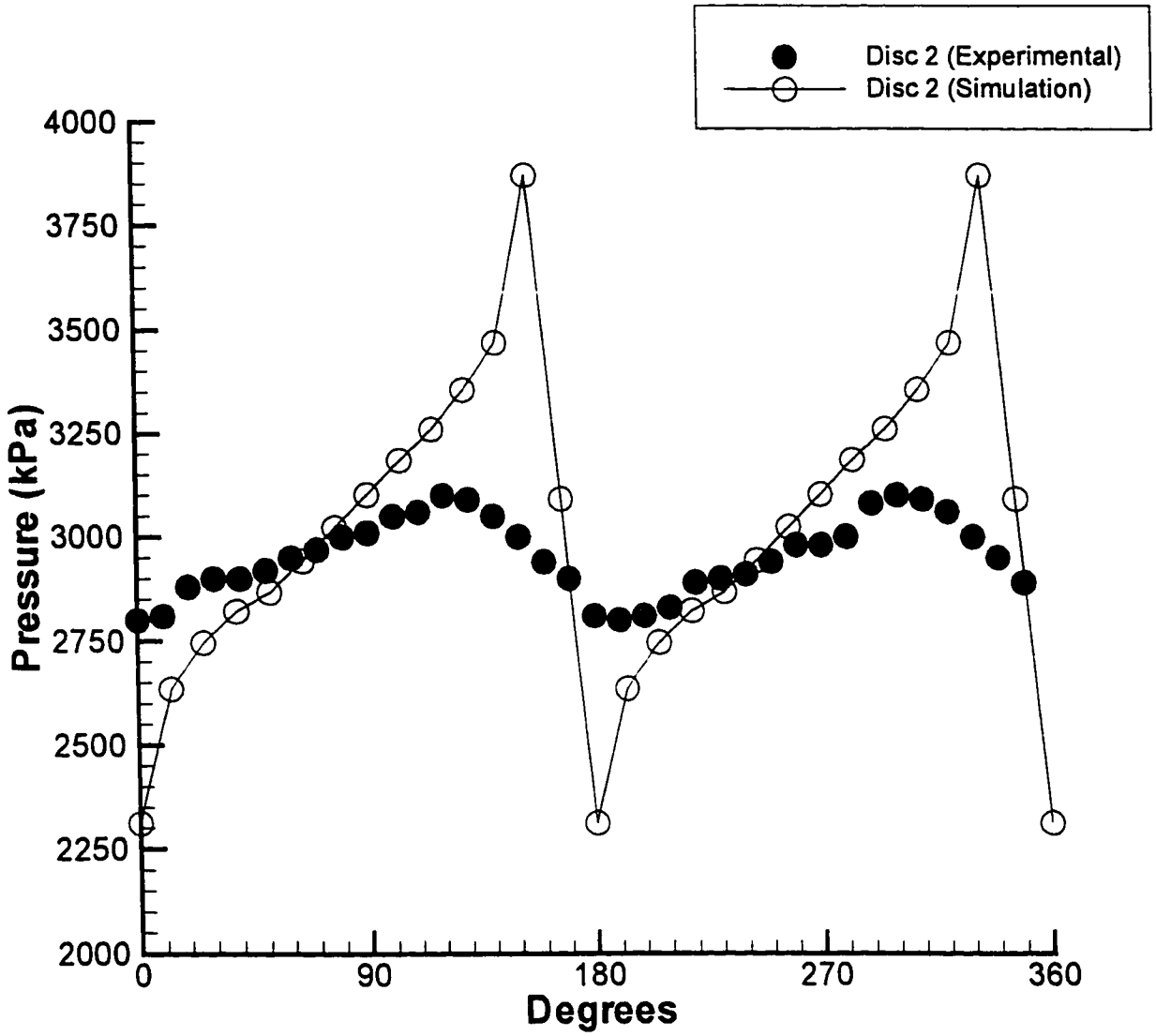

Figure 3.21. Experimental and simulation pressure profiles as function of rotation angle for disc 2. Side port of the 45/5/42 configuration of kneading blocks.

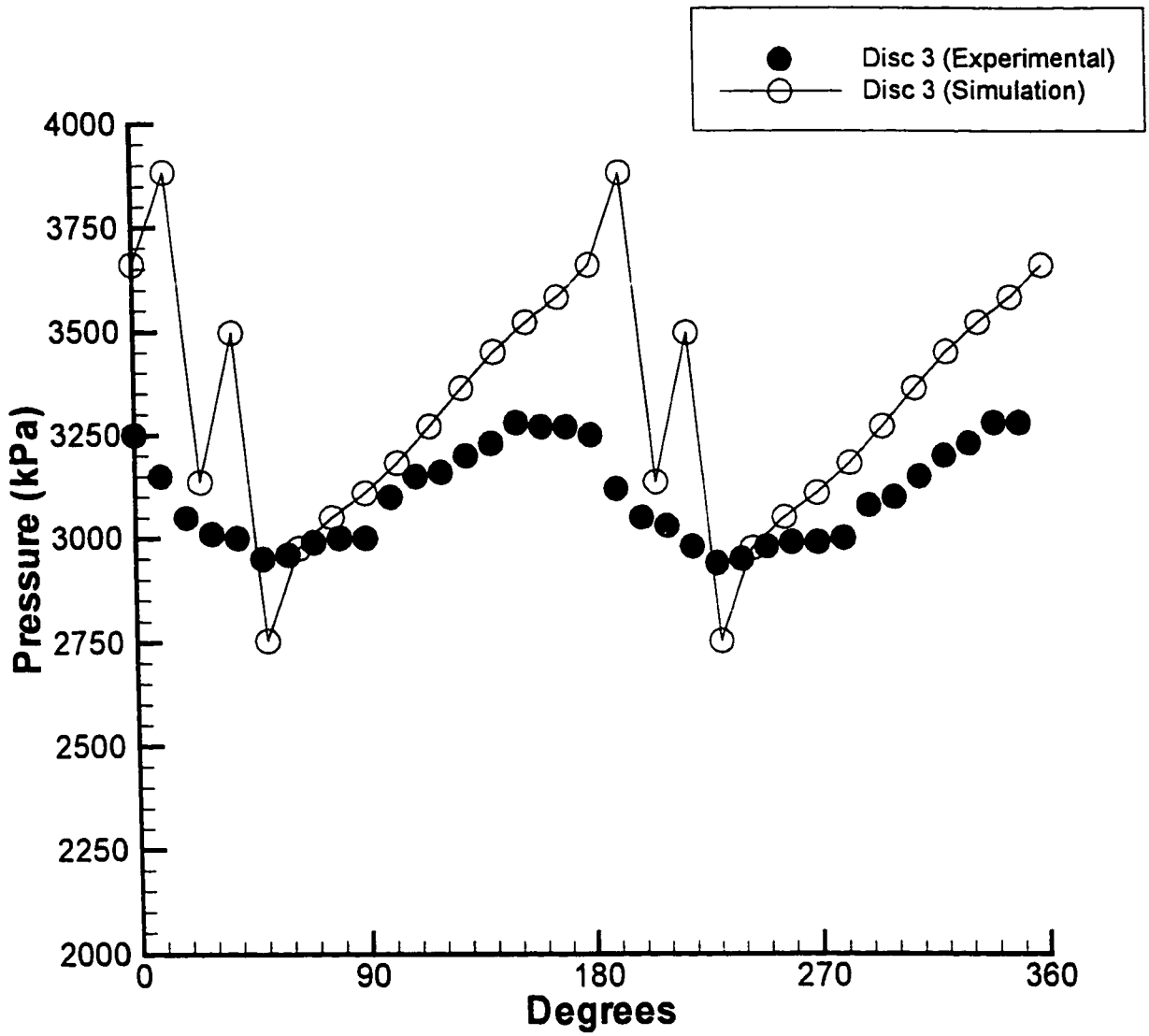

Figure 3.22. Experimental and simulation pressure profiles as function of rotation angle for disc 3. Side port of the 45/5/42 configuration of kneading blocks.

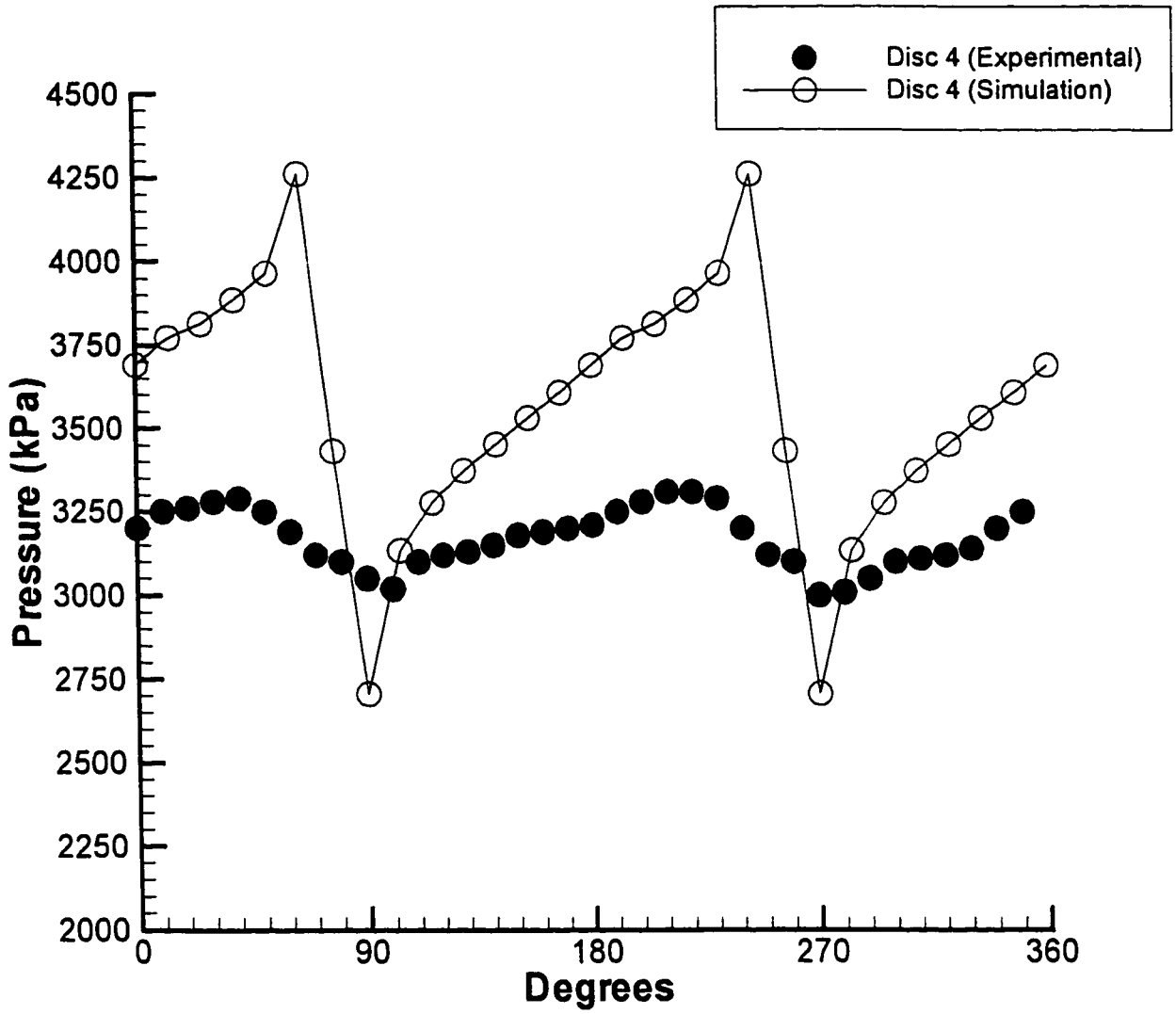

Figure 3.23. Experimental and simulation pressure profiles as function of rotation angle for disc 4. Side port of the 45/5/42 configuration of kneading blocks.

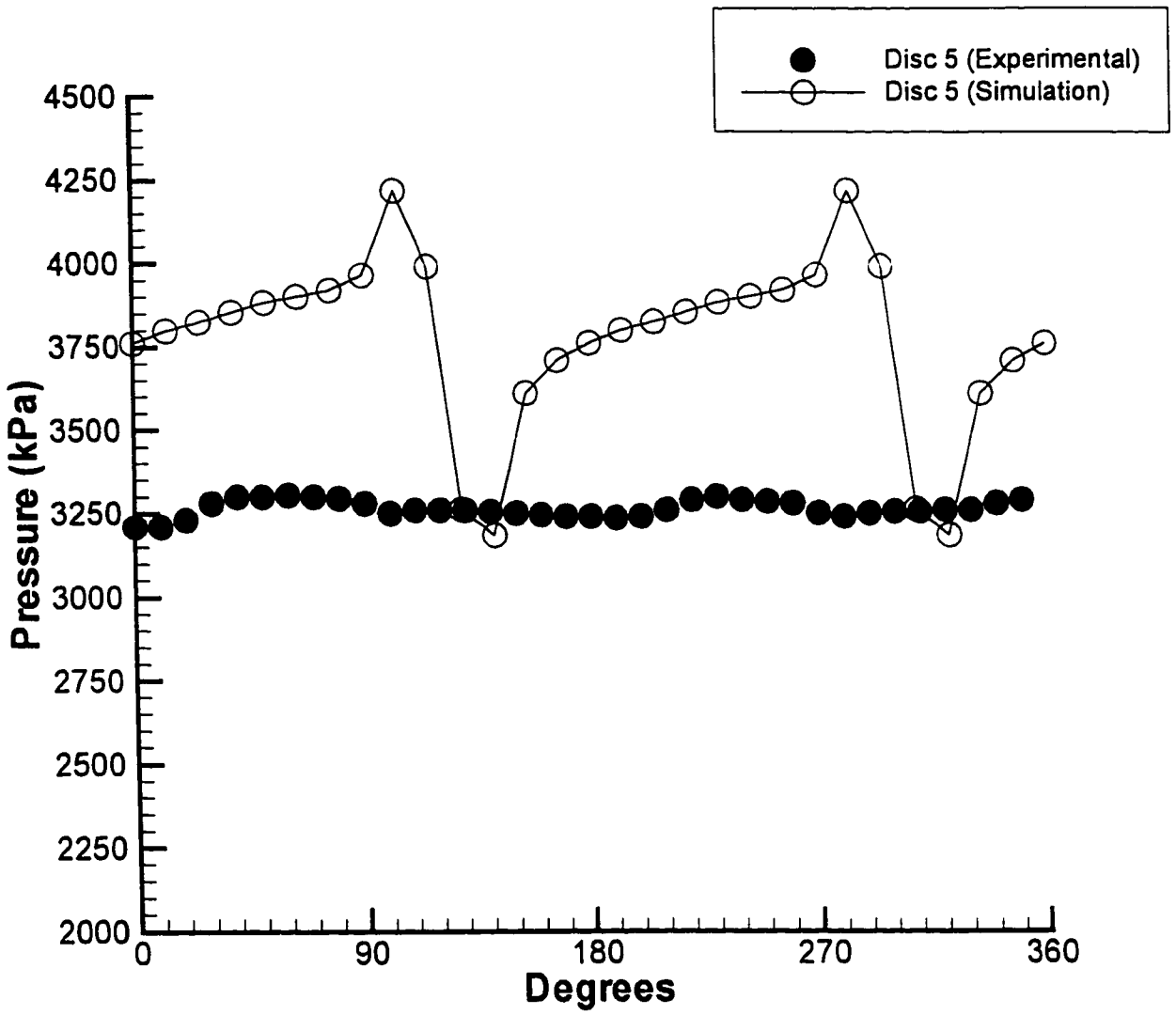

Figure 3.24. Experimental and simulation pressure profiles as function of rotation angle for disc 5. Side port of the 45/5/42 configuration of kneading blocks.

3.5. Discussion

An increasing pressure in the axial direction is observed in the experimental results for the configuration of forward kneading blocks, as predicted by the simulation results. Although the staggering of the discs reduces the conveying capacity of kneading blocks, they still maintain some ability to move material forward. The forward conveying is produced by the dragging effect whereas the axial pressure induces a back flow component that ensures a fully filled channel and hence better mixing performance. The normal stress boundary condition determines whether there is a positive or negative conveying effect for specific pressure drop and rotation speed conditions.

The motion of the rotors causes the fluctuating pressures observed experimentally and predicted with the model. Different mechanisms cause the pressure fluctuations in the side and apex. At the side observation point, high-pressure peaks are caused by the advancing tip of the discs that create a converging region between the disc and the barrel. The trailing side of the disc creates a diverging region that produces the low pressures, as illustrated in Figure 3.25. The high pressures at the apex are originated from the encounter of the tips of the two discs. A small chamber is created and then reduced in size until it completely disappears, squeezing the fluid and creating the high peaks of pressure. Immediately after the chamber disappears, a small chamber appears again and increases in size until it communicates with the wide channels at both sides of the chamber, creating the low pressure values, as illustrated in Figure 3.26.

The oscillating pressures observed in Figures 3.7 and 3.8 show that the pressure valleys at one disc coincide with the highest pressure peaks in the subsequent disc, generating the experimentally observed back flows at the rear side of the discs. This effect is very much affected by the stagger angle as well as the thickness of the discs. It is expected that thicker discs would generate wider valleys of pressure and therefore greater back flows. The 45° stagger angle kneading blocks have the particular property of the coincidence of the highest pressure peaks on the advancing side of the disc's tip with the lowest pressure valleys on the rear side of the contiguous disc's tip. Based on this observation and from the model calculations, the phenomena

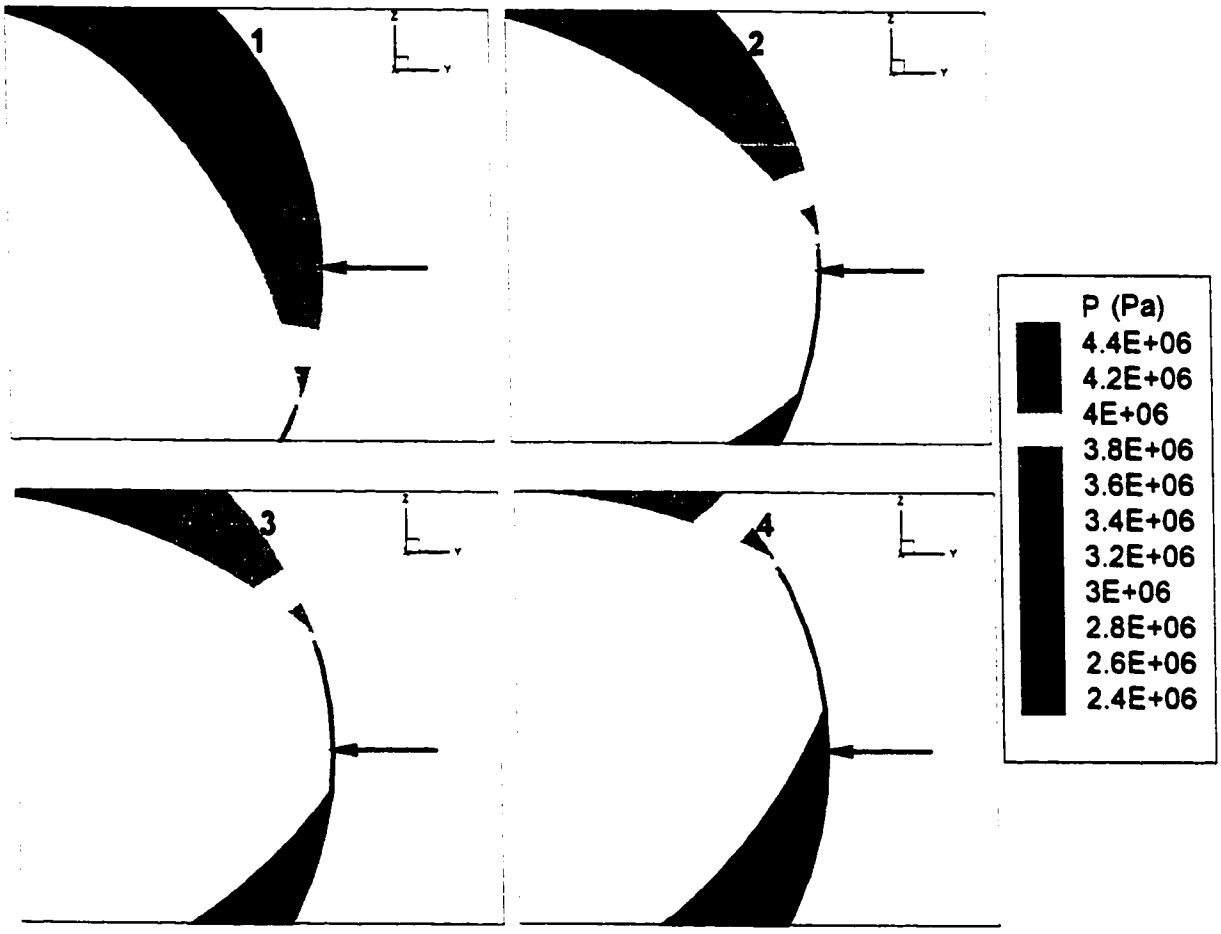

Figure 3.25. Mechanism of pressure fluctuation in side port

observed by McCullough & Hilton (1993) can be explained. Figures 3.11 and 3.12 show the pressure behavior as a function of the angle of rotation for disc 5 in the 45/5/20 configuration. As seen in Figure 3.2 this disc is adjacent and aligned with the first disc of the 45/5/42 configuration, making the effect of a long disc (adding the 4 mm thickness of the 45/5/20 disc 5 to the 8.2 mm of the 45/5/42 disc 1, resulting in 12.2 mm thickness). Simulations reveal that the pressure peaks for a single pair of discs under similar flow rate and rotational speed to those used in the experimental work are higher than the peaks produced in discs preceded and followed by other disc as occurs in real kneading blocks. This behavior has its explanation in the fact that the peaks and valleys of pressure for one disc are dampened by the effect of discs behind and ahead of it. In the case of disc 5 of the 45/5/20, the subsequent downstream staggered disc is at a distance of 8.22 mm, thus reducing its effect over the pressure profile of the preceding disc. This explains the experimental observation of an increase in the pressure fluctuations from the peaks to the valleys when approaching disc 5. It also explains why the amount of fluctuation decreases rapidly once the 45/5/42 configuration is reached. The intensity of pressure fluctuations is affected by the reverse elements located at the end of the 45/5/42 configuration that actually holds up the polymer melt and creates an almost uniform pressure distribution over the cross section of disc 5 of the 45/5/42 block . For the simulation of the 45/5/42 configuration the geometry depicted in Figure 3.2 representing 5 pairs of discs was used, whereas for the 45/5/20 configuration a system with two pairs of discs were used, one to emulate the preceding pair to a second one which is the focus of our attention. The fact that disc 5 of the 45/5/20 configuration is aligned with the first disc of the 45/5/42 configuration makes its situation different from the rest of the discs in the same configuration. Comparisons of the model with experimental data on the 45/5/20 configuration (Figures 3.11 and 3.12) show very good correlation, and together with the simulations for the 45/5/42 configuration help to explain the pressure behavior observed experimentally. Simulations for the 45/5/42 show also good correlation for all discs but disc 5, which is expected since it is adjacent to the configuration of reverse kneading blocks.

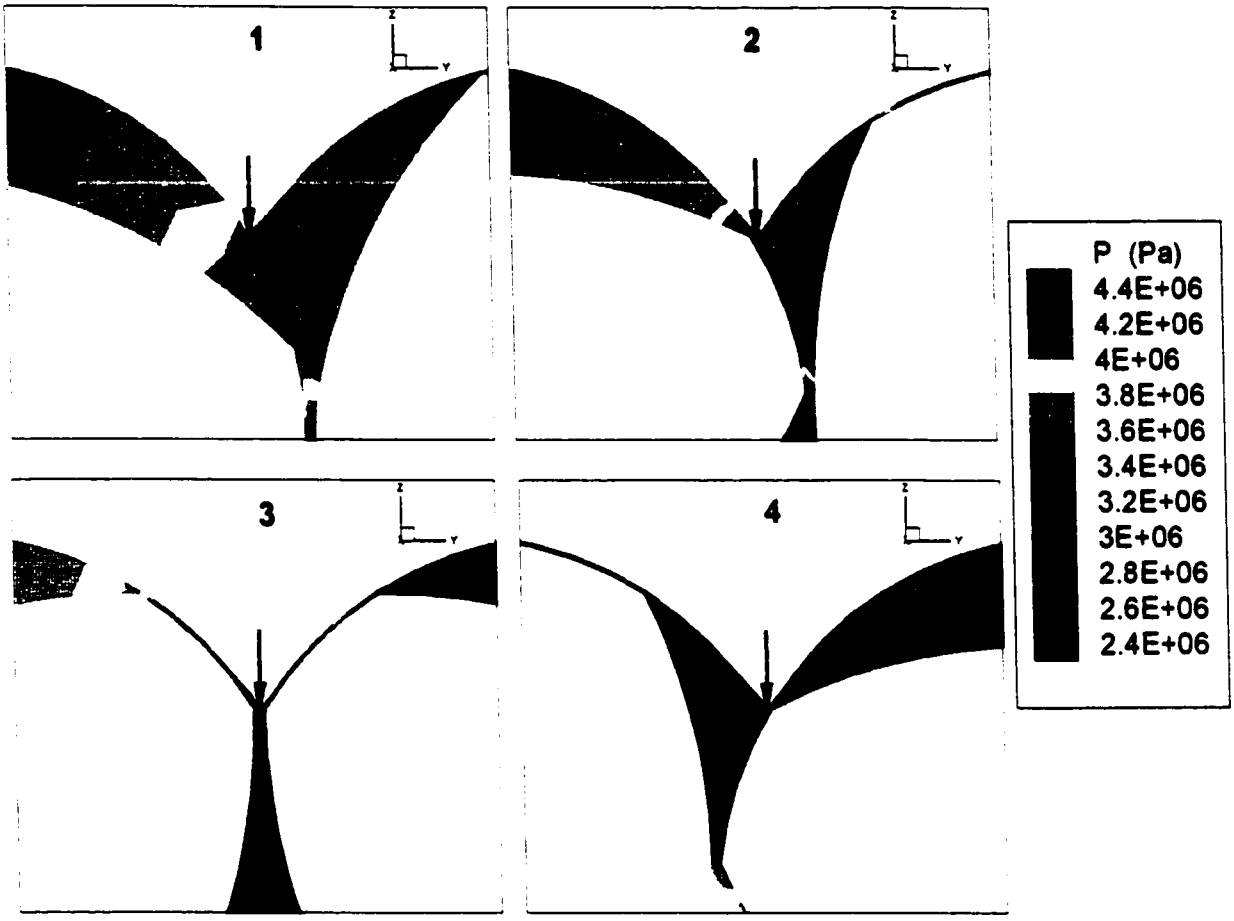

Figure 3.26. Mechanism of pressure fluctuation in apex port

Although the model predictions are reasonably close to experimental pressure data, there is a consistent difference in the pressure peaks. When analyzing the model, there are two main assumptions made among those discussed in Sections 2 and 3: the quasi-steady state and isothermal assumptions. The quasi steady state assumption is said to apply for systems where Re (Reynold number, $Re=\rho VD/\mu$)<<1 and Sr (Strouhal number $Sr=\omega D/V$) <<1. The assumption of Re <<1 for polymeric flows is valid due to the very high viscosity of polymer melts and hence acceleration terms are neglected. On the other hand, the assumption of Sr << 1 implies that the time scale of the perturbation, i.e. a periodic change in boundary conditions such as a pulsating flow or a moving boundary, must be much larger than the time scale of the diffusion of momentum so that $t >> D^2/\nu$ (Ottino, 1989). This assumption is again valid for polymeric flows that demonstrate very low values of D^2/ν. However, when considering the pressure peaks, there are very large gradients generated in a very small time interval due to the sudden transition from the narrow gap of the disc-barrel clearance to the wider channel that follows. These pressure peaks represent extremely small zones within the flow field that may not affect the flow quantities for purposes such as determining mixing performance from numerically calculated flow fields. Inclusion of transient terms and an algorithm to integrate the equations in time may capture the sharp pressure transitions accurately.

The system is assumed to be isothermal. In real systems, it is expected that zones of high shear would experience higher temperatures due to viscous dissipation and therefore lower values of viscosity than estimated from the isothermal model. It is well known that the zones where the pressure peaks occur are also the zones with the highest shear rates in the system. The assumption of isothermal flow could be a source of overestimation of the pressure peaks in the system.

An additional source of the differences between experimental and simulation pressures could be the model for the dependence of viscosity on the magnitude of the rate-of-strain tensor $\dot{\gamma}$ (see equations 2.5 to 2.7). The highest peaks of pressure occur at the narrow gaps where the $\dot{\gamma}$ values are the highest. The Carreau model fits data for a range of $\dot{\gamma}$ between 0 and 5,000 s^{-1}

according to Figure 3.3. Calculations have demonstrated that at the narrow gaps the values of $\dot{\gamma}$ can be grater that 5,000 s^{-1}. It is possible that an over-prediction of the viscosity at high values of $\dot{\gamma}$ could produce an overestimation of the pressure profiles.

Pressure transducers have limitations in the measurement of high gradients over small areas since they are usually designed to measure constant pressures over the area of the probe. Finally, limitations in the speed of response of the transducer that could produce a "dampening" of the signal at those locations where the gradients are the steepest.

3.6 Summary

A reliable 3D simulation model using the finite element method has been implemented and compared against experimental data provided by McCullough and Hilton (1993). For the purpose of comparison, simulation results were analyzed over small areas equivalent to that of the pressure transducers, since numerical interpolation determines the pressure value at an infinitesimal point. Differences are noticed at the pressure peaks produced by the tips of the kneading discs "sweeping" the surface of the barrel, whereas for the other regions the comparison is reasonably good. The results are also in qualitative agreement with circumferential pressure measurements presented by Kiani and Heidemeyer (1997) and calculations made by Szydlowski et al. (1987) and Cheremisinoff (1987). The assumptions of quasi-steady and isothermal flow may affect the accuracy of predictions for the pressure peaks, although physical limitations in the pressure transducers - i.e. speed of response, response to a non-uniform pressure in the face of the transducer, noise, etc. - may also introduce deviations from the prediction made by the model.

Chapter Four

PARTICLE TRAJECTORIES AND RESIDENCE TIME DISTRIBUTIONS

4.1 Introduction

The particle tracking technique was used to obtain residence times and analyze distributive mixing for different length to diameter ratios (L/D) of kneading discs. Previous studies (Kalyon et al, 1997; Cheng and Manas-Zloczower, 1997) have shown that the mixing performance of intermeshing co-rotating twin screw extruders is highly dependent on the combination of screw configuration and operating conditions. In the kneading discs of an ICRTSE, the finite width of the discs causes the material to flow in the axial direction both forward and backwards. By changing the disc widths the pressure profile in the cross section can also be varied, as explained by Cheremisinoff (1987) and demonstrated in Chapter 3 of the present work. By staggering the discs at various angles, the material flows axially on both sides of the discs into adjacent channels, resulting in a high degree of mixing from channel to channel. The complexity of the geometry and the transient character of the flow demand powerful computational tools to characterize the flow and to develop a prediction tool for the analysis of relative performance between different configurations. Difficulties arise in the particle tracking technique due to the time discretization and mesh density, and the presence of moving boundaries. Results show the importance of particle history on the evaluation of the relative performance of different configurations of kneading blocks and suggest a reevaluation of the use of average flow characteristics for the analysis of mixing. Results also confirm the importance of an accurate description of the geometry and clearances in order to obtain information about relative mixing performance.

4.2 Background on characterization of mixing.

The problem of polymer mixing involves the aspects of fluid dynamics and rheology. Mixing is usually obtained through a combination of mechanical motion of the mixing device and the resulting deformation induced in the flowing material. The quantitative description of the flow patterns is now feasible, even in the most complicated geometries, through the development of computational fluid dynamics and the continuous increase in computer resources. The intermeshing co-rotating twin screw extruder (ICRTSE) is one of the most commonly used pieces of equipment among the continuous mixers due to its self wiping properties. ICRTSE are usually built in a modular fashion to meet the diversity of tasks performed by this type of machine. There are two main types of element: full flight conveying elements and kneading block mixing elements. The kneading blocks have been the focus of attention for the theoretical analysis of flow due to their significant contribution to the mixing performance of the extruder and the fact that kneading blocks very frequently work under a fully filled channel condition, which is an important assumption in computational fluid dynamics (CFD) simulations.

One of the challenges in the area of twin screw extrusion, and for general polymer mixing technology, is the quantification of the mixing quality based on the predicted flow fields. The amount of distributive and/or dispersive mixing can vary depending on the application, and it is highly desirable to understand the factors that affect mixing efficiency. Of particular interest is the correlation between the screw configuration, extruder design and the mixing performance. Manas-Zloczower et al. (1989,1992) use λ, a parameter that relates the magnitudes of the rate-of-deformation tensor $|\dot{\gamma}|$ and the vorticity tensor $|\omega|$:

$$\lambda = \frac{|\dot{\gamma}|}{|\dot{\gamma}| + |\omega|} \tag{4.1}$$

where $|\dot{\gamma}|$ and $|\omega|$ are defined as:

$$|\dot{\gamma}| = \sqrt{\frac{1}{2}(\dot{\gamma} : \dot{\gamma})} \tag{4.2}$$

$$|\omega| = \sqrt{\frac{1}{2}(\omega : \omega)} \tag{4.3}$$

such that a value of λ=0 indicates pure rotation, λ=1 indicates pure elongation and λ =0.5 is the case of simple shear. λ is used to quantify the efficiency of dispersive mixing, based on the assumption that elongational flows are more effective than simple shear flows for the dispersion of liquids with high viscosity ratio and low interfacial tension and for solid aglomerates into liquids (Elmendorp, 1986; Manas-Zloczower et al., 1988, 1989a). More recently, Cheng and Manas-Zloczower (1997) used S_f, a frame invariant parameter defined by Larson (1985) as:

$$S_f = \frac{2\left(tr\,\underline{\underline{D}}^2\right)^2}{tr\left(\overset{0}{\underline{\underline{D}}}\right)^2} \tag{4.4}$$

The study of distributive mixing was examined by Spencer & Wiley (1951) who studied the stretch of a infinitesimal line, which represents the interface between two polymer melts, in a simple shear flow as a function of total shear. Zerafati and Bigio (1994) studied the stretch of an infinitesimal area to understand the nature of mixing. However, the quantifiable characterization of mixing is still not completely defined as a unique or definitive measure. Lawal and Kalyon (1993) analyzed the extensive mixing characteristics of twin screw extruders using various diagnostics tools of dynamics. They state that the effectiveness of a flow to generate the desired degree of distributive mixing is dependent on its ability to stretch material interfaces between components in order to reduce the striation thickness. In simple steady shear flows, the interfaces increase linearly with time, which produces poor distributive mixing. In contrast, flows governed by chaotic dynamics are characterized by exponential separation of particles and, therefore lead to good distributive mixing. When the trajectory of a particle is determined, its behavior defines the character of the flow. The use of the particle trajectory is probably the most physically meaningful technique to determine whether the flow is regular or

chaotic. Tools for determining whether a system is chaotic or not include the Lyapunov exponent, horseshoe mapping, the Poincaré section and Melnikov's method (Lawal and Kalyon, 1993a). In some cases, the correct interpretation of the nature of the flow requires the application of these tools in combination.

Ottino (1989) studied mixing in three-dimensional and open flows when chaotic flows are present. The studies of mixing are based on the velocity field. Poincaré sections are generated for various values of the mixing strength, which are defined as the measure of the cross-sectional stretching per element (of the mixer) as opposed to the axial stretching. A study of the exit time distribution was done by calculating the trajectories and residence times for a large number of particles, initially distributed uniformly (on a square grid) over the cross section at the entrance of the mixer. In some sense, the exit age distribution gives an indication of the inhomogeneity of the cross-sectional mixing.

Theoretical investigations of mixing, particularly those involving complex flow domains and time dependent flows, increasingly rely on numerical simulations (Souvaliotis et al, 1995). Accurate quantitative information, such as the location of periodic points, length of a deformed line or area deformation can be obtained from numerical simulations.

Cheng and Manas-Zloczower (1997) based their analysis on the average calculation of λ and S_f (Larson, 1985) over the rotation cycle of the extruder. They found that the average values of λ and S_f remain almost constant over the entire cycle, so that it was sufficient to analyze the data for one single geometry to characterize mixing. Values of λ obtained by Cheng and Manas-Zloczower for a cycle of rotation of kneading discs are shown in Table 4.1. The average values of λ were plotted against axial pressure drop for various types of elements including forward and reverse kneading blocks. The results show that the levels of parameter λ are not affected when changing from the forward to the reverse configuration. Elongational flow components are not affected, which implies that no conclusion can be drawn from the average values of λ in this case. The calculation of average values of λ, $\dot{\gamma}$ and τ (the magnitude of the stress tensor) as a function of rotation speed and pressure drop gives qualitative information that can be also predicted without the complication of a 3D finite element model. A complete analysis taking advantage of the accurate description of the flow field should include the effect of

residence time distribution, which is far from that of a plug type, and the stress distribution, which dictates the number of fluid particles that are submitted to a specific stress level. The present work addresses these aspects of the mixing problem through the determination of particle trajectories.

Geometry, α	λ
30°	0.5702
50°	0.5711
70°	0.5722
90°	0.5715
110°	0.5709
130°	0.5718

Table 4.1. Average values of λ for a cycle of rotation of kneading discs (Cheng and Manas-Zloczower, 1997)

4.3 Numerical considerations

4.3.1 Geometry and boundary conditions

The dimensions of the intermeshing co-rotating extruder are shown in Table 4.2 in dimensionless form, using the widest screw-barrel distance as the characteristic dimension. A stagger angle (ϕ) of 45° in a forward configuration was used for the simulations. Figure 4.1 describes the 3D velocity field and the location of the cross section plane where particle tracers are inserted in the geometry of the kneading discs.

One of the biggest problems in the 3D simulation of flow through kneading discs is the description and discretization of the complicated geometry that consists on sharp discontinuities, convergent-divergent channels and the very narrow clearances between discs and between discs and barrel. The mathematical description of the geometry is done according to the procedure explained in Chapter 2. The governing equations are the momentum equations without inertia terms and the continuity equation. The domain is discretized and the equations are solved using the finite element method, also explained in detail in Chapter 2.

Barrel bore diameter (Db)	6.461
Screw outside diameter (Do)	6.387
Screw root diameter (Di)	4.461
Disc depth (d)	0.859, 1.292, 1.809
Center distance of screws (C)	5.487
Clearance between discs (G)	0.042
Clearance disc-barrel (B)	0.037
Cross sectional area	22.25
Stagger angle (forward)	45°

Table 4.2. Technical data ICRTSE, 5 disc kneading block (dimensionless)

For the inlet boundary condition a value of the normal stress σ_{xx} involving the pressure term and the extra stress term is imposed at the entrance plane, while making the cross components of the velocity zero (v=w=0). The values of normal stress difference are presented in Table 4.5. The imposition of the normal stress and the condition of unidirectional flow at the entrance were found to be good approximations for the boundary condition when it is applied at a specified distance ($0.2D_b$) from the first pair of rotating discs. At the exit, zero cross flows (v=w=0) are imposed together with the value of normal stress at the outlet. The zero cross flow condition for the outlet is placed at a distance equivalent to 0.2 D_b away from the last pair of rotating discs. It has been determined that for circular tubes there is a developing length on the order of L_e= 0.035D Re required for the flow to build-up to the parabolic profile (Bird et al, 1984). Using this criterion, for a Re of 0.01, the development length is 0.00035D. The distance from the rotating discs to the plane where the boundary condition is imposed is such that an increase in the length does not alter the results within the region of interest. Between the last pair of rotating discs and the plane where the outlet boundary condition is imposed, the wall velocities are set to zero. Physically, the interpretation is that the flow leaves the

kneading disc region into a figure-of-eight shaped space where it develops into a unidirectional flow, since there is no further rotation of the rotors, until it finally reaches the exit. Similarly, between the plane where the entrance boundary condition is applied and the first pair of rotating discs, the wall velocities are set to zero. In this case, the fluid would be allowed to change from a unidirectional flow to a more complex flow with velocity components in all three directions.

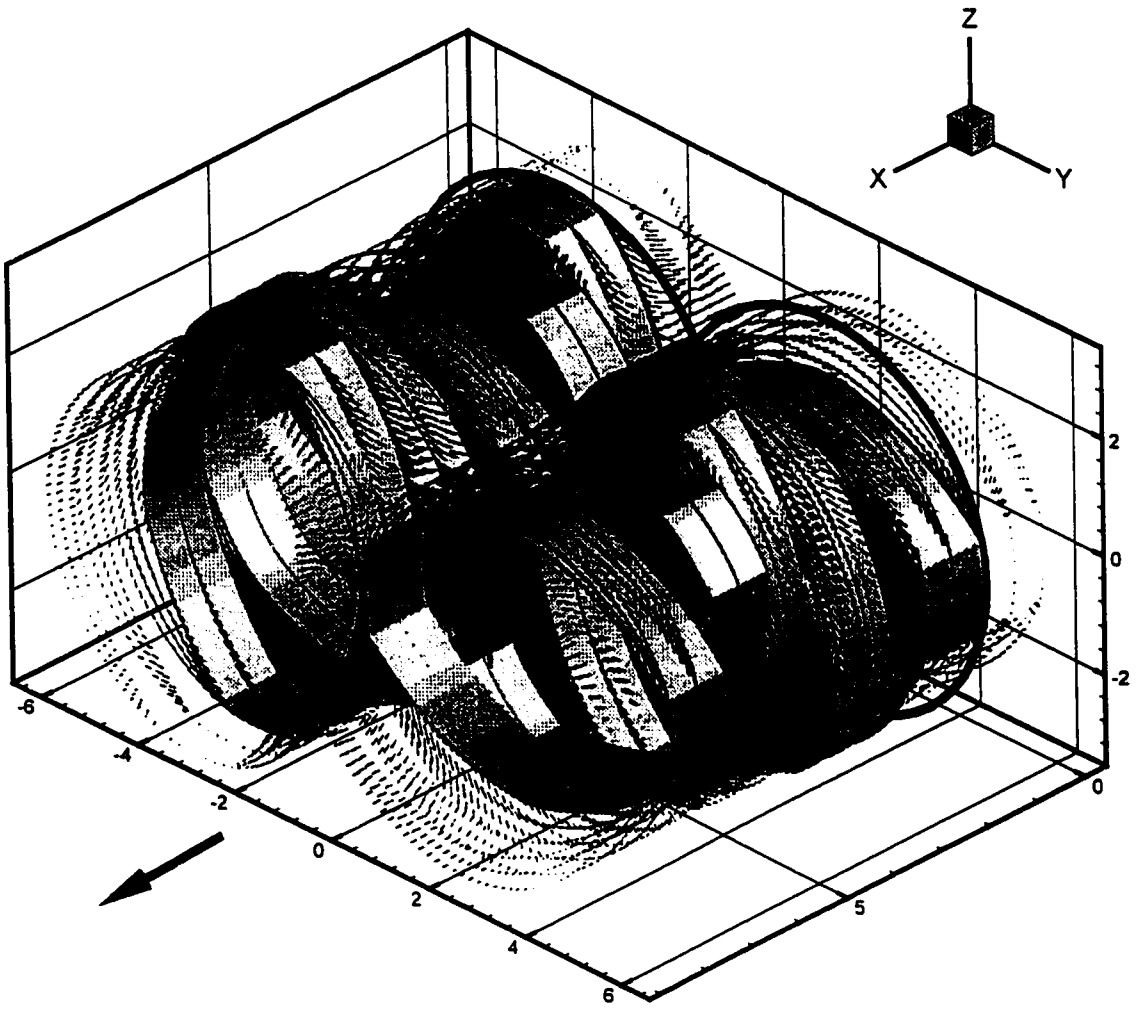

Figure 4.1. 3D velocity field and location of the cross section plane where particle tracers are inserted.

4.4 Particle trajectories

From the Eulerian velocity field $u=u(x,t)$ the particle path of X is given by the solution of :

$$\frac{dx}{dt} = u(x,t) \quad with \quad x = (x_0, y_0, z_0) \quad at\ t = 0 \tag{4.5}$$

Equation **(4.5)** is solved numerically using the Euler predictor-corrector algorithm. A description of the Euler predictor-corrector algorithm can be found in any standard book on numerical analysis (for example, Gerald and Wheatley, 1989). The algorithm has a truncation error of $O(\Delta^3)$. Starting from X_0 , the new position is obtained by integrating equation **(4.5)** within the geometry describing the initial position of the discs. For the next time interval, the solution $u(x,t)$ corresponding to the new position of the discs is used to determine the new location of X.

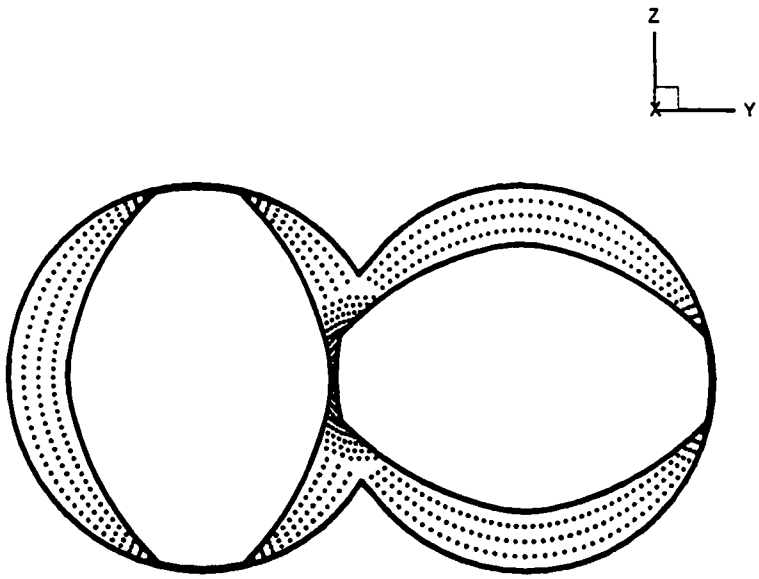

Figure 4.2. Initial location of particle tracers at x=0

A total of 692 non-diffusing particles were initially located to cover a complete cross section of the extruder at the plane x=0, according to Figure 4.2.

The numerical determination of particle trajectories in problems involving moving boundaries has the potential problem that particles can appear to intercept the solid moving parts. This problem arises due to the discretization of time in the numerical approximation. As the time step is decreased, the numerical determination of particle positions will improve and a smaller number of particles will fall outside the flow domain. The problem is critical at the narrow clearances encountered in ICRTSE where very high velocities are also frequently present. A time step of 0.0241 seconds was used, corresponding to an angle of 12.58° for a rotation speed of 100 rpm.

Particles that went outside the flow domain into the discs were reincorporated to the flow at the position they crossed the solid boundary. The point where the trajectory of the particle intersected the solid walls was determined and then the particle was re-inserted at that same location, creating the effect of a particle bouncing back from the solid wall into the flow field.

It is well known that particle trajectories in an ICRTSE kneading block flow field are very sensitive to their initial locations. Two particles starting close together can diverge into completely different paths, as demonstrated by Bravo (1995) and Lawal and Kalyon (1995). The re-incorporation of particles into the flow domain is an approximation used to account for variable distributions as function of time rather than the study of the individual trajectories of particles.

4.5 Operating conditions and material properties

Three configurations of kneading blocks were used for the simulations. The ratio L/D is defined for a single disc. The three values of L/D used were 0.133, 0.2 and 0.28. Table 4.3 shows the operating conditions used for the simulations.

RPM	100
Mass flow rate	376.58 Kg/hr
Volumetric flow rate	1.42321×10^{-4} m^3/s
Average axial velocity of the fluid	5.6098×10^{-2} m/s

Table 4.3. Operating conditions

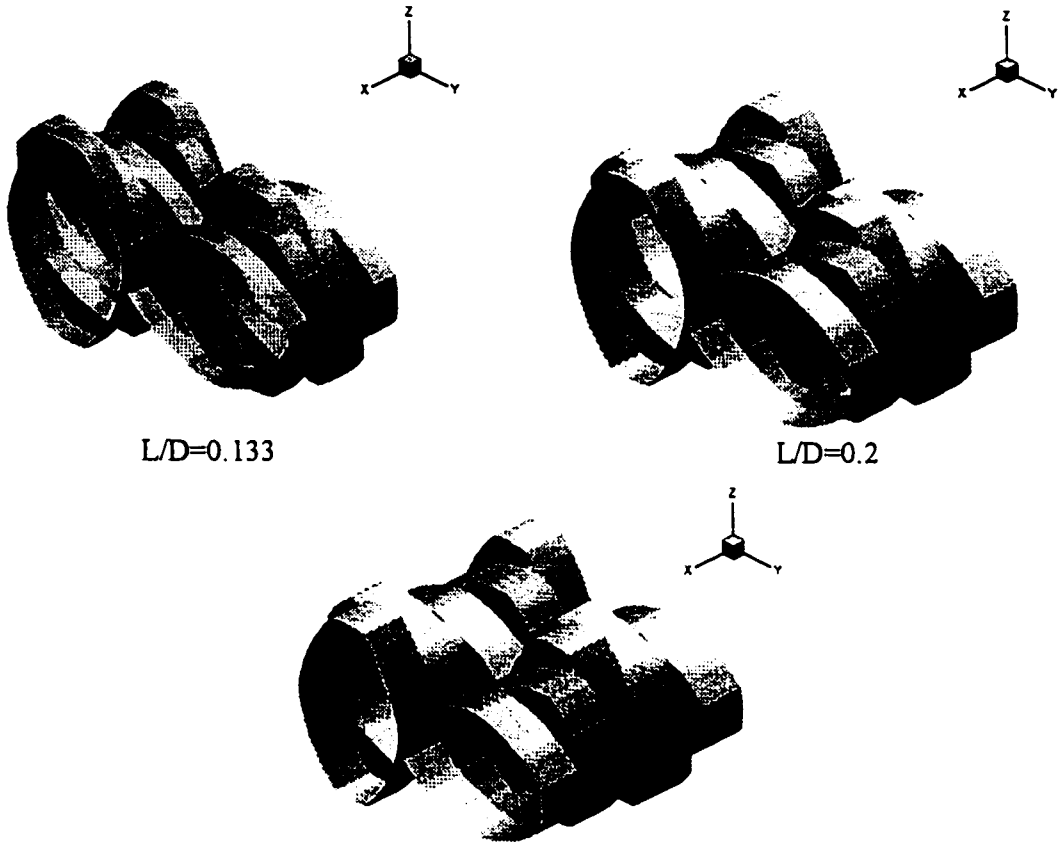

Figure 4.3. Configurations of kneading blocks used in the study

The three configurations used are depicted in Figure 4.3. The material parameters for the Carreau model are specified in Table 4.4.

Density(ρ)	735.00 Kg/m^3
Consistency index (μ_0)	2000 Pa.s
Relaxation time (λ)	0.85247 s
Power index (n)	0.514

Table 4.4. Carreau parameters

The normal stress difference for the three cases is presented in Table 4.5.

L/D	Normal stress difference (kPa)
0.133	839.51
0.2	397.12
0.28	231.65

Table 4.5. Normal stress difference

4.6 Results

4.6.1 Residence time distributions and distributive mixing

Residence time distributions were obtained based on the calculation of particle trajectories. The residence time density function $f(t)$ is defined as the fraction of particles that have a residence time in the interval $(t,t+\Delta t)$. The cumulative residence time distribution function, $F(t)$ is defined as the probability that a particle has a residence time less than t . Its mathematical expression is:

$$F(t) = \int_0^t f(t')dt' \tag{4.6}$$

The complementary function to the cumulative residence time distribution is defined as the probability that a particle has had a residence time greater than t, or

$$W(t) = \int_t^\infty f(t')dt' \tag{4.7}$$

Figure 4.4 helps to explain the effect of stagger angle on the conveying properties of kneading blocks. An analogy between the conveying model in a full flight screw and the

kneading discs assuming that the kneading discs create a pseudo channel that, as opposed to the full flight screw, has geometrical discontinuities at the side walls and at the bottom wall. The helix angle can be defined for a flighted element as :

$$\tan\theta = \frac{L_S}{\pi D_0} \tag{4.8}$$

where L_S is the axial distance of one full turn of the discs and D_0 is the outside diameter of the discs. It is obvious that the pseudo helix angle is a function of the stagger angle as well as the width of the discs. An expression for the pseudo-helix angle θ_s can be derived as:

$$\tan\theta_s = \frac{\pi \mathrm{d}}{\phi \mathrm{D}_0} \tag{4.9}$$

where d is the disc width, ϕ is the stagger angle and D_0 is the outside diameter of the discs. The pseudo helix angle affects the conveying properties of the kneading blocks. An increase in the stagger angle produces back flow gaps between adjacent discs. This effect is not found in regular full flight elements. The effect of stagger angle on the size of back flow gaps is shown in Figure 4.5. The back flow is generated when a zone of high pressure is generated due to the effect of an advancing disc that tends to compress the fluid. The fluid escapes through the path of least resistance. A zone of low pressure is generated at the trailing side of the preceding disc that is adjacent to the high pressure zone in the following disc as shown in Figure 4.6, creating the experimentally observed back flows. The back flow gaps are not present in the 30 °configuration, but increase in size for the 45 ° and the 60 ° configurations, as shown in Figure 4.5.

In this section, the plots for the residence time distribution with normalized times are presented. Figure 4.7 shows the distribution function f(t) and Figure 4.8 shows the cumulative distribution function F(f). The time is normalized using the mean residence time. For incompressible fluids in closed systems, Danckwerts (1953) showed that the mean residence time $\bar{t}$ is

$$\bar{t} = \frac{V}{Q} \tag{4.10}$$

where V is the volume of the system and Q is the volumetric flow rate. For every L/D case, $\bar{t}$ is calculated as the ratio of the total volume occupied by the fluid to the volumetric

flow rate. The volume occupied by the fluid can be calculated from the parameters specified in Table 4.2. In each case the axial distance traveled by a particle before exiting is equal to five times the disc depth (see Table 4.2). The plot of f(t) (Figure 4.7) shows a scattered behavior that is expected due to the non-diffusive nature of the particle tracers and the relatively low number of particles, which makes it difficult to analyze. However, the cumulative distribution shown in Figure 4.8 displays a smoother behavior expected since the data is integrated over time, having the same trends observed by other researchers. The curves for the three cases are similar in shape, with the case L/D=0.133 showing the narrower distribution and the case L/D=0.28 showing the broader distribution. To analyze Figure 4.8 consider a vertical line at the normalized residence time $t/\bar{t} = 1$ as the narrowest possible distribution corresponding to an ideal plug flow, and the deviation from this as the broadening of the distribution. Cheng and Manas-Zloczower (1997) and Lawal and Kalyon (1995) have discussed the conveying properties of kneading blocks. Lawal and Kalyon (1995) determined that lower stagger angles have better conveying capabilities.An increase in disc width, while keeping the same stagger angle, produces more discontinuities in the path of particles and therefore longer residence times, as observed in Figures 4.7 and 4.8.

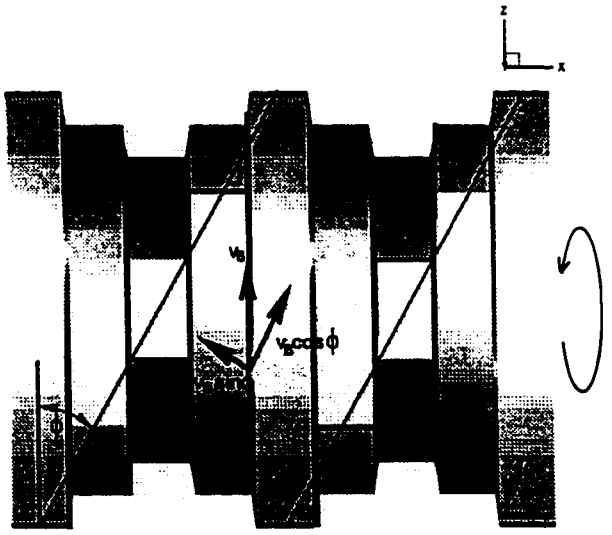

Figure 4.4. Analogy with model for fully flighted screws

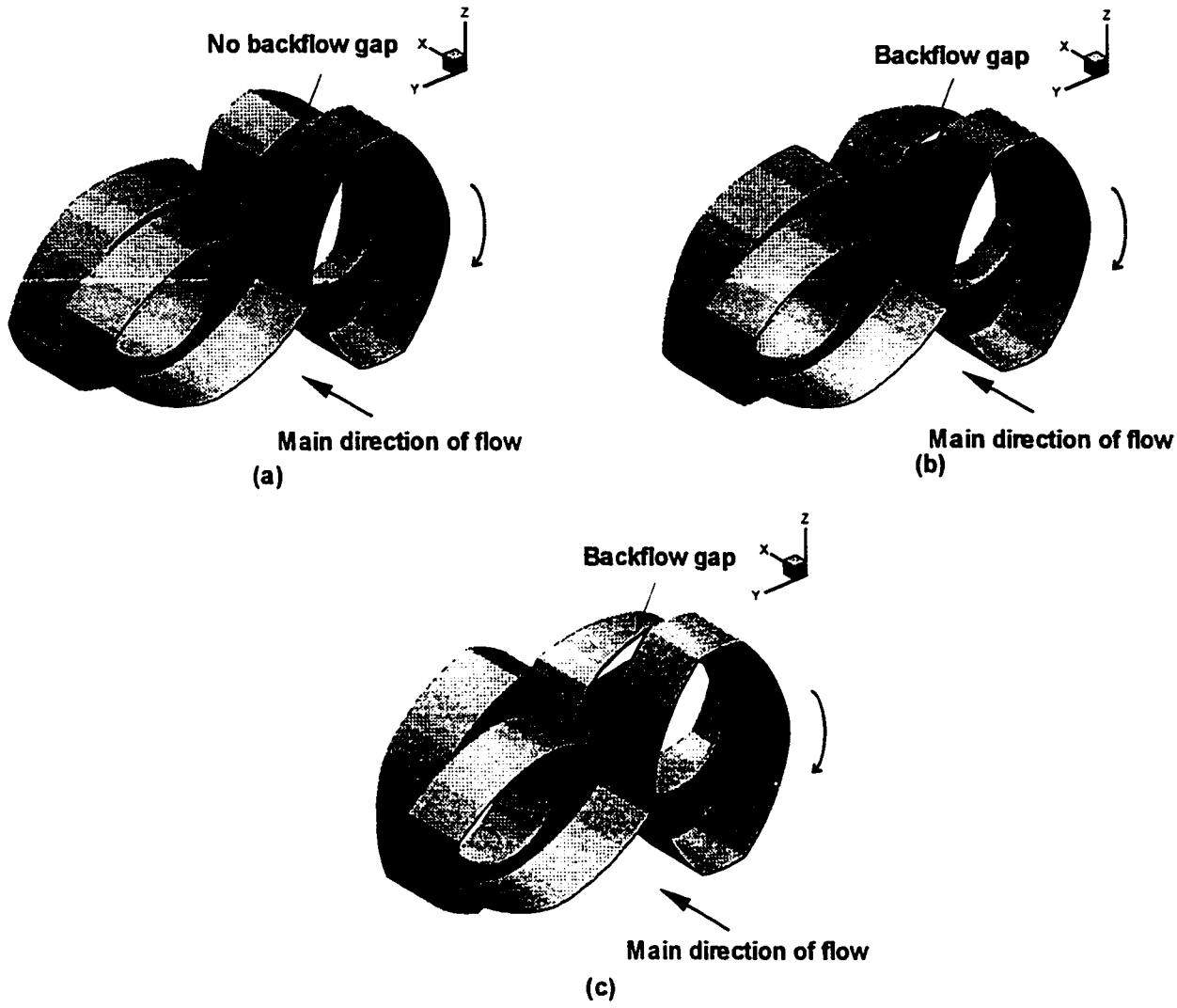

Figure 4.5. Effect of stagger angle on the back flow gap. a) 30°; b) 45°;c) 60°

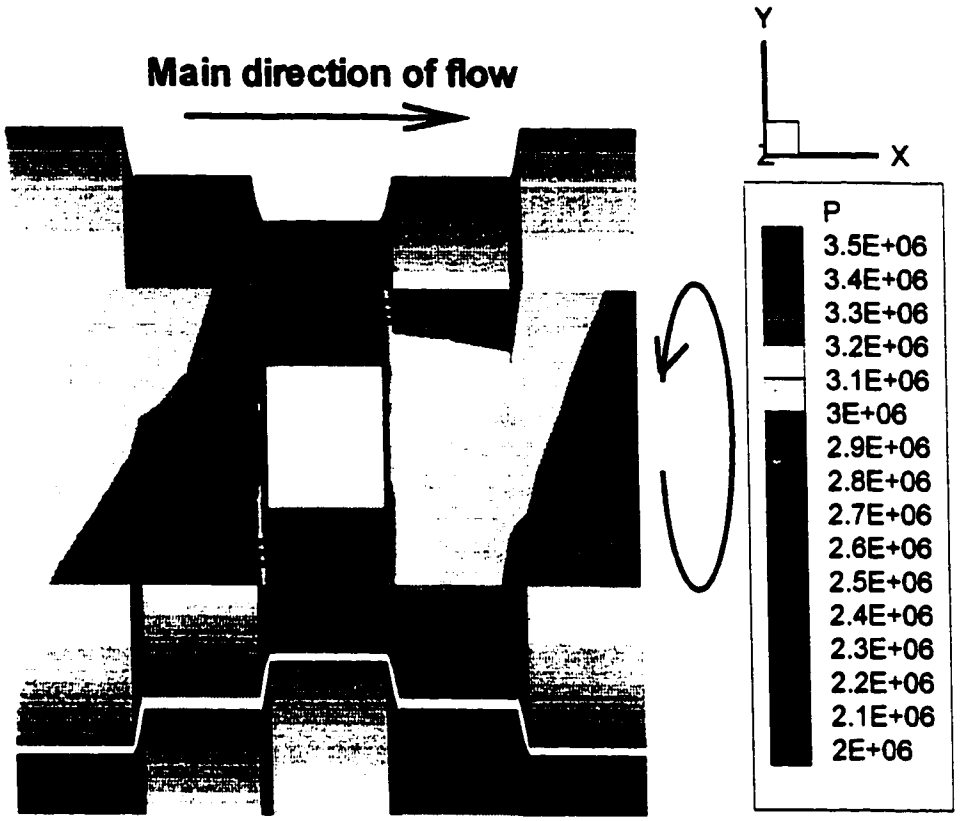

Figure 4.6. Generation of back flow in a 45 °stagger angle configuration

Channel discontinuity, although an important factor, should not be seen as the only aspect affecting conveying capabilities and residence time distribution (RTD). The flow patterns and hence, the distributive mixing ability of the kneading discs is affected by all aspects of geometry as well as the operating conditions. Figure 4.7 shows that the lowest value of L/D (0.133) produces shorter residence times and a narrow RTD when compared to the larger values of L/D. The introduction of particle tracers at the plane x=0 as presented in Figure 4.2 allows the measurement of the number of particles moving backwards as an estimate of the amount of back flow for the three configurations studied. Results are shown in Table 4.5.

L/D=0.133	L/D=0.2	L/D=0.28
8.8%	24.4%	27.7%

Table 4.6. Percentage of back flow as function of L/D at x=0.

The amount of back flow increases with L/D. The mechanism for the generation of back flow zones is explained in Figure 4.6. The high pressure zone generated in the advancing front of the discs forces the fluid to the regions of low pressure, some of them located upstream, thus creating the back flows. Increasing the width of the discs creates an increase in the size of the high pressure and low pressure zones inducing higher amounts of back flow. A further increase in L/D does not produce a proportional increase in the amount of back flow, but increases the amount of circumferential flow and also increases the areas of very high strain rates, as discussed in section 4.2.

The determination of particle trajectories allows the calculation of the distribution of particles in the axial direction. The axial distribution value (ADV) is defined as the average distance of the particles from the axial location defined by the position of a particle travelling at average axial velocity U,

$$ADV = \frac{\sum_{i=1}^{n} \left(x_i^t - x_U^t \right)}{n} \qquad (4.11)$$

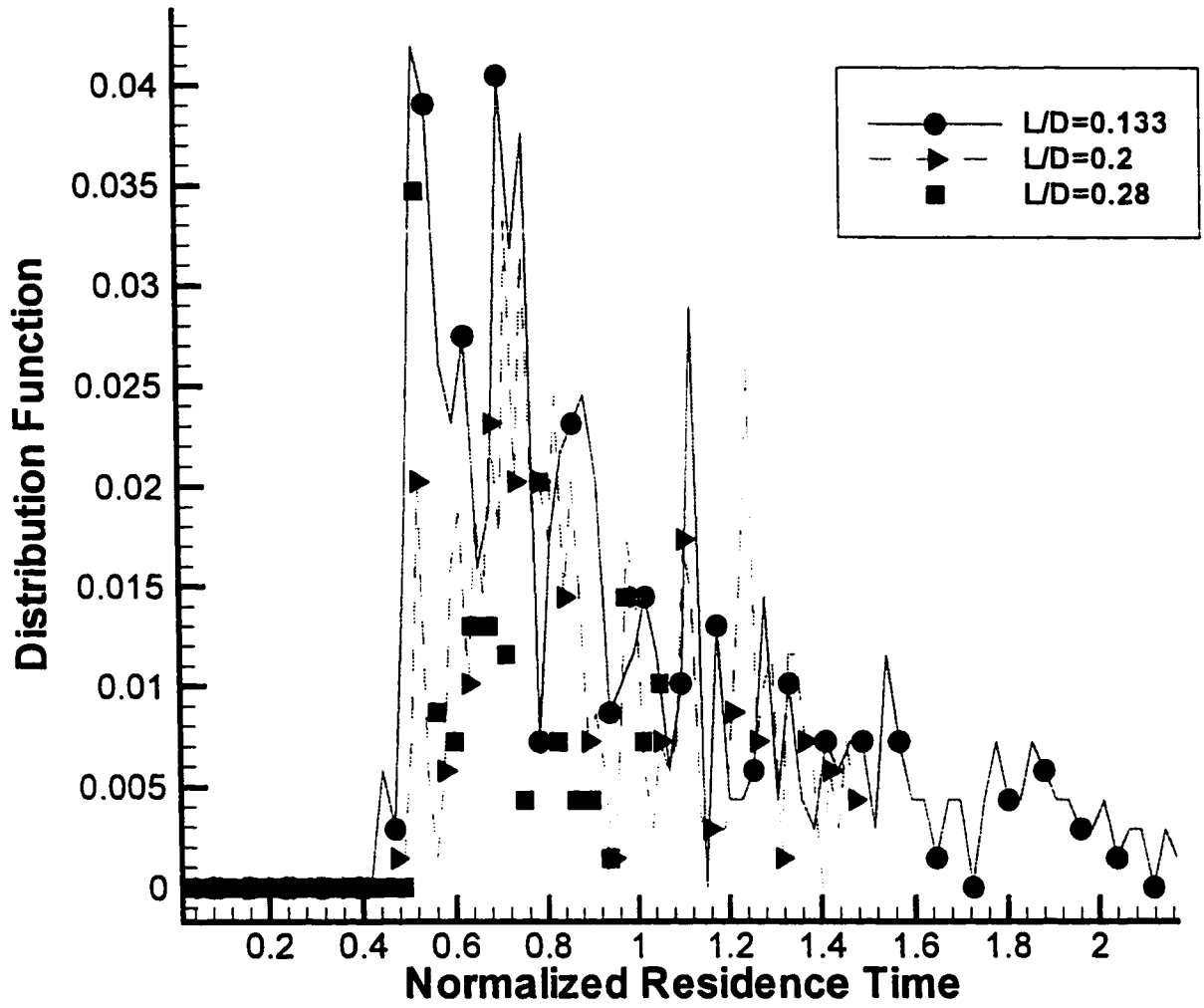

Figure 4.7. Residence time distributions for the three cases of L/D.

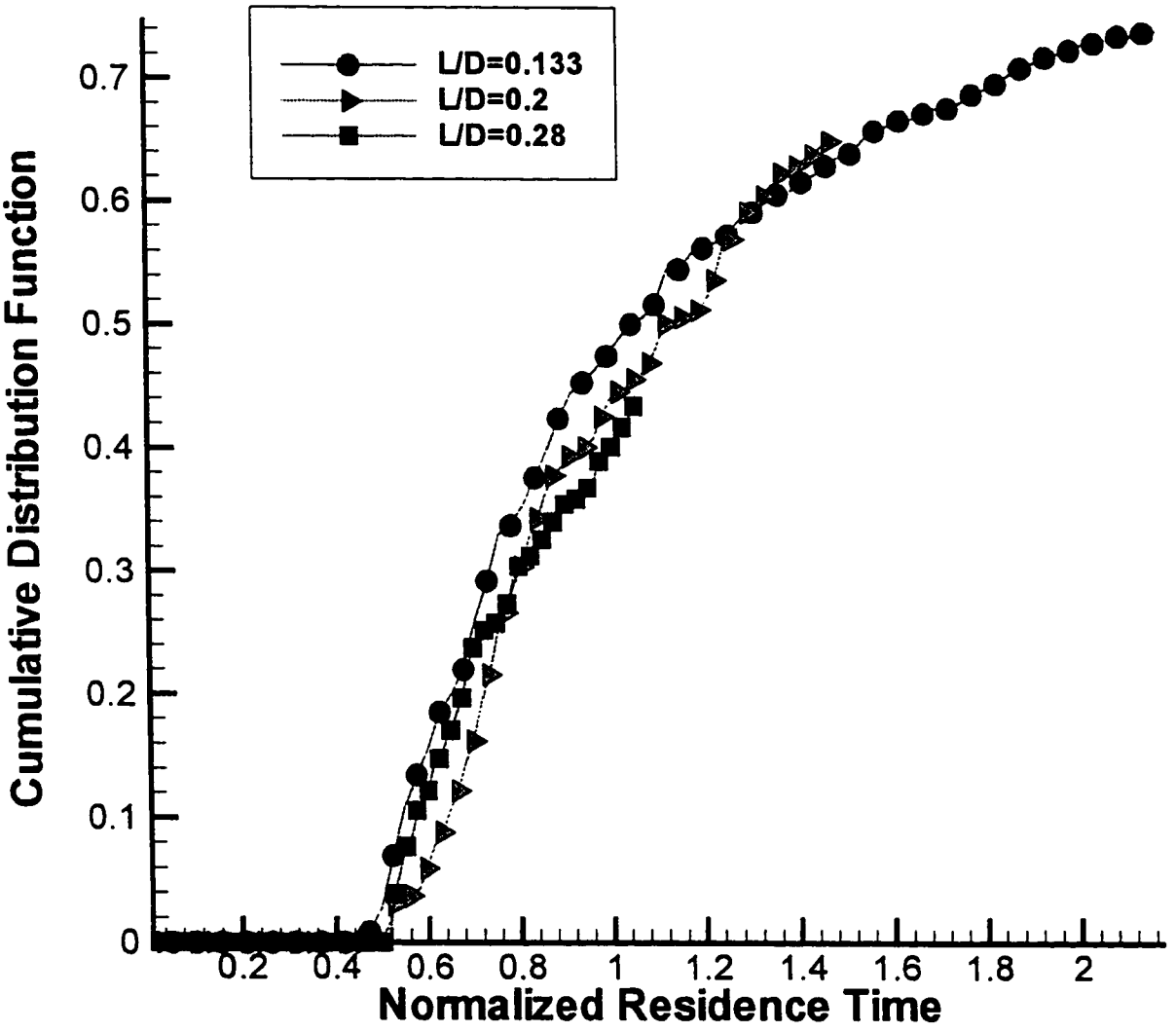

Figure 4.8. Cumulative residence time distribution for the three cases of L/D.

In Equation (4.11), x_i^t is the axial position of a single particle at time t, x_U^t is the axial position of a particle travelling at velocity U, and U is the axial average velocity x_U^t.

Values of ADV were measured for a period equal to the shortest first appearance time (Nauman and Buffham, 1983) of the three configurations, corresponding to L/D=0.133. This is done for the purpose of comparison between the different configurations, since the value of ADV is not applicable once particles leave the domain of study. The value of ADV is a measure of the departure of the flow profile from a plug type. A value of ADV=0 represents perfect plug flow. The curves in Figure 4.9 show the values of ADV for the various L/D studied. All curves start from a value of zero, corresponding to the initial location of the particle traces at the plane x=0. The value of ADV increases with time, with L/D=0.28 having the highest values. This is consistent with the observation that L/D=0.28 produces greater amounts of back flow, which generates a larger distribution of particles in the axial direction. The lowest values of ADV are produced by L/D=0.133, also consistent with previous observations. Values of ADV were also determined for a configuration of two co-rotating cylinders having the same length and cross section area as the L/D=0.28 configuration. The curve shows a linear increase in the value of ADV with time, well under the values for the kneading disc configurations. The two-cylinder configuration does not produce any back flows as expected, and the absence of the converging- diverging gaps produces a narrow axial distribution of the particles.

The ratio $t_{min}/\bar{t}$ frequently referred as first appearance time is the fraction of the mean residence time that takes for the first particle to reach the exit. The first appearance times are characteristic of most laminar flow models (Nauman and Buffham, 1983). Kalyon (1995) reports values of the first appearance times between 0.4 and 0.6 for kneading blocks staggered at 30, 45, 60 and 90°, with the value for 45° being approximately 0.4. The values of the first appearance times obtained in the present work are shown in Table 4.7.

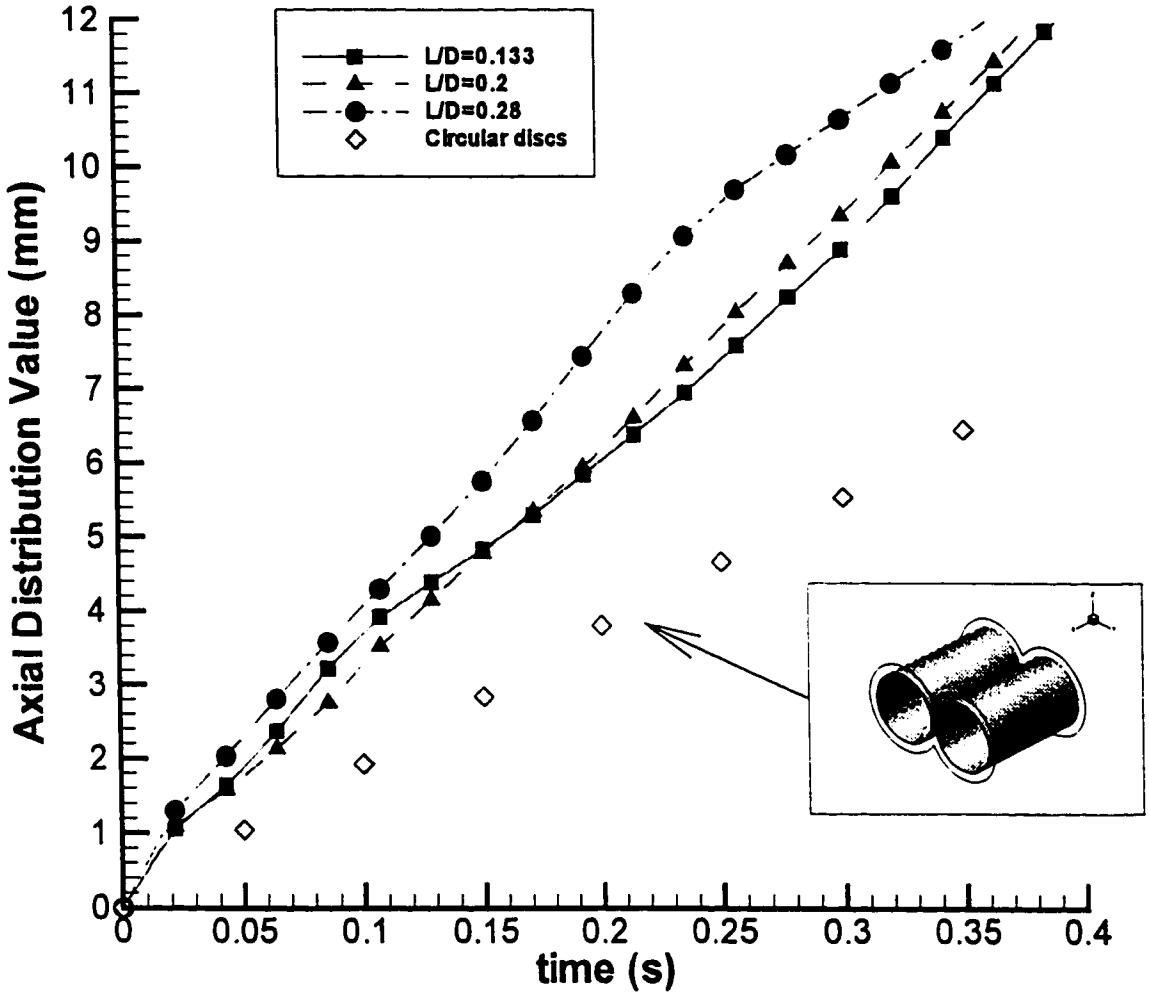

Figure 4.9. Axial distribution value (ADV) vs time.

L/D	$t_{min}/\bar{t}$
0.133	0.419
0.2	0.456
0.28	0.500

Table 4.7. Values of the first appearance times

4.6.2 Strain rate analysis and dispersive mixing

In this section the strain rate plots are presented. Figure 4.10 shows the 3D distribution of number of particles with a given strain rate at a given residence time for the case L/D=0.133. Figure 4.11 shows the 2D distribution of strain rate vs. time for the case L/D=0.133 with the color scale indicating the number of particles. Figure 4.12 shows data extracted from Figure 4.10 for three ranges of strain rate. Figure 4.13 displays the various gaps present in the kneading blocks. Figures 4.14, 4.15 and 4.16 are associated with the case of L/D=0.2 and Figures 4.17, 4.18 and 4.19 with the case of L/D=0.28. From the 2D plots (Figures 4.11,4.15,4.18) it seems that the case L/D=0.2 produces high amounts of strain rate on a larger number of particles, suggesting that an optimal length of the discs could be determined for a specified flow rate and material properties. Also, for the cases of L/D=0.2 and L/D=0.28 there is a more noticeable periodic behavior than case L/D=0.133 for values of strain rate greater than 2000 s^{-1}. Figures 4.10 and 4.11 display a large number of particles being submitted to strain rates between 750 and 1000 s^{-1}. The number of particles with a given range of strain rates fluctuates as a function of time. The presence of this periodic behavior shows that particles are under time varying amounts of strain rate on their way out the kneading block section. The number of periods is 6 and it is the same for the three L/D cases, which indicates that the periods are associated with the rotation speed. These periods are produced when particles travel through the narrow gaps created between discs. For the larger values of L/D it is expected that more particles will travel through the high shear rate gaps since the disc surface area is increased. A clear difference between the performance of the three configurations can be seen in Figures 4.12, 4.16 and 4.19 presenting the number of particles submitted to a range of strain rate

as a function of time. Figure 4.12 shows large numbers of particles submitted to the values of strain rate between 750 and 1000 s^{-1} for the configuration L/D=0.133. This effect is associated to the channeling created by the pseudo-helix angle. Large amounts of particles can travel through the kneading blocks without being submitted to the zones of high deformation. Figure 4.16 shows the behavior for the case L/D=0.2 in which a smaller number of particles fall in the range 750-1000 s^{-1} and more particles are submitted to higher values of strain rate. Figure 4.19 shows the behavior for the case L/D=0.28 in which there is a larger number of particles consistently being submitted to high values of strain rate and the number of particles within the interval 750-1000 s^{-1} is the smallest of the three cases. A periodic behavior is observed in the case of L/D=0.133 for a large number of particles at values of strain rate in the interval 750-1000 s^{-1}. This indicates that, during some time intervals, a large number of particles are not submitted to the zones of high deformations. This periodic behavior for the strain rate interval of 750-1000 s^{-1} is reduced for the case L/D=0.2 and almost eliminated for the case L/D=0.28

There are two types of narrow gaps in extruders: the disc-barrel gap and the disc-disc gaps. The disc-disc gaps produce the highest amounts of strain rate since they involve the motion of two surfaces in opposite directions. The fluid is forced to flow through disc-disc gaps in the intermeshing zone from which they are accelerated in either a forward or reverse direction. The disc-disc gaps are subdivided into axial gaps and transverse gaps, as shown in Figure 4.13. The highest values of shear strain are found in the transverse gaps. Figures 4.14 and 4.15 show a more pronounced periodicity in the number of particles submitted to strain rates higher than 2000 s^{-1}. This effect is produced by the increase in surface area of the discs, specifically in the region of high strain rate generation. White (1990) analyses the relative importance of forward flow, Q_L, reverse flow, Q_b, and circumferential flow, Q_C, and correlates the mixing effects to the magnitudes of the different flows. Q_b is representative of the distributive mixing by creating recirculation of fluid within the kneading regions, whereas Q_C is related to dispersive mixing as it represents flow over the tips of kneading discs. For L/D=0.2, there is a large number of particles submitted to shear rates between 1000 and 2000 s^{-1}, similar to L/D=0.133, but

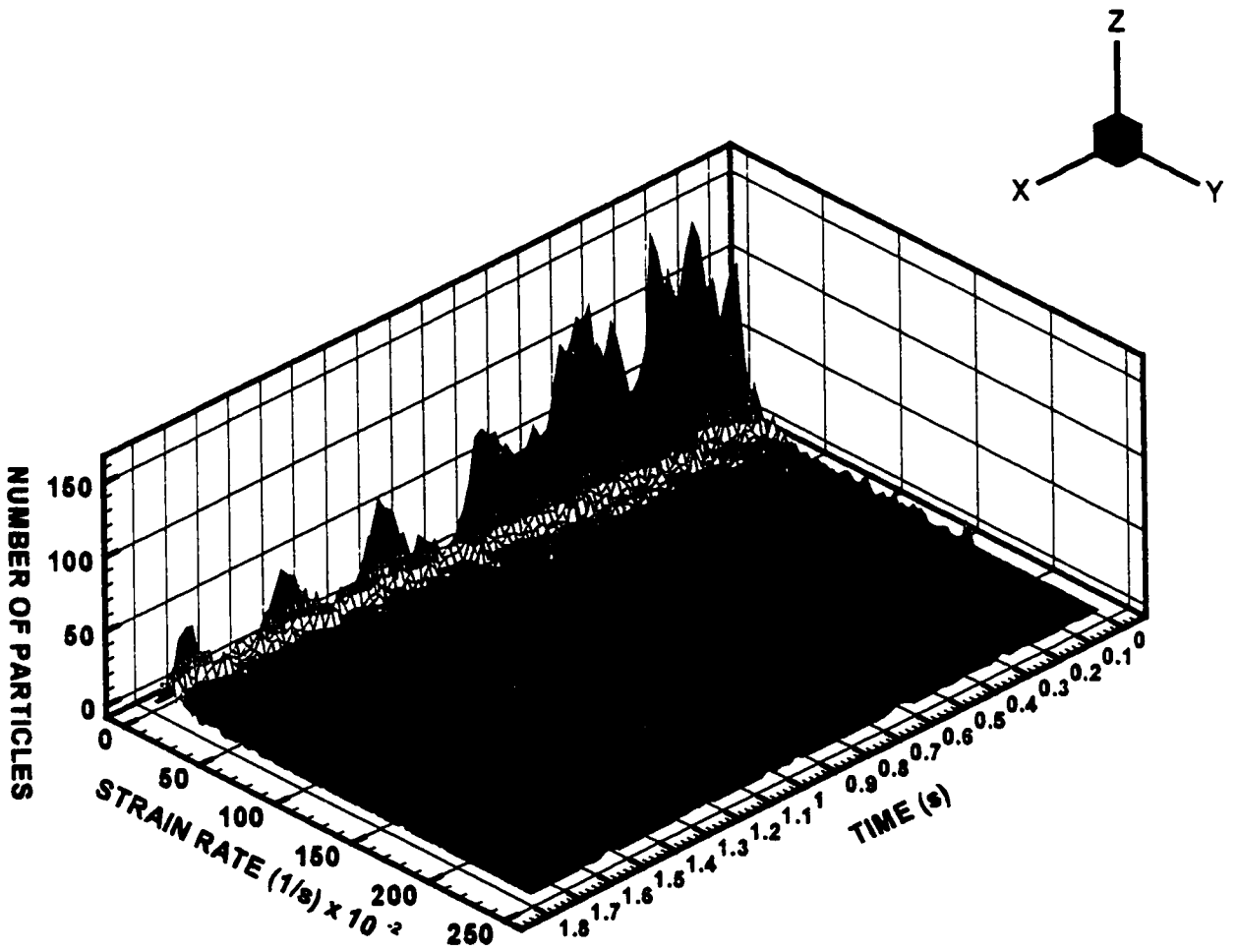

Figure 4.10. Number of particles vs strain rate vs time, L/D=0.133.

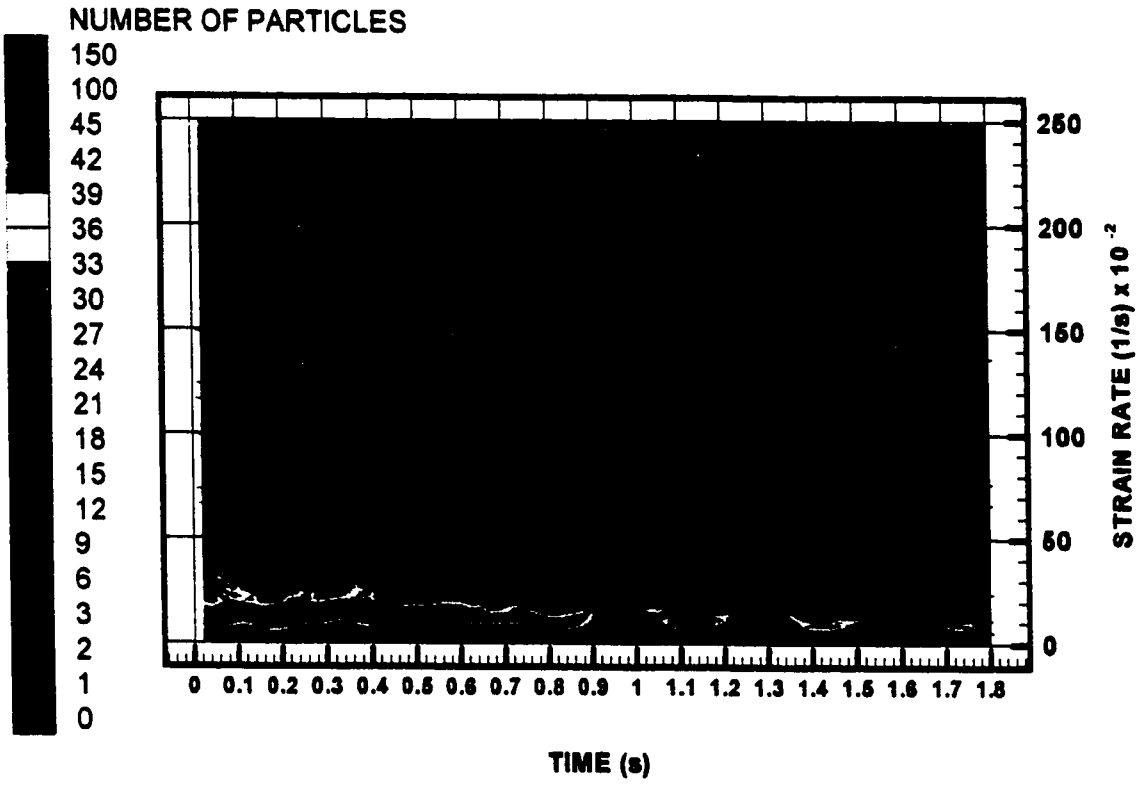

Figure 4.11. Number of particles vs strain rate vs time, L/D=0.133.

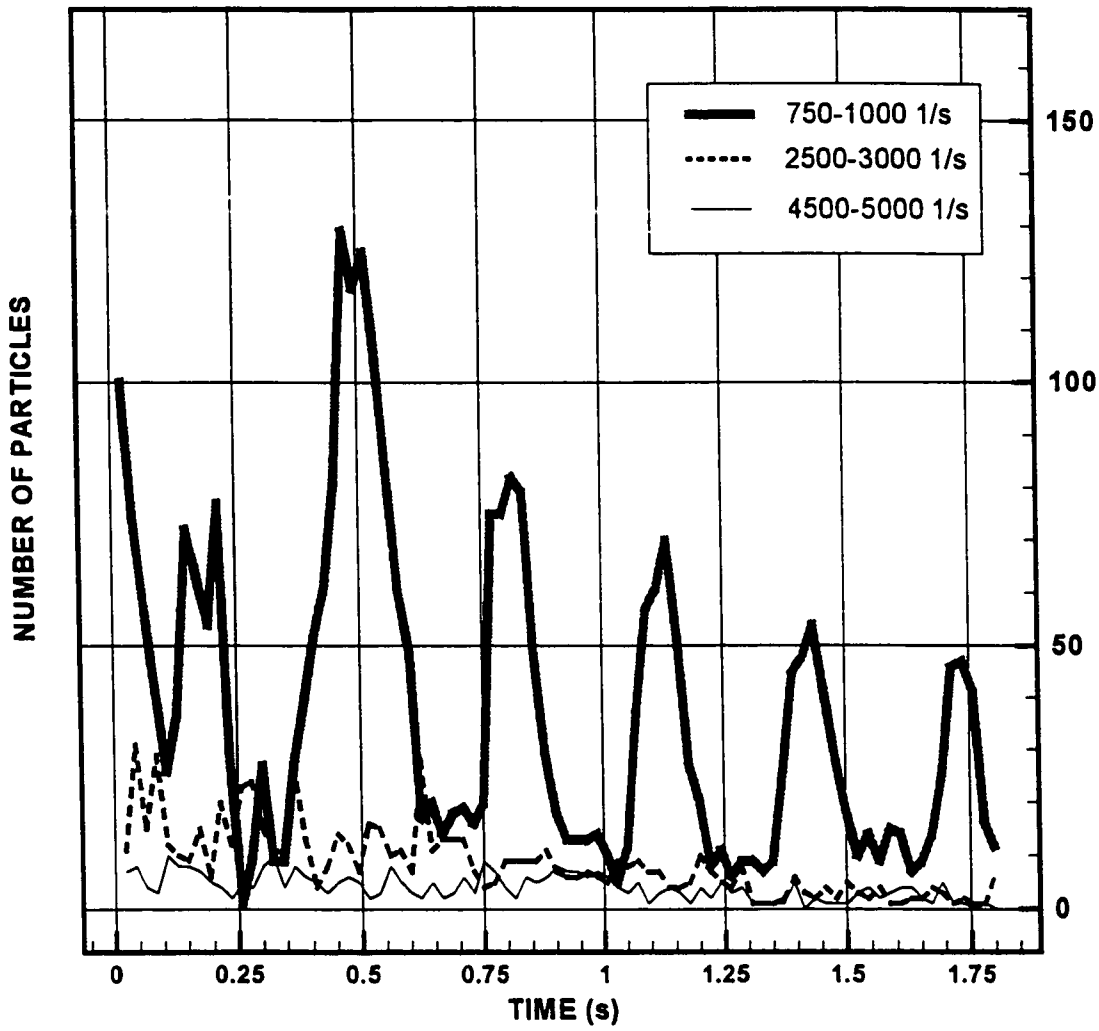

Figure 4.12. Number of particles submitted to a range of strain rate as a function of time, L/D=0.133.

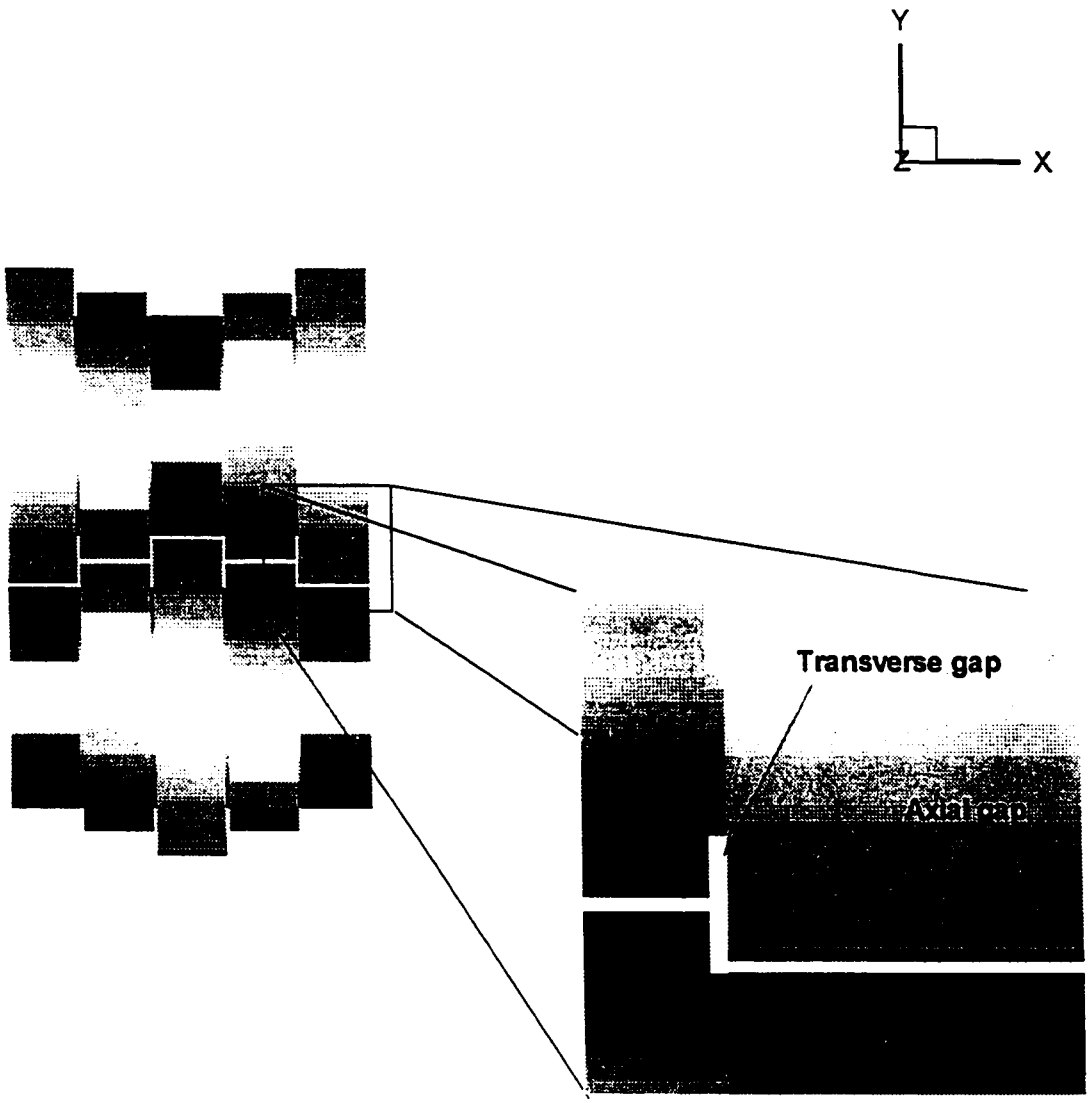

Figure 4.13. Disc-disc clearances: transverse and axial gaps.

the number of particles with strain rates over 2000 s^{-1} increases and the periodicity is more pronounced.

Figures 4.20, 4.22 and 4.24 show a three-dimensional representation of the number of particles experiencing a strain rate greater than the specified value as a function of time. The case for strain rates greater than 0 represents the standard washout function. Figures 4.21, 4.23 and 4.25 are a two-dimensional representation of the residence time as a function of the strain rate.

A study of the history of individual particles reveals that they experience very different levels of strain rate on their way out of the kneading blocks. This is illustrated in Figure 4.26 using five particle trajectories starting from x=0. Particle 1 starts near the barrel wall and shows very short axial movement since it remains close to the stationary surface. Particle 2 shows a longer axial trajectory. Particle 3 reaches the end of the kneading section, whereas particle 4 circulates around one disc, since its starting point is very close to the surface of the disc. Particle 5 has also a long trajectory. Figure 4.27 shows the amounts of strain rate experienced by every particle as a function of time. The different profiles show that particle strain rate history vary from being submitted to extreme fluctuations reaching very high values of strain rate as for Particles 1 and 2 (which also are the particles with the shortest axial displacement) to particles experiencing uniform low strain rate throughout the complete trajectory as for Particle 3.

There is a pronounced difference between the strain rate profiles experienced by different particles. The study also shows that some particles experience very low and uniform amounts of strain rate through their way out the kneading discs. This shows that it is not sufficient to analyze average flow characteristics for a specific position of the discs to characterize the mixing intensity, but the analysis of particle trajectories based on the transient flow field is necessary.

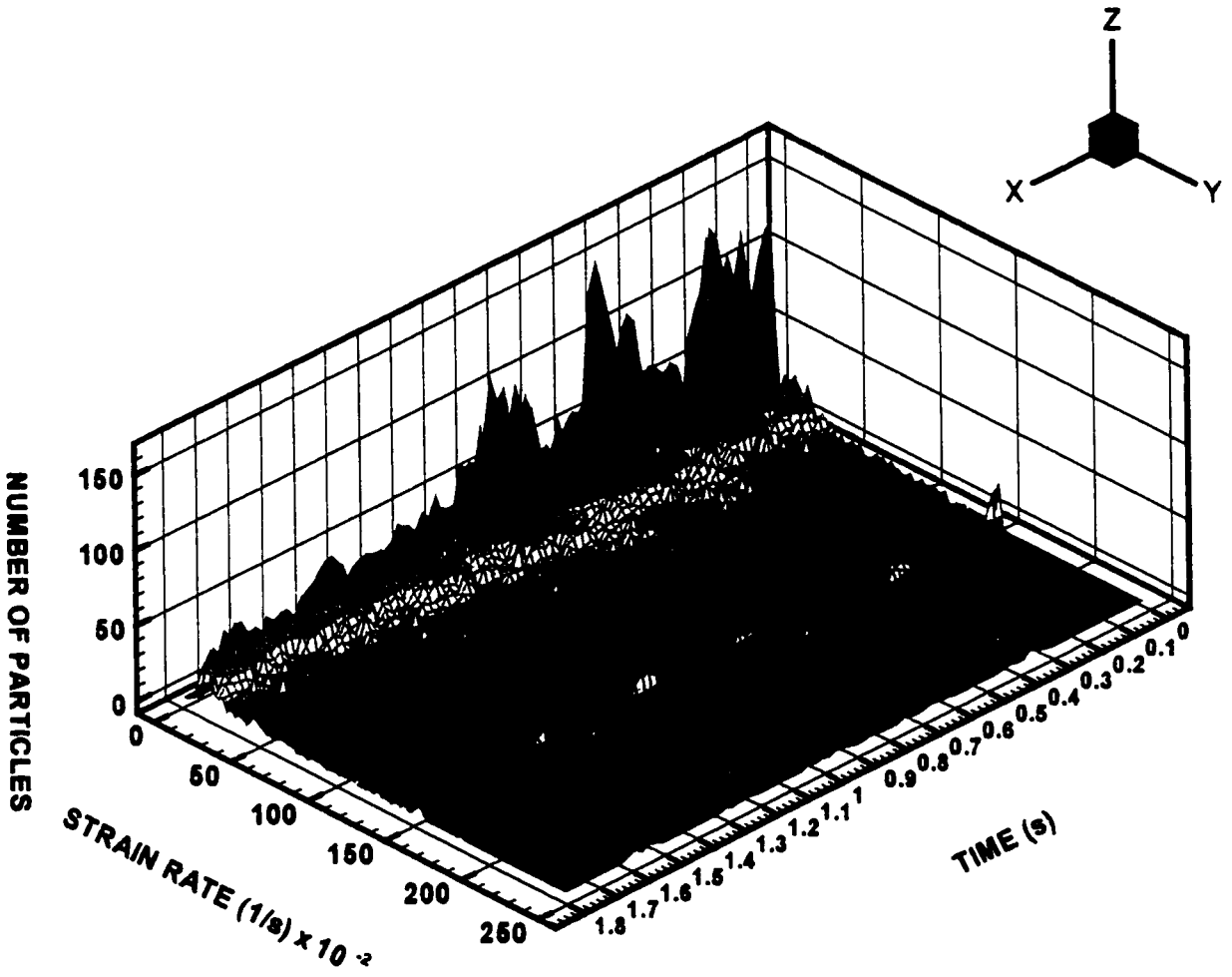

Figure 4.14. Number of particles vs strain rate vs time, L/D=0.2.

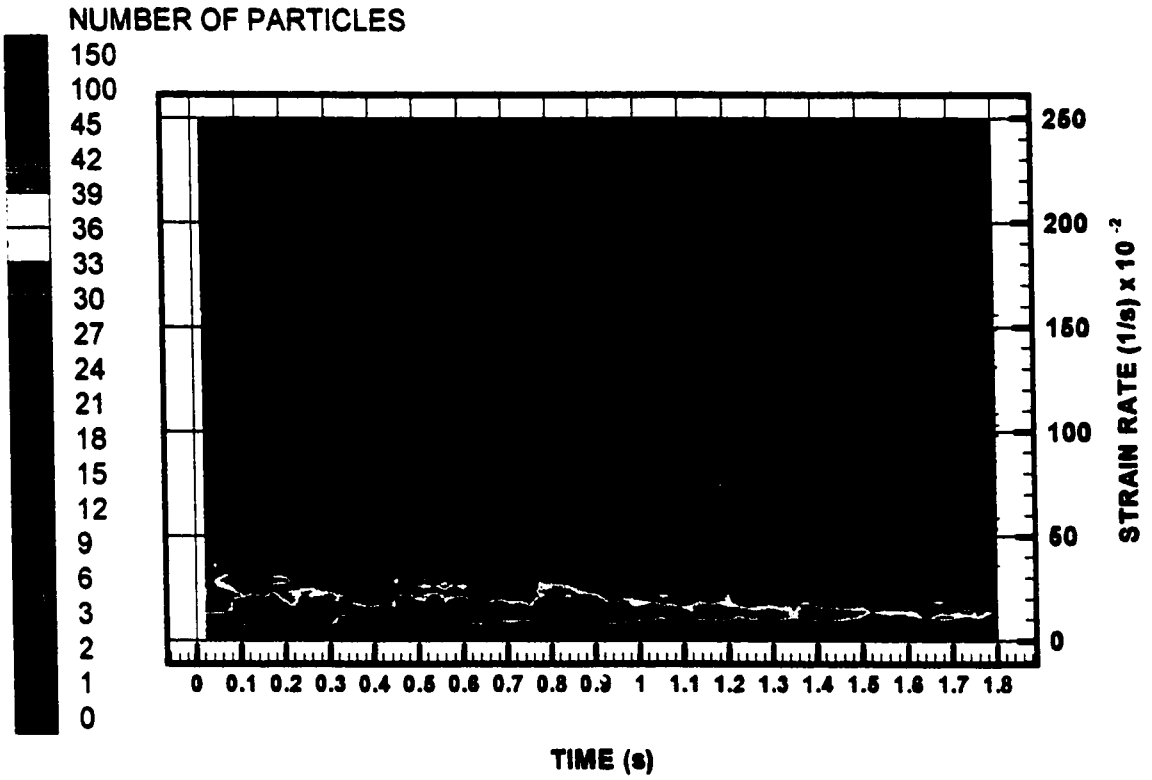

Figure 4.15. Number of particles vs strain rate vs time, L/D=0.2.

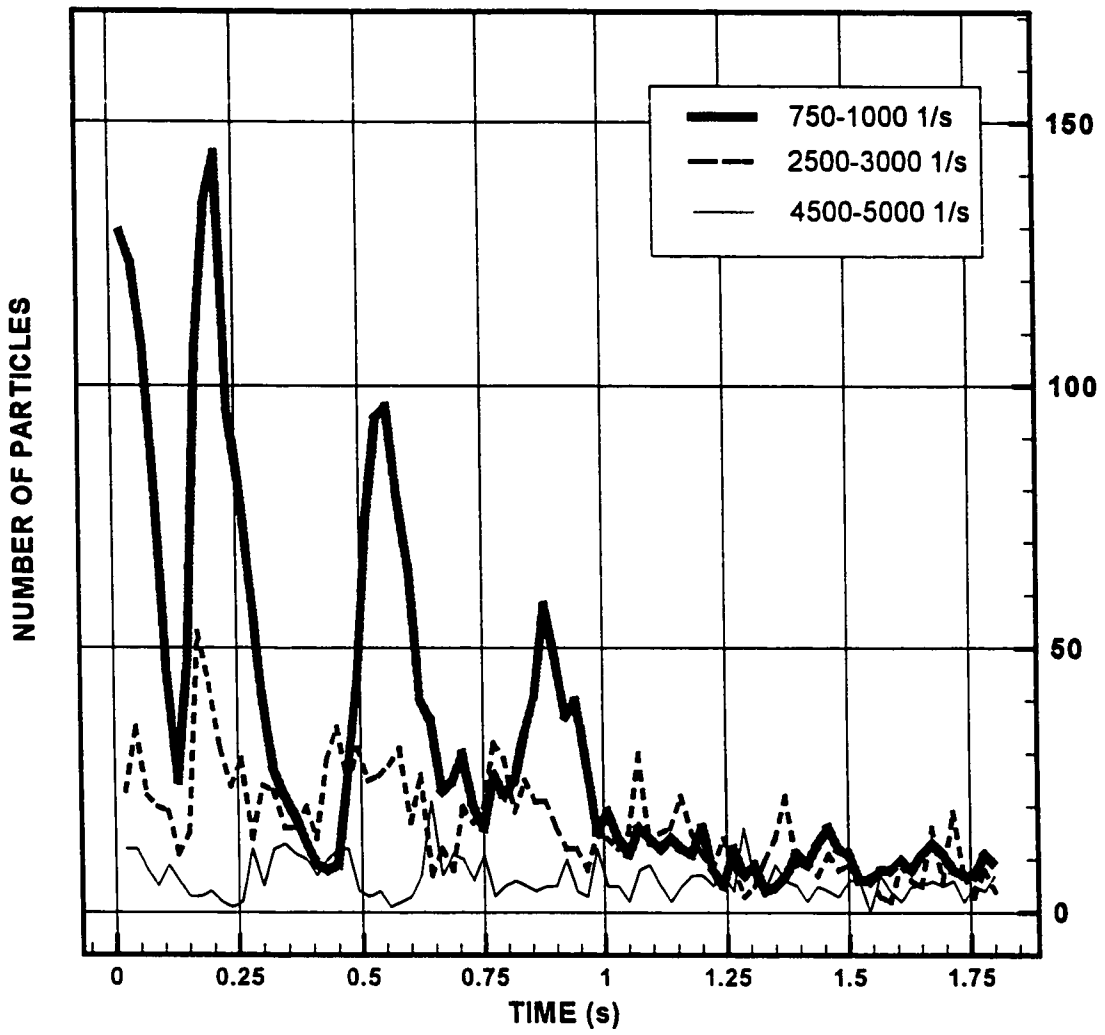

Figure 4.16. Number of particles submitted to a range of strain rate as a function of time, L/D=0.2.

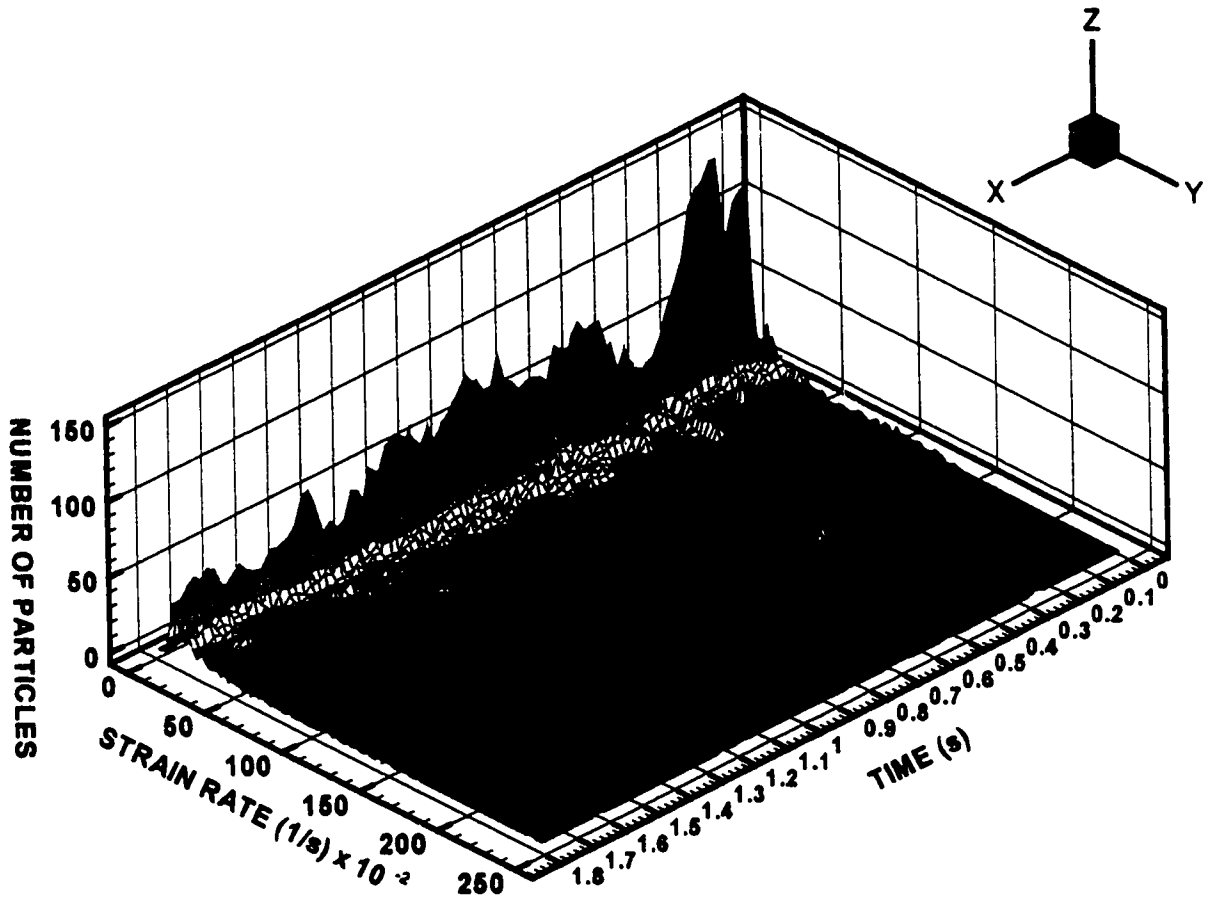

Figure 4.17. Number of particles vs strain rate vs time, L/D=0.28.

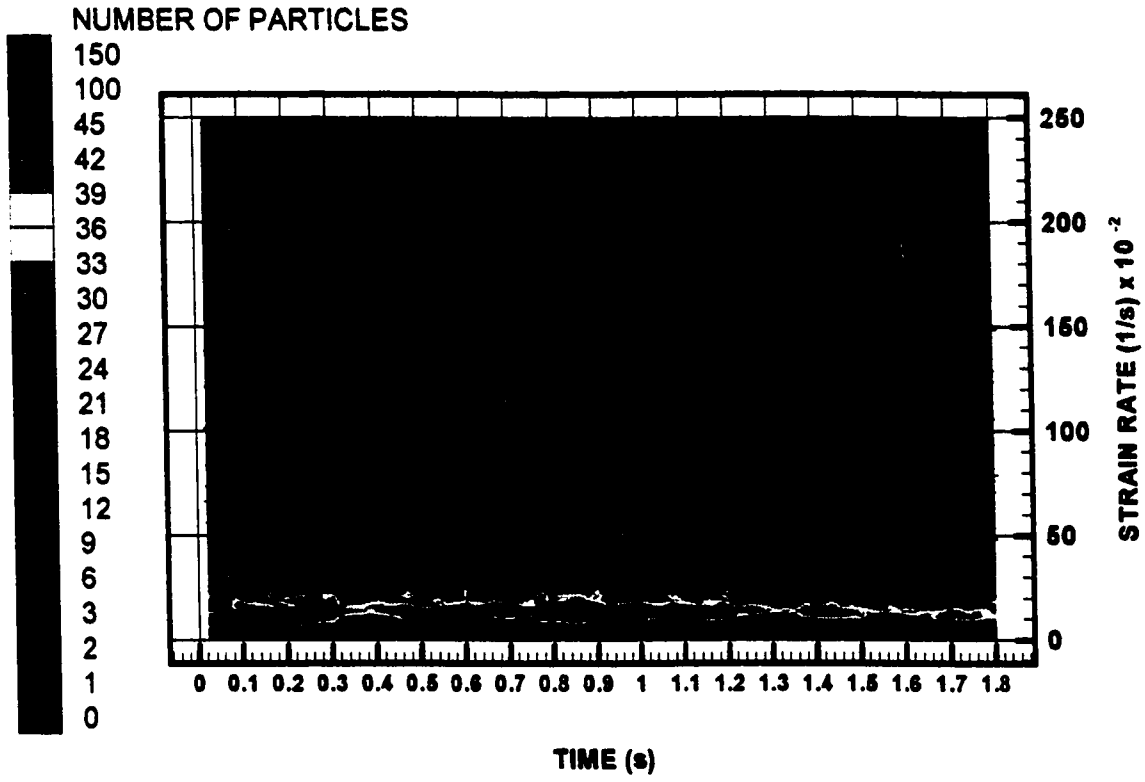

Figure 4.18. Number of particles vs strain rate vs time, L/D=0.28.

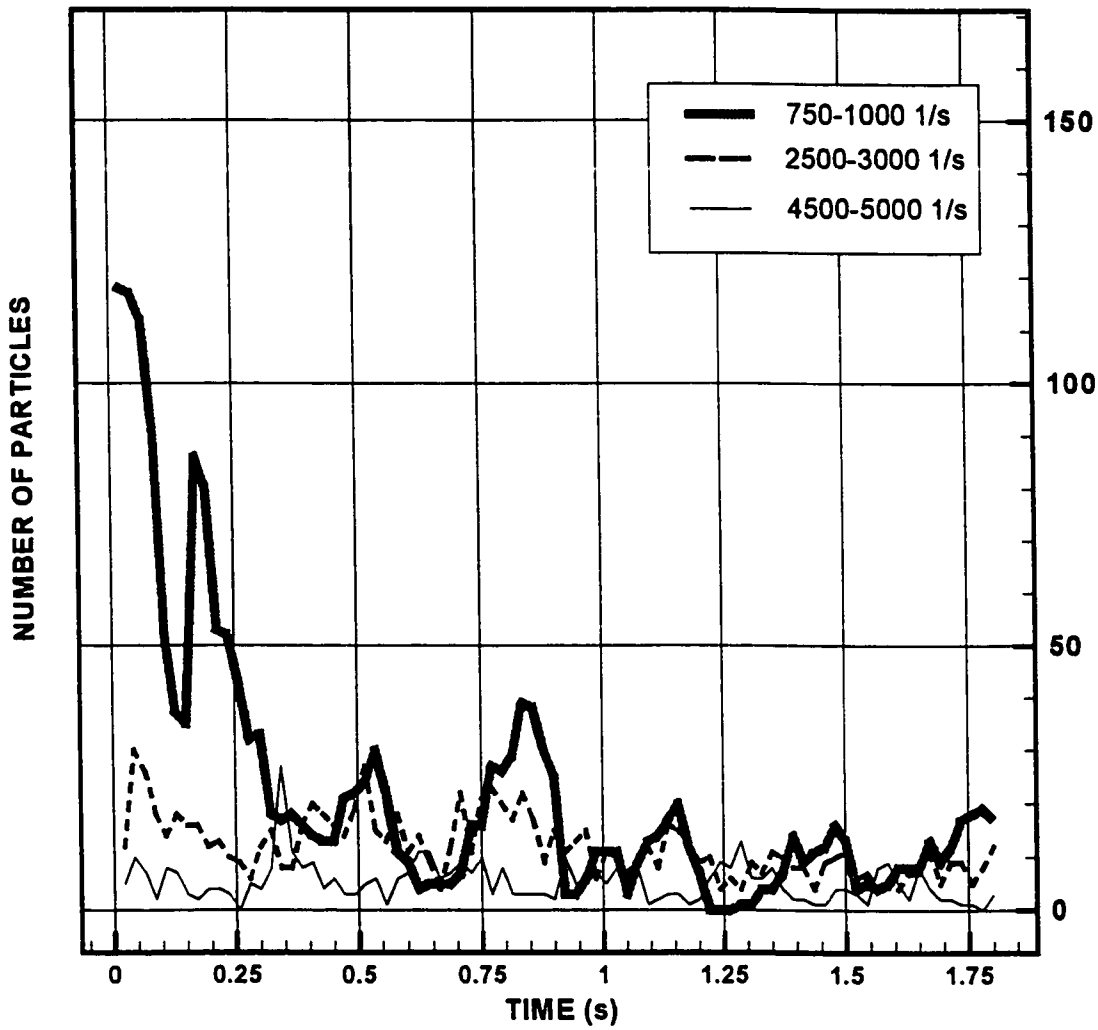

Figure 4.19. Number of particles submitted to a range of strain rate as a function of time, L/D=0.28.

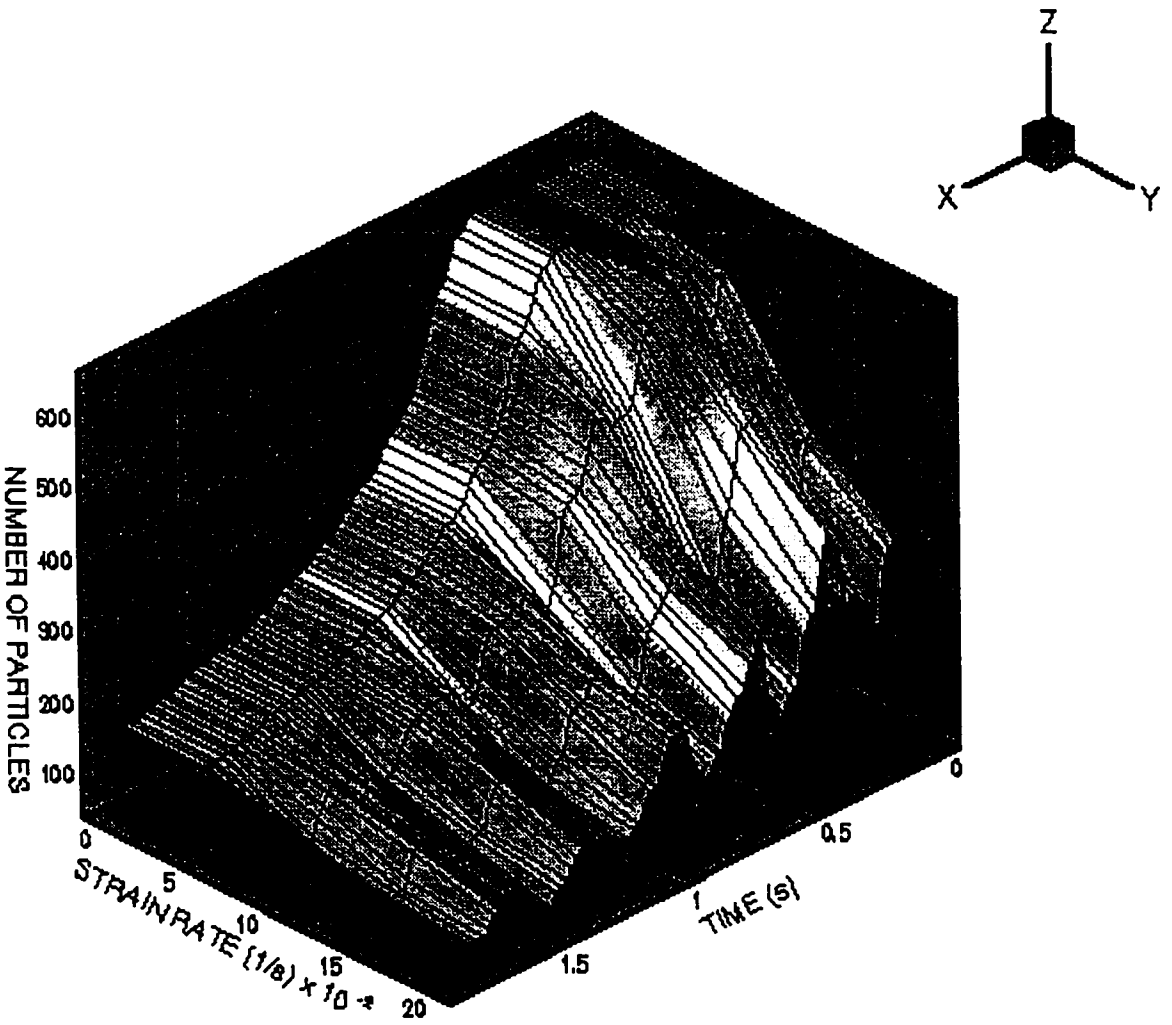

Figure 4.20. Number of particles experiencing specific levels of strain rate vs time, L/D=0.133.

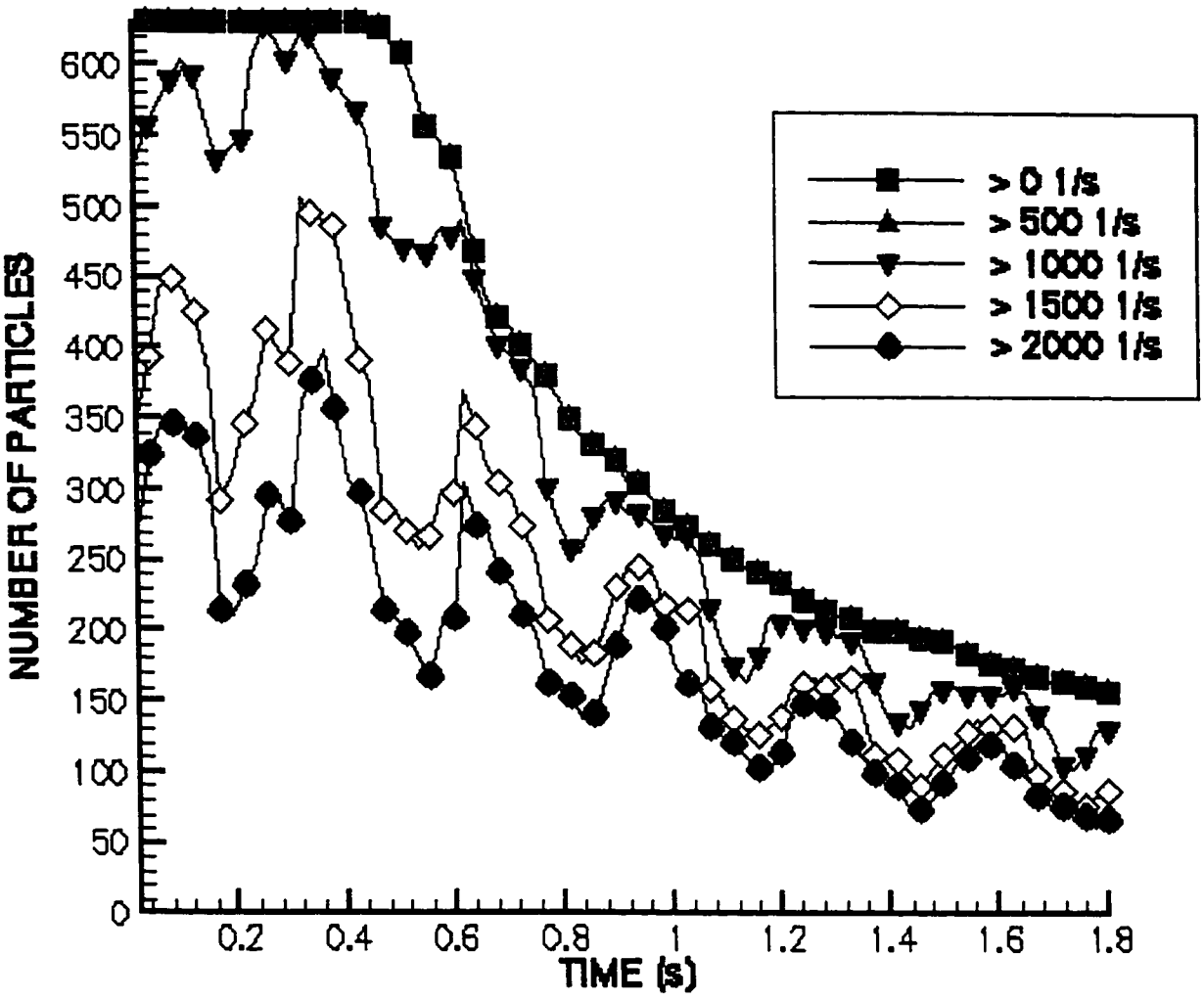

Figure 4.21. Number of particles experiencing specific levels of strain rate vs time, L/D=0.133

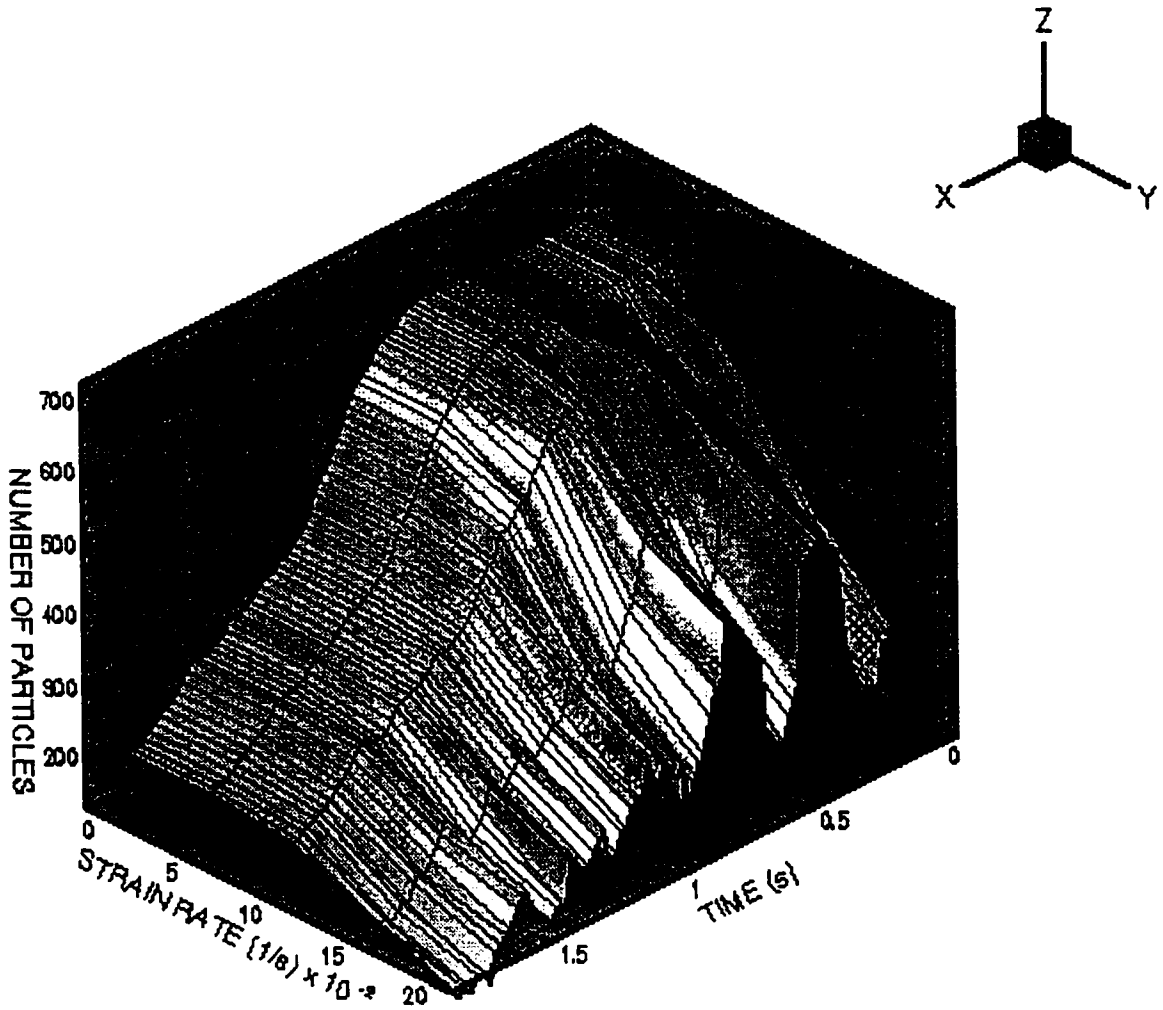

Figure 4.22. Number of particles experiencing specific levels of strain rate vs time, L/D=0.2

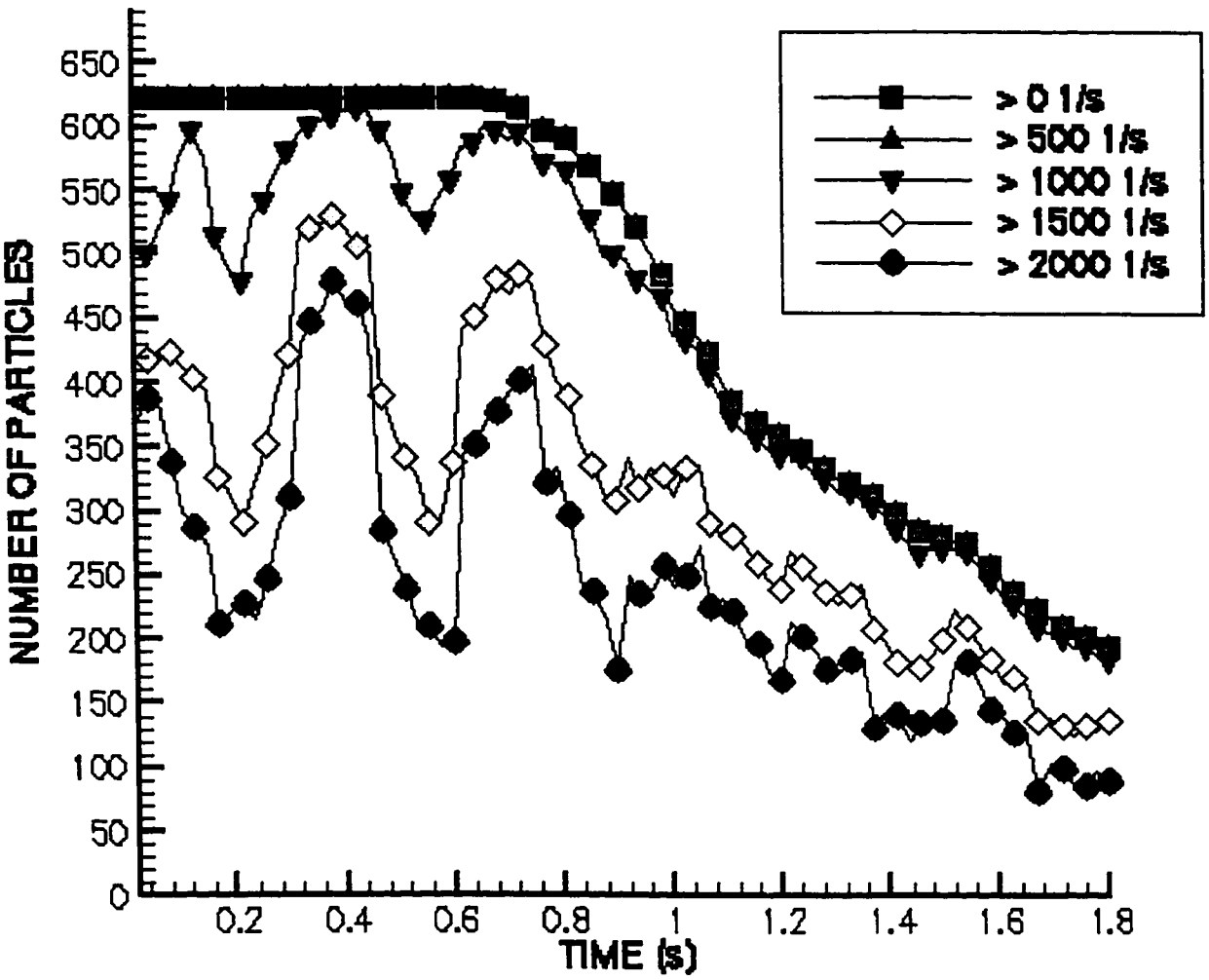

Figure 4.23. Number of particles experiencing specific levels of strain rate vs time, L/D=0.2.

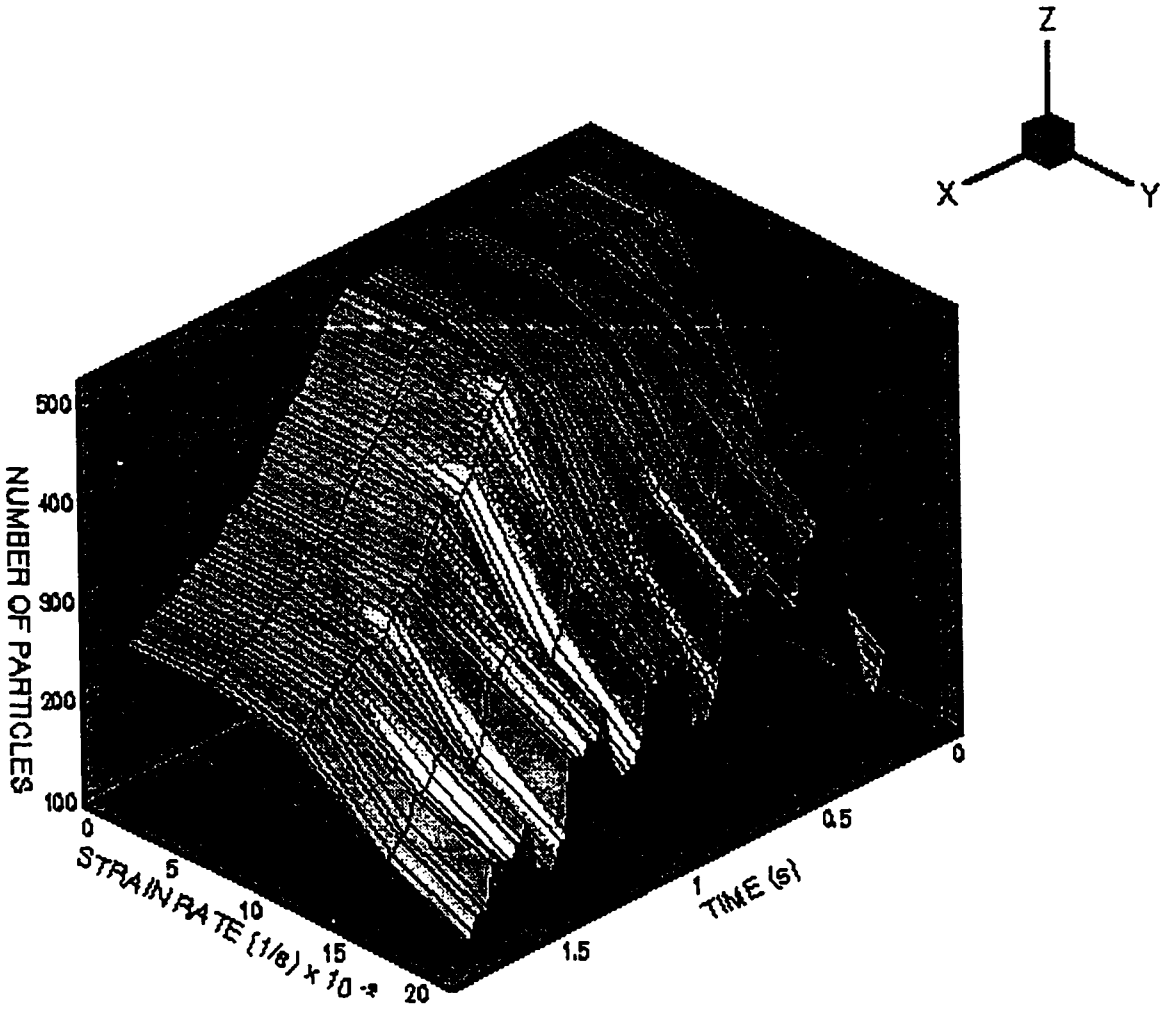

Figure 4.24. Number of particles experiencing specific levels of strain rate vs time, L/D=0.28

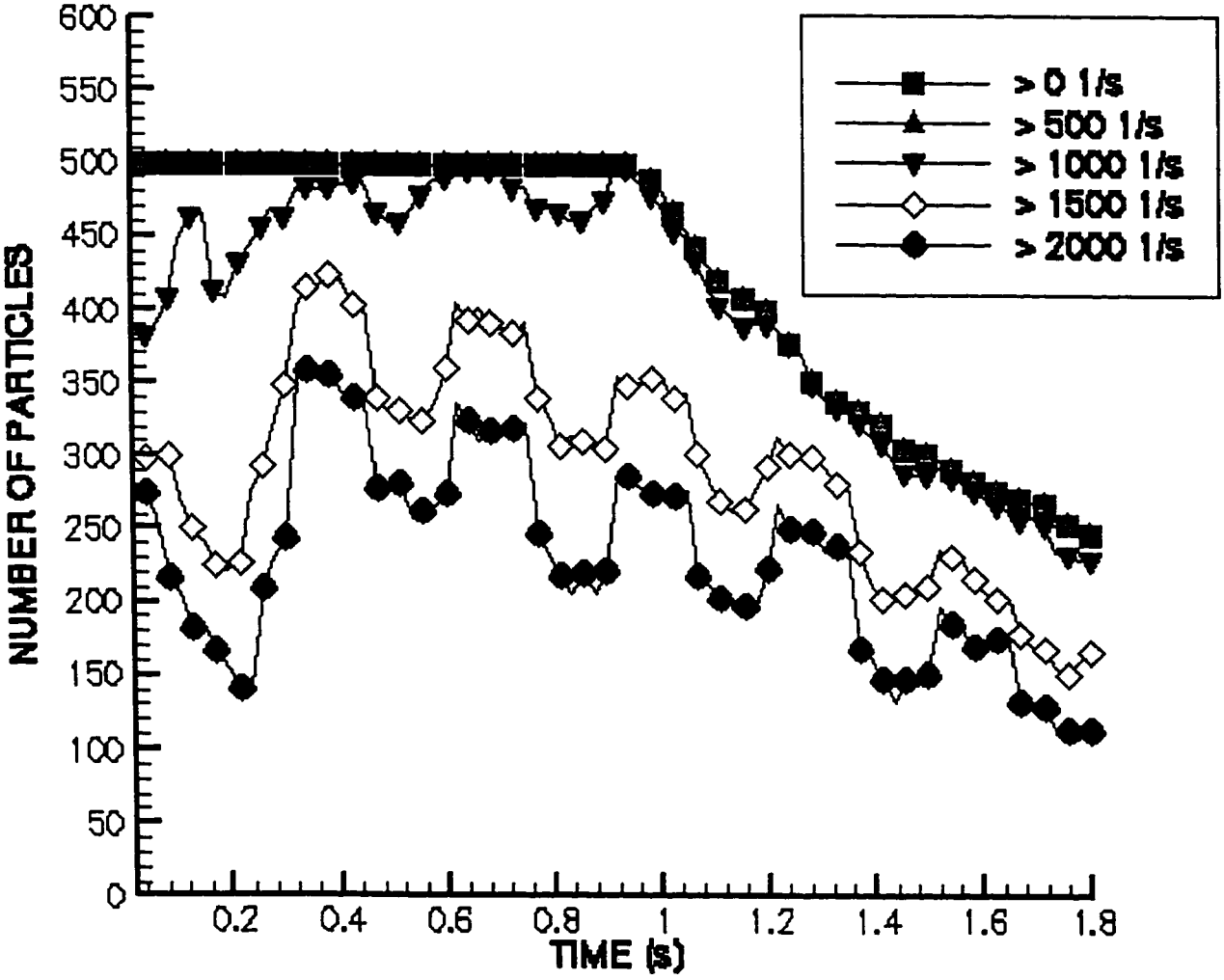

Figure 4.25. Number of particles experiencing specific levels of strain rate vs time, L/D=0.28.

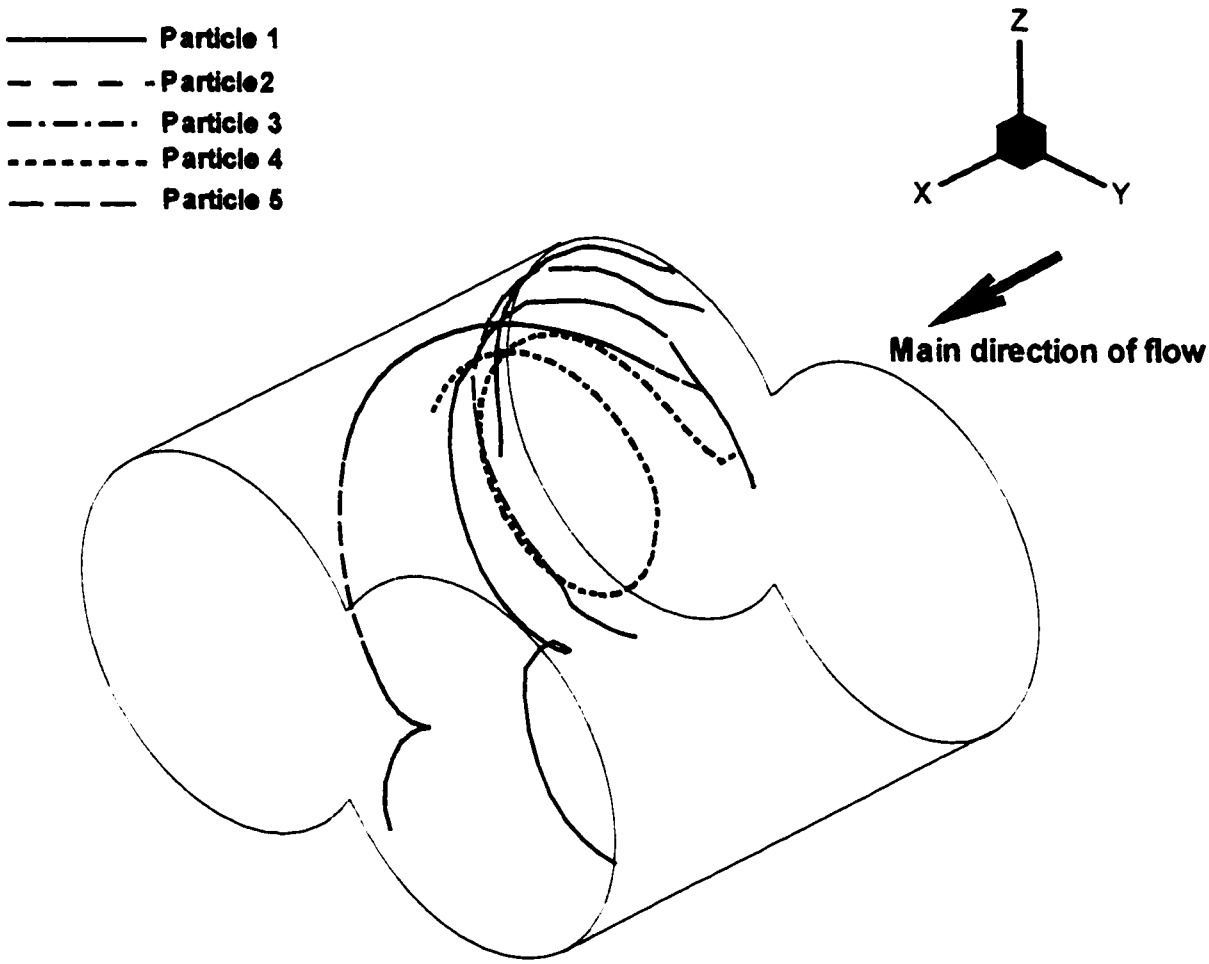

Figure 4.26. Trajectory of various particles, case L/D=0.28. Elapsed time: 0.9s.

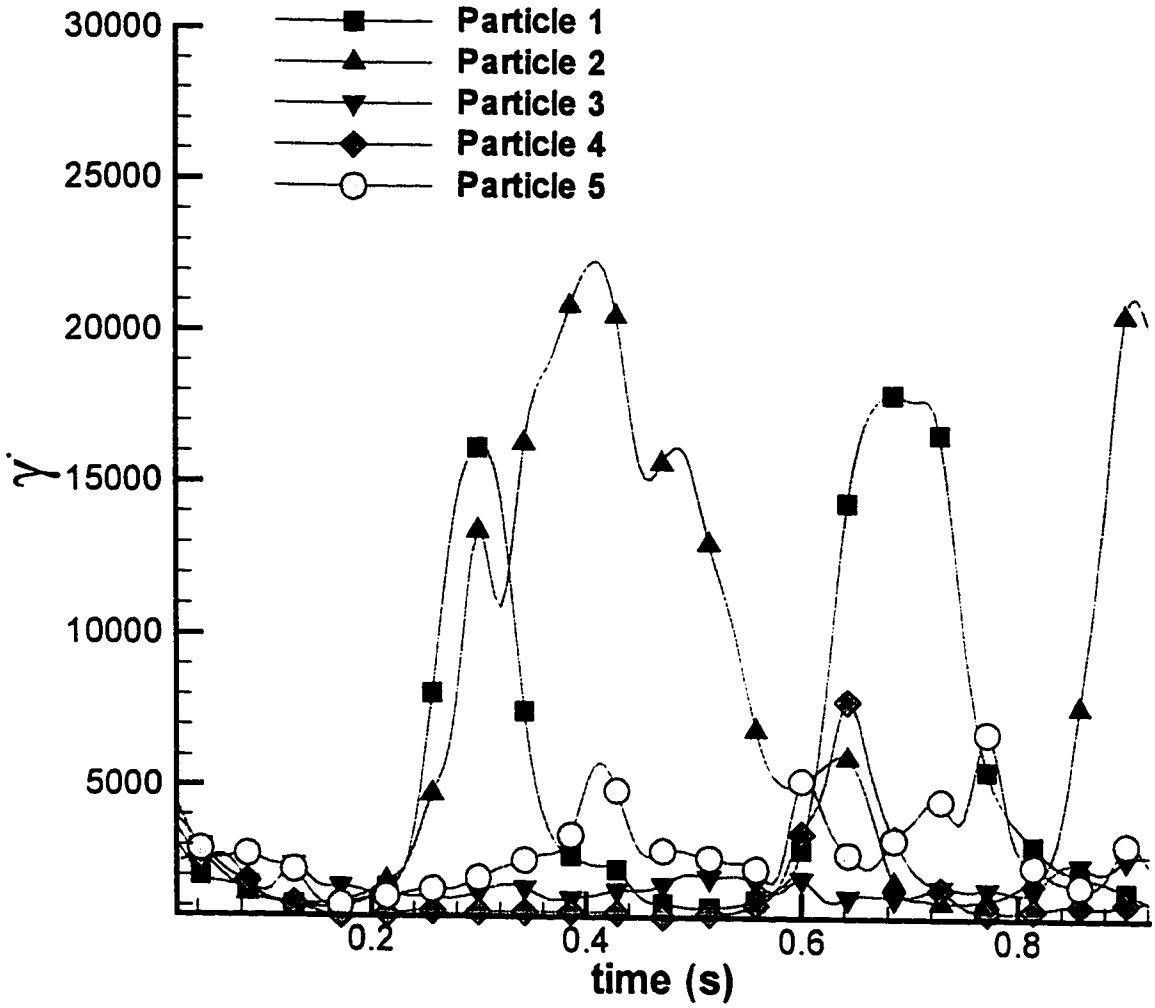

Figure 4.27. Rate of strain history of the various particles in Figure 4.26

4.7 Summary

A procedure has been developed to evaluate the relative mixing performance of different configurations of kneading blocks. The quasi-steady state flow field was calculated by solving the 3D conservation equations of mass and momentum using the finite element method. Particle tracers are introduced at the entrance plane of the kneading blocks covering a complete cross section of the channel. Residence time distributions were determined as a way to study aspects of distributive mixing. The mechanism for the generation of back flows was explained through the numerical results. Back flow has traditionally been a way to characterize distributive mixing.

An increase in the width of the discs increases the amount of back flow generated. The increase of the amount of back flow is not proportional to the increase in the width of the discs. The increase of L/D from L/D=0.133 to 0.2 produces a notable increase in the back flow generation. The increase from 0.2 to 0.28 produces a smaller increase in back flow. A further increase in the width of the discs would not reflect in a significant increase in back flow but would create a serious reduction in the conveying properties of the discs. An increase in the width of the disc increases the amount of particle tracers submitted to high strain rates. This effect is attributed to the increase in surface area in the regions of high strain rate generation. The study of strain rate history reveals that particles are submitted to highly fluctuating strain rates through their path through the kneading blocks. There are particles that undergo several regions of high strain rate, while other particles never get to experience any high strain rate. These results show that it is not sufficient to analyze average flow characteristics for a specific position of the discs to characterize the flow. The analysis of particle trajectories based on the flow field provides information about the time-varying strain history experienced by the fluid elements.

Chapter Five

EXPERIMENTAL VALIDATION: PARTICLE IMAGE VELOCIMETRY

5.1 Introduction

A validation of the simulation results against experimental values of pressure was carried out and presented in Chapter 3. Pressure measurements can give some indication of the flow patterns as explained by Christiano and Lindenfelzer (1997). However, the flow pattern is better described by the velocity profile. Particle image velocimetry allows capture of two fluid velocity components across a plane of flow at a single instant in time. This establishes the main advantage of this technique over hot-wire and laser Doppler anemometry, which measure velocity at a single point in space and time.

This chapter compares simulation to experimental results obtained from the application of the PIV to a transparent, acrylic-made twin screw extruder model developed by Jaffer (1998). The dimensions of the model were based on the ZSK-30 extruder. The specification of all dimensions and the reference coordinate system are explained in Chapter 2. The results are presented in the form of velocity vectors and contours of the velocity components.

5.2 Particle Image Velocimetry

This section contains an overview of the experimental technique used by Jaffer (1998) for the measurements of velocity. The results obtained by Jaffer were used for the purpose of comparison and validation of the numerical model developed in this thesis.

The technique of particle image velocimetry (PIV) has been described rigorously by Adrian (1991) and Buchhave (1992). PIV falls within a broader range of experimental techniques known as pulsed-light velocimetry (PLV). This class of measuring techniques has a commonality in that all members observe the motion of small marked regions of

fluids. These fluid elements are observed at two or more instants in time and the marked fluids are recorded on one image or multiple images. The objective of PIV is to measure the magnitude and direction of velocities in a region of a fluid flow. The flow is illuminated by a strong light source, such as a laser beam, and the particle positions are recorded by imaging the light scattered from the tracer particles onto a recording medium, such as a digital image that is later analyzed in a computer. As the particles are expected to act as transmitters of information in the form of scattered light, they must have the right size to achieve this goal. Since the particles are also expected to capture the motion of the fluid, they must be present in sufficient concentration to give an accurate description of the flow field. The amount and size of the particles is limited by their effect over the flow field. The flow field is illuminated with a series of short laser light pulses with a known time separation. A sequence of images of the illuminated region with the light scattered from the particles is recorded. The displacement of the particles is then determined from the difference in location between the first and subsequent images. In this study, the fluid elements were marked by particles and illuminated through a pulsed light source. These fluid elements are observed with a video camera coupled with an analogue to digital image acquisition computer board. The resulting digital images have a speckle pattern or particle trajectory image.

The light source can be pulsed at distinct frequencies and periods. In the double pulse operation mode, the image obtained would contain pairs of particles. These pairs of particles are analysed using various techniques to resolve the velocity components. These techniques can include Yonge's fringes coupled with optical fast Fourier transforms (FFT) to digital FFT. The various techniques of analysing PIV images are discussed in a review article by Adrian (1991).

The technique used for these experiments was cross correlation (Figure 5.1) since the velocity magnitudes of interest in the twin screw extruder are relatively small (~0.1m/s) at the operating conditions used in the experimental work. Cross-correlation requires two images, each having a single pulse, to be captured with a short time, t, between the images. These images are superimposed creating a single image that would appear to have been double pulsed. This technique has a significant advantage over the double pulse technique. Namely, the directionality ambiguity is resolved as each pulsed particle is labelled as 1 or 2

depending on which image it originated from. Therefore, the velocity calculations can only occur for pairs of particles having 1 and 2 labels. The double pulse technique can not be used since there is no knowledge *a priori* of the velocity field. Therefore, there is no way of determining which was the first pulse and hence the direction of the particle. This technique usually is coupled with image shifting techniques to resolve directionality (Adrian 1991). This technique is similar to frequency shifting in LDA.

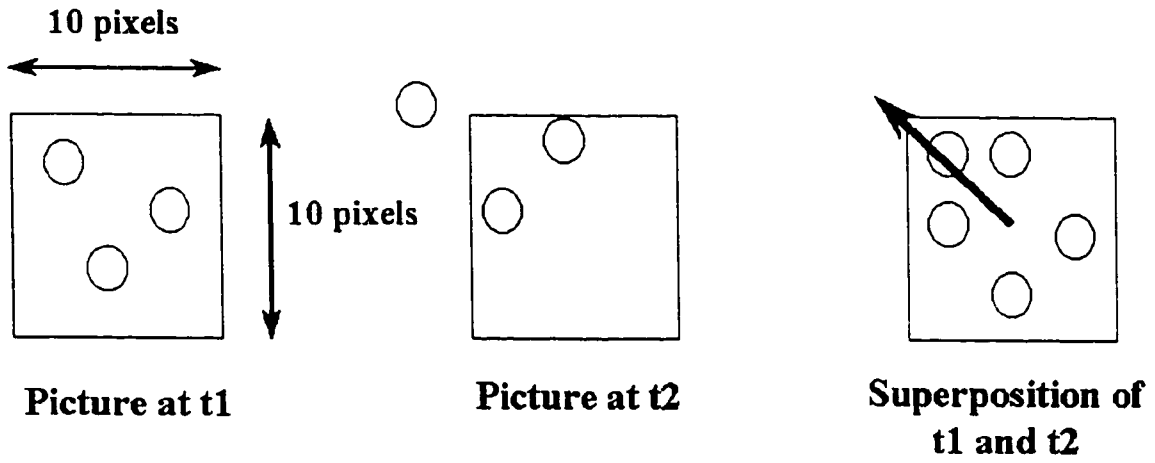

Figure 5.1. Principle of particle image velocimetry: cross correlation.

The benefits of PIV are:

- An entire 2D flow field can possibly measured in a single image
- The method is non-intrusive
- Reduced times for measuring flow fields

The drawbacks of this technique are:

- The loss of time dependent structures due to computer limitations
- The problem of determining adequate numbers of data points for averaging results
- The bias of the technique towards higher velocities

There are other technical problems associated with PIV. One of the main problems is the determination of the optimum particle size, which is a compromise between the requirement that particles follow the flow and the need for the particles to scatter enough light to create images of sufficient quality (Buchhave, 1992). Another important specification in PIV is the ability to resolve small spatial velocity scales. This is associated with the thickness of the laser sheet. Good spatial resolution is obtained when the thickness

of the laser sheet is kept small. The particle concentration is also an important specification. Particle concentration should be high enough to have a minimum number of particle image pairs in the interrogation area. Buchhave (1992) proposed a criterion of 5 to 10 particle images in the interrogation area as a minimum quantity to ensure a reliable velocity determination. There are other possible sources of error associated with optical deviations.

5.3 Experimental setup and material properties

Jaffer (1998) fabricated an intermeshing co-rotating twin screw extruder model out of acrylic, including barrel, shafts, conveying and disc elements. The purpose of making the model out of acrylic is to facilitate the optical experimental methods of laser induced fluorescence and digital particle image velocimetry (PIV). The fluids used are bright mineral oils (Petro-Canada). These oils have indexes of refraction, n_{do}, of 1.465, almost identical to the index of refraction of the acrylic, 1.47. With the indicies of refraction being very similar, distortion and diffraction of the laser sheet was reduced. However, even the small difference in the indexes of refraction of the two materials caused some diffraction within the intermeshing region of the elements. The mineral oil used has a Newtonian behavior and its properties are presented in Table 5.1

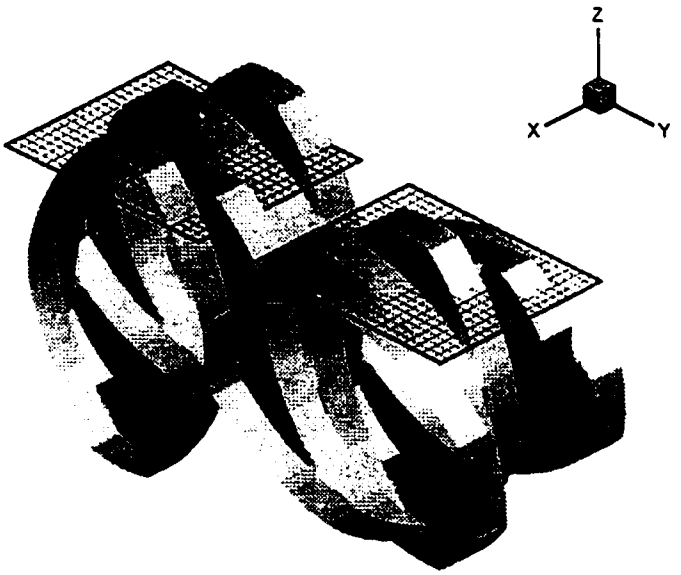

Figure 5.2. Cutting plane at z=10 mm. Density of the data grid.

The light source is a 6W argon ion laser, which is concentrated into a light sheet. The laser beam creates a sheet of light after passing through the cylindrical lens and the convex lens focuses the sheet to a thickness of 100 to 500 μm. This thin sheet is a requirement for PIV as it creates a very well defined two-dimensional flow visualization. The light sheet was passed through the TSE along the constant plane z=11.0 mm (Figure 5.2).

Density	740 Kg/m^3
Viscosity	1 Pa.s
Index of refraction	1.465

Table 5.1. Mineral oil properties

5.3.1 Geometry

Figure 5.3 displays the configuration of elements placed on the shafts of the extruder for the various cases. A special configuration, as shown in Figure 5.3a, was specially fabricated to study the effect of the boundary condition used for the mathematical model. Long discs placed before and after the 45/5/20 kneading blocks were designed to isolate the studied region, and to verify the normal stress boundary condition used for the simulations. For the configuration shown in Figure 5.3b, 20mm forward conveying elements were placed before and after the 45/5/20 kneading blocks

5.3.2 Experimental Procedure (Jaffer, 1998)

Thirty instantaneous image pairs were obtained for each location in the TSE. The images were interrogated with TSI's Insight NT 1.0, which determined the velocity vectors over each pair of images. The area of interrogation used was 10 by 10 pixels in size, which corresponds to areas of about 1 by 1 mm. The kneading block, composed by 5 discs staggered at 45° in a forward configuration, have a total length of 20 mm. As a result, the mesh chosen for velocity measurements was 20 by 20 mm, such that the areas of interrogation did not overlap. The thirty sets of data were processed to obtain the average and r.m.s. values at each node of the mesh. If the r.m.s. was less than 5 percent of the measured velocity data the data was kept, otherwise the run was repeated.

(a)

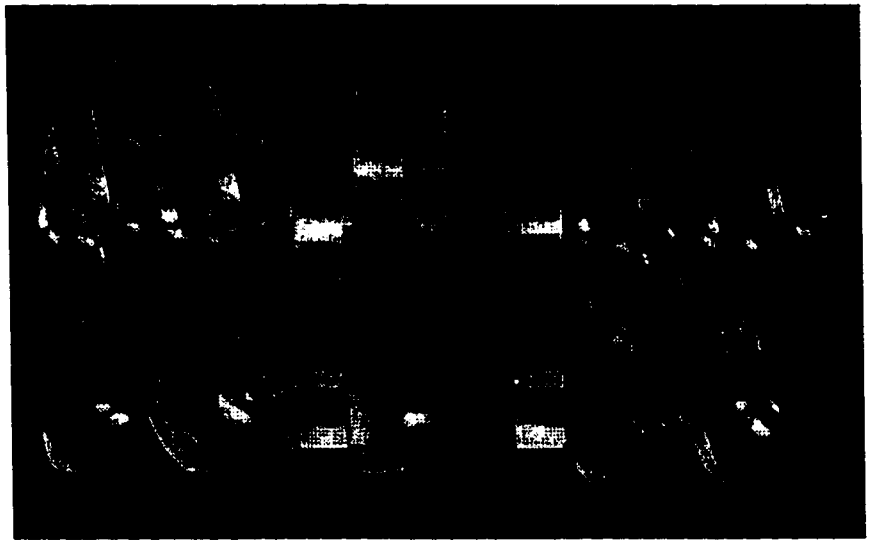

(b)

Figure 5.3. Geometry of the elements used by Jaffer (1998) for the various cases. a) From left to right: 40 mm straight element, 20 mm 45° stagger angle forward kneading block, 40 mm straight element; b) From left to right: 20 mm forward conveying element, 20 mm 45° stagger angle forward kneading block, 20 mm forward conveying element.

5.4 Numerical considerations

The numerical solution of the governing equations (2.1 and 2.2) is obtained according to the method explained in Chapter Two. The normal stress boundary condition is used to model the inlet and outlet problem. To obtain the flow rate of 5 mL/s at 60 rpm the normal stress difference imposed was 200 Pa. For the case of 8.5 mL/s and 60 rpm the normal stress difference was 800 Pa. The solution is obtained using 27 node triquadratic brick elements for velocities. Each triquadratic elements is subdivided into 8 trilinear elements, as shown in Figure 5.4, for the purpose of interpolating the data values into a 2D slice cut. A slice cut is made to the three dimensional mesh to obtain a two-dimensional field at the same plane where the PIV measurements are made. The interpolation of the data values is done from the original 3D field into the 2D mesh using linear interpolation. A mesh density of 21 by 21 nodes was used for each one of the two kneading blocks, as shown in Figure 5.2.

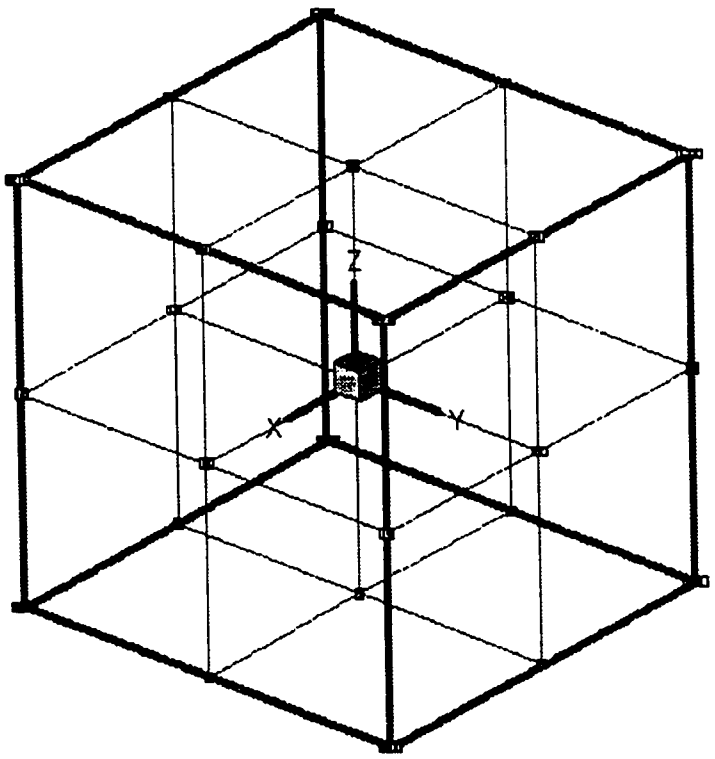

Figure 5.4. Conversion from one triquadratic brick element into 8 linear brick elements

The two-dimensional simulation mesh is created with the same number of nodes as the experimental mesh showed in Figure 5.2, such that a comparison can be made at the same spatial location. This requires the interpolation of the velocity values from the nodal points in the 3D field to the 2D mesh. A linear interpolation is performed at every 2D element. Linear interpolation finds the velocity values in the destination mesh based on their location within the elements of the source zones. The velocity value is linearly interpolated to the destination data points using only the data points at the vertices of the elements in the source mesh.

Comparisons are made using velocity vectors and velocity contours. The effect of inlet and outlet boundary conditions was studied by using the long straight elements shown in Figure 5.3a. Two different finite element meshes were necessary to simulate the flow field with and without the long elements. In both cases, the normal stress boundary condition was applied. Figure 5.5 shows the surface finite element mesh for the two cases studied. In case (a) the inlet and outlet boundary conditions are imposed at the ends of the kneading blocks whereas in case (b) long straight elements are deployed before and after the kneading blocks to move the inlet and outlet boundary conditions away from the kneading blocks. The main purpose was to establish the effect of the adjacent elements on the measured flow field and to analyze the ability of the proposed numerical model and boundary conditions to describe the actual flow field.

5.5 Results

Runs were carried out for 6 different conditions varying flow rate, rpm and the geometry of the elements before and after the region of study. For half of the cases, conveying elements with a pitch and length of 20 mm were located before and after the kneading blocks studied, whereas the rest of the cases were carried out using a specially designed long element resembling a single long disc, as shown in Figure 5.3a. These long discs were designed to move away the effect of the interface between elements on the flow patterns in the studied region. The conditions used are listed in Table 5.2.

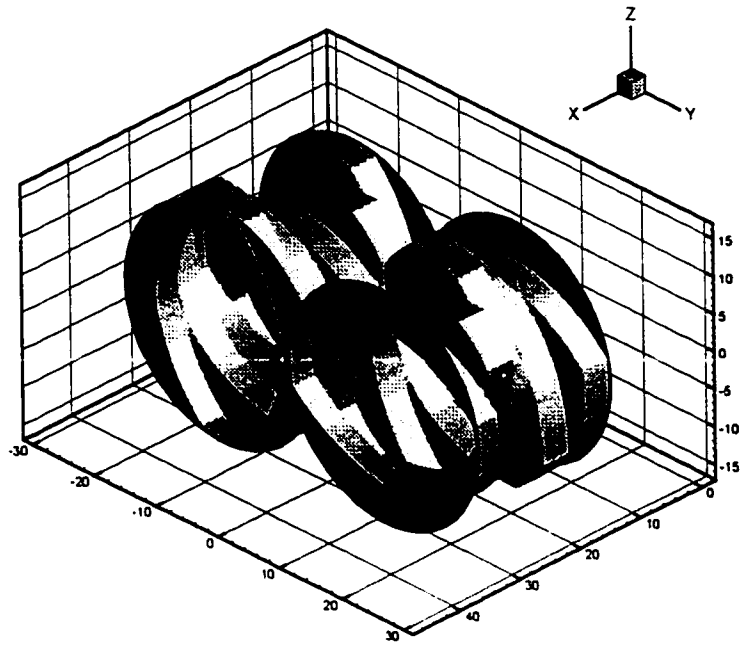

(a)

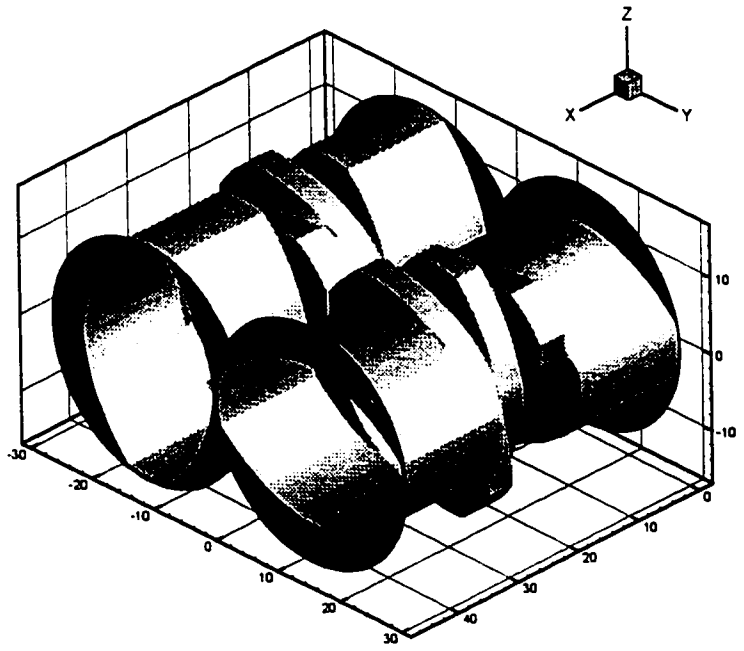

(b)

Figure 5.5 Kneading disc configuration and location of inlet/outlet boundary conditions. a) Inlet and outlet boundary condition at the ends of the kneading blocks; b) Inlet and outlet boundary condition at the ends of long elements.

Rpm	Flowrate (mL/s)	Type of elements before and after kneading blocks
60	5.0	60 mm long disc
60	5.0	20 mm forward conveying
60	8.5	60 mm long disc
60	8.5	20 mm forward conveying
0	5.0	60 mm long disc
60	0	60 mm long disc

Table 5.2. Experimental conditions

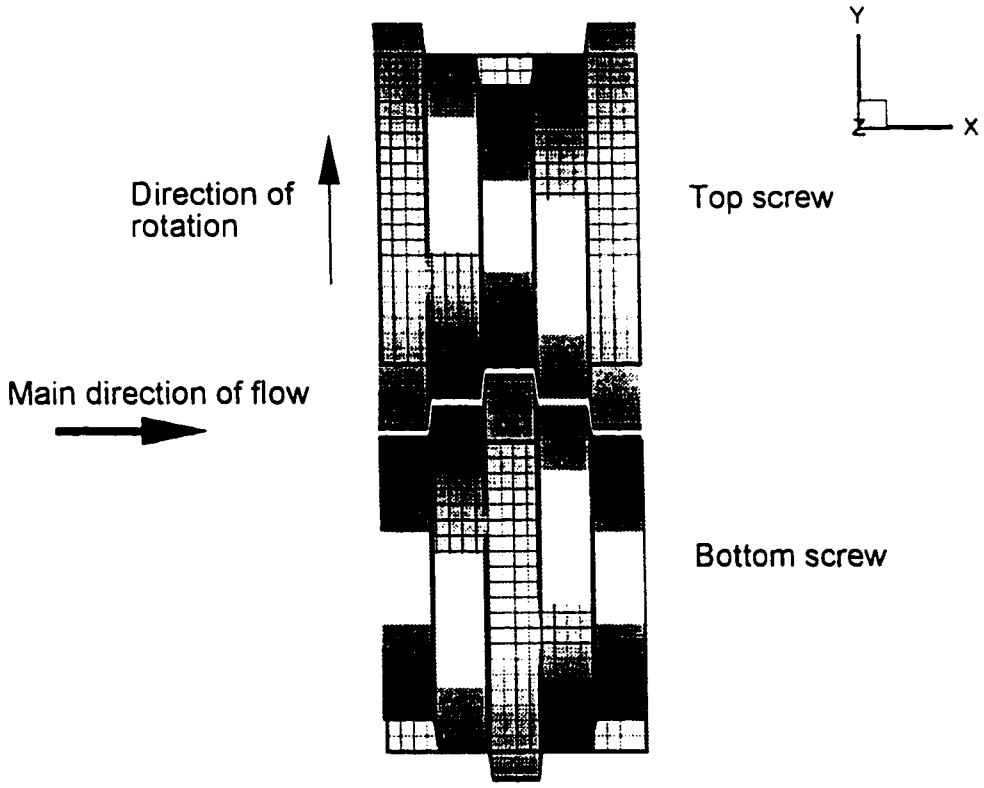

Figure 5.6. Schematic view of the data grids used for experimental and simulation results.

The magnitudes of the velocity vectors in Figure 5.7 show very good correlation between the experimental and simulation results. The axial component of velocity is larger in the bottom left part of the field where the axial gap is wider and material is being pushed by the bottom screw into the intermeshing region. The flow splits between the first and second discs. The part of the flow that goes into the first disc follows a circumferential type of motion with very little axial component, whereas the part of the flow that goes into the second disc is accelerated in the axial direction. The bottom left part of the field shows excellent qualitative and quantitative agreement. The top right part of the field does not show an agreement as good as that of the bottom left. Simulation results in the top left part of the field predict an axial component larger than the experimental measurements. These differences are attributed to the effect of the adjacent long elements in the experimental runs, which is discussed in Section 5.6.

Figure 5.8 shows the velocity vectors for the bottom screw. Experimental results show a channeling effect produced when flow being driven by an axial pressure gradient is forced into a pseudo-channel (see Figure 4.4), thus opposing the direction of rotation of the screws. This behavior was predicted by Bravo (1995) for specific combinations of pressure drop and rotation speed. Present simulation results do not predict this behavior under the experimental conditions. Simulation results predict velocity components following the rotation of the discs with a strong axial component at the locations where the axial gaps are the widest. Figures 5.9 and 5.10 are the contours of the u (axial) component of velocity and corroborate the observations made in Figure 5.7 where the agreement on the bottom left part of the field was good while the results on the top left showed significant differences. Figure 5.9 demonstrates the presence of the maximum axial components located at the widest axial gaps and the minimum axial component located near the discs, which actually present an obstacle to the flow. Very low axial components are also present at the top of the field due to the proximity of the stationary barrel. Figures 5.11 and 5.12 display the u component of velocity contours for the bottom screw. The order of magnitude of the predicted velocities is in good agreement with the experimental data measurements. There are noticeable differences between simulation results in Figure 5.11 and experimental results in Figure 5.12 at the top left part of the field. Figures 5.13 and 5.14 show the v component contours

obtained via simulation and experimentally with good agreement. Both simulation and experimental results show a velocity magnitude of approximately 0.05 m/s around the discs, with a decreasing gradient where the fluid approaches the barrel walls. Figures 5.15 and 5.16 are the v velocity contours for the bottom screw. Simulation results consistently predict the largest v components of velocity near the discs. Experimental results in Figure 5.16 show the highest values of v around discs 1 and 2 but show very small values of v around disc 4 and 5.

Analysis and comparison between experimental and simulation results is complex with 2D plots. Extracting data from the 2D planes into a 1D form can facilitate the quantitative analysis of results on specific lines. Figure 5.17 shows the location of the data extraction lines. At the top screw, the extraction line is located at x=2.83 mm from the left edge, 2.87 mm $\leq$ y $\leq$ 26.08 mm , z=11 mm. 21 points were extracted from the 2D planes. For the bottom screw, the extraction line was located at x=10 mm, -26.08 mm $\leq$ y $\leq$ -2.96 mm , z=11 mm. Figure 5.18 shows the results obtained for the extracted data. The u component shows a maximum difference of 20% at a distance of 2.5 mm, whereas the maximum difference for the v component is less that 10%.. The trends observed on the experimental data are reproduced well for both u and v components.

Figures 5.19 and 5.20 are the velocity vector obtained via simulation using the boundary condition depicted in Figure 5.5a, and the experimental velocity vectors using conveying elements before and after the kneading blocks. Results show good qualitative agreement for the complete field. The conveying elements deployed before and after the kneading blocks guide the bulk of the flow into a helix-type of motion that is kept during the flow through the kneading blocks. This helix-type of motion creates uniformity in the flow field that is observed in the experimental results. The u component contours in Figures 5.21 and 5.22 show qualitative agreement between experimental and simulation values. The minimum values of u are located near the discs as in the previous cases studied. The maximum values of u are located at the bottom left and top right where the axial gaps are wider. Figures 5.23 and 5.24 show very good qualitative and quantitative agreement for the v component of velocity, as do Figures 5.25 and 5.26. However, Figure 5.27, showing the simulation results for the v component of velocity are not in good agreement with the experimentally measured v component presented in Figure 5.28. A set of data was extracted

from experimental and simulation cases according to the diagram in Figure 5.17. The results for the extracted data are shown in Figure 5 29. There is a pronounced difference between experimental and simulation results for both u and v components, although the prediction of the experimental trend is still reasonable. The maximum differences for the u component are around 57%, whereas for the v component the maximum difference is 28%.

For the following set of runs, the rotating speed was kept at 60 rpm while the flow rate was increased from 5 mL/s to 8.5 mL/s. Figures 5.30 and 5.31 show the comparisons between experimental and simulation velocity vectors under the previously described conditions using the long straight element before and after the kneading blocks. Results show a strong disagreement between experimental and simulation results. The experiment data shows a split in the flow field with part of the flow that enters the kneading disc region moving in the positive direction of y while part moves in the negative direction of y, as observed in Figure 5.30. The numerical model does not predict this behavior. It is presumed that the assumption of creeping flow under the higher flow rate is not valid, and that inertial terms play an important role in the fluid dynamics under these conditions. In general, all the results for the flow rate 8.5 mL/s show a poor correlation between experiments and simulation, as shown in Figures 5.30 to 5.39. Figure 5.40 show a comparison for data extracted at x=2.83 mm, where the strong differences between simulation and experimental results can be quantified. The most interesting results are obtained for the flow 8.5 mL/s using the conveying elements before and after the kneading blocks. The qualitative agreement between experimental and simulation results is surprisingly better than for the case with the long straight elements. Again, the helix-type of motion created by the conveying elements is not altered drastically by the kneading blocks. On the contrary, the kneading blocks tend to maintain the same type of ordered helix-type motion. The agreement is not as good as for the case of 5 mL/s. Figures 5.41 to 5.50 show the velocity vectors and the u and v contour plots for the case 8.5 mL/s, 60 rpm using conveying elements before and after the kneading blocks for the experimental runs. The comparison between experimental and simulation results in Figure 5.51 shows a good prediction of the trends. The quantitative agreement is very good for the u component of velocity, and reasonably good for the v component.

Two runs were done to study the limiting cases of no rotation (0 rpm) and no flow (0 flow rate). The case of 0 rpm has a predictable behavior. The flow follows the pseudo-helix angle of the kneading blocks. The comparison between experimental and simulation velocity vectors is presented in Figures 5.52 and 5.53. A comparison of extracted data is shown in Figures 5.54 and 5.55 with very good prediction of the experimental trend, but with some significant quantitative differences. The case of no flow rate and rotation speed of 60 rpm is also predictable, with a predominance of circumferential flow following the rotation of the screws. Results for the 0 flow rate condition are presented in Figures 5.56 and 5.57 for the velocity vectors. Figures 5.58 and 5.59 show the extracted values at the top and bottom screws. A comparison was made between the simulation results obtained with and without the long disc elements before and after the kneading blocks. Results show a moderate effect on the magnitude of the u component near the intermeshing region at the entrance of the kneading blocks. In general, the effect of the long elements in the flow patterns was very significant in the experimental results. In the simulation results the effect of the long elements on the flow patterns was not as intense as in the experiments due to the assumption of creeping flow.

A comparison was made between the simulation results obtained with the two boundary conditions used. Results show significant differences in the magnitude of the axial component of velocity, especially near the intermeshing region. However, the velocity profiles predicted with the two boundary conditions show similar patterns.

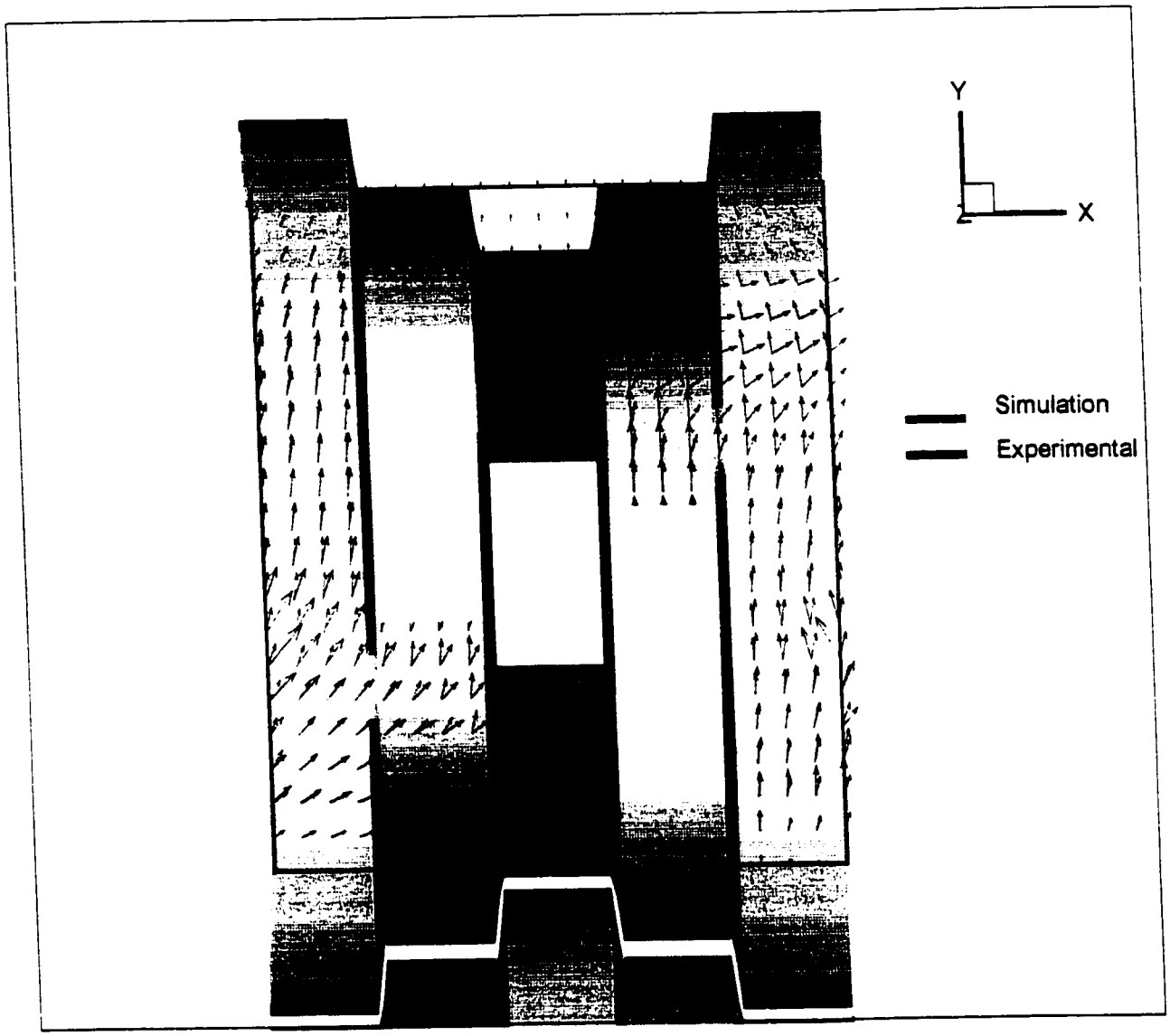

Figure 5.7. Velocity vectors obtained experimentally and via simulation. Top screw, 60 rpm, 5 mL/s. Long straight elements are deployed before and after the kneading blocks.

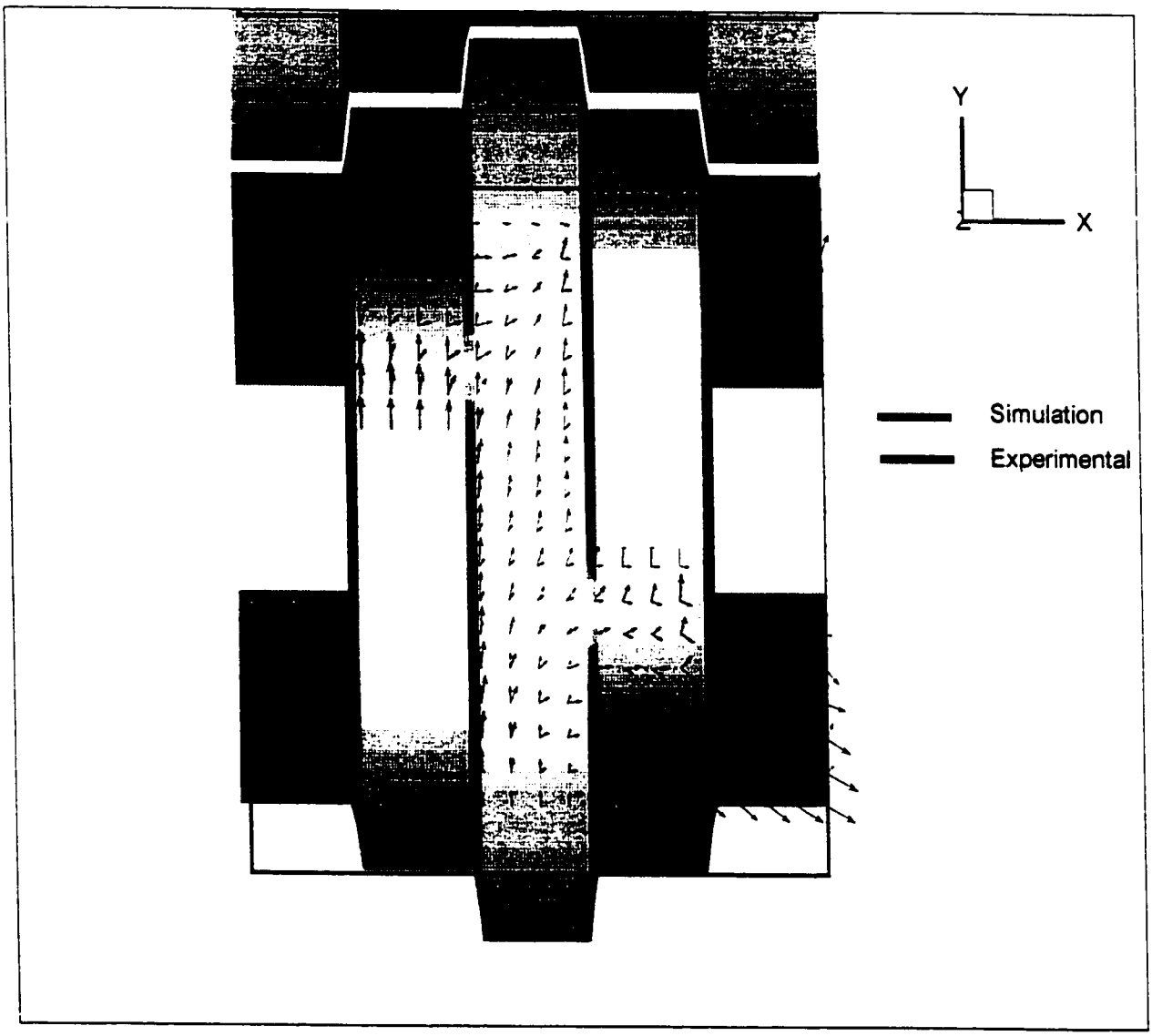

Figure 5.8. Velocity vectors obtained experimentally and via simulation. Bottom screw, 60 rpm, 5 mL/s. Long straight elements are deployed before and after the kneading blocks.

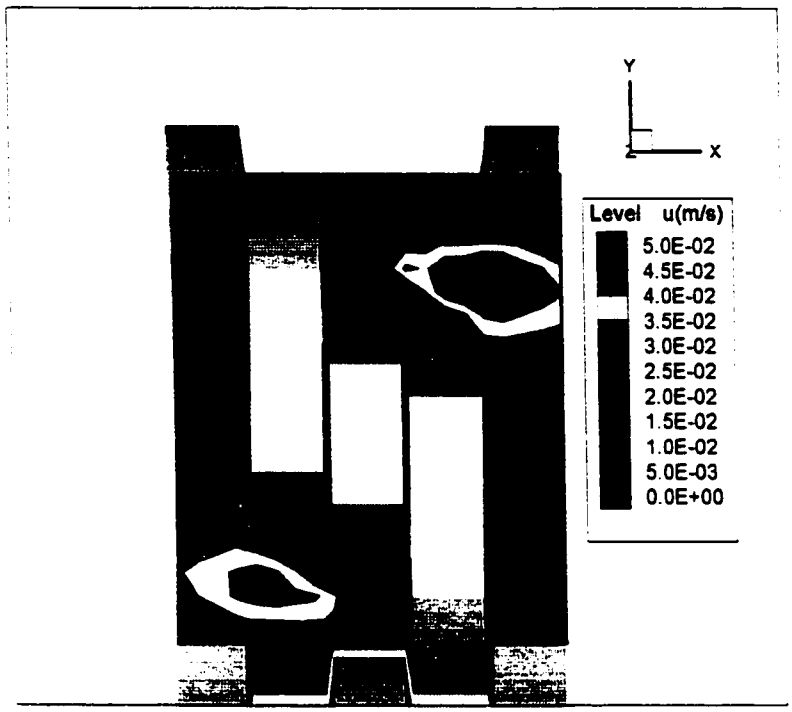

Figure 5.9. Contours of the u-component of velocity obtained via simulation. Top screw, 60 rpm, 5 mL/s. Long straight elements are deployed before and after the kneading blocks.

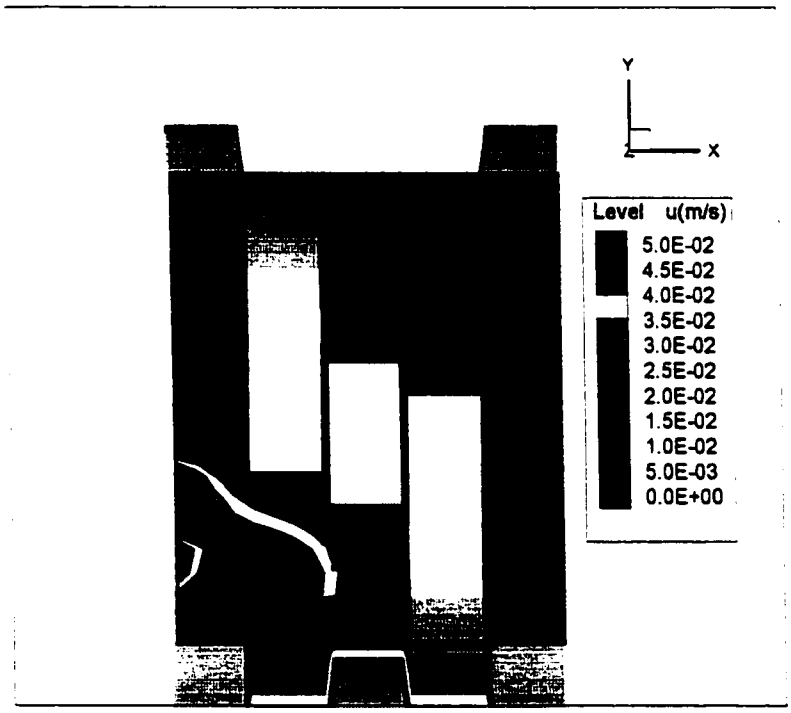

Figure 5.10. Contours of the u-component of velocity obtained experimentally. Top screw, 60 rpm, 5 mL/s. Long straight elements are deployed before and after the kneading blocks.

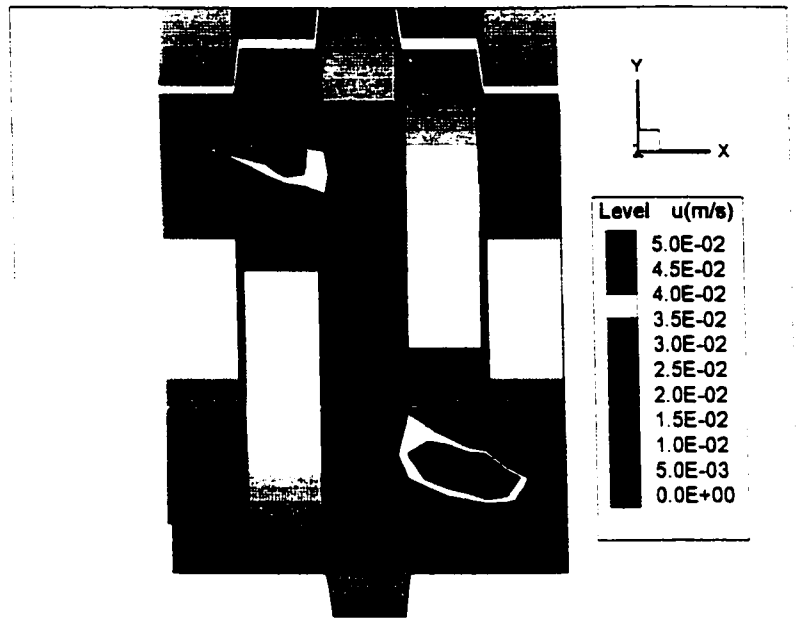

Figure 5.11. Contours of the u-component of velocity obtained via simulation. Bottom screw, 60 rpm, 5 mL/s. Long straight elements are deployed before and after the kneading blocks.

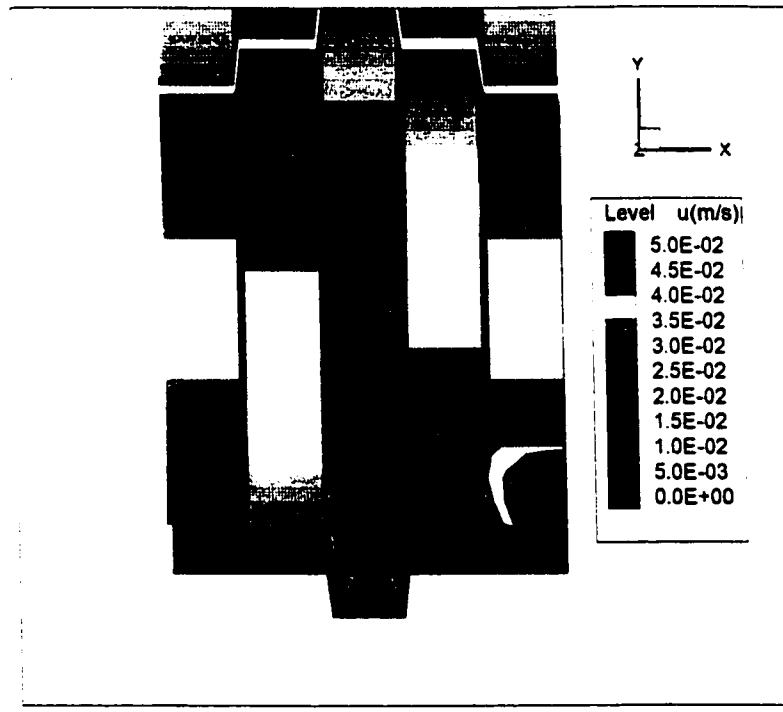

Figure 5.12. Contours of the u-component of velocity obtained experimentally. Bottom screw, 60 rpm, 5 mL/s. Long straight elements are deployed before and after the kneading blocks.

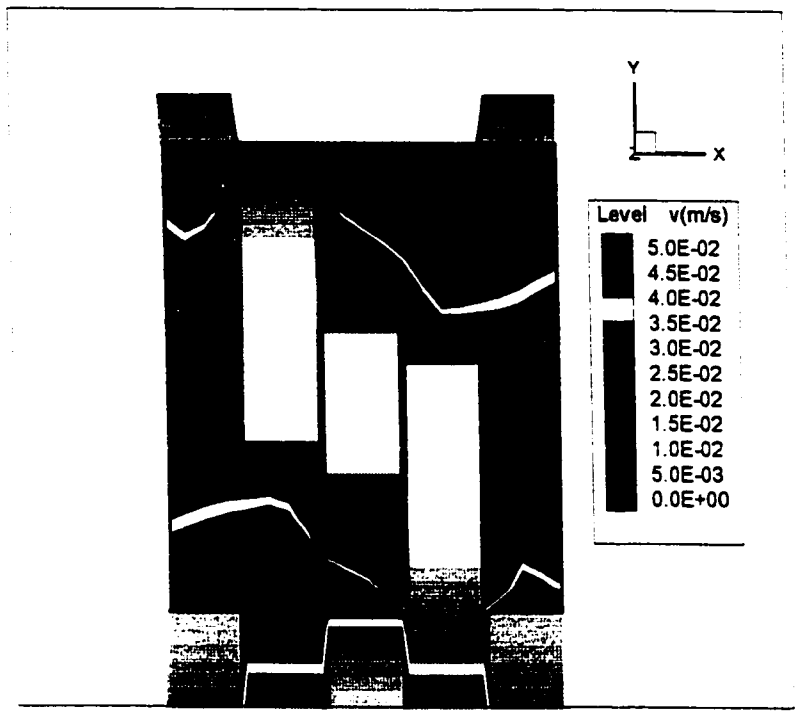

Figure 5.13. Contours of the v-component of velocity obtained via simulation. Top screw, 60 rpm, 5 mL/s. Long straight elements are deployed before and after the kneading blocks.

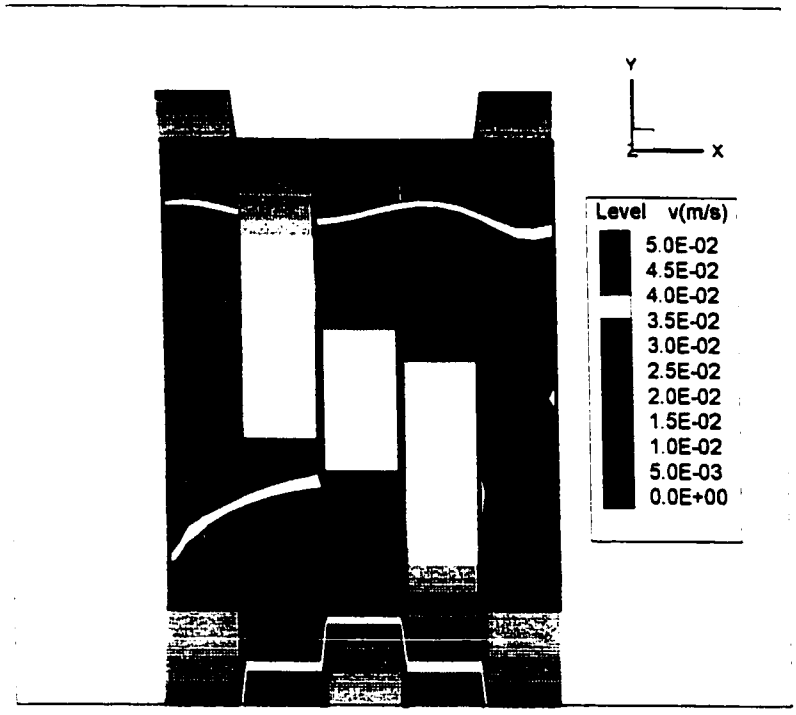

Figure 5.14. Contours of the v-component of velocity obtained experimentally. Top screw, 60 rpm, 5 mL/s. Long straight elements are deployed before and after the kneading blocks.

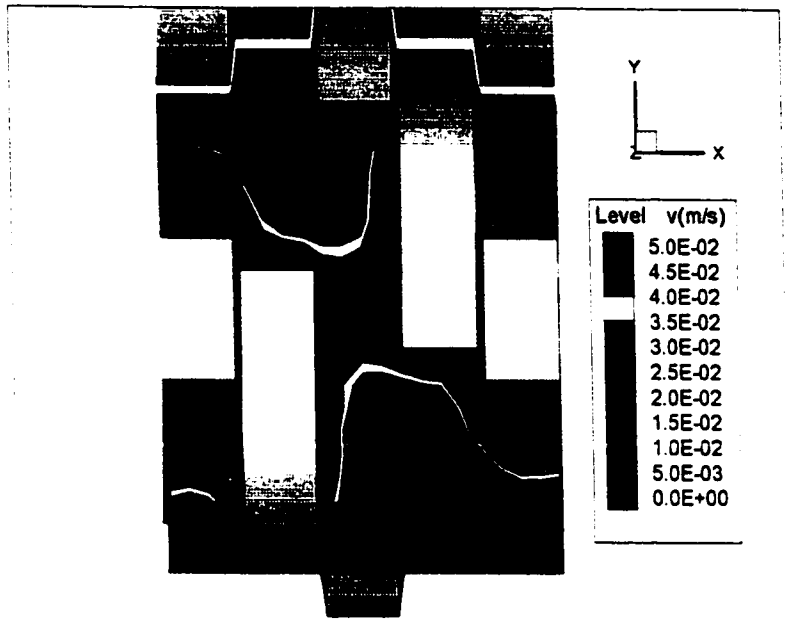

Figure 5.15. Contours of the v-component of velocity obtained via simulation. Bottom screw, 60 rpm, 5 mL/s. Long straight elements are deployed before and after the kneading blocks.

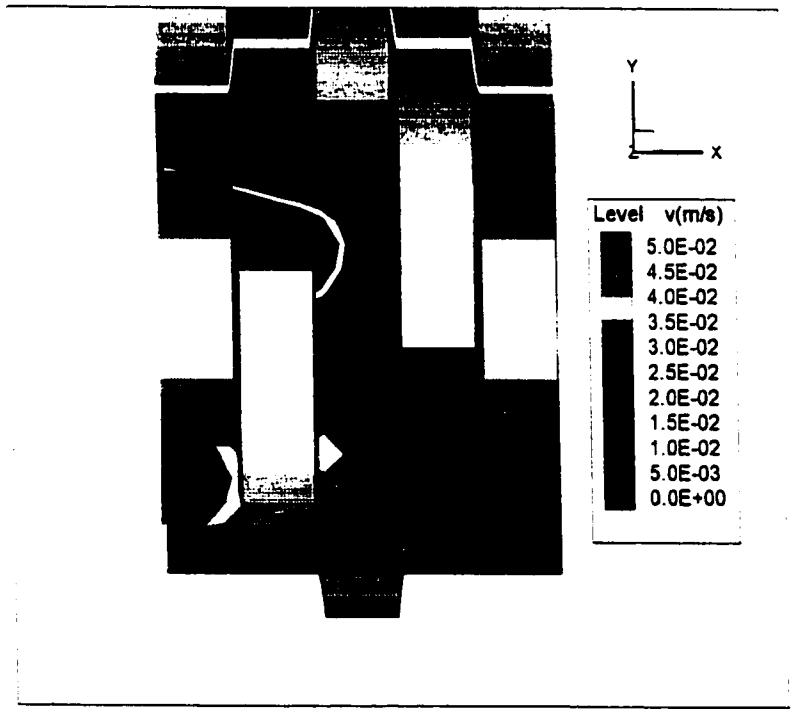

Figure 5.16. Contours of the v-component of velocity obtained experimentally. Bottom screw, 60 rpm, 5 mL/s. Long straight elements are deployed before and after the kneading blocks.

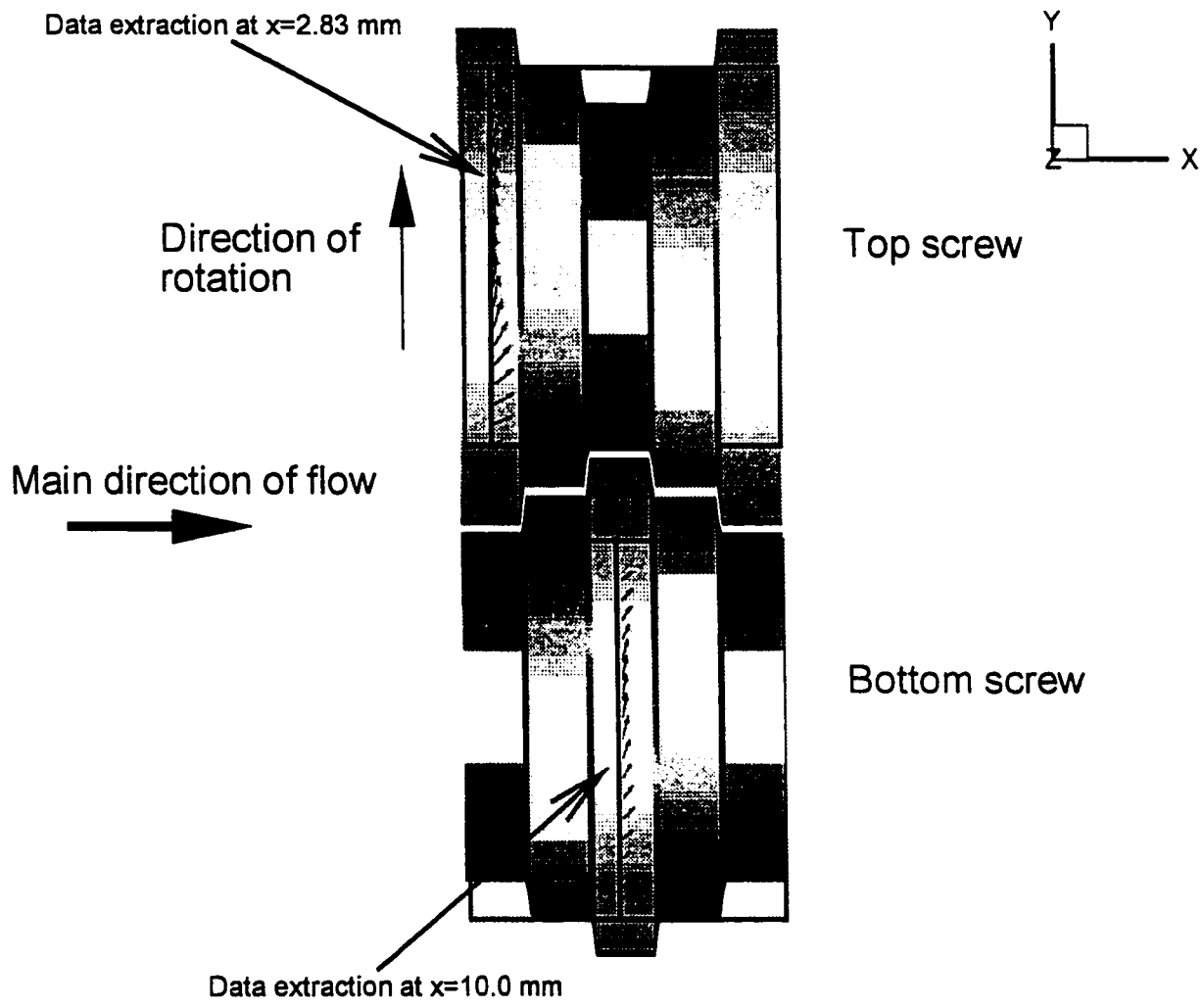

Figure 5.17. Location of the data extraction zone for the comparison of experimental and simulation velocity components. At the top screw the extraction line is at x=2.83 mm, y from 2.87mm to 26.08 mm and z=11.0 mm. At the bottom screw the extraction line is at x=10 mm , y from –26.08 to –2.96 mm and z=11.0 mm .

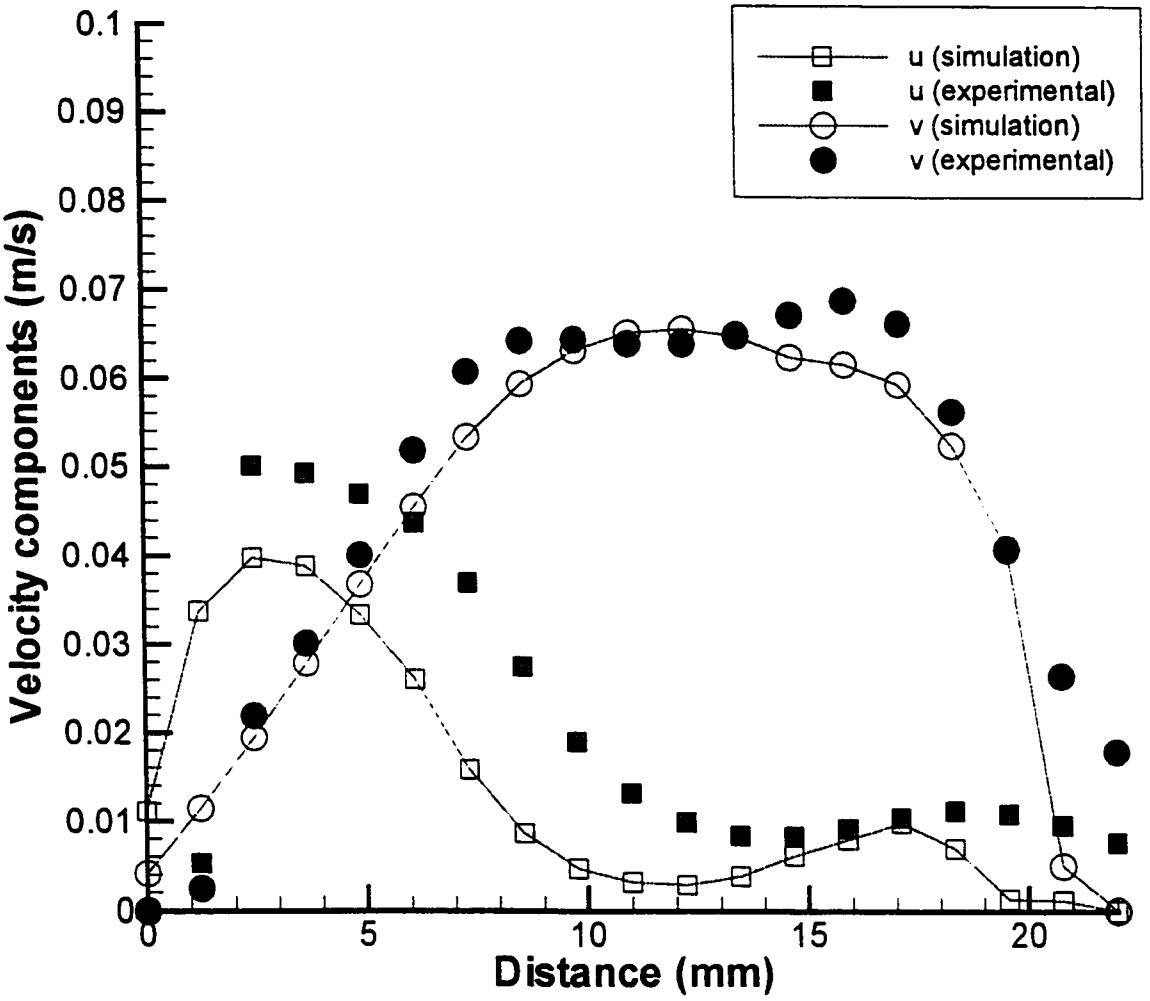

Figure 5.18. Comparison between simulation and experimental u and v components of velocity at x= 2.836 mm. Top screw, 60 rpm, 5 mL/s. Long straight elements are deployed before and after the kneading blocks.

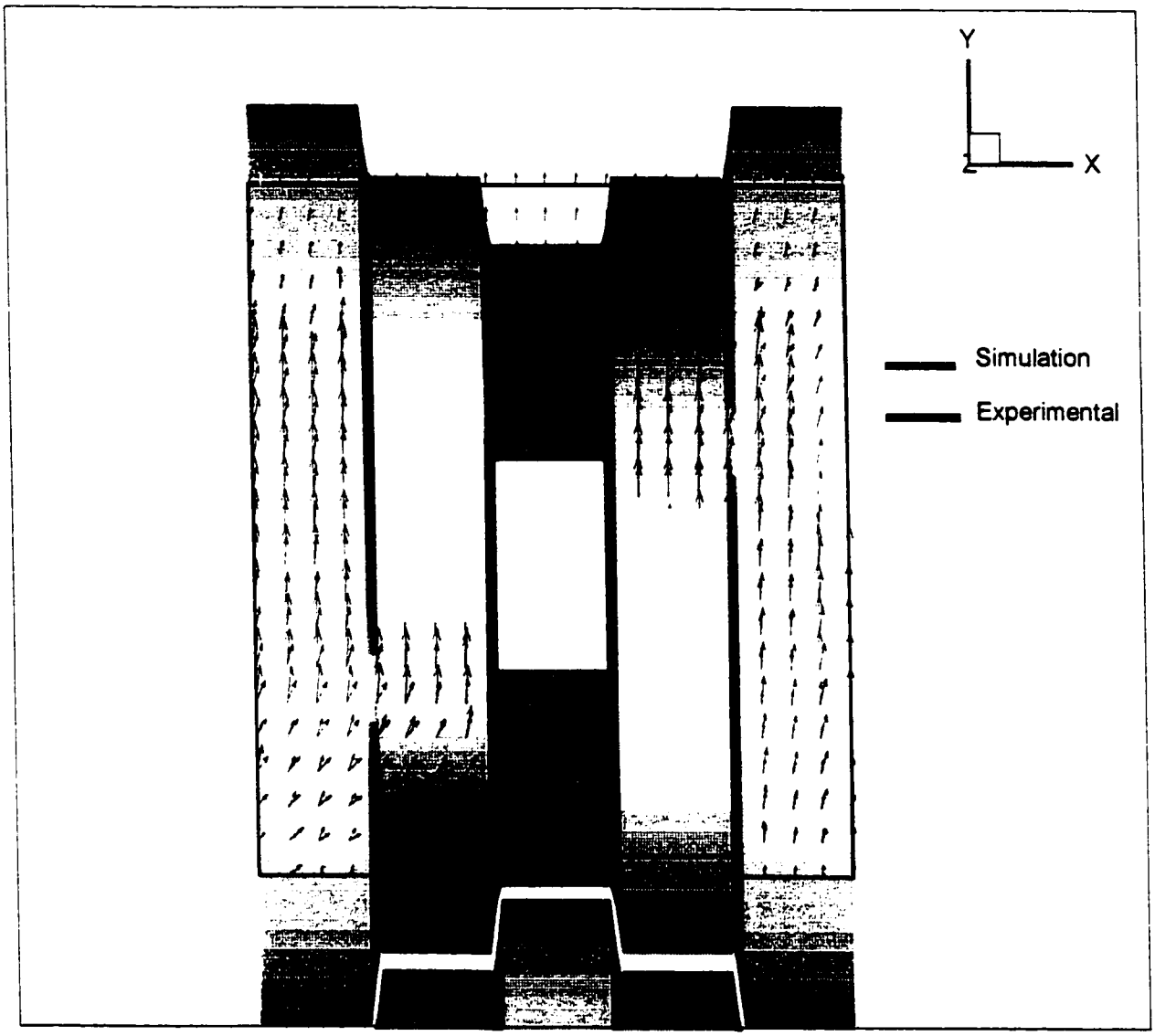

Figure 5.19. Velocity vectors obtained experimentally and via simulation. Top screw, 60 rpm, 5 mL/s. Conveying elements are deployed before and after the kneading blocks for the experimental runs. No elements deployed before and after the kneading blocks for simulations.

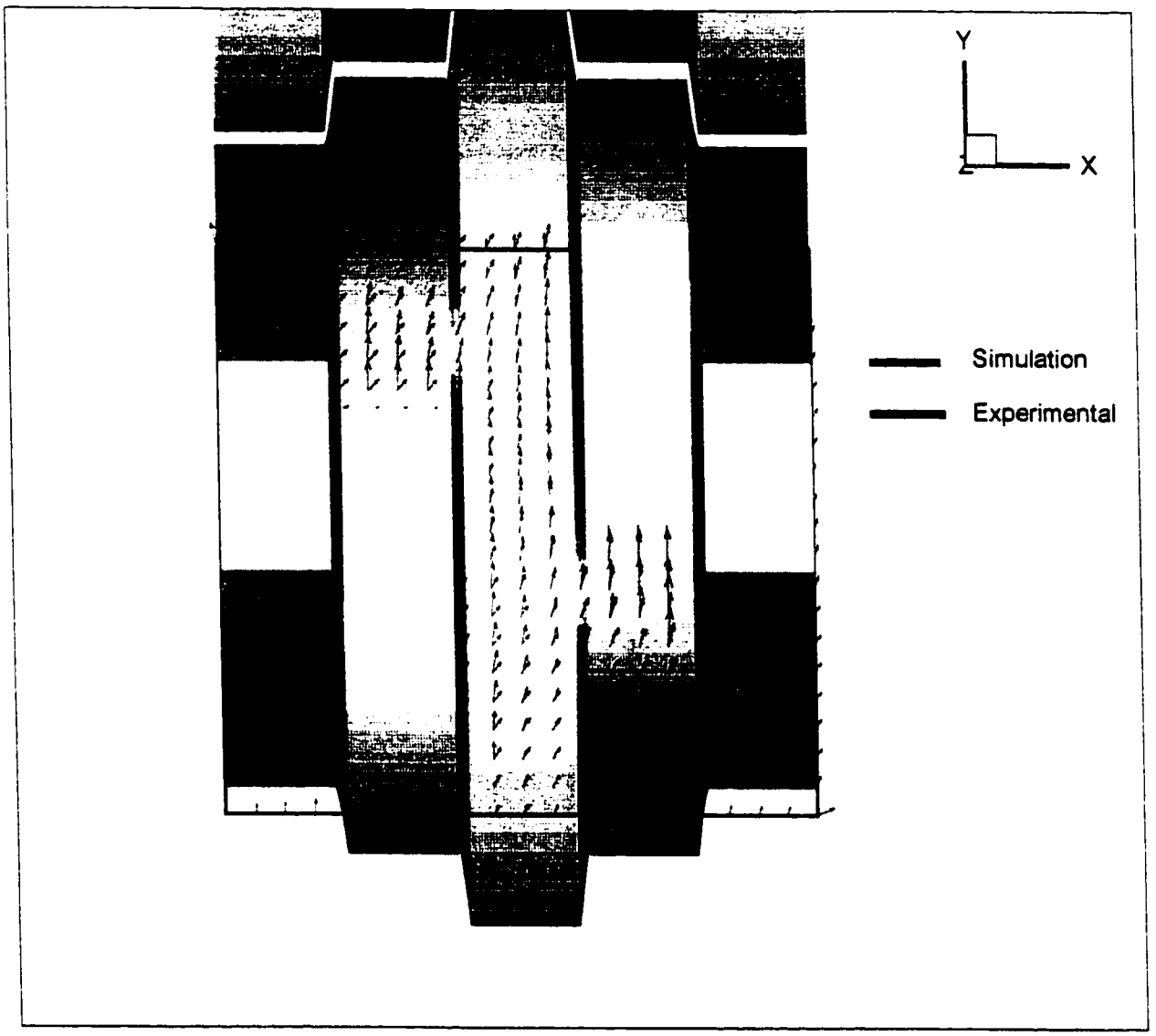

Figure 5.20. Velocity vectors obtained experimentally and via simulation. Bottom screw, 60 rpm, 5 mL/s. Conveying elements are deployed before and after the kneading blocks. No elements deployed before and after the kneading blocks for simulations.

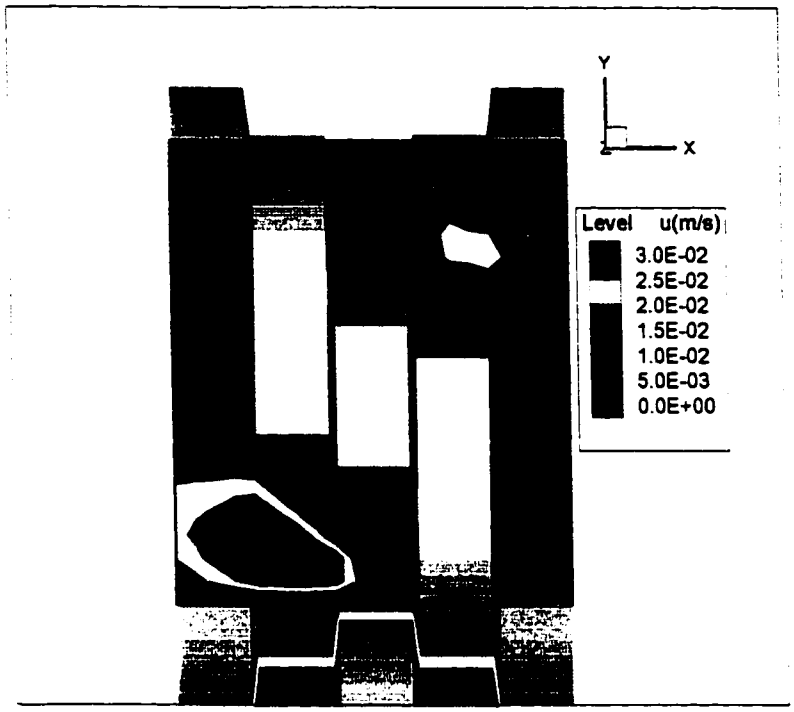

Figure 5.21. Contours of the u-component of velocity obtained via simulation. Top screw, 60 rpm, 5 mL/s. No elements deployed before and after the kneading blocks.

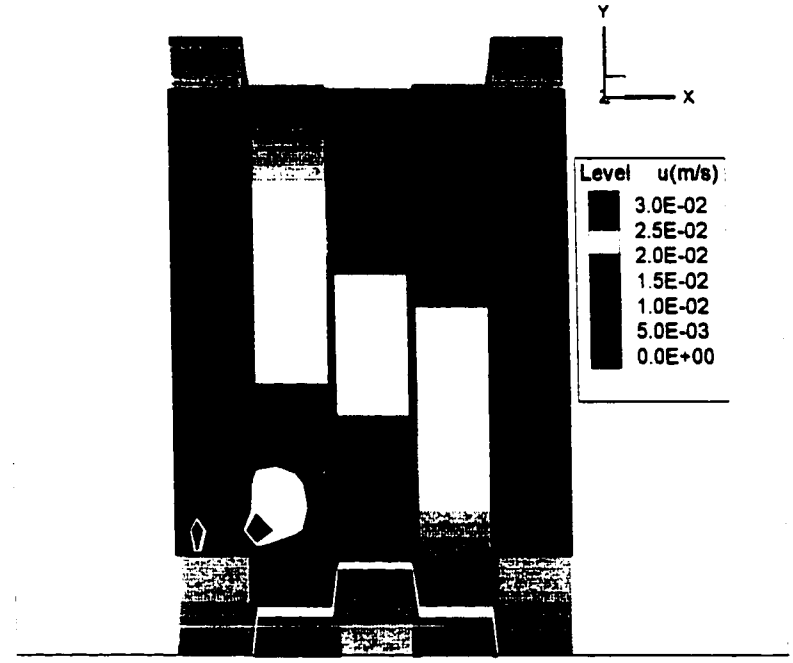

Figure 5.22. Contours of the u-component of velocity obtained experimentally. Top screw, 60 rpm, 5 mL/s. Conveying elements are deployed before and after the kneading blocks.

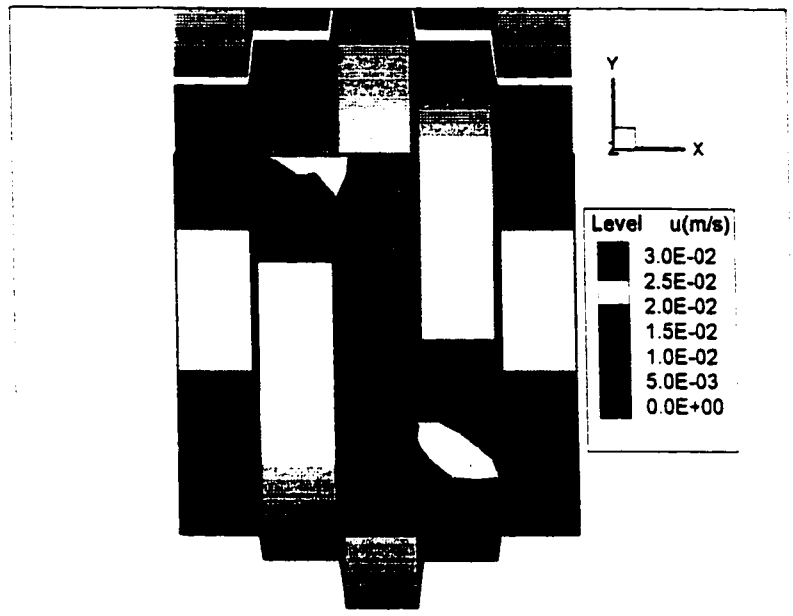

Figure 5.23. Contours of the u-component of velocity obtained via simulation. Bottom screw, 60 rpm, 5 mL/s. No elements deployed before and after the kneading blocks.

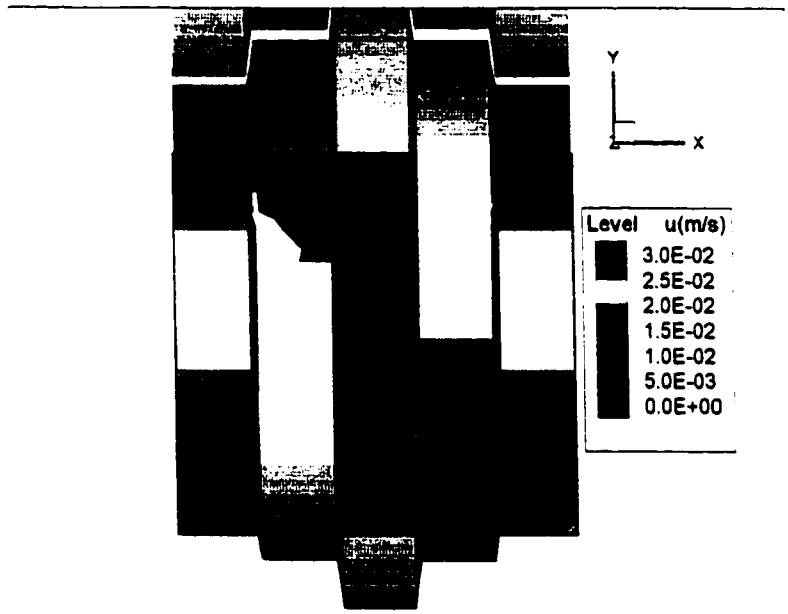

Figure 5.24. Contours of the u-component of velocity obtained experimentally. Bottom screw, 60 rpm, 5 mL/s. Conveying elements are deployed before and after the kneading blocks.

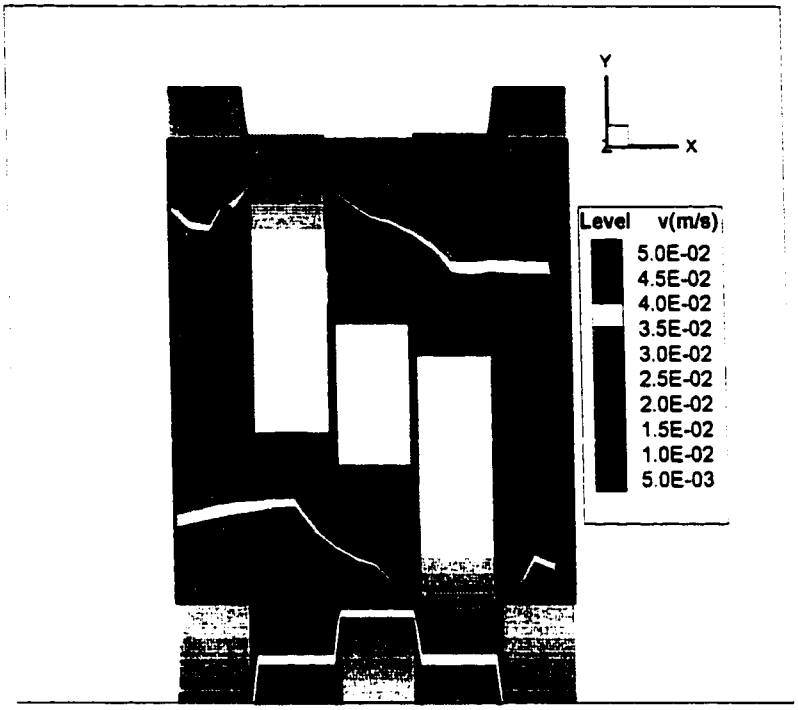

Figure 5.25. Contours of the v-component of velocity obtained via simulation. Top screw, 60 rpm, 5 mL/s. No elements deployed before and after the kneading blocks.

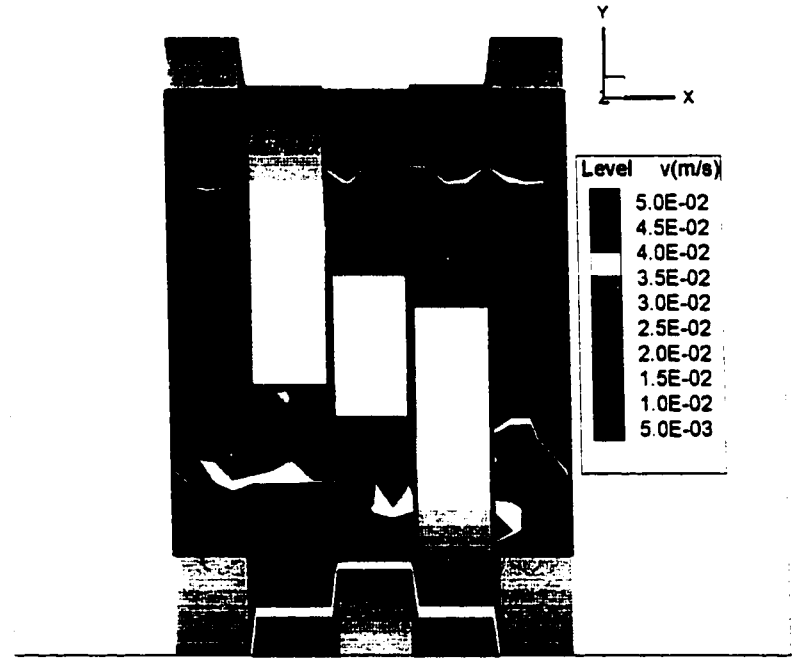

Figure 5.26. Contours of the v-component of velocity obtained experimentally. Top screw, 60 rpm, 5 mL/s. Conveying elements are deployed before and after the kneading blocks.

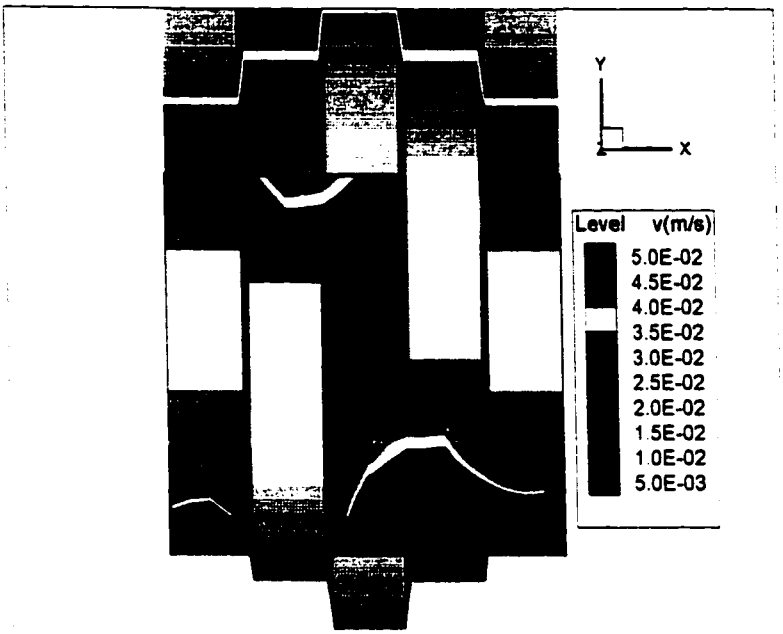

Figure 5.27. Contours of the v-component of velocity obtained via simulation. Bottom screw, 60 rpm, 5 mL/s. No elements deployed before and after the kneading blocks.

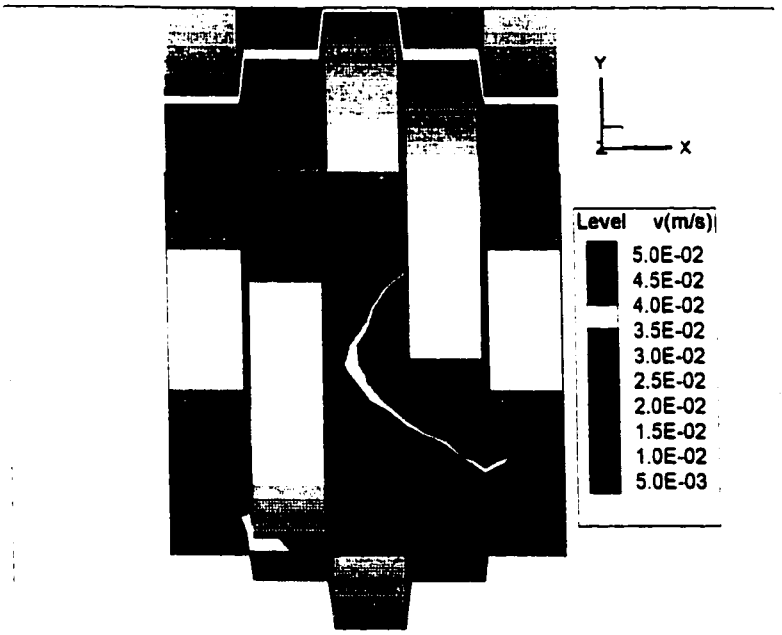

Figure 5.28. Contours of the v-component of velocity obtained experimentally. Bottom screw, 60 rpm, 5 mL/s. Conveying elements are deployed before and after the kneading blocks.

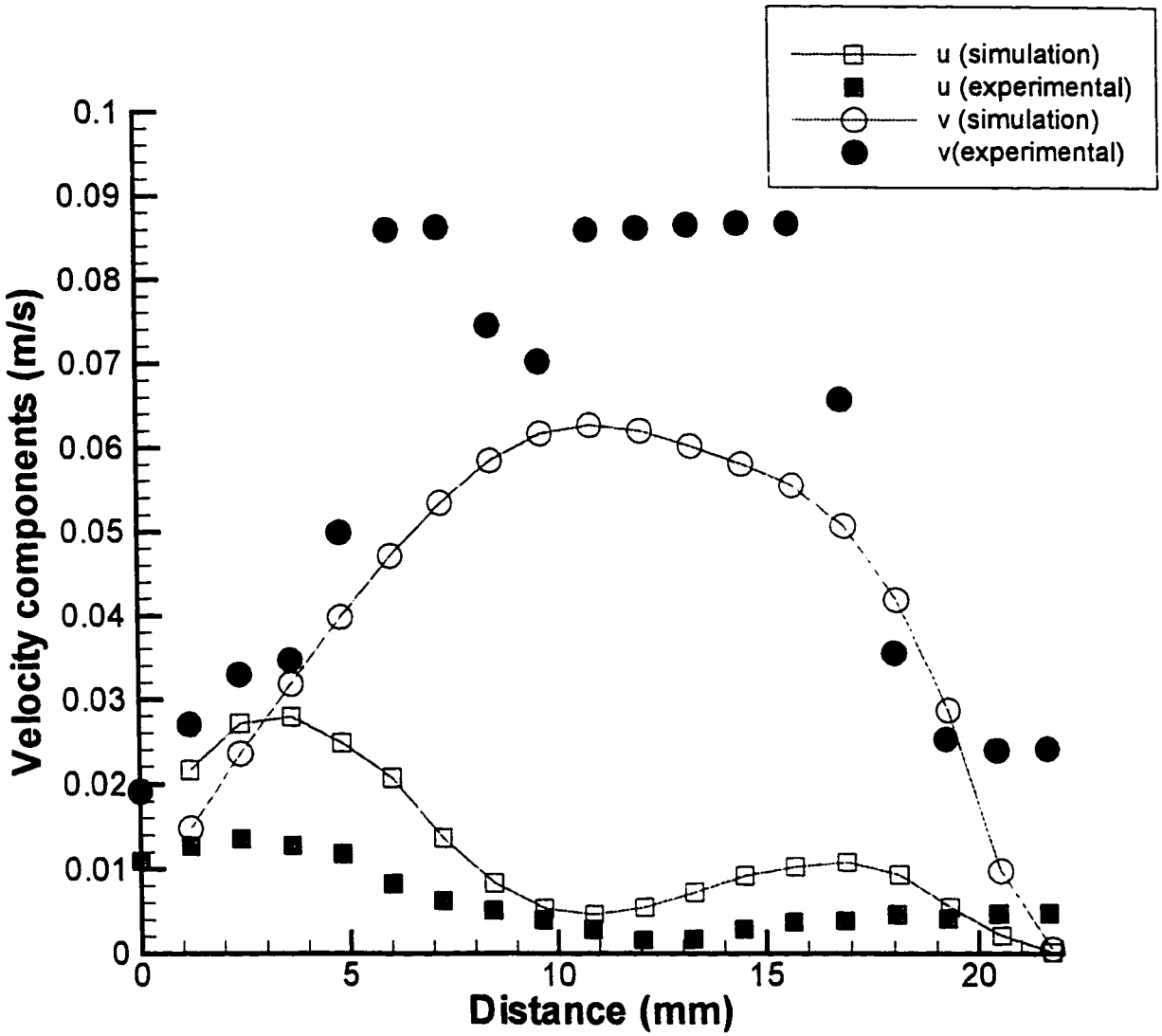

Figure 5.29. Comparison between simulation and experimental u and v components of velocity at x= 2.836 mm. Top screw, 60 rpm, 5 mL/s. Conveying elements are deployed before and after the kneading blocks for the experimental runs.

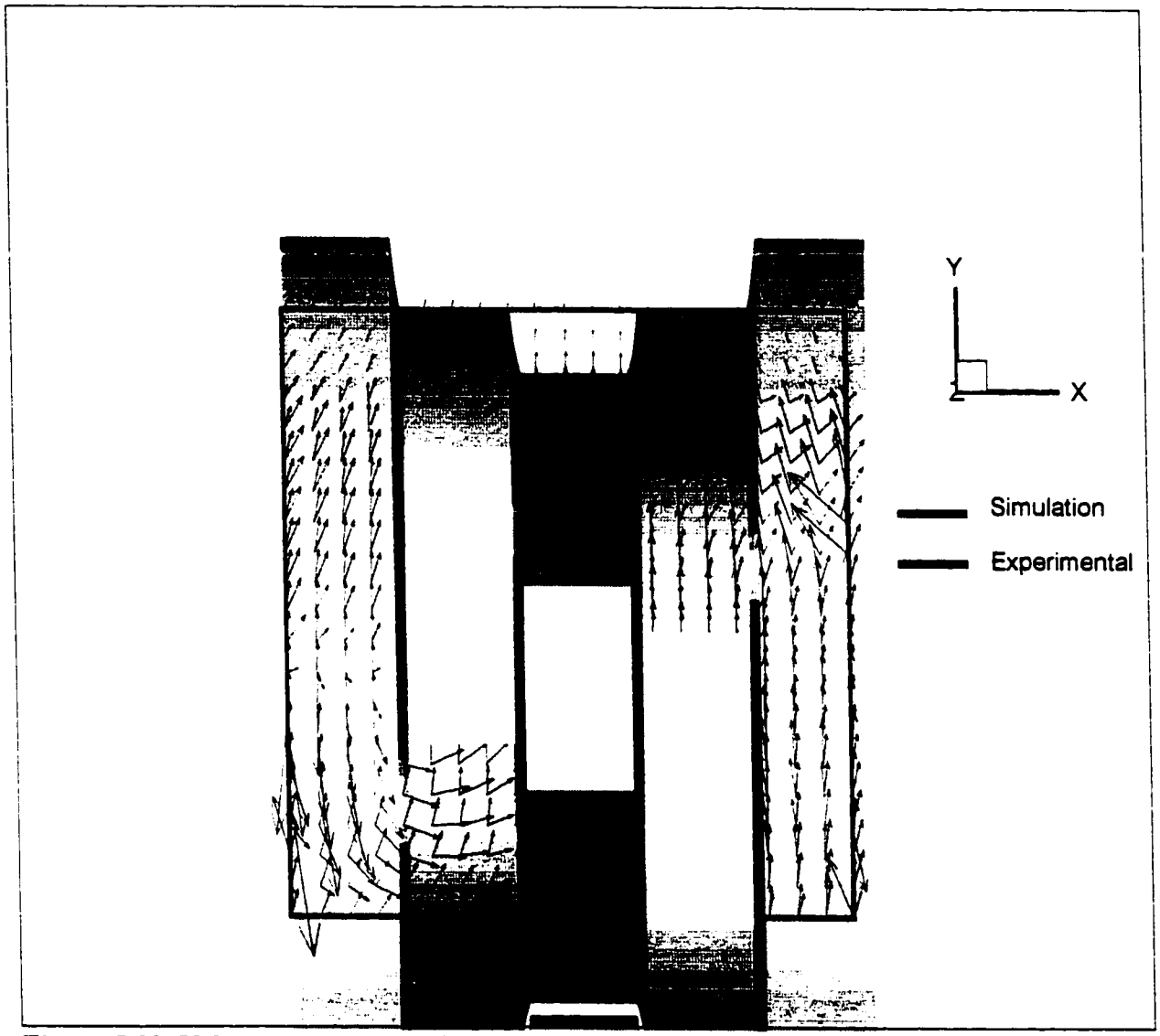

Figure 5.30. Velocity vectors obtained experimentally and via simulation. Top screw, 60 rpm, 8.5 mL/s. Long straight elements are deployed before and after the kneading blocks.

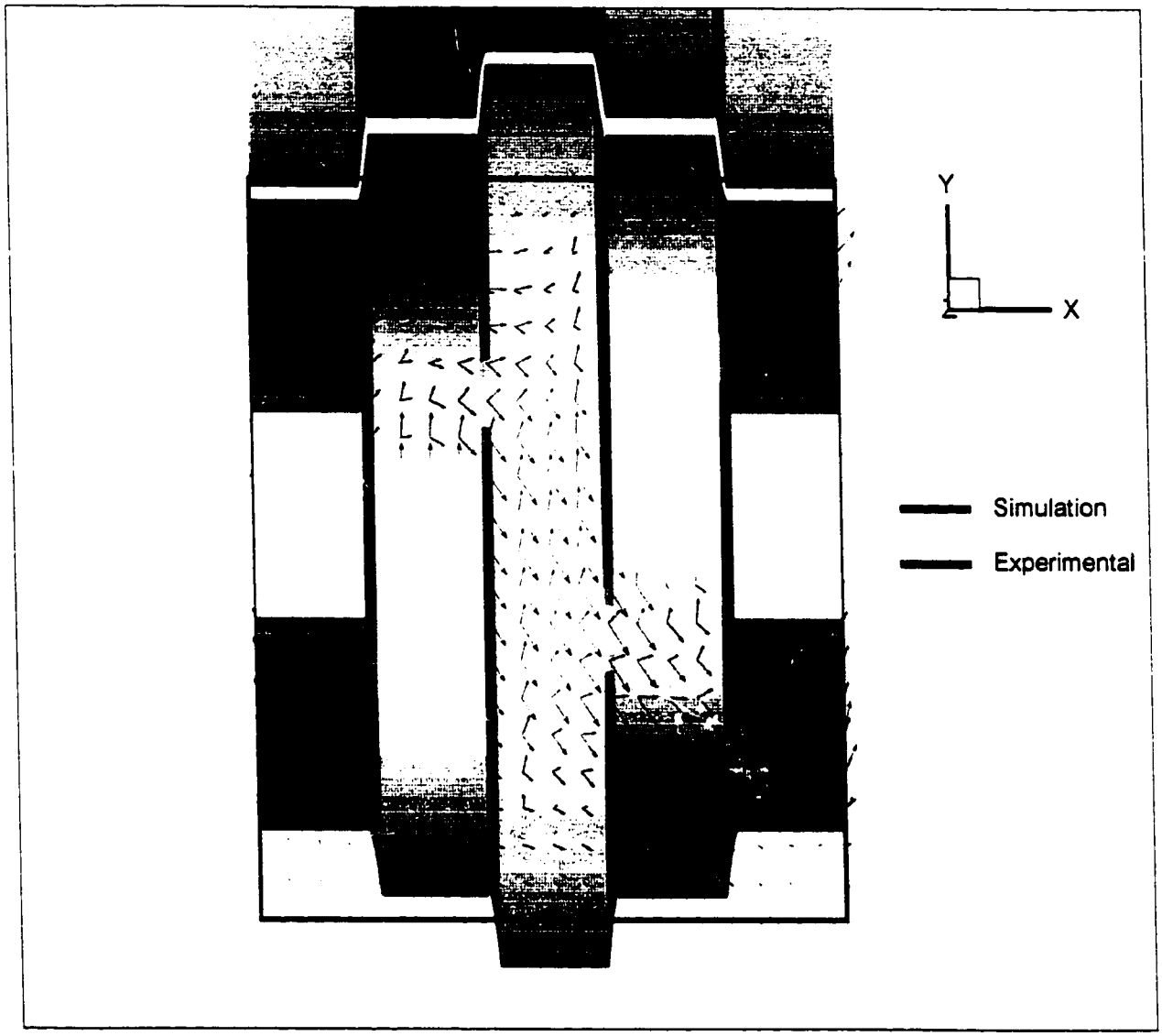

Figure 5.31. Velocity vectors obtained experimentally and via simulation. Bottom screw, 60 rpm, 8.5 mL/s. Long straight elements are deployed before and after the kneading blocks.

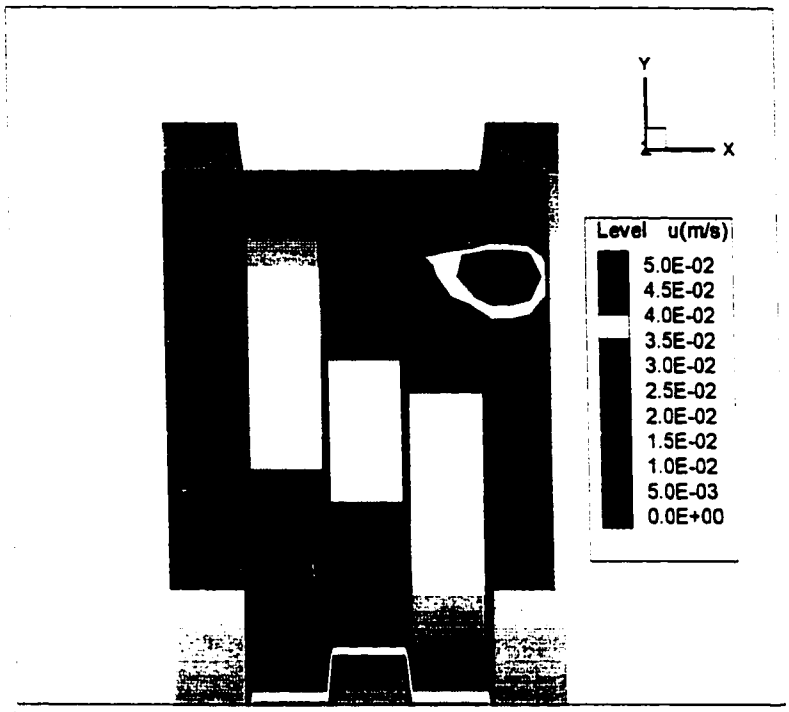

Figure 5.32. Contours of the u-component of velocity obtained via simulation. Top screw, 60 rpm, 8.5 mL/s. Long straight elements are deployed before and after the kneading blocks.

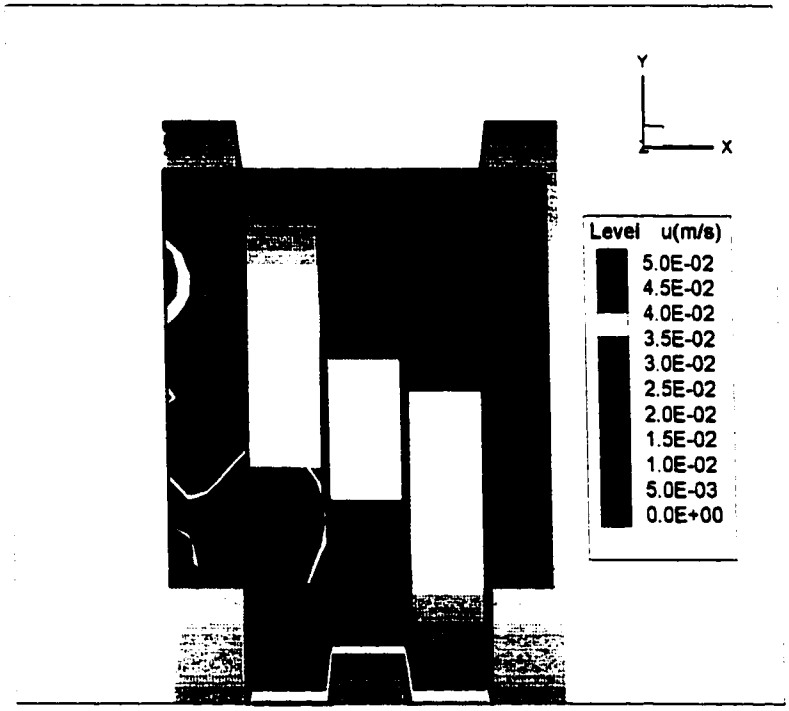

Figure 5.33. Contours of the u-component of velocity obtained experimentally. Top screw, 60 rpm, 8.5 mL/s. Long straight elements are deployed before and after the kneading blocks.

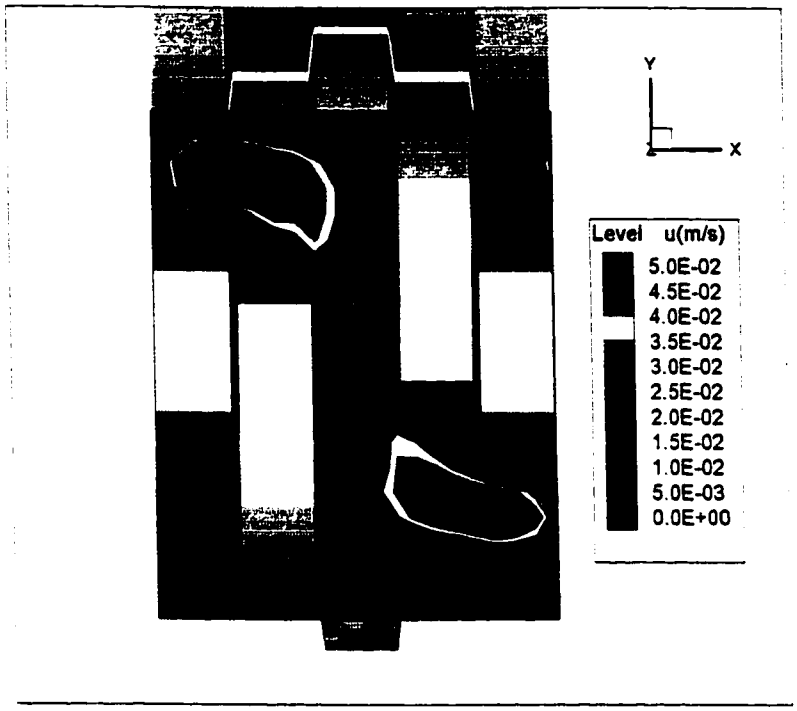

Figure 5.34. Contours of the u-component of velocity obtained via simulation. Bottom screw, 60 rpm, 8.5 mL/s. Long straight elements are deployed before and after the kneading blocks.

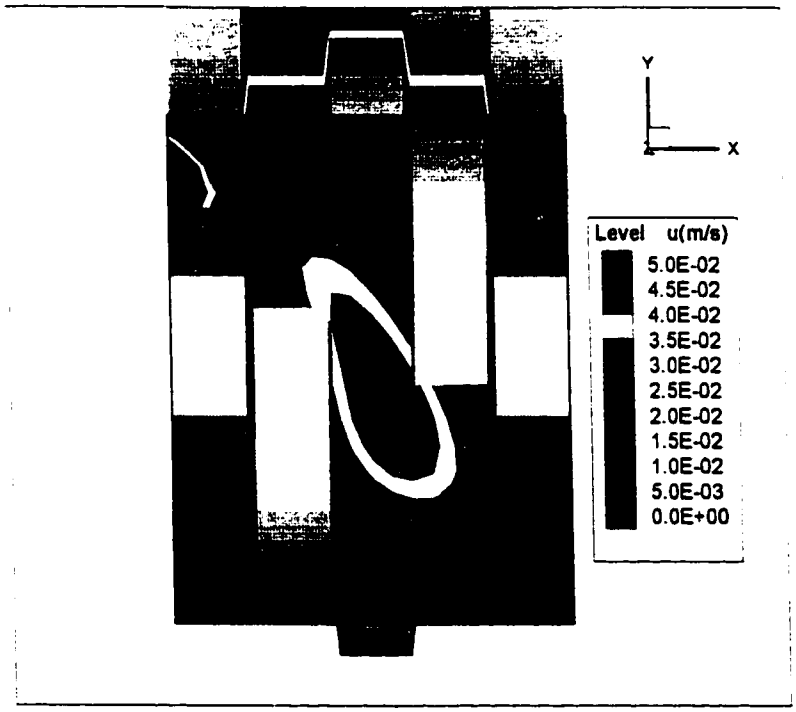

Figure 5.35. Contours of the u-component of velocity obtained experimentally. Bottom screw, 60 rpm, 8.5 mL/s. Long straight elements are deployed before and after the kneading blocks.

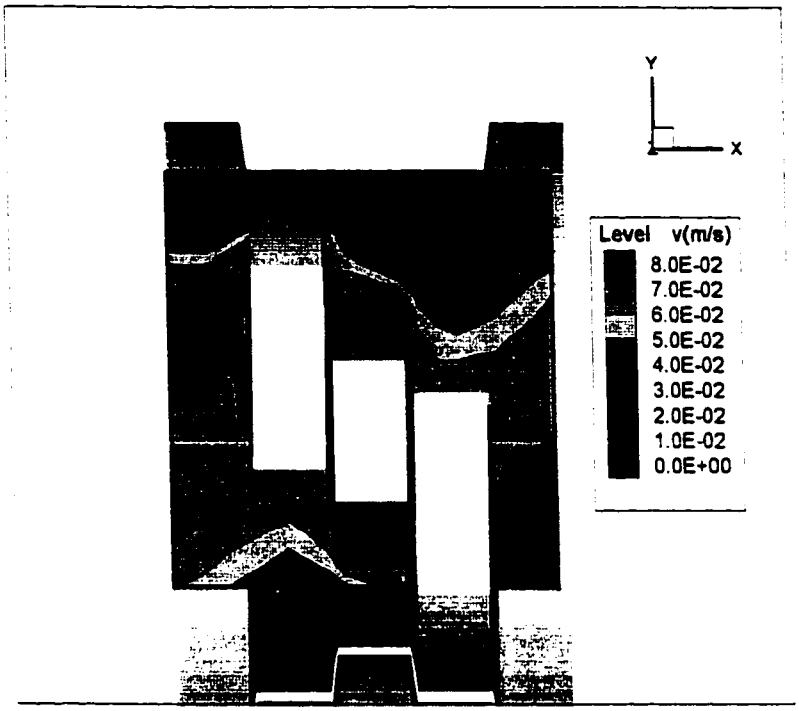

Figure 5.36. Contours of the v-component of velocity obtained via simulation. Top screw, 60 rpm, 8.5 mL/s. Long straight elements are deployed before and after the kneading blocks.

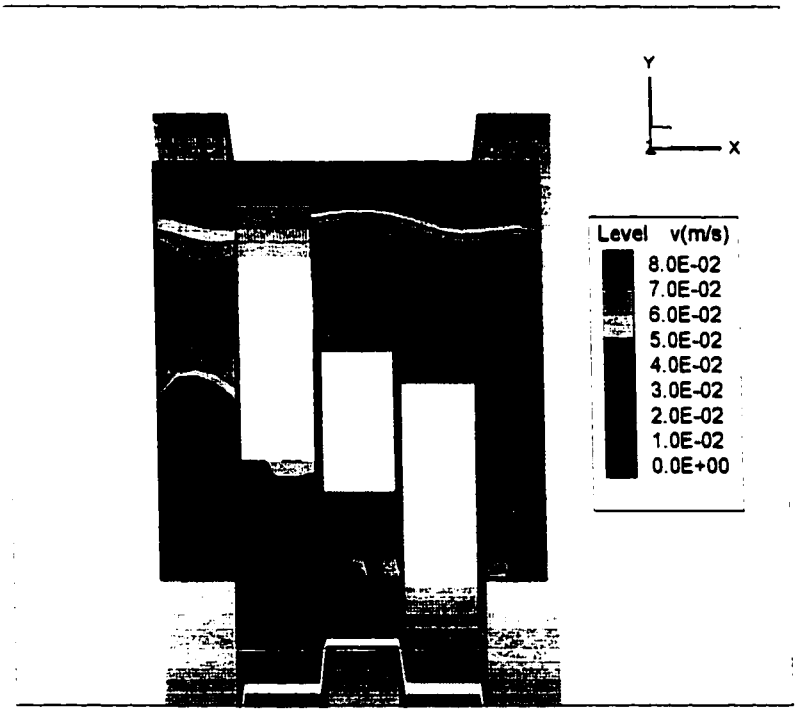

Figure 5.37. Contours of the v-component of velocity obtained experimentally. Top screw, 60 rpm, 8.5 mL/s. Long straight elements are deployed before and after the kneading blocks.

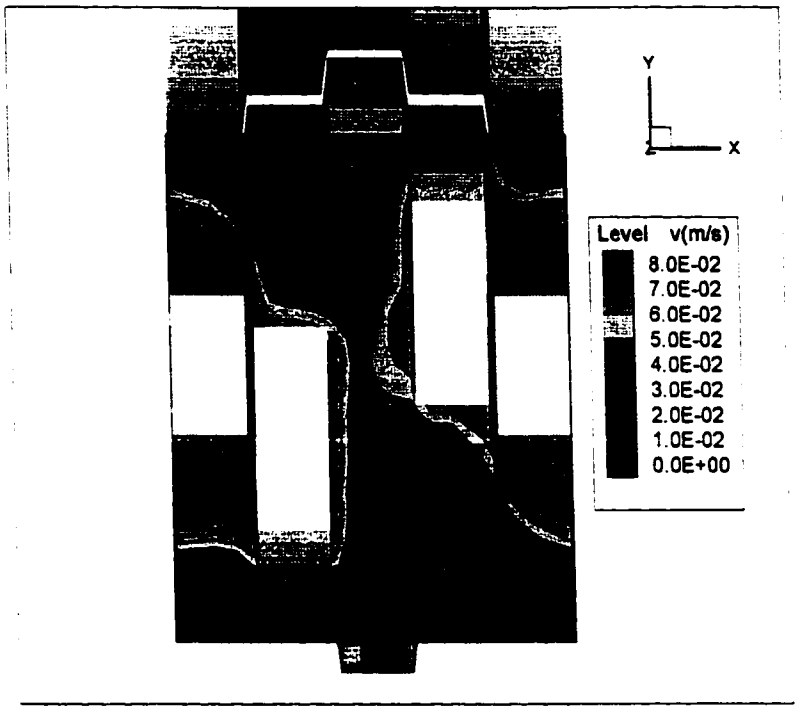

Figure 5.38. Contours of the v-component of velocity obtained via simulation. Bottom screw, 60 rpm, 8.5 mL/s. Long straight elements are deployed before and after the kneading blocks.

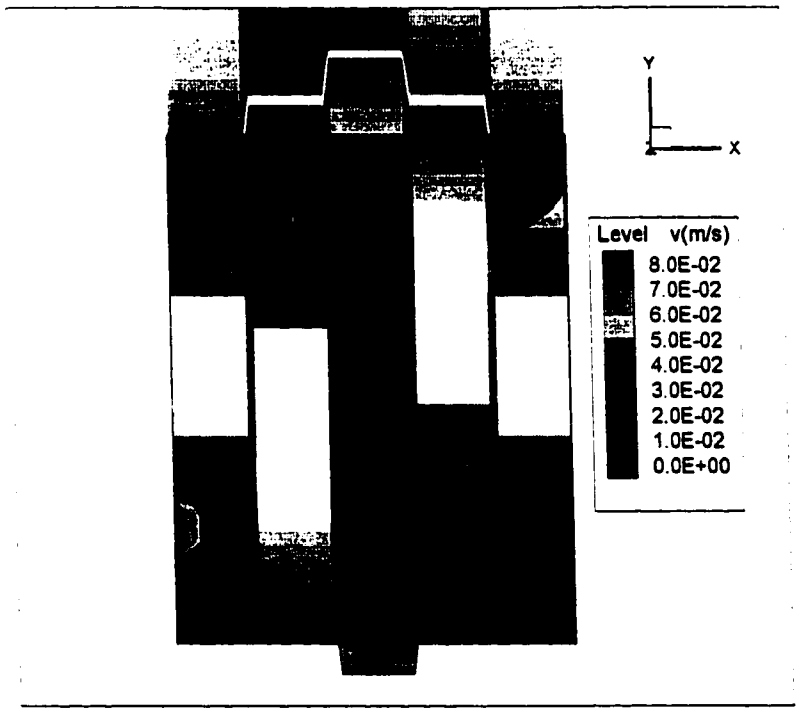

Figure 5.39. Contours of the v-component of velocity obtained experimentally. Bottom screw, 60 rpm, 8.5 mL/s. Long straight elements are deployed before and after the kneading blocks.

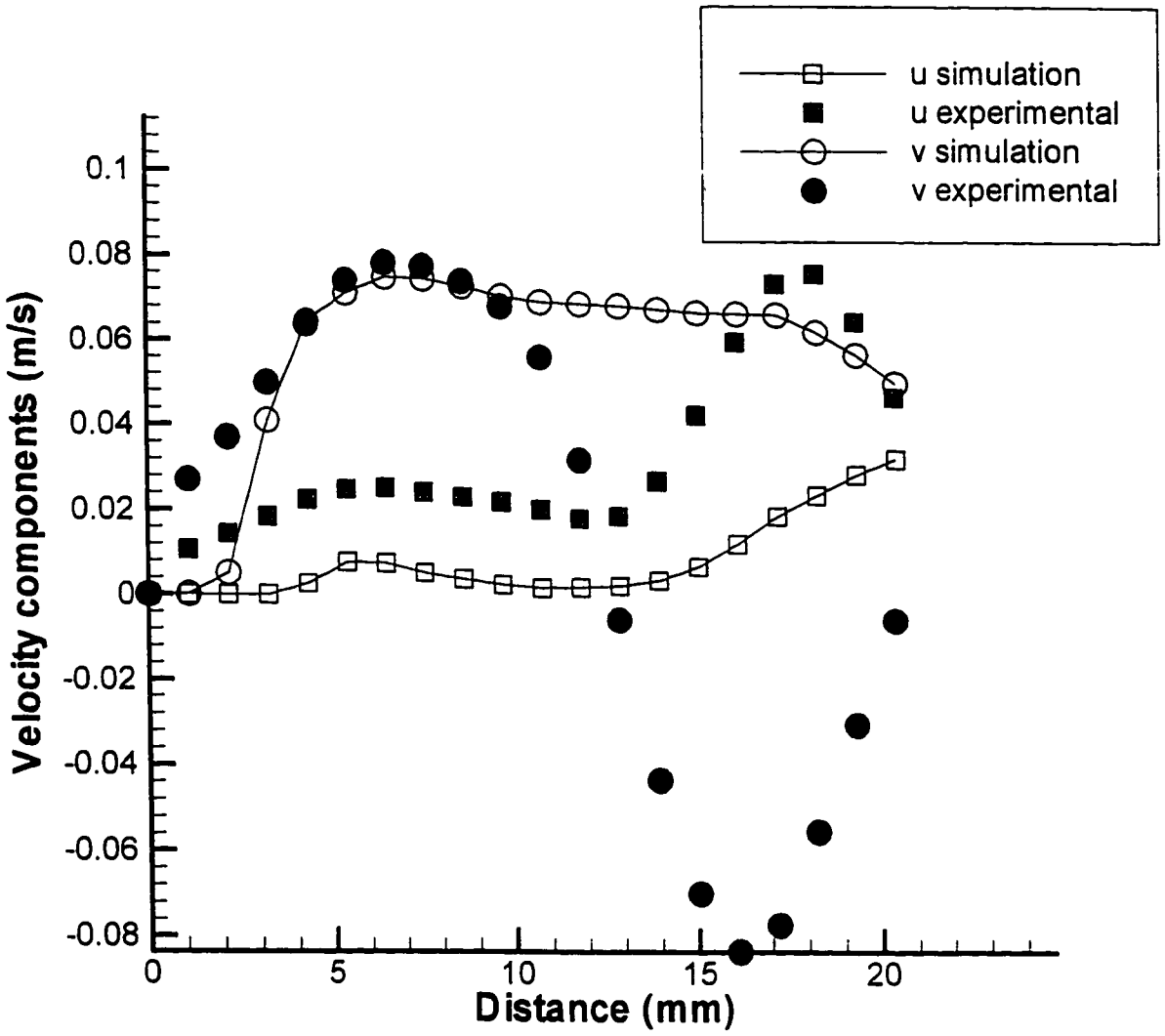

Figure 5.40. Comparison between simulation and experimental u and v components of velocity at x= 2.836 mm. Top screw, 60 rpm, 8.5 mL/s. Long straight elements are deployed before and after the kneading blocks for the experimental runs.

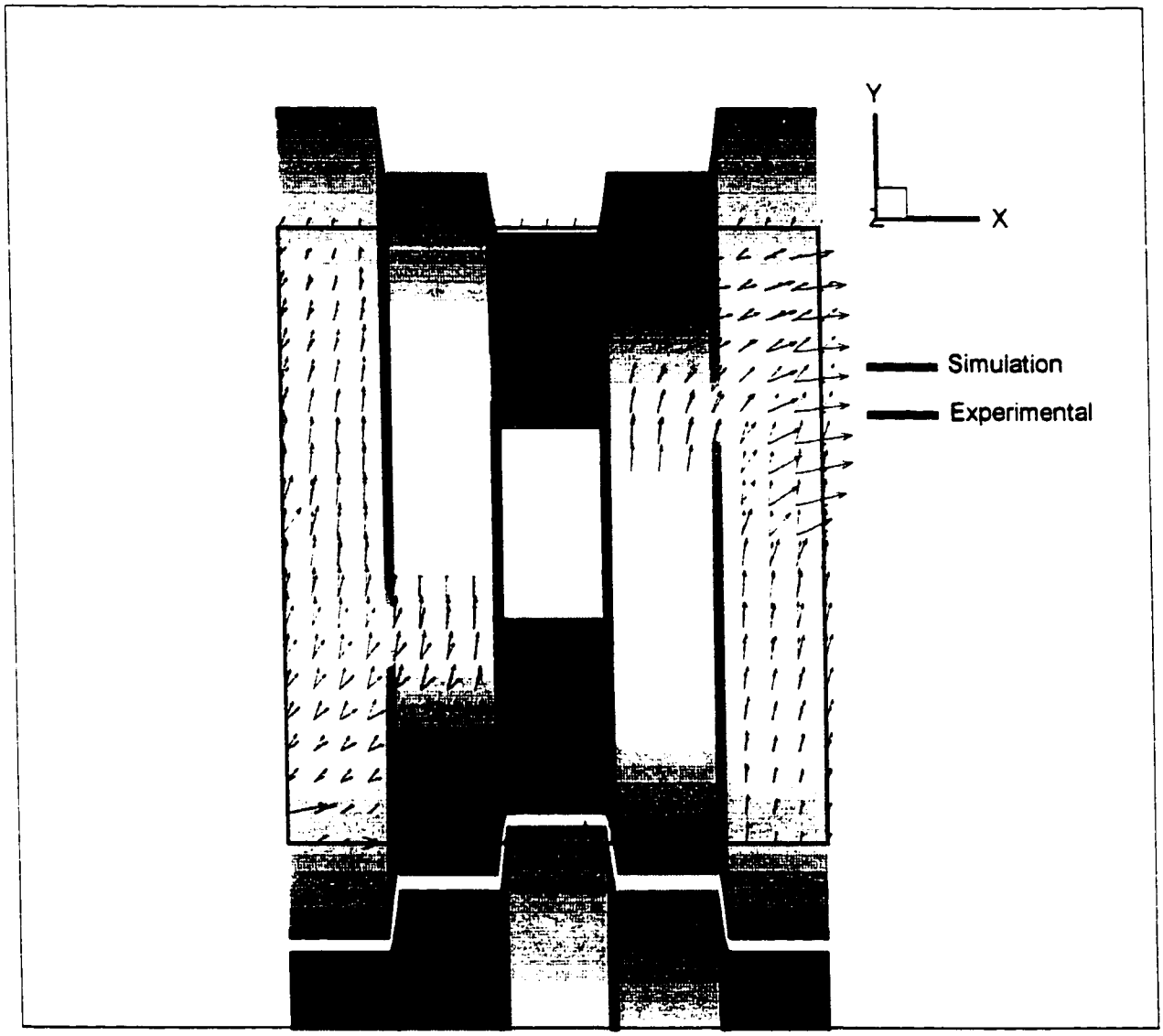

Figure 5.41. Velocity vectors obtained experimentally and via simulation. Top screw, 60 rpm, 8.5 mL/s. Conveying elements are deployed before and after the kneading blocks in the experimental run. No elements are deployed before and after for simulation.

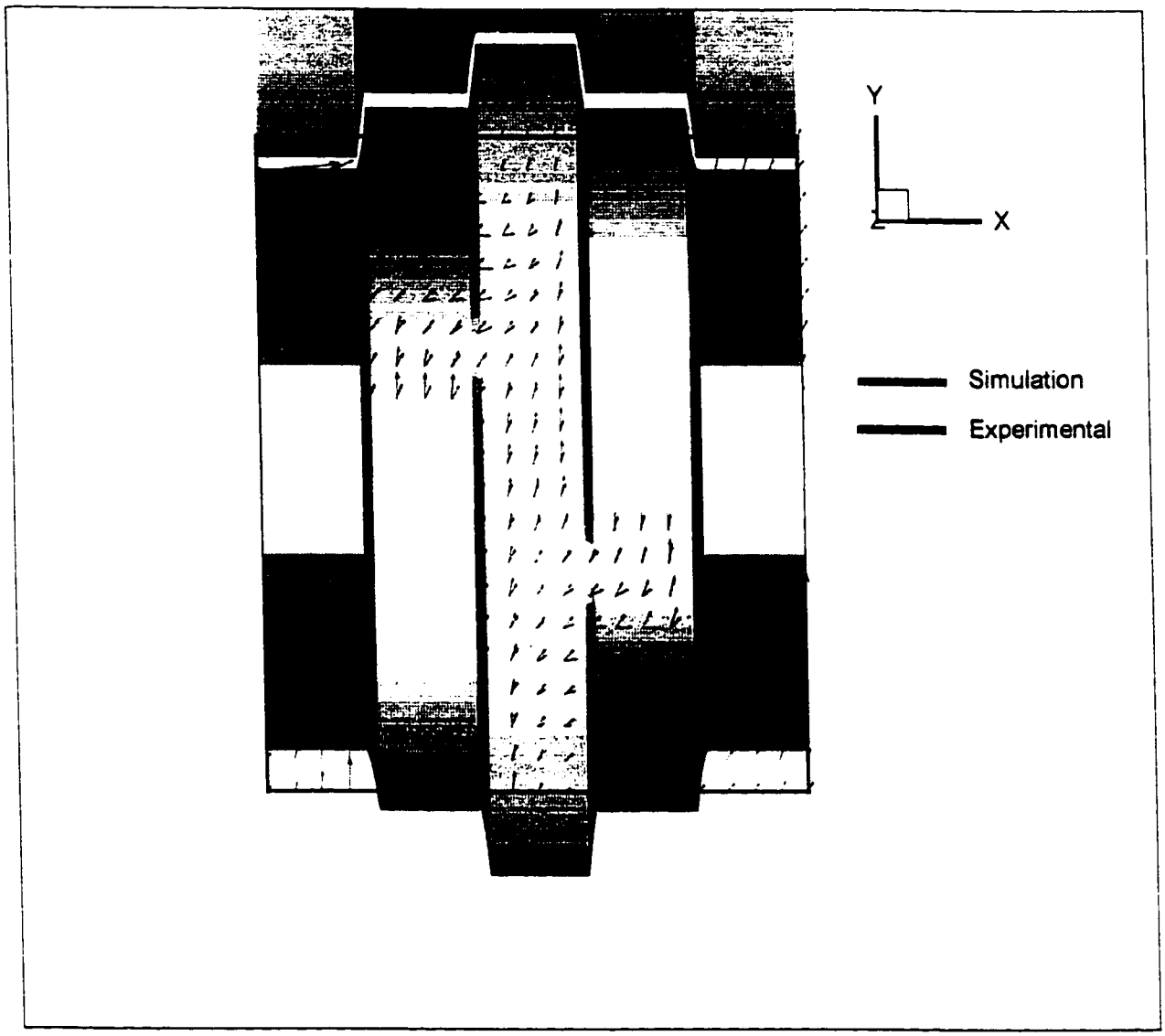

Figure 5.42. Velocity vectors obtained experimentally and via simulation. Bottom screw, 60 rpm, 8.5 mL/s. Conveying elements are deployed before and after the kneading blocks in the experimental run. No elements deployed before and after for simulation.

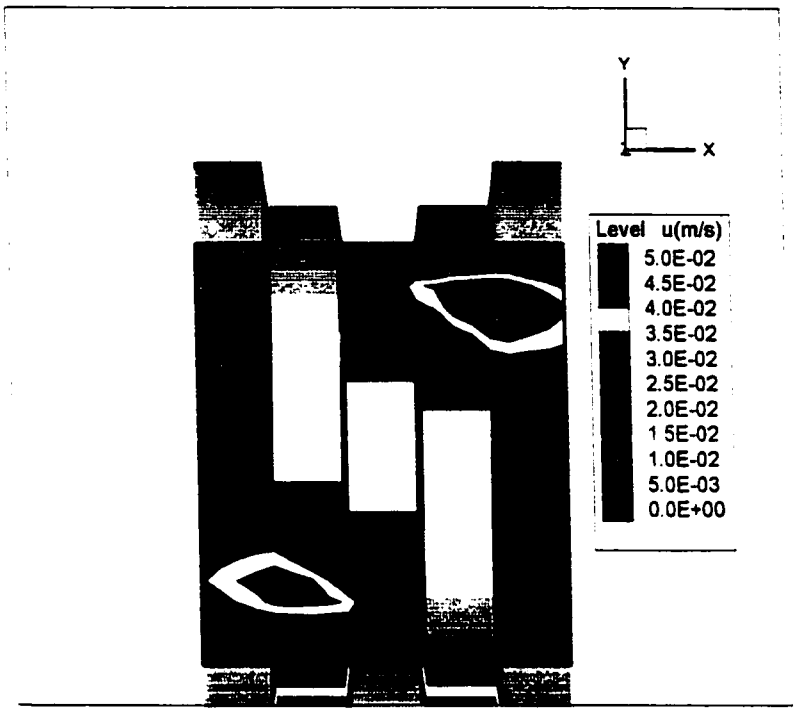

Figure 5.43. Contours of the u-component of velocity obtained via simulation. Top screw, 60 rpm, 8.5 mL/s. No elements deployed before and after the kneading blocks.

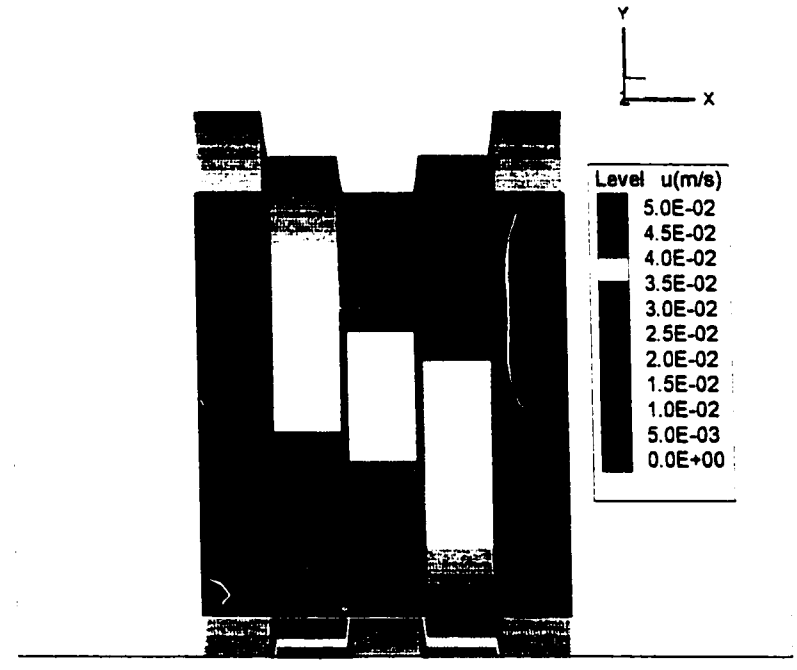

Figure 5.44. Contours of the u-component of velocity obtained experimentally. Top screw, 60 rpm, 8.5 mL/s. No elements deployed before and after the kneading blocks.

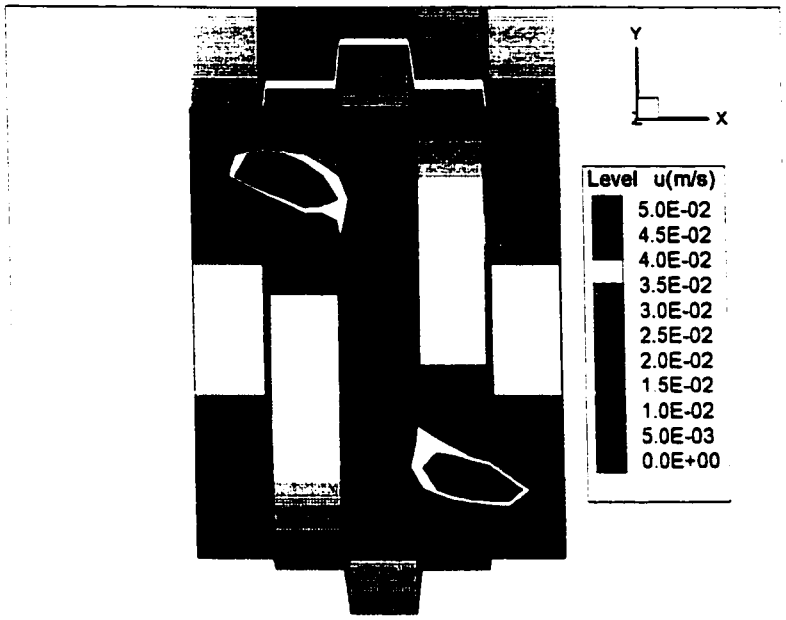

Figure 5.45. Contours of the u-component of velocity obtained via simulation. Bottom screw, 60 rpm, 8.5 mL/s. No elements deployed before and after the kneading blocks.

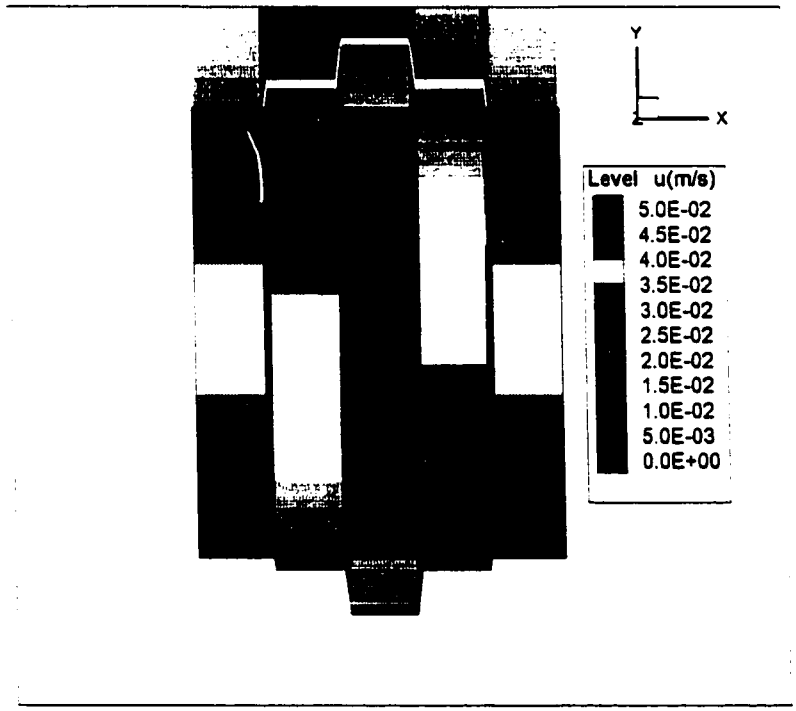

Figure 5.46. Contours of the u-component of velocity obtained experimentally. Bottom screw, 60 rpm, 8.5 mL/s. Conveying elements deployed before and after the kneading blocks.

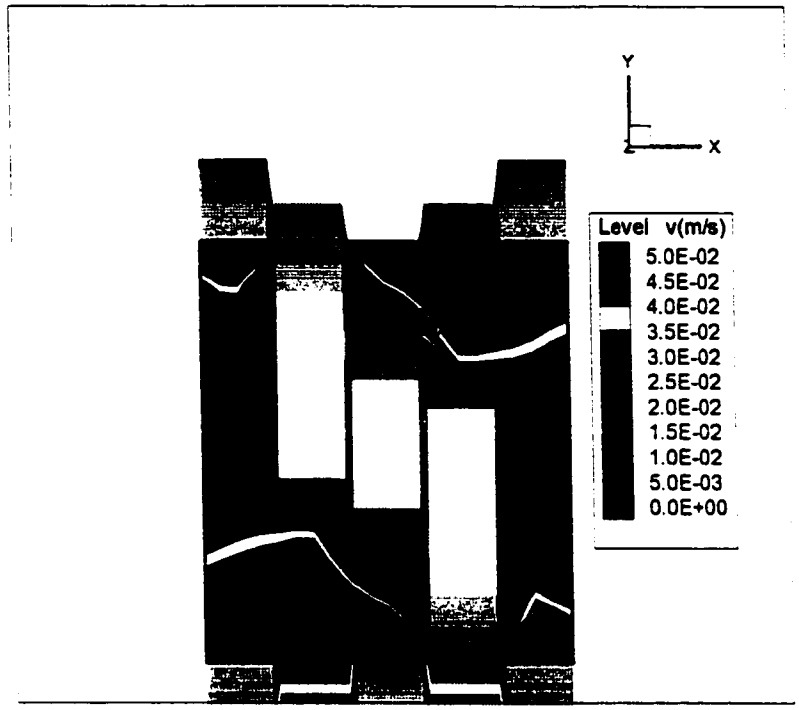

Figure 5.47. Contours of the v-component of velocity obtained via simulation. Top screw, 60 rpm, 8.5 mL/s. No elements deployed before and after the kneading blocks.

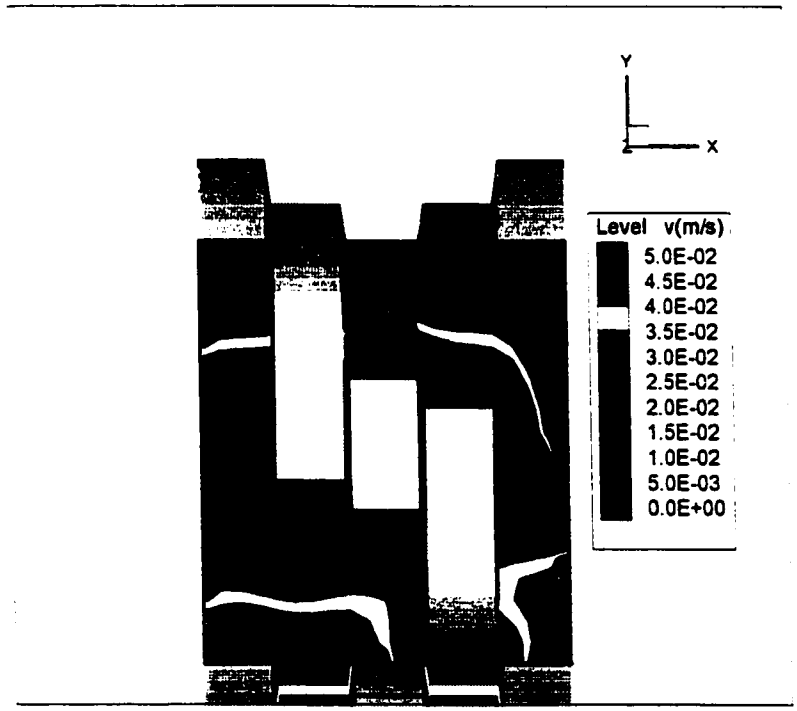

Figure 5.48. Contours of the u-component of velocity obtained via simulation. Top screw, 60 rpm, 8.5 mL/s. Conveying elements are deployed before and after the kneading blocks.

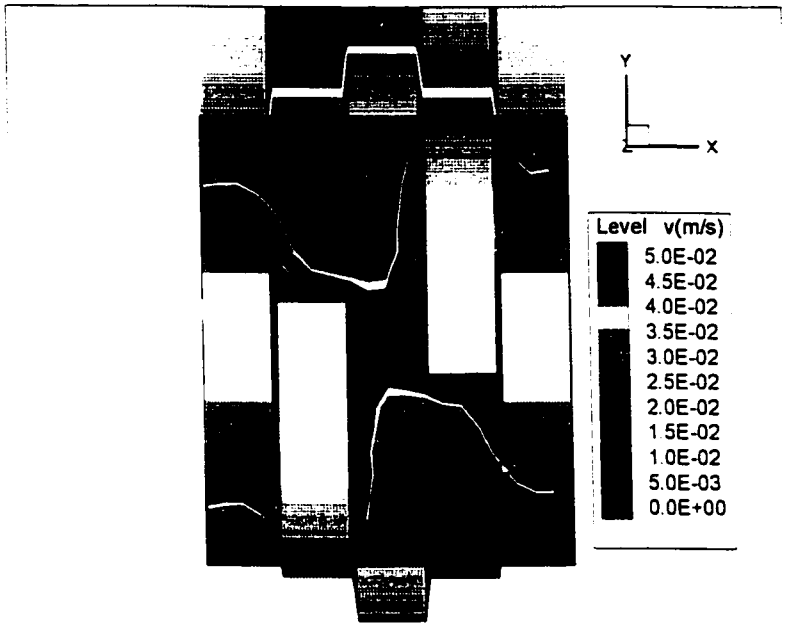

Figure 5.49. Contours of the v-component of velocity obtained via simulation. Bottom screw, 60 rpm, 8.5 mL/s. No elements deployed before and after the kneading blocks.

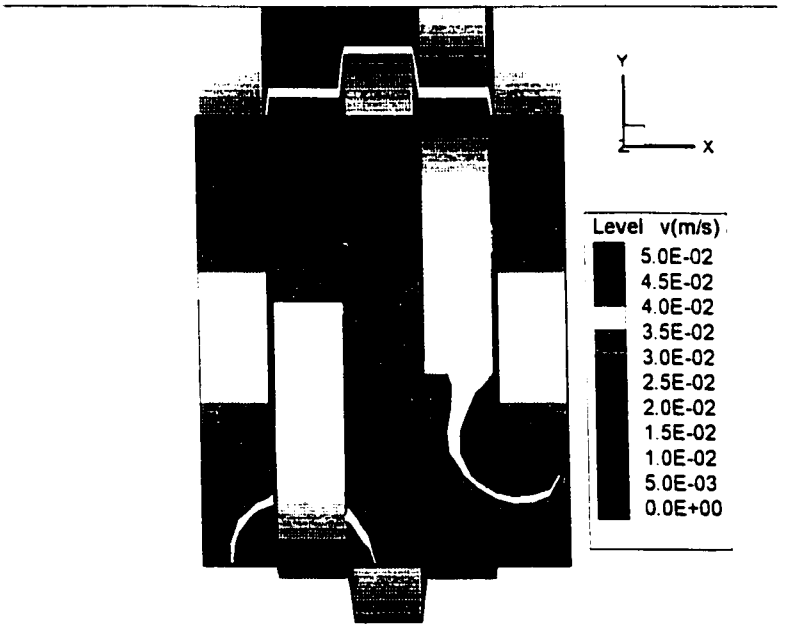

Figure 5.50. Contours of the v-component of velocity obtained experimentally. Bottom screw, 60 rpm, 8.5 mL/s. Conveying elements are deployed before and after the kneading blocks.

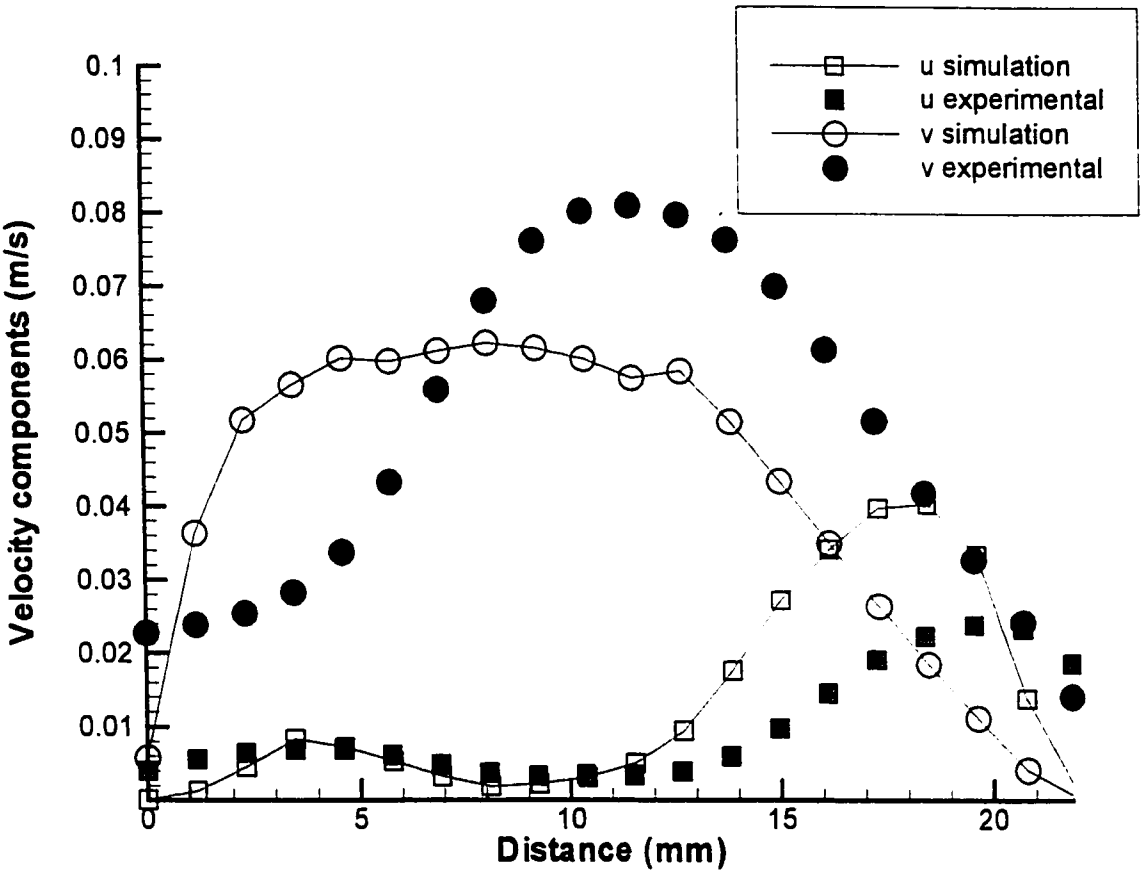

Figure 5.51. Comparison between simulation and experimental u and v components of velocity at x= 2.836 mm. Top screw, 60 rpm, 8.5 mL/s. Conveying elements are deployed before and after the kneading blocks for the experimental runs.

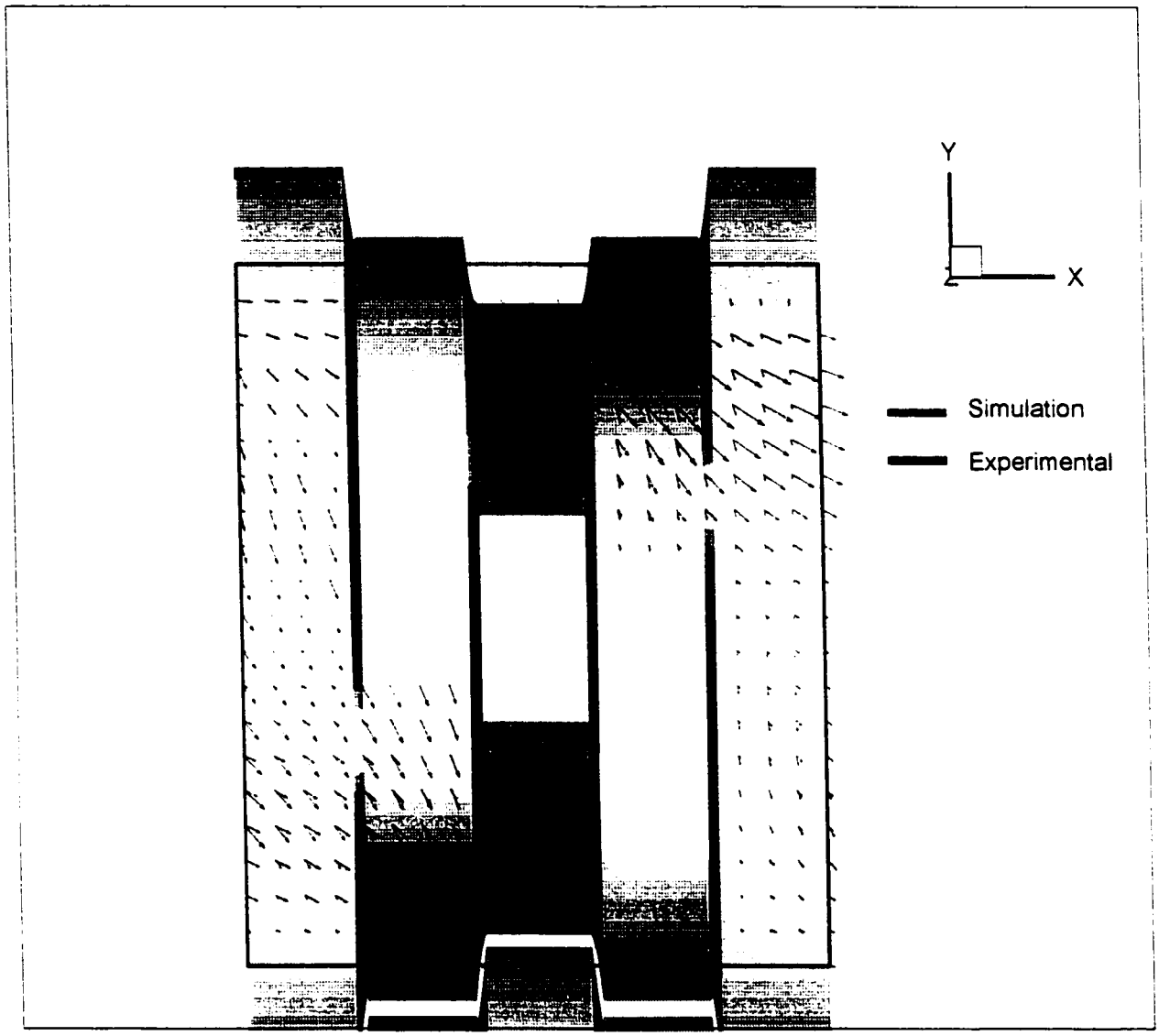

Figure 5.52. Velocity vectors obtained experimentally and via simulation. Top screw, 0 rpm, 5 mL/s. Long straight elements are deployed before and after the kneading blocks.

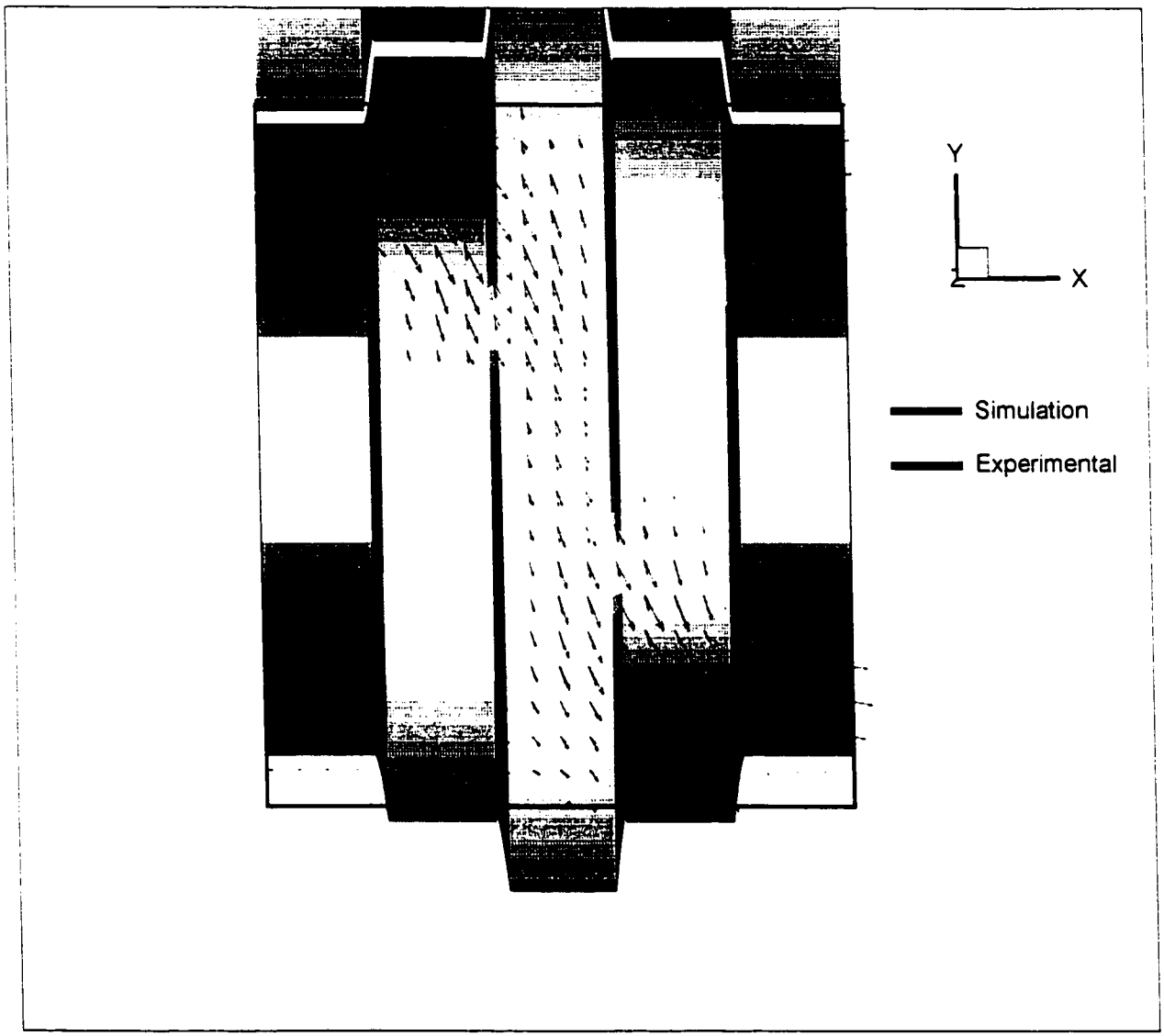

Figure 5.53. Velocity vectors obtained experimentally and via simulation. Bottom screw, 0 rpm, 5 mL/s. Long straight elements are deployed before and after the kneading blocks.

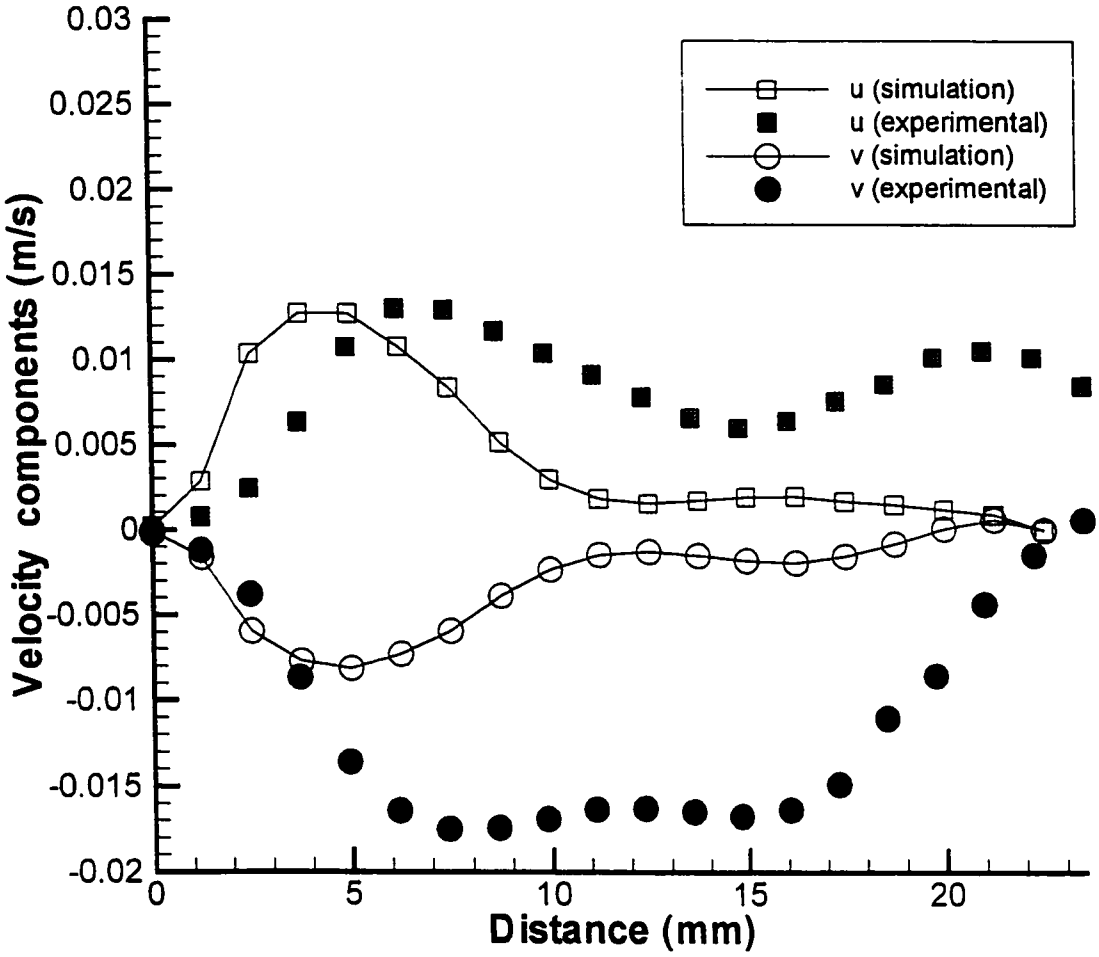

Figure 5.54. Comparison between simulation and experimental u and v components of velocity at x= 2.836 mm. Top screw, 0 rpm, 5 mL/s. Long straight elements are deployed before and after the kneading blocks.

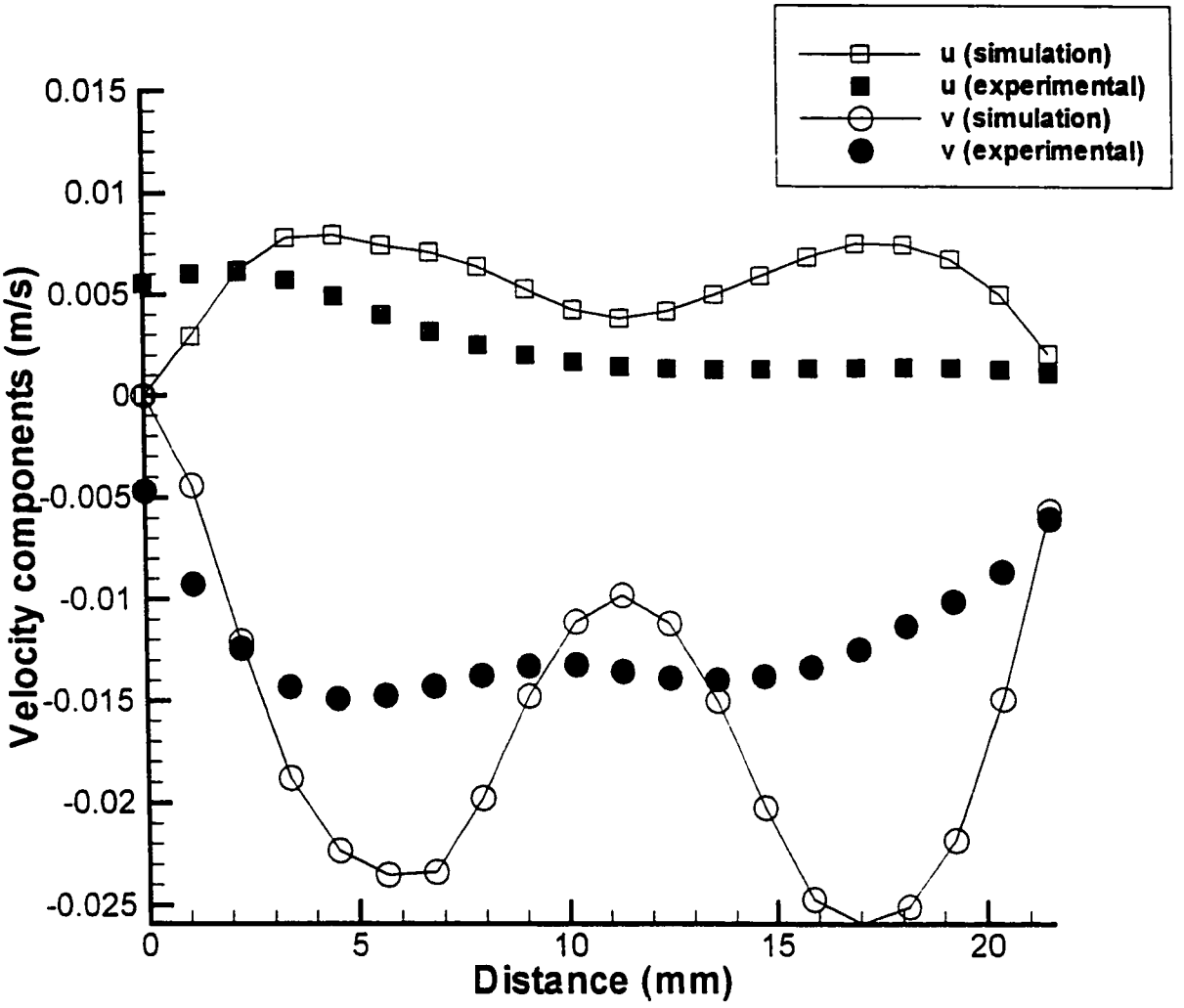

Figure 5.55. Comparison between simulation and experimental u and v components of velocity at x= 10.0 mm. Bottom screw, 0 rpm, 5 mL/s. Long straight elements are deployed before and after the kneading blocks.

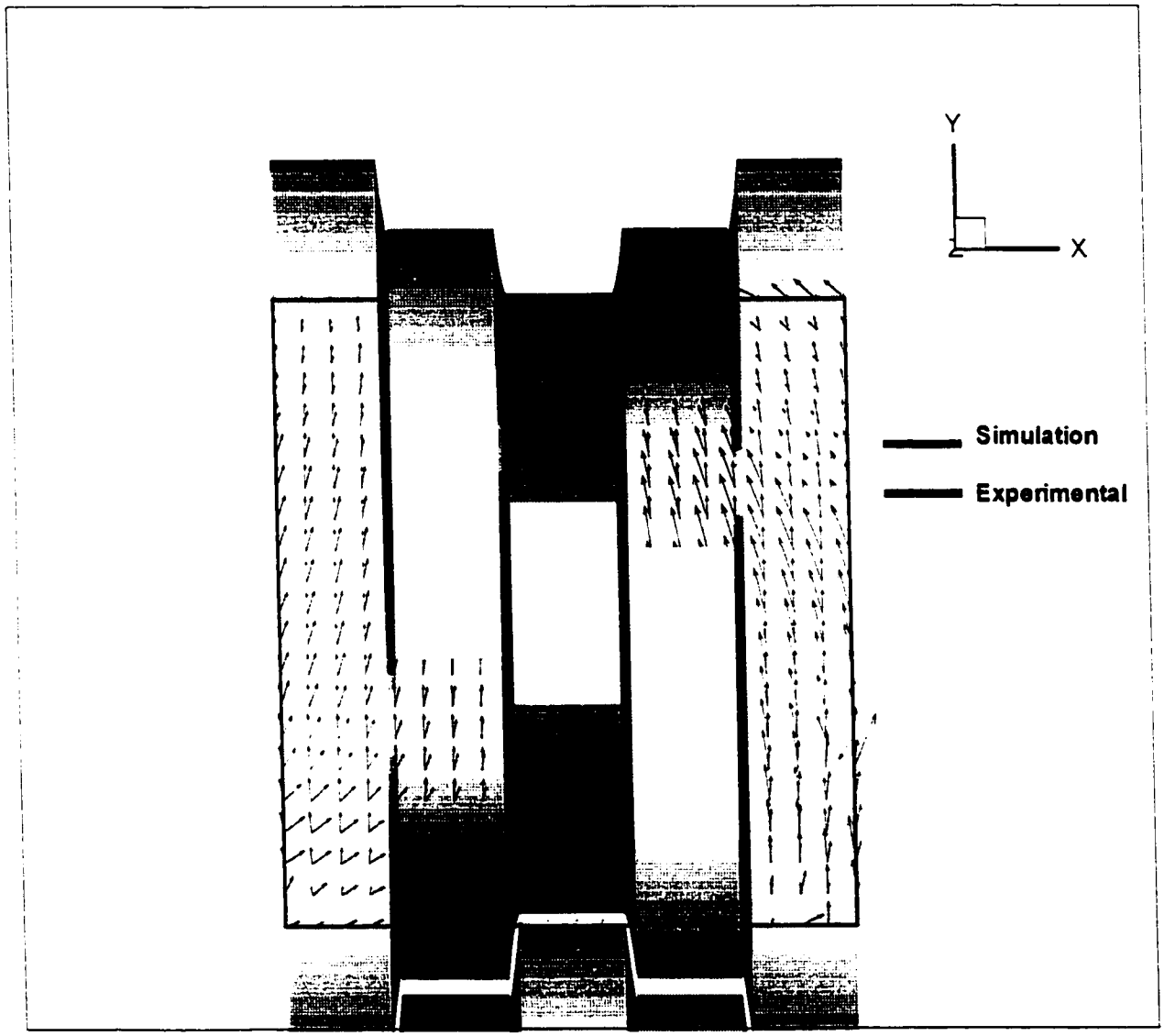

Figure 5.56. Velocity vectors obtained experimentally and via simulation. Top screw, 60 rpm, 0 mL/s. Long straight elements are deployed before and after the kneading blocks.

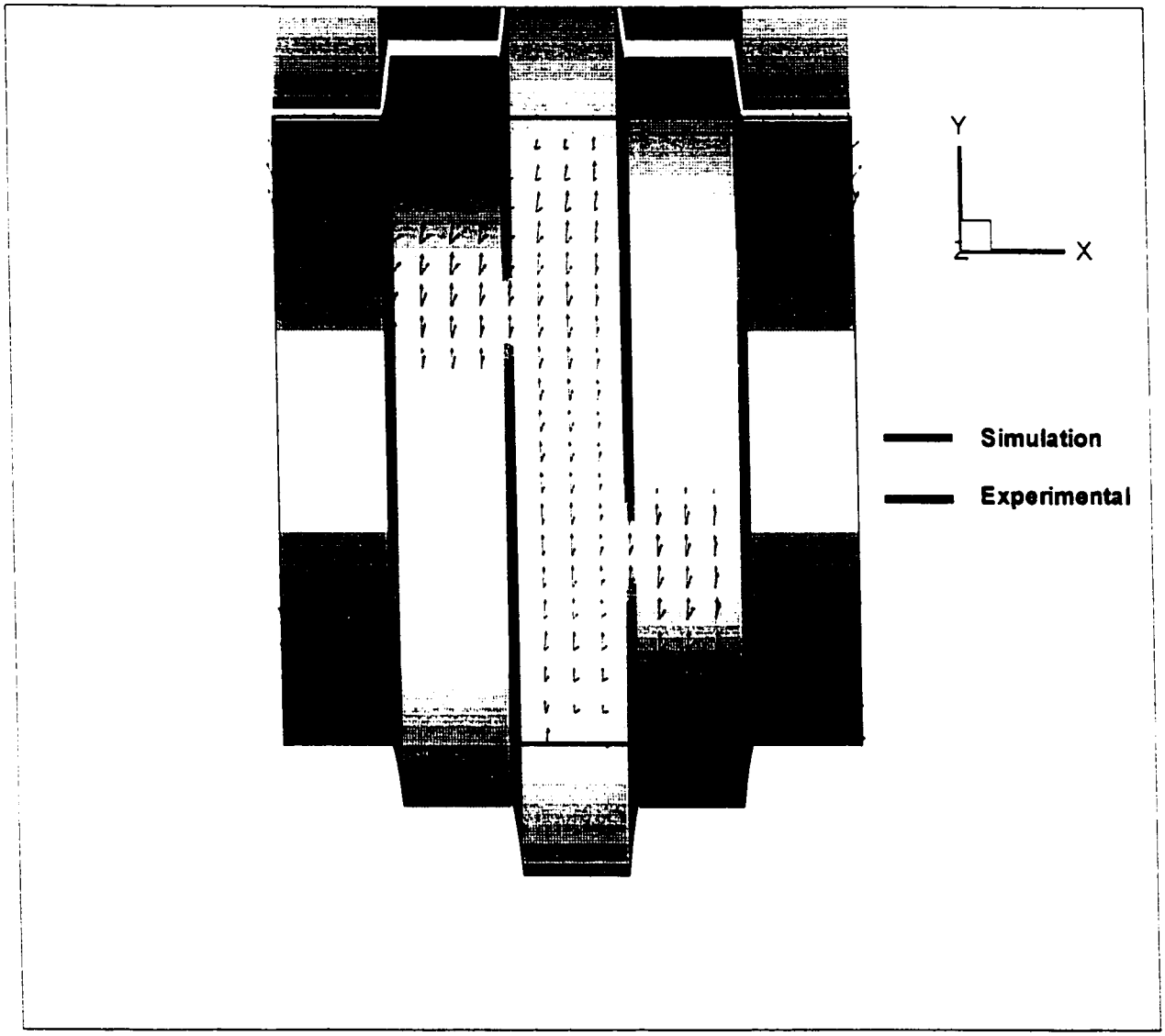

Figure 5.57. Velocity vectors obtained experimentally and via simulation. Bottom screw, 60 rpm, 0 mL/s. Long straight elements are deployed before and after the kneading blocks.

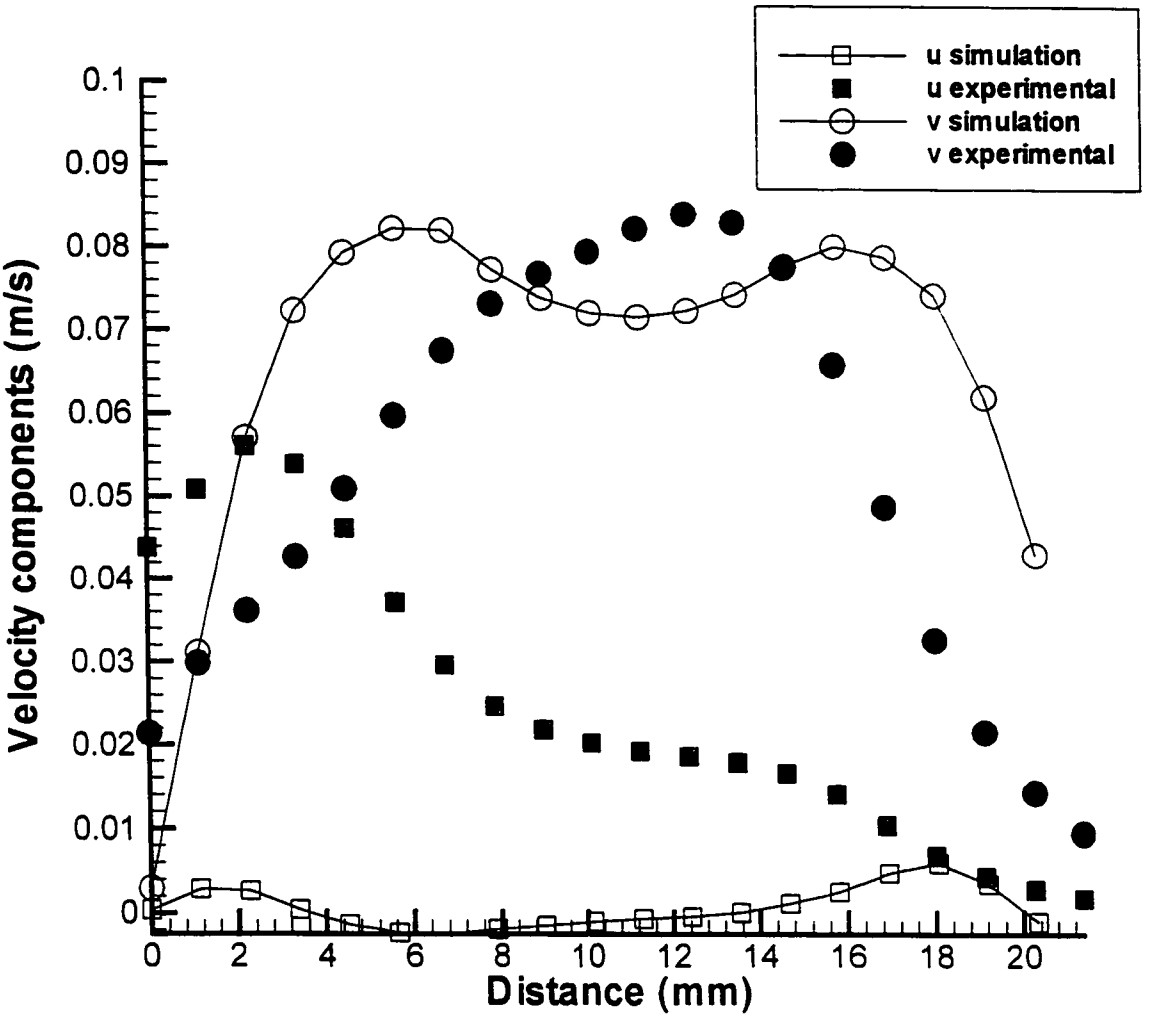

Figure 5.58. Comparison between simulation and experimental u and v components of velocity at x= 2.83 mm. Top screw, 0 rpm, 5 mL/s. Long straight elements are deployed before and after the kneading blocks.

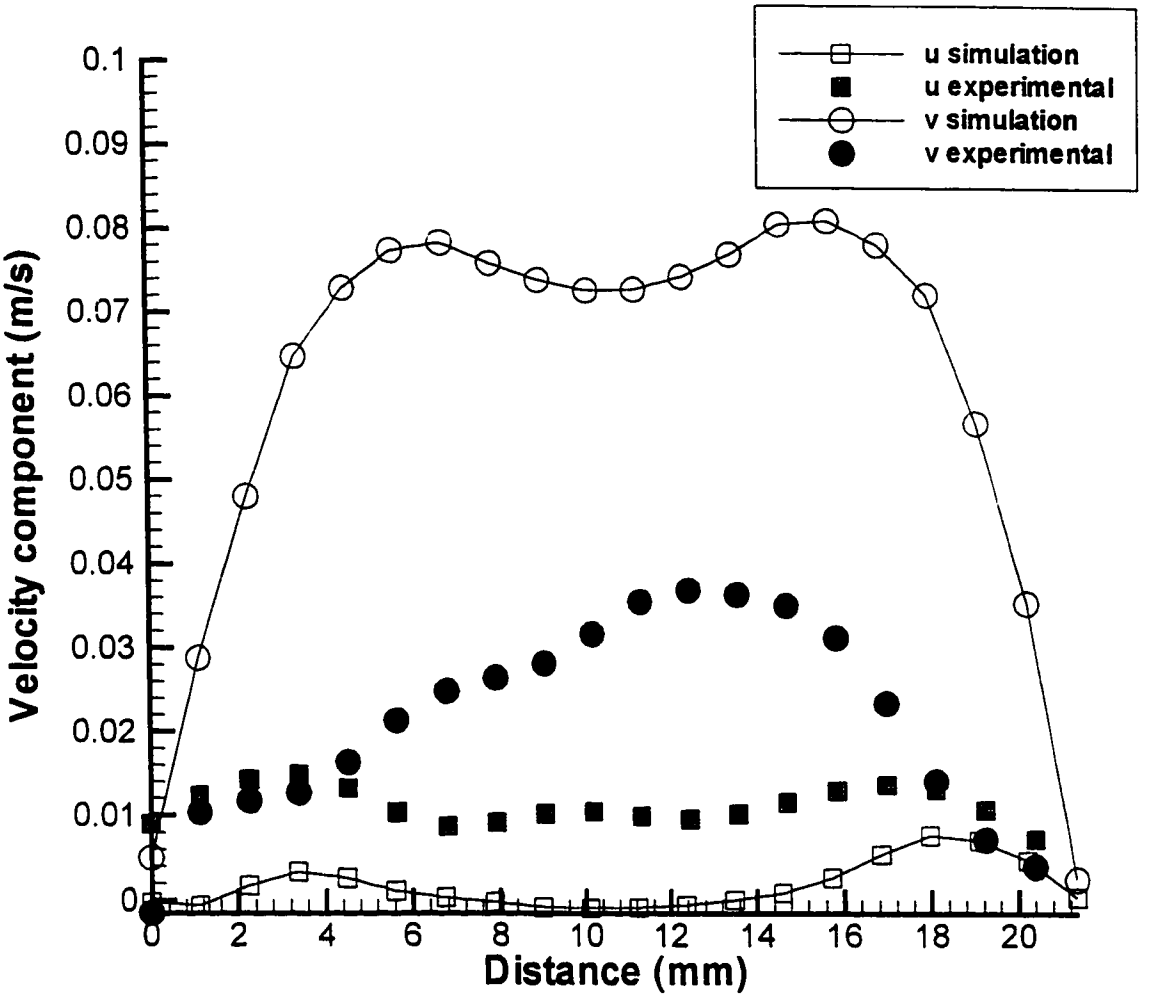

Figure 5.59. Comparison between simulation and experimental u and v components of velocity at x= 10.0 mm. Bottom screw, 0 rpm, 5 mL/s. Long straight elements are deployed before and after the kneading blocks.

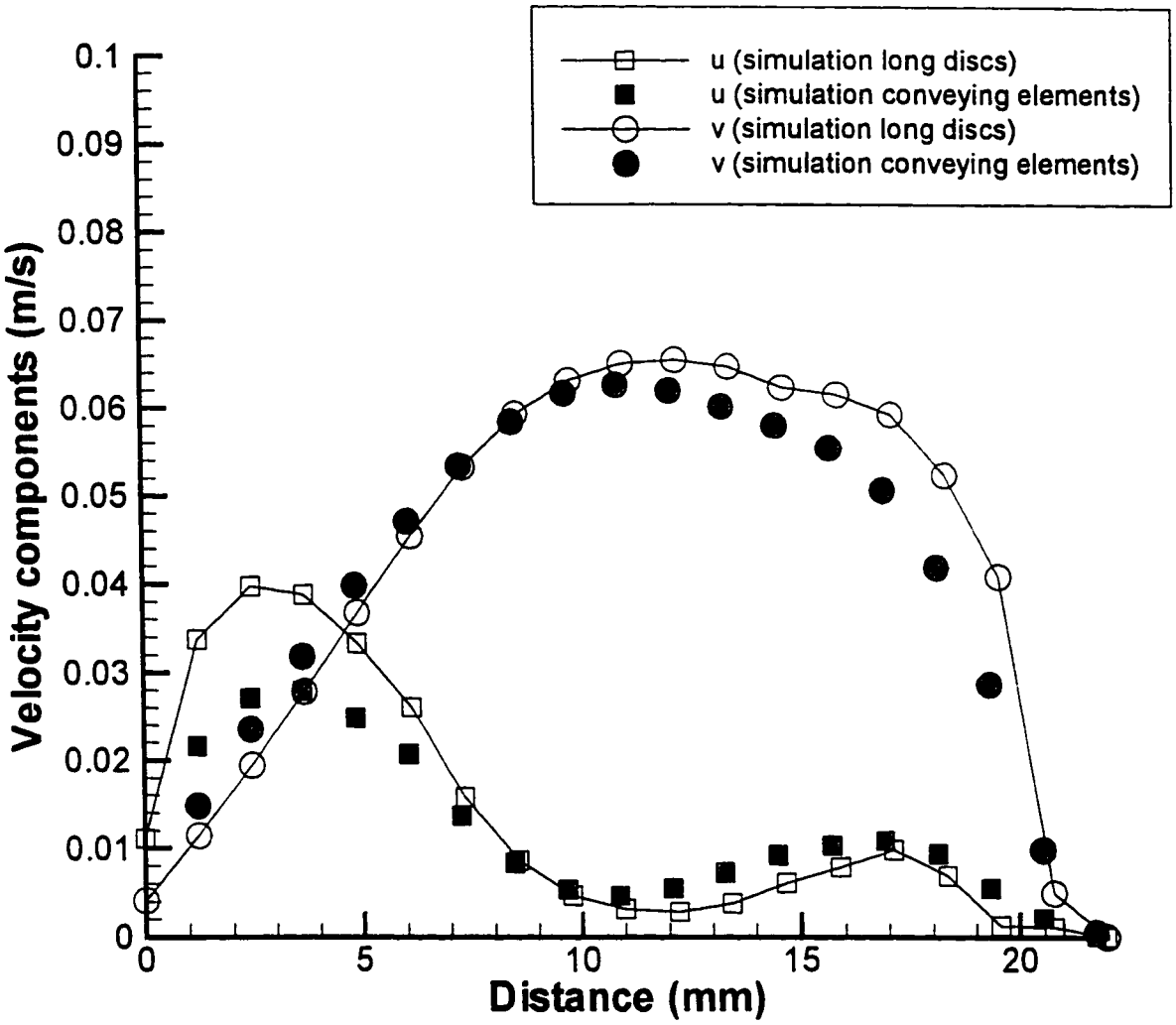

Figure 5.60. Comparison between simulation using long discs and simulation using conveying elements for u and v components of velocity at x= 2.83 mm. Top screw, 60 rpm, 5 mL/s.

5.6 Discussion

The model developed for the flow of polymer melts in the kneading disc section of an ICRTSE was based on the assumption of creeping flow. The assumption is based on the fact that polymer melts show high viscosities that make viscous forces predominant in the system, being many orders of magnitude larger than other forces such as inertial or body forces. The experimental setup was designed and constructed for visualization purposes. The acrylic material used for the construction of the barrel and screw elements introduced a limitation in the viscosity of the fluid that can be used for the visualization experiments due to the high pressures generated within the system. With the use of a fluid with relative low viscosity when compared with a polymer melt, the assumption of creeping flow only holds for conditions of low rotation speed and flow rate. At 100 rpm, inertia forces become as significant as viscous forces for a fluid of 1 Pa.s . Under these conditions, the creeping flow model does not predict the flow behavior accurately. For the runs made at 60 rpm, the Reynolds number can be calculated using the tangential velocity of the discs as characteristic velocity and the widest gap between disc and barrel as characteristic diameter. The calculated Re is approximately 0.2. Neglecting inertia forces under these conditions is assumed to be the main source of discrepancies between experiments and simulations.

The experimental and simulation results were in reasonable agreement for the run at 60 rpm and 5 mL/s. The comparisons of the extracted data showed good agreement when the long disc elements where used. However, the flow patterns showed even better agreement when the conveying elements were used. The use of conveying elements created an ordered pattern on the flow prior to entering the kneading blocks. The long discs created a pattern that was disrupted by the kneading blocks creating the split behavior observed experimentally, where a fraction of the fluid follows the rotation of the discs whereas the rest follows the pseudo helix angle of the channel. The numerical model could not predict this behavior. The results obtained for the limit cases of 0 rpm and 0 flow rate demonstrated that the model can predict the flow patterns with reasonable agreement. The qualitative flow behavior on these limit cases was intuitively predictable.

Future work should include the inertia effects on the model equations because of the relative low viscosity fluids used in the visualization model.

5.7 Summary

A comparison of the 3D model for the simulation of flow in the kneading disc region of an ICRTSE has been done against PIV experimental data for the first time. The various cases studied were aimed to test the model at various conditions of rpm and flow rate. The results show good agreement for the case of a flow rate of 5 mL/s and a rotation speed of 60 rpm. The case of a flow rate of 8.5 mL/s and 60 rpm showed good agreement when conveying elements were deployed before and after the kneading blocks. The simulation results using the long straight elements are not in good qualitative agreement with experiments. It is assumed that due to the relatively low viscosity of the fluid, inertia forces play a significant role in the fluid dynamics of the system. A split in the velocity patterns observed in the experimental runs when the fluid encounters the first disc (Figure 5.30) was not predicted by the model.

Results confirm the importance of a 3D model for the prediction of the flow behavior in the kneading blocks. Results highlight the importance of the use of appropriate boundary conditions for the accurate prediction of the flow field. The validation of results against experimental data opens the way for further use of the model as a design tool for the improvement in mixing performance of the kneading elements. Further work should include the study of additional cross sections and the combined use of experiments and simulations for the analysis of mixing performance.

The assumption of creeping flow is assumed to produce the discrepancies between experiments and simulations in some of the cases studied. Discrepancies can also be attributed to limitations in the experimental technique (Jaffer, 1998).

Chapter Six

CONCLUSIONS AND RECOMENDATIONS

6.1 Conclusions

The present work has extended the analysis based on the 3D simulation of the flow field in the kneading blocks of ICRTSE presented in literature to date. Different boundary conditions for the inlet-outlet problem were tested and compared with experimental data. The normal stress difference was found to be the most realistic boundary condition because it allows the rotational speed to affect the flow rate of the system. The normal stress difference boundary condition also gave the best correlation with visualization experiments.

Comparisons with experimental pressure data have been carried out. Previous researchers (Kalyon, 1997) have compared pressure drop along the kneading blocks as validation for the numerical models. Pressure drop in the axial direction gives some indication of the accuracy of the results but does not give any information about the flow patterns in the cross sections. In the present work, measurements made by McCullough and Hilton (1993) on various mixing kneading blocks were used for the comparison of pressure data along the barrel. These measurements help to understand the flow patterns developed and provide a more comprehensive approach of validating the numerical model.

The relative performance of the different configurations of kneading blocks was characterized by particle trajectories. Particles were initially located to cover a complete cross section at the inlet of the kneading block. The idea was to create a unique measurement of residence time distribution, avoiding the problem of the initial location of the blob, and to account for the number of particles that go through the kneading block without experiencing specific levels of shear rate.

A unique comparison with visualization experiments was performed. Experimental velocity profiles obtained via particle image velocimetry (PIV) by Jaffer (1998) were processed and compared with numerically obtained profiles showing similar trends on an initial study that involved a kneading block preceded and followed by conveying elements, and simulation results obtained using the velocity inlet-outlet boundary condition. A more recent study which included a set of long discs preceding and following the kneading block and the inclusion of the normal stress boundary condition showed excellent correlation even at the inlet and outlet boundaries.

The research work extends from the prediction of the flow field using the finite element method for the numerical solution of the conservation equations, to the experimental verification of the model's predictions and the calculation of particle trajectories for the analysis of mixing performance. The achievements can be classified in two main categories: i) extension and evaluation of results obtained in literature and ii) original contributions. As a summary, the main achievements on the extension and evaluation of results obtained in literature are:

- The development of a three-dimensional finite element model for the simulation of Carreau flows in the kneading disc section of an ICRTSE. The model has been developed to emulate accurately the real system including the narrow clearances between two discs and between disc and barrel.
- A comprehensive analysis of the flow phenomena in the kneading block section that includes the effects of disc width, stagger angle and clearances on the flow patterns, as well as the analysis of the effect of operating conditions on the performance of the system.
- The study of inlet-outlet boundary conditions and their effect of the validity of the numerical model. The normal stress boundary condition was found to provide more reasonable results than the velocity boundary condition.
- A critical evaluation of the models available in literature based on the results obtained, exposing their strengths and weaknesses.

The original contributions of the project are:

- The analysis of relative performance between different configurations of kneading blocks based on particle trajectories, using a novel analysis approach. Residence time

and cumulative residence time distributions were obtained and compared. The initial location of the particle tracer was set to cover the entire cross section of the extruder channel. A study was carried out for three L/D under the same conditions of flow rate, rpm and material properties. Analyses of residence time and stress distributions were done to characterize the relative performance of the three configurations. Previous researchers (Lawal and Kalyon, 1993) have used particle tracers to study the rate of spreading of a blob. In our work, the particle tracers are initially located to cover a cross section of the extruder channel at the beginning of the kneading blocks. This procedure is taken to approach the ideal situation in the measurement of residence times by having plug flow and complete mixing in the radial direction at the point of injection of the tracer. Since large velocity gradients are present in the inlet of a kneading block section, the initial location of a blob would affect the measurement of residence times. The results of this research will report for the first time in literature the strain rate history of the particles tracers. The strain rate history is used to analyze the number of particles undergoing a specific level of strain rate. This study also demonstrates that characterization of mixing based on average values of strain rate is not sufficient. Particle tracking shows that different particles experience different strain rate histories and that a percentage of them never experience specific levels of strain rate. The study of particle history is an important tool in the analysis of relative performance of kneading disc configurations.

- The validation of the numerical model through comparison with experimental pressure profiles along the extruder. The presence of intermittent zones of high and low pressure within the kneading blocks is the reason for the occurrence of recirculating flows and the key in the distributive mixing performance of the system. A comparison with experimental pressure profiles along the extruder's barrel is crucial in the validation of the numerical model for the ultimate purpose of evaluating mixing performance. Comparisons were done with pressure measurements made by McCullough and Hilton (1993) using the complete data provided for two configurations of kneading discs, a 45/5/20 and a 45/5/42 of a 30 mm ICRTSE. The data provided by McCullough and Hilton describes dynamic pressure profiles measured along the barrel for a complete revolution of the screws. For the first time a

validation of simulation results is done using the circumferential pressure profiles measured experimentally. Previous researchers have reported comparisons with experimental axial pressure drop. The new results highlight the importance of boundary conditions as well as the accurate description of the geometry on the accuracy of the simulation results. The implementation of the normal stress boundary condition allowed a reasonably good matching of the experimental conditions.

- The validation of velocity profiles through comparison with visualization experiments using PIV, performed at McMaster University. Comparisons were made using velocity vectors and velocity contours for specific planes across the flow region. A procedure was developed to collect and display both the experimental and simulated results for the purpose of comparison. Visualization experiments using the PIV techniques have allowed comparisons of the velocity vectors obtained via numerical simulation with experimental velocity profiles. This type of comparison is presented for the first time in literature for velocity profiles in kneading blocks. A unique experimental setup consisting of a 30mm diameter twin screw model made out of transparent acrylic was used (Jaffer et al., 1997). Various combinations of flow rate (controlled by a feeding pump) and rotational speed were evaluated to study the different flow patterns developed in the kneading blocks. A special set of long discs was designed and located at the inlet and outlet of the kneading blocks to study the problem of boundary conditions. There is an excellent correlation between experiments and simulation that validates the numerical model and establishes a solid starting point for further analysis of mixing based on the numerical model. Results also show the importance of boundary conditions.

6.2 Recommendations

The comparisons of the numerical model with experimental results of pressure and velocity revealed some of the limitations of the model, but also gave indications of the potential improvements that can be introduced in the model equations. Future work in the area of simulation of flow in mixing elements of ICRTSE should include:

- The inclusion of thermal effects in the formulation of the model. It is well known that temperature plays a significant role when a polymer is processed in a twin screw extruder. The non-isothermal flow condition significantly affects the melt extrusion process. Rigorous solution of the non-isothermal flow requires the simultaneous solution of the energy and momentum equations. For the flow in the kneading disc region of an ICRTSE, a three-dimensional non-Newtonian and non-isothermal solution of the problem is necessary.
- Inclusion of inertia terms in the momentum equations for the comparison with visualization experiments. Due to the nature of the acrylic transparent material used for the components of the experimental model, the viscosity of the fluids that can be processed is limited. The inclusion of inertia terms in the equations would allow a more rigorous comparison between simulations and experiments.
- The use of alternative methods for the analysis of the flow involving moving boundaries. For the present thesis, the re-generation of the finite element mesh was necessary in order to represent the different geometries associated to the rotation of the screws. Lawal and Kalyon (1995) and Bertrand et al. (1994) have proposed two different methods in which only a single mesh covering the volumetric enclosure is necessary and the process of re-meshing is eliminated. These methods require the use of adaptive meshing and a large number of elements to describe with enough accuracy the kinematics of the internal moving parts.
- The extension of the analysis of mixing using particle tracers for different geometries and operating conditions. The problem of particles intersecting the solid boundaries can be reduced by increasing the density of the finite element mesh in the small clearance zones and reducing the time step.
- The simulation of complete sections of the TSE involving combinations of kneading and conveying elements.

REFERENCES

Adams, R.L.,"Continuous Process Molten Plastics" Paper Soc. Plast. Eng, p7-10, (1972).

Bertrand, F., Tanguy, P.A., Thibault, F., "A Three-Dimensional Fictitious Domain Method for Incompressible Flow Problems in Enclosures Containing Moving Parts", Personal Communication, (1994).

Bigio, D., Erwin, L., "Mixing Studies in Co-rotating Twin Screw Extruders",Technical Papers SPE ANTEC, p.45-52, (1984).

Bird, R.B., Stewart, W.E., Lightfoot, E.N., Transport Phenomena. John Wiley & Sons, (1984).

Booy, M.L., "Geometry of Fully Wiped Twin Screw Equipment", Polym. Eng. Sci.,18, p.973, (1978).

Booy, M.L., "Isothermal Flow of Viscous Liquids in Corotating Twin Screw Devices", Polym. Eng. Sci., 20, p.1220, (1980).

Bravo, V.L. "3-D Simulation of Quasi-Steady Sate Flow Field in Twin Screw Extruders", M.Eng Thesis, McMaster University, (1995).

Burbank, F.; Brauer, F.; Andersen, P., "Experimental Study of Distributive Mixing in a Co-rotating Twin Screw Extruder", Technical Papers SPE ANTEC, v.37, p 149-152, (1991).

Burnett, D., Finite Element Analysis. Addison Wesley, (1987).

Buzbee, B.L., Dorr, F.W., George, J.A., Golub, G.H., "The Direct Solution of the Discrete Poisson Equation on Irregular Region", SIAM J. Numer. Anal.,722-736, (1971).

Campbell, W.B., Plastics World, 26, p. 70, (1972).

Canedo,E.L.,Valsamis, L.N.,"Selecting Continuous Compounding Equipment Based on Process Consideration", Intern. Polym. Proc., IX, p. 225. (1994).

Chen, Z., White,J.L., "Dimensionless Non-Newtonian Isothermal Simulation and Scale –up Considerations for a Modular Intermeshing Corotating Twin Screw Extruders", Intern. Polym. Proc., VI, p. 304. (1991).

Cheng, H., Manas-Zloczower, I., "Study of Mixing Efficiency in Kneading Discs of Co-Rotating Twin Screw Extruders", Polym. Eng. Sci., v37, 6 (1997).

Cheremisinoff, N.P. Polymer Mixing and Extrusion Technology . Marcel Dekker Inc. (1987).

Christiano, J., Lindenfelzer, M., "Investigation of Mixing Patterns in Co-Rotating Fully Intermeshing Twin Screw Extruders Mixing Elements Using Dynamic Pressure Distributions", Technical Papers, SPE ANTEC, v.1, p 78, (1997).

Coleman, C.J., "A Finite Element Routine for Analysing Non-Newtonian Flows. Part I: Basic Method and Preliminary Results", J. Non-Newt Fluid Mech, 7, p. 289 (1980).

Crochet, M.C., Davies, A., Walters, K., Numerical Simulation of Non-Newtonian Flow. Elsevier, (1984).

David, D., Sapir, A., Tadmor, Z., "Modelling Twin Rotor Mixers and Extruders", Intern. Polym. Proc. VII, p.204, (1992).

Dhatt, G., Touzot, G.. The Finite Element Method Displayed. John Wiley and Sons (1984).

Eise,K., Werner, H., Herrmann, H. , "An Analysis of Twin Screw Extruders Mechanism" , in Advances.in Plastics Technology, Vol. 1, No. 2, Van Nostrand Reinhold , (1981).

Elmendorp, J., J. Polym.Eng.Sci., 26,418,(1986).

Fumatsu, K., Nagashima, Y., Nakamo, Y., Kajiwara, T., "Direct Simulation of 3-D Flows in Various Twin Screw Extruders", PPS Tenth Annual Meeting, p.46, (1994).

Galt, J. and Maxwell, B.,"Velocity Profiles for Polyethylene Melts", Modern Plastics, p. 165, Dec. (1964).

Gotsis, A.D., Kaylon, D.M. ,"Simulation of Mixing in Corotating Twin Screw Extruders", Technical Papers SPE ANTEC, (1989).

Gotsis, A. D., Ji, Z., Kaylon, M. ,"3-D Analysis of the Flow in Corotating Twin Screw Extruders", Technical Papers, SPE ANTEC, p.139, (1990).

Hovey, V. M.,"History of Extrusion Equipment for Rubber and Plastics", Wire and WireProd.,36, p.192, (1961).

Huyakorn, P.S., Taylor, C., Lee, R.L., Gresho, P.M.,"A Comparison of Various Mixed Interpolation Finite Elements in the Velocity-Pressure Formulation of Navier-Stokes Equations", Comp. and Fluids, 6, p. 25 (1978).

Iga, M., Reddy, J.N., "Penalty Finite Element Analysis of Free Surface Flows of Power-Law Fluids", Int. J. Non-Lin Mech, 24, 5, p. 383 (1989).

Jaffer, S., Bravo, V.L., Hrymak, A.N., Wood, P.E, Wright, J.D., "Visualization Experiments in an Intermeshing Co-rotating Twin Screw Extruder", PPS Thirteenth Annual Meeting, (1997)

Jaffer, S., PhD Thesis, McMaster University, (1998)

Janssen, L.P.B.M., Twin Screw Extrusion, Elsevier Sci. Publish. Co. (1978).

Janssen, L.P.B.M., Smith, J.M. , Proceedings Congress on Polymer Rheology and Plastics Processing, PRI/BSR, Loughborough, p. 160, (1975).

Jewmenow, J.D., Kim, W.S., Plaste und Kautschuk, 20, p. 356,(1973).

Kalyon, D.M., Gotsis, A.D., Yilmazer, U., Gogos, C., Sangani, H., Aral, B., Tsenoglou, C., "Development of Experimental Techniques and Simulation Methods to Analyze Mixing in Co-rotating Twin Screw Extrusion", Advances in Polymer Technology, Vol. 8, No. 4, 337-353, (1988).

Kalyon, D.M., Sangani, H.N., "An Experimental Study of Distributive Mixing in Fully Intermeshing Co-rotating Twin Screw Extruders", Polym. Eng. Sci. Vol. 29, No. 15, (1989)

Kalyon, D.M., Jacob, C.; Yaras, P.,"Experimental Study of the Degree of Fill and Melt Densification in Fully-Intermeshing, Co-rotating Twin Screw Extruders", Plastics, Rubber and Composites Processing and Applications, v16,n3, p 193-200, (1991).

Kalyon, D.M., Lawal, A., Yacizi, R., Yaras, P., Railkar, S., "Mathematical Modeling and Experimental Studies of Twin Screw Extrusion Processing of Filled Polymers", Polyblends 97, SPE Retec, p 188-234, (1997)

Kaplan, A., Tadmor, Z., "Theoretical Model for Non-intermeshing Twin Screw Extruders", Polym. Eng. Sci. ,14, 1, p.58, (1974).

Karagiannis, A.. Ph. D. Thesis. McMaster University, Hamilton. (1989a).

Karagiannis, A., Hrymak, A.N., Vlachopoulos, J.,"Three-Dimensional Non-Isothermal Extrusion Flows", Rheol Acta, 28, p. 121 (1989b).

Keunings, R. "An Algorithm for the Simulation of Transient Viscoelastic Flows with Free Surfaces", J. of Comput. Phys.,62, p.199, (1986).

Keunings, R., "Progress and Challenges in Computational Rheology. Rheol Acta, 29, p. 556 (1990).

Kiani, A., Rakos, R., Sebastian, D.H., "Three Dimensional Computational Analysis of Fluted Mixing Devices" , Technical Papers SPE ANTEC, (1989).

Kiani, A., Andersen, P., Curry, J., "Modelling of Flow Fields in Distributive Mixing Elements", Technical Papers SPE ANTEC, (1992).

Kiani, A., Grald, E.W., Subbiah, S.,"Spectral Element Analysis of the Mixing Characteristics of Twin Screw Extruders", Simposium of Numerical Simulation of Mixing Phenomena, AiChE, (1992a).

Kiani, A., Samann, H. J., "Transient Flow Calculation of Corotating Twin Screw Extruders", Technical Papers, SPE ANTEC, (1993).

Kim, P.J., White, J.L.,"Flow Visulization and Residence Time Distributions in a Modular Co-rotating Twin Screw Extruder". Inter. Polym. Proc., IX, p. 108, (1994)

Kistler, S.F., Scriven, L.E., "Coating Flows", from Chapter 8 of Parson,J. and Richardson, S., Computational Analysis of Polymer Processing, Applied Science Publishers LTD, (1983).

Lawal, A., Kalyon, D.M., Zhenghua, J.,"Computational Study of Chaotic Mixing in Co-rotating Two Tipped Kneading Paddles: Two Dimensional Approach", Polym. Eng. Sci., Vol 33, No. 3, (1993).

Lawal, A., Kalyon, D.M., "Three Dimensional Analysis of Co-rotating Twin Screw Extrusion using Tools of Dynamics", Technical Papers SPE ANTEC, p.3397, (1993a)

Lawal, A., Kalyon, D.M., "Simulation of Intensity of Segregation Distributions Using Three-Dimensional FEM Analysis: Application to Corotating Twin Screw Extrusion Processing", J. App. Polym. Sci., Vol 58, p.1501-1507, (1995)

Liu, L., Funatsu, K. ,"Study of Flow and Mixing in Full Flight Twin Screw Extruders", AIChE Annual Meeting, (1996).

Liu, T.J., "An Efficient Matrix Solver for Finite Element Analysis of Non-Newtonian Fluid Problems", Int. J Num Meth Fluids, 5, p. 929 (1985).

Lynch, D., "Unified Aproach to Simulation on Deforming Elements with Application to Phase Change Problems", J. of Comput. Phys., 47, p.387, (1982).

Mack, A., Eise,K. , Science and Technology of Polymer Processing, N.P. Suh and N.Sung Eds., MIT Press, (1977).

Manas-Zloczower, I., Feke D. L. ,Inter.Polym.Proc. II.,185,(1988).

Manas-Zloczower, I., Cheng, J. J., Polym. Eng. Sci.,29,1059, (1989).

Manas-Zloczower, I., Feke D. L., Inter.Polym.Proc. IV,3,(1989a).

Manas-Zloczower, I., Wong T. H. ,Tech. Papers, SPE ANTEC, 1788,(1992).

Marchuk, G.I., Kuznetsov,Y.A., Matsokin, A.M., "Fictitious Domain and Domain Decomposition Methods", Soviet J. Numer. Anal Math Modelling, 1, 3-35, (1986).

Martelli, F.G., Twin Screw Extruders: A Basic Understand ,Van Nostrand Reinhold, (1983).

Mavridis, H., Finite Element Studies in Injection Mold Filling, Ph.D.Thesis, McMaster University, Hamilton,(1988)

McCullough, T.W., Hilton, B.T., "The Extrusion Performance of Co-rotating Intermeshing Twin Screw Extruder Screw Elements - An Experimental Investigation", Technical Papers SPE ANTEC, p 3372, (1993).
Mitsoulis, E., Mirza, F.A., Vlachopoulos, J., "A Numerical Study of the Effect of Normal Stresses and Elongational Viscosity on Entry Vortex Growth and Extrudate Swell", Polym. Eng. Sci., 25, p. 677 (1985).

Mitsoulis, E., Finite Element Analysis of Two-Dimensional Polymer Melt Flows, Ph. D. Thesis, McMaster University, Hamilton. (1984).

Nauman, E.B., Buffham, B.A., Mixing in Continuous Flow Systems , John Wiley & Sons, (1983).

Nguyen, K.T., "Finite Element Modeling of a Counter-rotating,Non-intermeshing Twin Screw Extruder" , Polym. Eng. Sci., 29,11, p.709, (1989).

Nguyen, K.T., Lindt, J.T., "Finite Element Modelling of a Counter-rotating, Non - intermeshing Twin Screw Extruder", Technical Papers SPE ANTEC, (1989).

Noh, W.F., in : Methods of Computational Physics, 3, p. 117, (1964).

Oberlehner, J., Cassagnau, P., Michel, A.,"Local Residence Time Distribution in a Twin Screw Extruder", Chem. Eng. Sci. ,49, p 3897-3907, (1994).

Ottino, J.M., The Kinematics of Mixing: Stretching, Chaos, and Transport, Cambridge University Press, (1989).

Patera, A.T., "A Spectral Element Method for Fluid Dynamics: Laminar Flow in a Channel Expansion", Journal of Computational Physics, 54, p.468, (1984).

Rakos, R., Kiani, A., Sebastian, D.H.,"Computer Design Aids for Non-Axisymetric Profile Dies", Technical Papers SPE ANTEC, (1989).

Ramamurthy, A.V. , "Wall Slip in Viscous Fluids and Influence of Materials and Construction", J. Rheo,30,p. 337 (1986).

Rauwendaal, C., Polymer Extrusion, Hanser Publish., (1986).

Rauwendaal, C., "Analysis and Experimental Evaluation of Twin Screw Extruders", Polym. Eng. Sci., 21, 16, p. 1092, (1981).

Rauwendaal, C., "Which Twin Screw Extruder is for You?", Plastics Formulating and Compounding, November/December, (1995)

Reddy, J.N., Introduction to the Finite Element Method. McGraw-Hill, (1984).

Robichaud, M.P., Tanguy, P.A., Fortin, M., "An Iterative Implementation of the Uzawa Algorithm for 3-D Fluid Flow Problems". Int. J Num Meth Fluids, 10, p. 429, (1990).

Samann, H., Werner & Pleiderer Co., Internal Report, from: Kiani, A., Grald, E.W., Subbiah, S.,"Spectral Element Analysis of the Mixing Characteristics of Twin Screw Extruders", Symposium of Numerical Simulation of Mixing Phenomena, AIChE, (1992).

Sastrohartono, T.; Esseghir, M.; Kwon, T. H.; Semas, V,"Numerical and Experimental Studies of the Flow in the Nip Region of a Partially Intermeshing Co-rotating Twin-Screw Extruder", Polym. Eng.Sci. v 30 n 21, p 1382-1398, (1990).

Sebastian, D.H., Rakos, R., "New Insights into the Modeling of Corotating Intermeshing Twin Screw Extruders", Technical Papers SPE ANTEC, (1990).

Sloan, S.W., Randolph, M.F., "Automatic Element Reordering for Finite Element Analysis with Frontal Solution Schemes". Int. J Num Met Eng, 19, p. 1153 (1983).

Souvaliotis, A., Jana, S. C., Ottino, J. M., "Potentialities and Limitations of Mixing Simulations", AIChE Journal, Vol. 41, No. 7, p. 1605, (1995).

Spencer, R.S., Wiley, R.N., "The Mixing of Very Viscous Liquids", J. Colloid Sci.,6, p. 133,(1951).

Stasiek, J., Plaste und Kautschuk, 20,90, (1973).

Street, L.F. , Technical Papers SPE ANTEC, (1969).

Szydlowski, R., Brzoskowski, R., White, J.L. ,"Modelling Flow in an Intermeshing Co-rotating Twin Screw Extruder:: Flow in Kneading Discs" , Intern. Polym. Processing, 4, (1987).

Tadmor, Z., Klein, I. , Engineering Priciples of Plasticating Extrusion, Van Nostrand Reinhold, (1970).

Tadmor, Z., Broyer, E., Gutfinger, C., "Flow Analysis Network (FAN) - A Method for Solving Problems in Polymer Processing" , Polym. Eng. Sci., 14, 9, p. 660, (1974).

Tadmor, Z., Gogos, C.G., Principles of Polymer Processing , John Wiley & Sons, (1979).

Taylor, C., Hood, P.,"A Numerical Solution of the Navier-Stokes Equations Using the Finite Element Technique". Comp. Fluids, 1, p. 73 (1973).

Taylor, C., Hughes, T.G., Finite Element Programming of the Navier-Stokes Equations. Pineridge Press, Ltd. (1981).

TECPLOT, User's Manual, Version 6, Amtec Engineering, (1993).

Todd, D.B., Polym. Eng. Sci.,15,p.437, (1975).

Todd, D.B., "Drag and Pressure Flow in Twin Screw Extruders", Technical Papers, ANTEC, p. 168, (1989).

Torres, A., Finite Element Analysis of Layer Non-Uniformity in Polymer Coextrusion Flows, Ph.D. Thesis, McMaster University, (1995).

Vrentas, J.S., Vrentas, C.M., Ling, H.C.,"Boundary Conditions at Inflow and Outflow Planes", J Non-Newt. Fluid Mech., 19, 1-13, (1985).

Wang, H.P., Lee, H.S., "Numerical Techniques for Free and Moving Boundary Problems", in Chapter 8 from Charles Tucker III, Computer Modeling for Polymer Processing, Hanser P. (1989).

Wang, Y, White, J., Szydlowski, W.,"Flow in a Modular Intermeshing Co-rotating Twin Screw Extruder", Intern. Polym. Proc. IV, p.262, (1989a)

Werner, H.,Dr. Ing. Diss, TU Munich, (1976).

White, J. L., Twin Screw Extrusion: Technology and Principles Hanser, NY, (1990)

White, J.L., Montes, S., Kim, J.K., "Experimental Sudy and Practical Engineering Analysis of Flow Mechanisms and Starvation in a Modular Intermeshing Co-rotating Twin Screw Extruder", Kautsch. Gummi Kunstst.,43, p.20, (1990a)

Yang, H.H., Flow Field Analysis of Batch and Continuous Mixing Equipment, Ph D. Thesis. Western Reserve University, (1993).

Zerafati, S., Bigio, D., "Area Deformation as a Base for Mixing Prediction in 3-D Complex Flow Fiels", PPS Tenth Annual Meeting, 54,(1994).

Zienkiewicz, O.C.. The Finite Element Method Displayed. McGraw-Hill, (1984).

APPENDIX A
AUTOMATIC FINITE ELEMENT MESH GENERATOR

The complex geometry of the volume occupied by the fluid in the kneading disc section of an ICRTSE required the development of a tailored finite element generator. The mesh generator was designed to use 27-node triquadratic brick elements. The objective was to produce a mesh from a minimum number of input data values. The mesh generator requires the specification of system dimensions and number of elements. These parameters are specified in Tables A.1 and A.2.

• Center distance of the discs
• Screw outside diameter
• Screw root diameter
• Barrel bore diameter
• Number of discs
• Stagger angle
• Disc width
• Axial clearance between discs
• Radial clearance between disc
• Clearance disc-barrel

Table A.1. Geometry parameters used by the mesh generator

• Number of element in the axial direction
• Number of elements in the radial direction
• Number of elements in the circumferential direction

Table A.2. Mesh parameters used by the mesh generator

The mesh generation also includes the imposition of boundary conditions. For the flow calculations in the kneading disc section of an ICRTSE, two types of boundary conditions are used. Essential boundary conditions are imposed on the solid boundaries using the assumption

of no-slip. For the rotating screws, it is necessary to specify the rotational speed whereas at the barrel walls the velocity is set to zero. For the inlet and outlet boundary condition, a nominal value of normal stress difference is imposed between inlet and outlet planes.

Figure A.1 shows the flow chart with the general instructions performed by the mesh generator. The generator was specifically designed for two tipped kneading blocks, although its extension to different disc shapes such as one or three tipped discs is possible. Figure A.2 shows four meshes with stagger angles of 30, 45, 60 and 90 degrees in forward configurations. Note that the meshes for 30 and 60 degrees have seven pairs of disc, whereas the mesh for 45 has five pairs and the mesh for 90 degrees has four. Figure A.3 shows only the surface mesh for the purpose of visualization of the complex geometry of the kneading blocks.

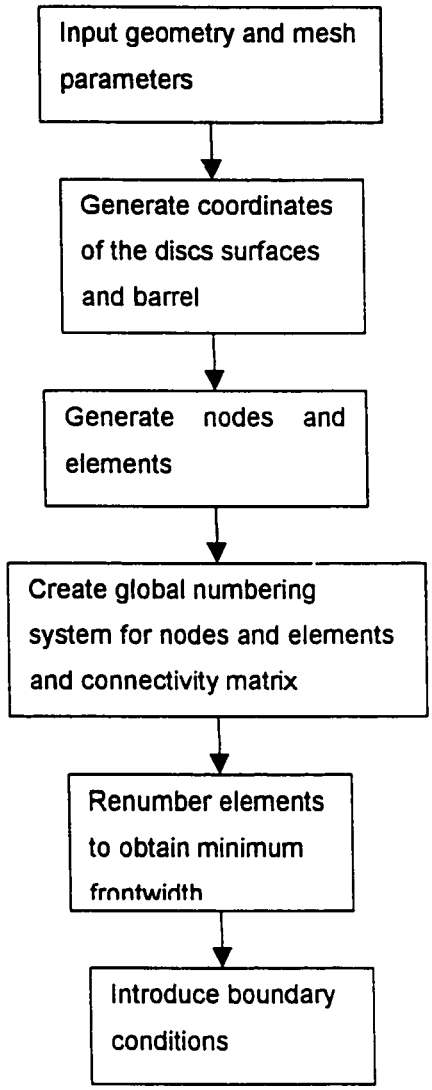

Figure A.1. Flow chart of the mesh generation code

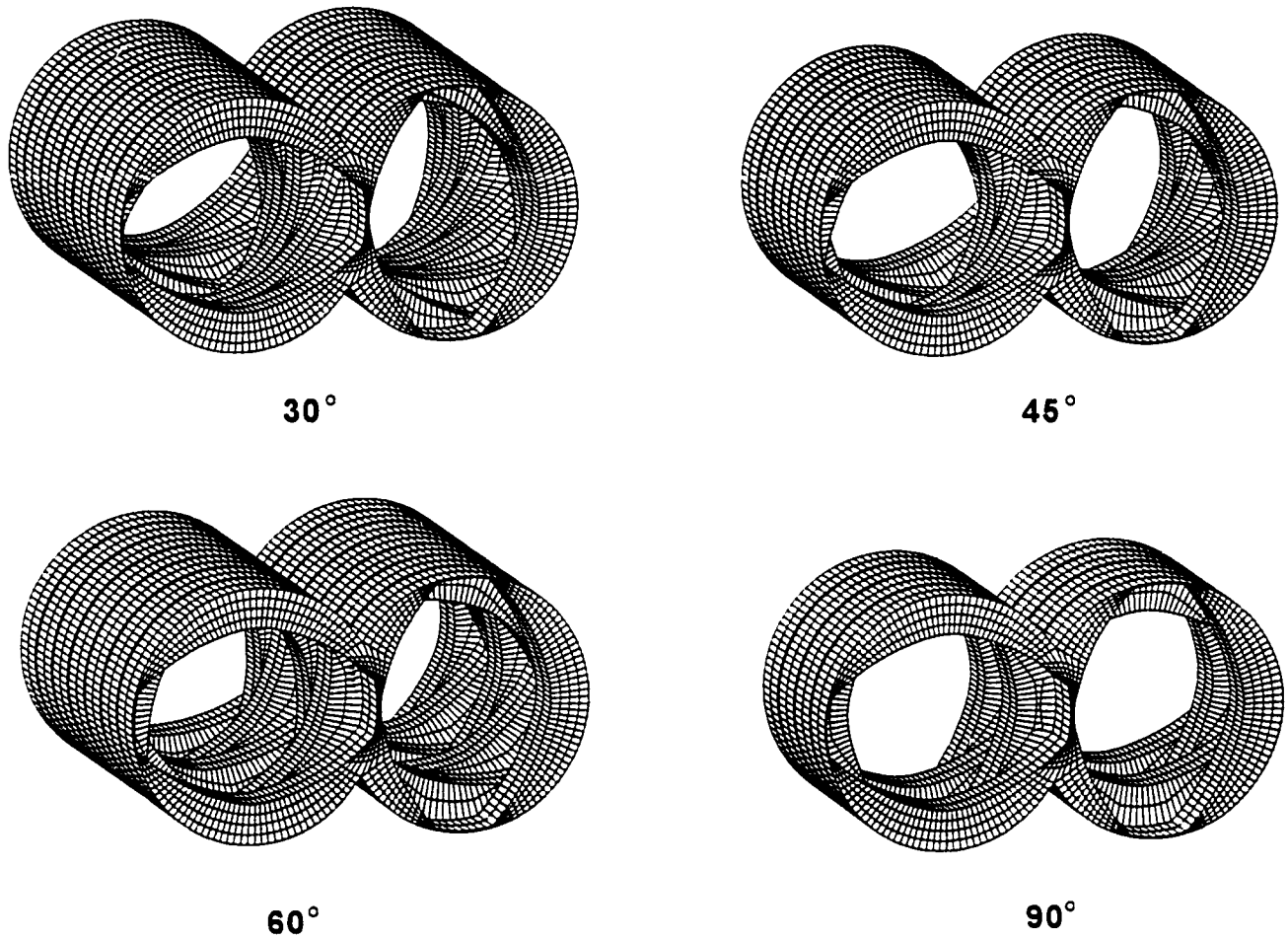

Figure A.2. Finite element mesh for various stagger angles.

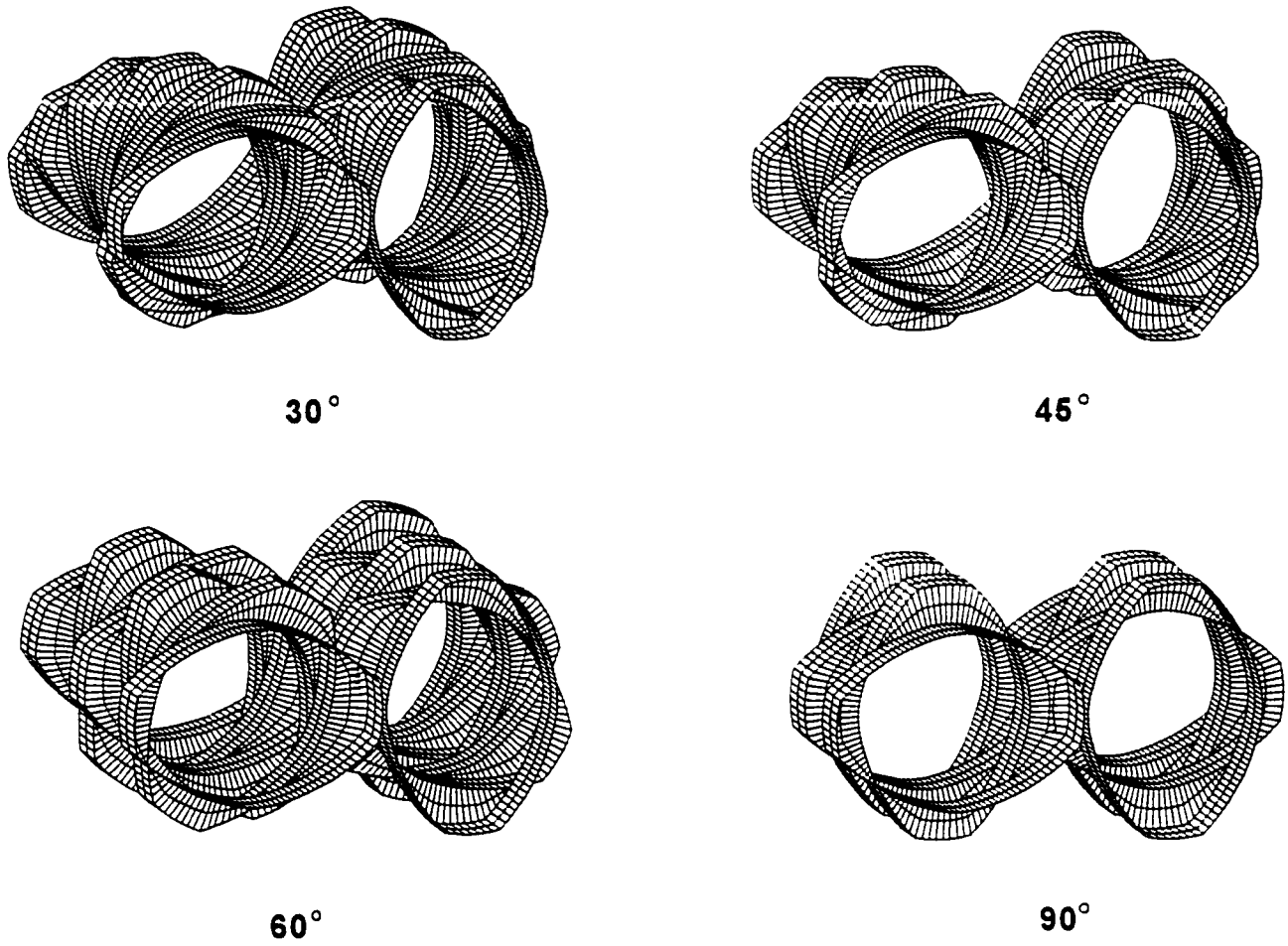

Figure A3. Surface finite element mesh for various stagger angles

Fortran code for the finite element mesh generator

```
subroutine mesh
      include 'commons.bi'
C=======================================
C- MESH: Program for mesh generation
C- in the three-dimensional codes.
C- By: Victor Bravo . August 11th, 1993.
C-
C- Generate kneading disc twin screw geometry
C- March 20th, 1994
C- Victor Bravo
C-
C=======================================
      DIMENSION ESP(400),GAMMAT(400),R(400),THETA(400)
      DIMENSION X(400),PSIRAD(400),BOUN(4000),PSICIRR(400)
      DIMENSION X1(400),Y(400),THETADEG(400),THETA1RAD(400)
      DIMENSION PSI(400),VXX(400),VYY(400),XB(400),YB(400),ZS(400)
      DIMENSION YS(400),Z(400),XCIR(400),YCIRA(400),ZCIRA(400)
      DIMENSION VXA(400),VYA(400),XBA(400),YBA(400),YCIR(400),ZCIR(400)
      DIMENSION PSICIR(400),YNODY(400,10),ZNODZ(400,10),XNODX(400,10)
      DIMENSION YSA(400),ZA(400),VELO(400),XMODUA(400),XMODUB(400)
      DIMENSION YSB(400),ZSB(400),ZSA(400),YCIRB(400),ZCIRB(400)
      DIMENSION ILASS(400),PSICIRRA(400),PSICIRRB(400),ZZ(400)
C---------------------------------------
C- SUBROUTINE GRID
C---------------------------------------
      OMEGA=0.
      X0=0.
      READ(60,*) CENT,GAP,DI,D0,DB,XLGTH
      READ(60,*) NW,NPHI,NELX
      R0=D0/2.d0
      RI=DI/2.d0
      RB=DB/2.d0
      XX=(CENT-GAP)/2.d0
      XXX=XX/R0
      ALPHA=ATAN(SQRT(1.d0-XXX*XXX)/XXX)
      ALPHA=180.d0*ALPHA/(4.d0*ATAN(1.d0))
      PHI=45.d0-ALPHA
      WW=1.d0/NW
      DO I=1,NW+1
        WEIGHT(1,I) = (I-1)*WW
      ENDDO
      SPAN=X0-DB
      SPAN1=X0+DB
      NPY=INT((2*NPHI*ALPHA)/PHI) + 1
      THETA1=-ALPHA/NPY
      ANGLE1=90.d0-ALPHA
      ANGLE2=90.d0
      ANGLE3=90.d0+ALPHA
      NP1=INT(ABS(ANGLE1/THETA1/2)+1)
      NP2=INT(ABS(ANGLE2/THETA1/2)+1)
      NP3=INT(ABS(ANGLE3/THETA1/2)+1)
      NE1=NP1/2
      NE2=(NP2+1)/2
      NE3=NP3/2
```

```
      NELTH=4*NPHI+2*NPY
      NELR=NW/2
      NNR=2*NELR+1
      NNTH=2*NELTH
      NNX=2*NELX+1
      NNX1=NNX/2-1
      NNX2=NNX-NNX1-1
      POSX=XLGTH/(.1d0*NNX1+NNX2+3*NN)
      NN=2*NNX*NNTH*NNR-NNX*(ABS(NP3-NP1+1))
      NEL=2*NELTH*NELR*NELX
      NEL2DCS=NEL/NELX
      NEL2DCSH=NELR*NELTH
      NN2DCS=NN/NNX
      NN2DCSH=NNTH*NNR
      NFREE2D=4*NELTH
      NVAR=5
      NTOTV=NVAR*NN
      LNODE27=27
      NVEL27=NVAR*LNODE27
      NOFDSC=2
      nodes=nn
      maxnod=27
      maxdeg=124
      do i=1,nel
         npe(i)=27
      enddo
C-----------------------------------------------------------------------
      write(*,*)
      WRITE(*,*) '*****Entering FEM generation*****'
      write(*,*)
      write(*,*) 'Elements :',NEL,' Nodes :' ,NN
      write(*,*)
      write(*,*) 'Phase 1:generation of cross section of kneading discs'
      DO 2 I=1,NPY
        THETA1=THETA1+(ALPHA/NPY)
        THETA1RAD(I)=(4*ATAN(1.)/180)*THETA1
        X1(I)=R0*COS(THETA1RAD(I))
        Y(I)=R0*SIN(THETA1RAD(I))
        X(I)=(CENT-GAP)-X1(I)
        R(I)=X(I)/COS(THETA1RAD(I))
        GAMMAT(I)=90.d0-(2.d0*THETA1+PHI)
    2 CONTINUE
      NN1=0
      NNN=0
      DO 3 I=1,NPHI+1
        PSI(I)=(I-1)*PHI/ NPHI
        Z(I)=R0
    3 CONTINUE
      J=NPY
      DO 4,I=NPHI+2,NPY+NPHI+1
        PSI(I)=GAMMAT(J)
        Z(I)=R(J)
        J=J-1
    4 CONTINUE
      DO 5 I=NPY+NPHI+2,NPY+2*NPHI+1
        PSI(I)=PSI(I-1)+PHI/NPHI
        Z(I)=RI
```

```
    5 CONTINUE
      I0=I
      J=I0-2
      DO 6 I=I0,2*(NPY+2*NPHI)+1
        PSI(I)=180.d0-PSI(J)
        Z(I)=Z(J)
        J=J-1
    6 CONTINUE
      I0=I
      J=2
      DO 7 I=I0,4*(NPY+2*NPHI)+1
        PSI(I)=PSI(J)+180.d0
        Z(I)=Z(J)
        J=J+1
    7 CONTINUE
      NBOU=0
      IFLAG=0
      IFLAG1=0
      XPOS=-POSX
      FACT=1.d0
      ICN=0
      NNA=0
      ict=0
      ic2=112
      kt=0
c-----------------------------------------------------
      write(*,*)
      write(*,*) 'Phase 2: generation of coordinates'
c-----------------------------------------------------
      DO 8 K=1,NNX
        if ((ICN.LT.2).and.(k.lt.nnx-1).and.(k.gt.3)) then
            ic2=ic2-7
          endif
        if (k.gt.1) then
            if ((k.gt.5).and.(ICN.LT.2).and.(k.lt.nnx-3)) then
               FACT=.1d0
               ICN=ICN+1
             else
              if ((k.lt.4).or.(k.gt.nnx-2)) then
                 FACT=3.d0
                 ICN=ICN+1
               else
                 FACT=1.d0
                 ICN=ICN+1
               endif
             endif
           ENDIF
          IF (ICN.EQ.4) THEN
           ICN=0
          ENDIF
         XPOS=XPOS+FACT*POSX
         DO I=1,4*(NPY+2*NPHI)
           ZZ(I+ic2)=Z(I)
         ENDDO
         DO I=1,ic2
           PSI(4*(NPY+2*NPHI)+I)=PSI(I)
         ENDDO
```

```
      DO 9 I=1,4*(NPY+2*NPHI)
        ZZ(I+ic2)=ZZ(I+ic2)-0.0d0
        PSI(I+ic2)=PSI(I+ic2)+OMEGA
        PSICIR(I+ic2)=90.d0-PSI(I+ic2)
        PSIRAD(I+ic2)=PSI(I+ic2)*4.d0*ATAN(1.d0)/180.d0
        PSICIRRA(I+ic2)=PSICIR(I+ic2)*4.d0*ATAN(1.d0)/180.d0
        PSICIRRB(I+ic2)=PSICIRRA(I+ic2)+2.d0*ATAN(1.d0)
        YS(I+ic2)=X0+ZZ(I+ic2)*SIN(PSIRAD(I+ic2))
        ZS(I+ic2)=ZZ(I+ic2)*COS(PSIRAD(I+ic2))
        YCIR(I+ic2)=X0+RB*COS(PSICIRRA(I+ic2))
        ZCIR(I+ic2)=RB*SIN(PSICIRRA(I+ic2))
        tmpa=(YCIR(I+ic2)-YS(I+ic2))**2
        tmpb=(ZCIR(I+ic2)-ZS(I+ic2))**2
        XMODUA(I+ic2)=SQRT(tmpa+tmpb)
        XMODUB(I+ic2)=XMODUA(I+ic2)
    9 CONTINUE
      DO I=1,ic2
        PSI(I)=PSI(4*(NPY+2*NPHI)+I)
        PSICIR(I)=PSICIR(4*(NPY+2*NPHI)+I)
        PSIRAD(I)=PSIRAD(4*(NPY+2*NPHI)+I)
        PSICIRRA(I)=PSICIRRA(4*(NPY+2*NPHI)+I)
        PSICIRRB(I)=PSICIRRB(4*(NPY+2*NPHI)+I)
        YS(I)=YS(4*(NPY+2*NPHI)+I)
        ZS(I)=ZS(4*(NPY+2*NPHI)+I)
        YCIR(I)=YCIR(4*(NPY+2*NPHI)+I)
        ZCIR(I)=ZCIR(4*(NPY+2*NPHI)+I)
        XMODUA(I)=XMODUA(4*(NPY+2*NPHI)+I)
        XMODUB(I)=XMODUB(4*(NPY+2*NPHI)+I)
      ENDDO
C-----------------------------------------
      DO NO=1,NOFDSC
        IF (NO.EQ.1) THEN
          XSX=1.d0
          XSY=1.d0
          TTX=CENT/2.
          TTY=0.d0
          THETA2(3)=0.d0
        ELSE
          XSX=1.d0
          XSY=1.d0
          TTX=0.d0
          TTY=CENT/2.d0
          THETA2(3)=-4.d0*ATAN(1.d0)/2.d0
        ENDIF
        CALL TRANS
        DO I=1,4*(NPY+2*NPHI)
          COO(1,1)=YS(I)
          COO(2,1)=ZS(I)
          COO(3,1)=1.
          CALL MULT(XMM,COO,CC)
          IF (NO.EQ.1) THEN
            YSA(I)=CC(1,1)
            ZSA(I)=CC(2,1)
          ELSE
            YSB(I)=CC(1,1)
            ZSB(I)=CC(2,1)
          ENDIF
```

```
            COO(1,1)=YCIR(I)
            COO(2,1)=ZCIR(I)
            COO(3,1)=1.
            CALL MULT(XMM,COO,CC)
            IF (NO.EQ.1) THEN
              YCIRA(I)=CC(1,1)
              ZCIRA(I)=CC(2,1)
            ELSE
              YCIRB(I)=CC(1,1)
              ZCIRB(I)=CC(2,1)
            ENDIF
          END DO
        END DO
C-------------------------------------------------------------
C  THIS SPECIAL CONDITION IS FOR THE LAST SPINE, WHICH IS THE
C  SAME AS THE FIRST SPINE.
C-------------------------------------------------------------
          IF (I.EQ.4*(NPY+2*NPHI)+1) THEN
            NNN=0
          END IF
C-------------------------------------------------------------
        ICOUNT=0
C-------------------------------------------------------------
        KK=NP1+1-ict
        KK1=NP3-1-ict
        KK2=NP2-ict
        KK3=ABS(KK1-KK)/2
        DO KE=KK,KK1
          KN=KE
          IND1=(NP2+1)-KN-2*ict
          DO WHILE (IND1.LE.0)
            IND1=4*(NPY+2*NPHI)+IND1
          END DO
          DO WHILE (KN.LE.0)
            KN=4*(NPY+2*NPHI)+KN
          END DO
          IF (KE.EQ.KK) THEN
            KA=KN
          ENDIF
          RAA1=ZSA(KN)-ZCIRA(KN)
          RAA2=YSA(KN)-YCIRA(KN)
          RAA=SQRT(RAA1**2+RAA2**2)
          RBB1=ZSB(IND1)-ZCIRB(IND1)
          RBB2=YSB(IND1)-YCIRB(IND1)
          RBB=SQRT(RBB1**2+RBB2**2)
          PORC=DABS((ZSA(KN)-ZSB(IND1))/DB)
          IF (YSA(K).LT.0.) THEN
            IF (PORC.GT.1.D-4) THEN
              IF (ZSA(KN).GT.0.) THEN
                YSA(KN)=(1.5*YSA(KN)+.5*YSA(KN-1))/2.D0
                ZSA(KN)=(1.5*ZSA(KN)+.5*ZSA(KN-1))/2.D0
              ELSE
                YSA(KN)=(1.5*YSA(KN)+.5*YSA(KN+1))/2.D0
                ZSA(KN)=(1.5*ZSA(KN)+.5*ZSA(KN+1))/2.D0
              ENDIF
            ENDIF
          ELSE
```

```
            IF (PORC.GT.1.D-4) THEN
              IF (ZSB(IND1).GT.0.) THEN
                YSB(IND1)=(1.5*YSB(IND1)+.5*YSB(IND1+1))/2.D0
                ZSB(IND1)=(1.5*ZSB(IND1)+.5*ZSB(IND1+1))/2.D0
              ELSE
                YSB(IND1)=(1.5*YSB(IND1)+.5*YSB(IND1-1))/2.D0
                ZSB(IND1)=(1.5*ZSB(IND1)+.5*ZSB(IND1-1))/2.D0
              ENDIF
            ENDIF
          ENDIF
          IF (YSA(KN).LT.0.) THEN
            YCIRB(IND1)=(YSA(KN)+YSB(IND1))/2.
            ZCIRB(IND1)=(.5*ZSA(KN)+1.5*ZCIRB(IND1))/2.
           ELSE
            YCIRA(KN)=(YSB(IND1)+YSA(KN))/2.
            ZCIRA(KN)=(.5*ZSB(IND1)+1.5*ZCIRA(KN))/2.
           ENDIF
          IF (RAA.LE.1.05*(RB-R0)) THEN
            YCIRB(IND1)=YCIRA(KN)
            ZCIRB(IND1)=ZCIRA(KN)
          ENDIF
          IF (YSA(KN).LT.0.) THEN
            YCIRA(KN)=YCIRB(IND1)
            ZCIRA(KN)=ZCIRB(IND1)
          ELSE
            YCIRB(IND1)=YCIRA(KN)
            ZCIRB(IND1)=ZCIRA(KN)
          ENDIF
          TEM1=(YCIRB(IND1)-YSA(KN))**2
          TEM2=(ZCIRB(IND1)-ZSA(KN))**2
          XMODUA(KN)=SQRT(TEM1+TEM2)
          TEM1=(ZCIRB(IND1)-ZSA(KN))
          TEM2=(YCIRB(IND1)-YSA(KN))
          PSICIRRA(KN)=ATAN(TEM1/TEM2)
          TEM1=(YCIRB(IND1)-YSB(IND1))**2
          TEM2=(ZCIRB(IND1)-ZSB(IND1))**2
          XMODUB(IND1)=SQRT(TEM1+TEM2)
          TEM1=(ZCIRB(IND1)-ZSB(IND1))
          TEM2=(YCIRB(IND1)-YSB(IND1))
          PSICIRRB(IND1)=ATAN(TEM1/TEM2)
          PSICIRRB(IND1)=-(4.*ATAN(1.)-PSICIRRB(IND1))
        ENDDO
C-------------------------------------------------------------
C   SPECIAL CONDITION FOR THE LAST ROW OF NODES OF A AND B
C-------------------------------------------------------------
      YCIRB(4*(NPY+2*NPHI)+1)=YCIRB(1)
      ZCIRB(4*(NPY+2*NPHI)+1)=ZCIRB(1)
      XMODUB(4*(NPY+2*NPHI)+1)=XMODUB(1)
      PSICIRRB(4*(NPY+2*NPHI)+1)=PSICIRRB(1)
      YCIRA(4*(NPY+2*NPHI)+1)=YCIRA(1)
      ZCIRA(4*(NPY+2*NPHI)+1)=ZCIRA(1)
      XMODUA(4*(NPY+2*NPHI)+1)=XMODUA(1)
      PSICIRRA(4*(NPY+2*NPHI)+1)=PSICIRRA(1)
C-------------------------------------------------------------
      DO I=1,4*(NPY+2*NPHI)
        DO J=1,NW+1
          NNA = NNA + 1
```

```
          YNODY(I, J)=YSA(I)+WEIGHT(1, J)*XMODUA(I)*COS(PSICIRRA(I))
          ZNODZ(I, J)=ZSA(I)+WEIGHT(1, J)*XMODUA(I)*SIN(PSICIRRA(I))
2020      FORMAT(I6,2X,3(F10.4,2X))
          YNOD(NNA+kt*nnr)=YNODY(I, J)/(RB-RI)
          ZNOD(NNA+kt*nnr)=ZNODZ(I, J)/(RB-RI)
          XNOD(NNA+kt*nnr)=XPOS/(RB-RI)
        ENDDO
      ENDDO
            DO innw=1,kt*nnr
              ii1=(k-1)*nn2dcs+innw
              ii2=(k-1)*nn2dcs+nn2dcsh+innw
              YNOD(ii1)=YNOD(ii2)
              ZNOD(ii1)=ZNOD(ii2)
              XNOD(ii1)=XNOD(ii2)
            ENDDO
        NPP1=(NP2+1)-NP1-ict
        NPP3=(NP2+1)-NP3-ict
        DO WHILE (NPP1.LE.0)
          NPP1=4*(NPY+2*NPHI)+NPP1
        END DO
        DO WHILE (NPP3.LE.0)
          NPP3=4*(NPY+2*NPHI)+NPP3
        END DO
        ilass(1)=nnr
        DO I=1,4*(NPY+2*NPHI)
          IF ((NPP1-NPP3).LT.0) THEN
            IF ((I.GT.NPP1).AND.(I.LT.NPP3)) THEN
              ILAST=1
            ELSE
              ILAST=0
            ENDIF
          ELSE
            IF ((I.LE.NPP1).AND.(I.GE.NPP3)) THEN
              ILAST=0
            ELSE
              ILAST=1
            ENDIF
         ENDIF
          ilass(i)=ilast
          DO  J=1,NW+ILAST
            NNA = NNA + 1
            YNODY(I, J)=YSB(I)+WEIGHT(1, J)*XMODUB(I)*COS(PSICIRRB(I))
            ZNODZ(I, J)=ZSB(I)+WEIGHT(1, J)*XMODUB(I)*SIN(PSICIRRB(I))
            if (i.eq.1) then
               YNOD(NNA+kt*nnr)=YNODY(I, J)/(RB-RI)
               ZNOD(NNA+kt*nnr)=ZNODZ(I, J)/(RB-RI)
               XNOD(NNA+kt*nnr)=XPOS/(RB-RI)
            else
               YNOD(NNA+kt*(nw+ilass(i-1)))=YNODY(I, J)/(RB-RI)
               ZNOD(NNA+kt*(nw+ilass(i-1)))=ZNODZ(I, J)/(RB-RI)
               XNOD(NNA+kt*(nw+ilass(i-1)))=XPOS/(RB-RI)
            endif
          ENDDO
         ENDDO
            DO innw=1,kt*(nw+1)
              ii3=(k-1)*nn2dcs+nn2dcsh+innw
              ii4=k*nn2dcs+innw
```

```
              YNOD(ii3)=YNOD(ii4)
              ZNOD(ii3)=ZNOD(ii4)
              XNOD(ii3)=XNOD(ii4)
            ENDDO
    8 CONTINUE
      IEL=0
      ict=0
      IELX=0
      NN1=0
      NELE1=0
C--------------------------------------
C- Loop to create the connectivities
C- IN1 is the node indicator
C--------------------------------------
      write(*,*)
      write(*,*)'Phase 3: conectivities'
c--------------------------------------
c  This do indicates the inlet elements
c--------------------------------------
      call d2init(ind,28,nel)
      do i28=1,nel2dcs
           ind(28,i28)=1
      enddo
c--------------------------------------
c  This do indicates the outlet elements
c--------------------------------------
      do i28=nel2dcs*(nelx-1)+1,nel2dcs*nelx
           ind(28,i28)=2
      enddo
c--------------------------------------
      DO 11 IX1=1,NELX
      IELX=0
        DO 12 ITH=1,NELTH
          IELX=IELX+1
          DO 13 IR1=1,NELR
            IEL=IEL+1
            IF (IX1.EQ.1) THEN
              IN1=(ITH-1)*NNR*2+2*IR1-1
            ELSE
              IN1=(ITH-1)*NNR*2+2*IR1-1+NN1-NN2DCS
            END IF
            IND(1, IEL) = IN1 + 2 * NNR
            IND(2, IEL) = IND(1, IEL) + NN2DCS
            IND(3, IEL) = IND(1, IEL) + 2 * NN2DCS
            IND(4, IEL) = IN1 + 2 * NNR + 1
            IND(5, IEL) = IND(4, IEL) + NN2DCS
            IND(6, IEL) = IND(4, IEL) + 2 * NN2DCS
            IND(7, IEL) = IN1 + 2 * NNR + 2
            IND(8, IEL) = IND(7, IEL) + NN2DCS
            IND(9, IEL) = IND(7, IEL) + 2 * NN2DCS
            IND(10, IEL) = IN1 + NNR
            IND(11, IEL) = IND(10, IEL) + NN2DCS
            IND(12, IEL) = IND(10, IEL) + 2 * NN2DCS
            IND(13, IEL) = IN1 + NNR + 1
            IND(14, IEL) = IND(13, IEL) + NN2DCS
            IND(15, IEL) = IND(13, IEL) + 2 * NN2DCS
            IND(16, IEL) = IN1 + NNR + 2
```

```
            IND(17, IEL) = IND(16, IEL) + NN2DCS
            IND(18, IEL) = IND(16, IEL) + 2 * NN2DCS
            IND(19, IEL) = IN1
            IND(20, IEL) = IND(19, IEL) + NN2DCS
            IND(21, IEL) = IND(19, IEL) + 2 * NN2DCS
            IND(22, IEL) = IN1 + 1
            IND(23, IEL) = IND(22, IEL) + NN2DCS
            IND(24, IEL) = IND(22, IEL) + 2 * NN2DCS
            IND(25, IEL) = IN1 + 2
            IND(26, IEL) = IND(25, IEL) + NN2DCS
            IND(27, IEL) = IND(25, IEL) + 2 * NN2DCS
   13     CONTINUE
   12   CONTINUE
C---------------------------------------------------------------
C THIS LOOP CHANGES THE CONECTIVITIES FOR THE LAST SPINE
C ACCORDING TO THE NUMBERING OF FIRST SPINE.
C---------------------------------------------------------------
        INIT = IEL-NELR*NELTH+1
        IEL=IEL-NELR
        DO J=INIT,INIT+NELR-1
          IEL=IEL+1
          IND(1, IEL) = IND(19, J)
          IND(2, IEL) = IND(20, J)
          IND(3, IEL) = IND(21, J)
          IND(4, IEL) = IND(22, J)
          IND(5, IEL) = IND(23, J)
          IND(6, IEL) = IND(24, J)
          IND(7, IEL) = IND(25, J)
          IND(8, IEL) = IND(26, J)
          IND(9, IEL) = IND(27, J)
        ENDDO
c---------------------------------------------------------------
c Second disc ......
c---------------------------------------------------------------
      ILAST1=-2
      ilast2=0
      ilast3=0
      IFLOG=0
      IFLOG1=0
      NE1=NP1/2-ict
      NE2=(NP2+1)/2-ict
      NE3=NP3/2-ict
      INDEL1=NE2-NE1
      INDEL3=NE2-NE3
      DO WHILE (INDEL1.LE.NEL2DCSH/NELR)
        INDEL1=NEL2DCSH/NELR+INDEL1
      ENDDO
      DO WHILE (INDEL3.LE.NEL2DCSH/NELR)
        INDEL3=NEL2DCSH/NELR+INDEL3
      ENDDO
      DO ITH=1,NELTH
        IELX=IELX+1
        IFLUG=0
        DO IR1=1,NELR
          IEL=IEL+1
          IF ((IELX.GE.INDEL3).AND.(IELX.LE.NEL2DCS/NELR)) THEN
           IF (IFLUG.EQ.0) THEN
```

```
  IFLUG=1
  IF (IFLOG1.EQ.0) THEN
    ILAST1=ILAST1-2
    IFLOG1=1
  ENDIF
  ILAST1=ILAST1+2
  ilast2=ilast1+1
  ilast3=ilast2+1
 ENDIF
ELSE IF ((IELX.GT.NEL2DCSH/NELR).AND.(IELX.LT.INDEL1)) THEN
 IF (IFLUG.EQ.0) THEN
  IFLUG=1
  ILAST1=ILAST1+2
  ilast2=ilast1+1
  ilast3=ilast2+1
 ENDIF
ELSE IF (IELX.EQ.INDEL1) THEN
  IF (IFLOG.EQ.0) THEN
    ILAST1=ILAST1+2
    ILAST2=ILAST1+1
    ILAST3=ILAST1+1
    IFLOG=1
  else
    ilast1=ilast1
    ilast2=ilast1+1
    ilast3=ilast2
  ENDIF
ELSE
  IF (IFLOG.EQ.1) THEN
    ILAST1=ILAST1+1
    IFLOG=2
  ENDIF
    ILAST1=ILAST1
    ILAST2=ILAST1
    ILAST3=ILAST1
ENDIF
  IF (IX1.EQ.1) THEN
    IN1=(ITH-1)*NNR*2+2*IR1-1
  ELSE
    IN1=(ITH-1)*NNR*2+2*IR1-1+NN1-NN2DCS
  END IF
  IND(1, IEL) = (NN2DCSH)+IN1 + 2 * NNR-ILAST3
  IND(2, IEL) = IND(1, IEL) + NN2DCS
  IND(3, IEL) = IND(1, IEL) + 2 * NN2DCS
  IND(4, IEL) = (NN2DCSH)+IN1 + 2 * NNR + 1-ILAST3
  IND(5, IEL) = IND(4, IEL) + NN2DCS
  IND(6, IEL) = IND(4, IEL) + 2 * NN2DCS
  IND(7, IEL) = (NN2DCSH)+IN1 + 2 * NNR + 2-ILAST3
  IND(8, IEL) = IND(7, IEL) + NN2DCS
  IND(9, IEL) = IND(7, IEL) + 2 * NN2DCS
  IND(10, IEL) = (NN2DCSH)+IN1 + NNR-ILAST2
  IND(11, IEL) = IND(10, IEL) + NN2DCS
  IND(12, IEL) = IND(10, IEL) + 2 * NN2DCS
  IND(13, IEL) = (NN2DCSH)+IN1 + NNR + 1-ILAST2
  IND(14, IEL) = IND(13, IEL) + NN2DCS
  IND(15, IEL) = IND(13, IEL) + 2 * NN2DCS
  IND(16, IEL) = (NN2DCSH)+IN1 + NNR + 2-ILAST2
```

```
            IND(17, IEL) = IND(16, IEL) + NN2DCS
            IND(18, IEL) = IND(16, IEL) + 2 * NN2DCS
            IND(19, IEL) = (NN2DCSH)+IN1-ILAST1
            IND(20, IEL) = IND(19, IEL) + NN2DCS
            IND(21, IEL) = IND(19, IEL) + 2 * NN2DCS
            IND(22, IEL) = (NN2DCSH)+IN1 + 1-ILAST1
            IND(23, IEL) = IND(22, IEL) + NN2DCS
            IND(24, IEL) = IND(22, IEL) + 2 * NN2DCS
            IND(25, IEL) = (NN2DCSH)+IN1 + 2-ILAST1
            IND(26, IEL) = IND(25, IEL) + NN2DCS
            IND(27, IEL) = IND(25, IEL) + 2 * NN2DCS
          ENDDO
        ENDDO
C-------------------------------------------------------------
C THIS LOOP CHANGES THE CONECTIVITIES FOR THE LAST SPINE
C ACCORDING TO THE NUMBERING OF FIRST SPINE.
C-------------------------------------------------------------
        INIT = IEL-NELR*NELTH+1
        IEL=IEL-NELR
        DO J=INIT,INIT+NELR-1
          IEL=IEL+1
          IND(1, IEL) = IND(19, J)
          IND(2, IEL) = IND(20, J)
          IND(3, IEL) = IND(21, J)
          IND(4, IEL) = IND(22, J)
          IND(5, IEL) = IND(23, J)
          IND(6, IEL) = IND(24, J)
          IND(7, IEL) = IND(25, J)
          IND(8, IEL) = IND(26, J)
          IND(9, IEL) = IND(27, J)
        ENDDO
      NE1=NP1/2-ict
      NE2=(NP2+1)/2-ict
      NE3=NP3/2-ict
      DO KEO=NE1+1,NE3
        K=KEO
        INDEL=NE2-K-ict
        DO WHILE (INDEL.LE.NEL2DCSH/NELR)
          INDEL=NEL2DCSH/NELR+INDEL
        ENDDO
        DO WHILE (K.LE.0)
          K=NEL2DCSH/NELR+K
        ENDDO
        IND(7,NELR*INDEL+NELE1)=IND(25,NELR*K+NELE1)
        IND(8,NELR*INDEL+NELE1)=IND(26,NELR*K+NELE1)
        IND(9,NELR*INDEL+NELE1)=IND(27,NELR*K+NELE1)
        IND(16,NELR*INDEL+NELE1)=IND(16,NELR*K+NELE1)
        IND(17,NELR*INDEL+NELE1)=IND(17,NELR*K+NELE1)
        IND(18,NELR*INDEL+NELE1)=IND(18,NELR*K+NELE1)
        IND(25,NELR*INDEL+NELE1)=IND(7,NELR*K+NELE1)
        IND(26,NELR*INDEL+NELE1)=IND(8,NELR*K+NELE1)
        IND(27,NELR*INDEL+NELE1)=IND(9,NELR*K+NELE1)
      ENDDO
      IND(25,NELR*INDEL1+NELE1)=IND(7,NELR*(INDEL1-1)+NELE1)
      IND(26,NELR*INDEL1+NELE1)=IND(8,NELR*(INDEL1-1)+NELE1)
      IND(27,NELR*INDEL1+NELE1)=IND(9,NELR*(INDEL1-1)+NELE1)
      IND(7,NELR*(INDEL3-1)+NELE1)=IND(25,NELR*INDEL3+NELE1)
```

```
      IND(8,NELR*(INDEL3-1)+NELE1)=IND(26,NELR*INDEL3+NELE1)
      IND(9,NELR*(INDEL3-1)+NELE1)=IND(27,NELR*INDEL3+NELE1)
        IF (IX1.EQ.1) THEN
          NN1=NN1+3*NN2DCS
          NELE1=NELE1+NEL2DCS
          NFREE=NFREE+3*NFREE2D
        ELSE
          NN1=NN1+2*NN2DCS
          NELE1=NELE1+NEL2DCS
          NFREE=NFREE+2*NFREE2D
        END IF
   11 CONTINUE
c*****************************************************
c     write the unchanged connectivities for later use
c*****************************************************
      do i=1,nel
        write(71,200) I
        write(71,200) (IND(KK, I),KK=1,27)
      enddo
      close (71)
c-----------------------------------------------------
c Correction for the middle nodes in twisted elements
c-----------------------------------------------------
      do ielnum=1,nel
        call local
        XNOD(ICO(2))=(XNOD(ICO(1))+XNOD(ICO(3)))/2.
        XNOD(ICO(5))=(XNOD(ICO(4))+XNOD(ICO(6)))/2.
        XNOD(ICO(8))=(XNOD(ICO(7))+XNOD(ICO(9)))/2.
        XNOD(ICO(11))=(XNOD(ICO(10))+XNOD(ICO(12)))/2.
        XNOD(ICO(14))=(XNOD(ICO(13))+XNOD(ICO(15)))/2.
        XNOD(ICO(17))=(XNOD(ICO(16))+XNOD(ICO(18)))/2.
        XNOD(ICO(20))=(XNOD(ICO(19))+XNOD(ICO(21)))/2.
        XNOD(ICO(23))=(XNOD(ICO(22))+XNOD(ICO(24)))/2.
        XNOD(ICO(26))=(XNOD(ICO(25))+XNOD(ICO(27)))/2.
c-----------------------------------------------------
c       same thing for the y's
c-----------------------------------------------------
        YNOD(ICO(2))=(YNOD(ICO(1))+YNOD(ICO(3)))/2.
        YNOD(ICO(5))=(YNOD(ICO(4))+YNOD(ICO(6)))/2.
        YNOD(ICO(8))=(YNOD(ICO(7))+YNOD(ICO(9)))/2.
        YNOD(ICO(11))=(YNOD(ICO(10))+YNOD(ICO(12)))/2.
        YNOD(ICO(14))=(YNOD(ICO(13))+YNOD(ICO(15)))/2.
        YNOD(ICO(17))=(YNOD(ICO(16))+YNOD(ICO(18)))/2.
        YNOD(ICO(20))=(YNOD(ICO(19))+YNOD(ICO(21)))/2.
        YNOD(ICO(23))=(YNOD(ICO(22))+YNOD(ICO(24)))/2.
        YNOD(ICO(26))=(YNOD(ICO(25))+YNOD(ICO(27)))/2.
c-----------------------------------------------------
c       and same thing for the z's
c-----------------------------------------------------
        ZNOD(ICO(2))=(ZNOD(ICO(1))+ZNOD(ICO(3)))/2.
        ZNOD(ICO(5))=(ZNOD(ICO(4))+ZNOD(ICO(6)))/2.
        ZNOD(ICO(8))=(ZNOD(ICO(7))+ZNOD(ICO(9)))/2.
        ZNOD(ICO(11))=(ZNOD(ICO(10))+ZNOD(ICO(12)))/2.
        ZNOD(ICO(14))=(ZNOD(ICO(13))+ZNOD(ICO(15)))/2.
        ZNOD(ICO(17))=(ZNOD(ICO(16))+ZNOD(ICO(18)))/2.
        ZNOD(ICO(20))=(ZNOD(ICO(19))+ZNOD(ICO(21)))/2.
        ZNOD(ICO(23))=(ZNOD(ICO(22))+ZNOD(ICO(24)))/2.
```

```
        ZNOD(ICO(26))=(ZNOD(ICO(25))+ZNOD(ICO(27)))/2.
      enddo
c-------------------------------------------------
c-----------------------------------------
c Sloan and Randolph's algorithm
c-----------------------------------------
       call renum
       write(*,*) 'Enter Setup1'
       call setup1(.true.)
       write(*,*) 'Enter diam'
       call diam
       minmax=10**9
       write(*,*) 'Enter reseq1 (node renumbering)'
       call reseq1
       write(*,*) 'Enter reseq2 (element renumbering)'
       call reseq2(.true.)
       write(*,*) 'Changing element numbering in IND(I,J)(Sub newnod)'
       call newnod
  321  continue
C----------------------------------------
C PRINTS THE CONECTIVITIES
C----------------------------------------
      DO 15 I=1,NEL
        write(70,200) I
        write(70,200) (IND(KK, I),KK=1,lnode27+1)
   15 CONTINUE
      close (70)
  200 FORMAT(28I6,2X)
  445 continue
C--------------------
C- End of subroutine
C--------------------
      END
```